Development of Fibre optic bio-/chemical sensors for Healthcare applications

LiangLiang Liu, MSc

Thesis submitted to the University of Nottingham
for the degree of Doctor of Philosophy
March 2019



Table of Contents

Abstract 7

Acknowledgement 10

List of abbreviations 11

Chapter 1 Fibre optic sensor in healthcare: The applications 14

1.1 Aims and objectives 15

1.2 The structure of the thesis 16

1.3 Novelty statement 17

1.4 Background and Related Work for the target biomarkers 19

1.4.1 The role of IgM in the body 19

1.4.2 The detection of antibodies 20

1.4.3 The production of CO_2 in the body 23

1.4.4 CO_2 measurement techniques 27

1.4.5 Relative humidity (RH) in healthcare 31

1.4.6 The role of ammonia (NH_3) in healthcare 33

1.4.7 Monitoring of fentanyl in healthcare 36

Chapter 2 Introduction of fibre optic sensor 39

2.1 Introduction 39

2.2 Optical fibre sensor components 40

2.2.1 Optical fibres 40

2.2.2 Light sources 50

2.2.3 Detectors 51

2.3 Classification of FOSs 53

2.3.1 Configuration of extrinsic FOS 53

2.3.2 Grating-based optical fibre sensor 55

2.4 Functional film deposition techniques 65
2.4.1 LBL deposition technique 65
2.4.2 Sol-gel technique 68
2.5 Gas diffusion through the porous silica film 71
2.6 Summary 72
Chapter 3 LPG sensor fabrication and characterisation 74
3.1 Introduction 74
3.1 Fabrication of LPG sensor 74
3.1.1 Point-by-point method 76
3.1.2 Amplitude mask method 80
3.2 LPG simulation using *Optigrating* 83
3.3 LPG temperature measurement 87
3.4 LPG strain measurement 93
3.5 LPGs RI measurement 96
3.6 Preparation of reflection LPGs 98
3.6.1 The formation of silver mirrors via chemical reaction 99
3.6.2 The fabrication of reflection LPGs 99
3.7 Conclusion 102
Chapter 4 Synthesis of nanoparticles for LPG biosensor development 104
4.1 Introduction 104
4.1 Synthesis of SiNPs 105
4.1.1 Materials and Methods 106
4.1.2 Result and discussion 108
4.2 Synthesis of AuNPs 112
4.2.1 Materials and method 113

4.2.2 Result and discussion 115
4.3 Conclusion 121
Chapter 5 Sensing film preparation for the fabrication of FOS 123
5.1 Introduction 123
5.2 Materials 123
5.3 LPG based biosensor for protein detection 124
5.3.1 LPG modification for biotin detection 124
5.3.2 LPG modification for IgM detection 126
5.4 Reflection mode fibre optic CO_2 sensor 127
5.4.1 Sol-gel based sensing film preparation 127
5.4.2 Polymer-based sensing film preparation 128
5.4.3 The coating of the sensing film on the optical fibre 128
5.4.4 The coating of the CO_2 sensitive film for fabricating of Fabry–Pérot interferometer (FPI) sensor 129
5.5 Preparation of FOS for NH_3 and CO_2 sensing 129
5.5.1 CO_2 sensing film preparation 129
5.5.2 NH_3 sensing film preparation 129
5.5.3 Coating of the optical fibre with the sensing film 130
5.6 LPG sensor incorporated with molecularly imprinted polymer (MIP) nanoparticles for the detection of carboxyl-fentanyl 130
5.6.1 Fabrication of LPG array sensor 130
5.6.2 Functionalisation of an LPG sensor for the detection of carboxyl-fentanyl 131
5.7 Conclusion 132
Chapter 6 Development of LPG based biosensors 134
6.1 Introduction 134

6.2 Definition of LPG biosensor parameters 135
6.3 Method 136
6.3.1 Thin film characterisation 136
6.3.2 Streptavidin detection 136
6.3.3 IgM detection in solution 137
6.3.4 Detecting IgM from blood serum 137
6.3.5 Experiment set-up 137
6.4 Results and Discussion 138
6.4.1 LBL film deposition 138
6.4.2 LPG characterisation 142
6.4.3 Streptavidin detection 146
6.4.4 IgM detection 152
6.4.5 IgM detection in blood serum 159
6.5 Conclusion 160
Chapter 7 Development of FOS for the measurement of CO_2 & RH from breath 162
7.1 Introduction 162
7.2 Method 163
7.2.1 Sensing mechanism for CO_2 163
7.2.2 Sensing mechanism for RH 163
7.2.3 Determination of the sensor parameters 164
7.2.4 Experimental set-up 165
7.3 Fibre-optic sensor (FOS) for the CO_2 measurement 168
7.3.1 Experimental procedure 168
7.3.2 Results and discussion 169

7.4 Fibre optic Fabry–Pérot interferometer (FPI) sensor for the simultaneous measurement of CO_2 and RH 190
7.4.1 Experiment procedure 190
7.4.2 Results and discussion 191
7.5 The measurement of CO_2 and RH from human breath 208
7.6 Conclusion 210
Chapter 8 The simultaneous measurement of CO_2 and NH_3 using FOS 212
8.1 Introduction 212
8.2 Method 212
8.2.1 Sensing mechanism 212
8.2.2 Sensor characterisation 214
8.2.3 Experiment set-up 215
8.3 Result and discussion 216
8.3.1 The measurement of CO_2 217
8.3.2 The measurement of NH_3 220
8.4 Conclusion 226
Chapter 9 The detection of carboxyl-fentanyl using LPG functionalised with MIP nanoparticles 227
9.1 Introduction 227
9.2 Method 228
9.2.1 Sensing based on molecularly imprinted techniques 228
9.2.2 Experimental procedure 229
9.3 Results and Discussion 230
9.3.1 MIP nanoparticles on the optical fibre 230
9.3.2 Temperature calibration of the LPG array 232

9.3.3 Detection of carboxyl-fentanyl 233
9.4 Conclusion 239
Chapter 10 Conclusion and future work 241
10.1 Summary of current work 241
10.2 Future work 245
Bibliography 247

Abstract

Sensing by using optical fibres is a promising approach for application in the healthcare field due to their small dimension, the capability of working in a harsh environment (i.e. high electromagnetic interference (EMI), corrosive environment) and potential for remote sensing. The possibility to measure clinically significant biomarkers would allow the diseases to be tracked in real time and supports diagnostic activities at clinical point-of-care (POC). This PhD thesis aims to demonstrate the versatility of the fibre optic sensor (FOS) for sensing of multiple clinical parameters including antibodies, gases (CO_2, relative humidity (RH) and NH_3) and potential drugs detection (fentanyl). Four types of FOSs are fabricated and included in the thesis, which are (I) a long-period fibre grating (LPG) based IgM sensor, (II) a Fabry–Pérot interferometer CO_2 sensor for the simultaneous measurement of gaseous CO_2 and RH, (III) a reflection sensor for simultaneous measurement of gaseous CO_2 and NH_3, (IV) an LPG sensor for detecting carboxyl-fentanyl from liquid solution. Each sensor is prepared by combining an optical fibre sensing platform with the developed sensing materials for measuring of one or more of the mentioned parameters. Developed sensors were characterised in laboratory conditions for evaluating the critical parameters of the sensor, i.e. sensitivity, specificity and response time.

The developed IgM sensor is fabricated by depositing composite nanoparticles with a silica core and gold shell structure to create a porous structure and large surface area for IgM interaction to the receptors anchored on the shell. The sensor demonstrates the capability of detecting IgM in a wide concentration range from 15.6 µg/mL to 1000 µg/mL with limit of detection (LOD) of 0.015 ng/mm^2 and a minimum detected concentration of 15.6 µg/mL. It shows a high specificity to IgM with a negligible response to the interfering protein, i.e. Bovine serum albumin (BSA). The sensor with such detection range and LOD can potentially be applied for the diagnostics of IgM related diseases such as selective IgM deficiency (SIgMD) and neonatal infection. The ability to monitor the binding process kinetically supports the application of the sensor in POC diagnostics.

A Fabry–Pérot interferometer (FPI) hybrid sensor is prepared by combination of the FPI with a colourimetric measurement for measuring RH and CO_2. A sensing film comprised of silica matrix doped with thymol blue and tetramethylammonium hydroxide (TMAH) is dip coated on the tip of an optical fibre forming a cavity for the FPI sensor. The sensor responds to the concentration of CO_2 range from 0-6 % and RH level from 0 to 90 % with negligible cross-talk between the two parameters. The sensitivity for both parameters is 18 % of reflection value change per 5 % of CO_2 and 0.14 nm per 1 % of RH. It is immune to the temperature in the tested range from 25 ℃ to 40 ℃. Due to the slow response time, 98s for CO_2 and 32s for RH, the sensor is applicable to measure the CO_2 and RH in an application where the response time is not critical such as transcutaneous CO_2 ($TcCO_2$) measurement. The developed sensor was successfully implemented to measure breath gases from a healthy human volunteer with a percent error of 3.1 % and 2.2 % for CO_2 and RH respectively when taking the commercial datalogger (33 BLG, CO_2 Meter, USA) as the golden standard. The percent error is the difference between the measurement from developed sensor and the reference sensor, divided by the value of reference sensor and multiplied by 100 %.

The sensing of gaseous NH_3 in this thesis is achieved by using the sensitive dye Tetrakis-(-4-sulfophenyl) porphine (TSPP) that changes its colour after the interaction with NH_3. The FOS for the simultaneous measurement of NH_3 and CO_2 is fabricated by incorporating two sensitive dyes, TSPP and thymol blue into one fibre detection system. Two dyes are separately doped into a sol-gel matrix and an ethyl cellulose (EC) plastic film and coated on the two ends of a 2x2 optical fibre coupler. The two dyes have different spectral properties with distinctive absorption wavelengths across the detection range that facilitates detection of the target gases. The sensor exhibits a sensitivity of ~15 % of increase in intensity for responding ~5 % of CO_2 and sensitivity of -0.003 /ppm for gaseous NH_3. It shows no cross-talk between NH_3 and CO_2 measurement and demonstrates the ability to measure both gases simultaneously. The LOD for NH_3 is 3.9 ppm which is lower than the required concentration for breath analysis in diagnosis of diseases such as renal disease or stomach ulcers; therefore the sensor is not ready yet for breath analysis.

An LPG functionalised with molecularly imprinted polymer (MIP) nanoparticles is reported for the detection of carboxyl-fentanyl. A reference LPG was inscribed into a same optical fibre for compensating the temperature effect during the measurement. The sensor is tested in a concentration range from 0 ng/mL to 1000 ng/mL and shows a minimum detected concentration of 50 ng/mL. The wavelength shift is 4.95± 0.3 nm at a concentration of 1000 ng/mL after compensating the temperature effect.

From the research described in this thesis, the versatility of the FOS platform in measuring clinical biomarkers for the diagnostic purpose with the ability to measure multiple parameters simultaneously is demonstrated. FOS can be applied to meet unmet clinical needs. For example, measuring the relevant biomarker in a particularly clinical condition such as MRI scanning room in which conventional electronic sensors interfere with the electromagnetic field. FOS is a low-cost sensor and can be made as a portable sensor for home and emergency use. The FOS is believed having great impacts in the future healthcare field as it offers a competitive sensor in diagnosis and monitoring, especially in the home use and wearable sensors market due to its miniaturised size, excellent biocompatibility and immunity to electromagnetic interference (EMI). It also provides a new opportunity to study phenomenon or conduct research which has not been studied yet due to the limitations of conventional sensors (i.e. bulky size, non-compatible to biological samples and effect of EMI).

Acknowledgement

First of all, I would like to express my sincere gratitude and deep appreciation to my supervisors Prof. Stephen P. Morgan, Dr Sergiy Korposh and Dr Ricardo Goncalves Correia for the support of my PhD study, for their immense knowledge, motivation and patience in guiding me in developing my research, writing and presentation skills. It is genuinely my great honour and luck to have all of you during my PhD study.

Besides, I would like to thank my internal assessor Dr Kevin Webb for his insightful comments and encouragement for my research during the annual assessment.

I thank the rest of group members David Gomez, Ulises Hernandez, Jiri Hromadka, Chong Liu, Hattan Ballaji, Wan Zaki, Sandor Erdody, Chenyang He and Chalani Abeywardena for creating the warm environment.

Moreover, I would like to say thank you for our collaborators: Dr Paddy Tighe, Dr Andrew Norris from the School of Medicine, University of Nottingham for providing advice from a clinical perspective, Prof. Sergey Piletsky and his research group from Department of Chemistry, University of Leicester for providing the carboxyl-fentanyl sample and MIP nanoparticles.

I want to thank Engineering and Physical Sciences Research Council (EPSRC) for funding my PhD.

Thanks to the Nanoscale and Microscale Research Centre (nmRC), University of Nottingham for providing the training and permission to access the facilities.

List of abbreviations

(Abbreviations are sorted in alphabetical order)

11-Mercaptoundecanoic acid	11-MUA
3-aminopropyltriethoxysilane	APTES
3-Dimethylaminopropyl-N′-ethylcarbodiimide hydrochloride	EDC
Arterial carbon dioxide tension	$PaCO_2$
Bovine serum albumin	BSA
Charge-coupled device	CCD
Chemical Vapour Deposition	CVD
Dynamic light scattering	DLS
Electromagnetic interference	EMI
End-tidal CO_2	$ETCO_2$
End-tidal CO_2	$ETCO_2$
Enzyme-linked immunosorbent assay	ELISA
Ethyl cellulose	EC
Fabry–Pérot interferometer	FPI
Fibre Bragg grating	FBG
Fibre optic sensor	FOS
germanium-oxygen deficiency centre	GODCF

Gold nanoparticles	AuNPs
Heat moisture exchanger	HME
Immunoglobulin M	IgM
Intensive Care	IC
Isopropyl alcohol	IPA
Layer-by-Layer	LBL
linearly polarised	LP
Long period fibre grating	LPG
2-(N-Morpholino)ethanesulfonic acid hydrate	MES hydrate
Magnetic resonance imaging	MRI
Molecularly imprinted polymer	MIP
Nondispersive infrared sensor	NDIR
Nanoparticles	NPs
N-hydroxysuccinimide	NHS
Organically modified silica	Ormosil
Polydispersity index	PDI
Phase matching turning point	PMTP
Point-Of-Care	POC
Poly(allylamine hydrochloride)	PAH
Radio frequency interference	RFI

Refractive index	RI
Refractive index unit	RIU
Relative humidity	RH
Scanning electron microscopy	SEM
Selective IgM deficiency	SlgMD
Silica nanoparticles	SiNPs
Surface Plasmon Resonance	SPR
Tetraethyl Orthosilicate	TEOS
Tetrakis-(-4-sulfophenyl) porphine	TSPP
Tetramethylammonium hydroxide	TMAH
Transcutaneous CO_2	$TcCO_2$
Transmission electron microscopy	TEM
Triethoxymethylsilane	MTEOS
Ultraviolet	UV

Chapter 1 Fibre optic sensor in healthcare: The applications

Biosensors have always been and will continuously play a vital role in the healthcare field for supporting clinical diagnosis and health monitoring. There are numerous examples of such sensors around our life, for example, a medical thermometer measures body temperature, a blood pressure monitor measures blood pressure and a pregnancy test kit detects human chorionic gonadotropin (HCG) to indicate pregnancy. Their importance is obvious for the well-being of people, and from that emerges a huge market of multi-billion dollars. The biosensors market was valued at USD 15.96 billion in 2016 and is estimated to reach USD 27.06 billion by 2022 [1]. There is an emergence of nanotechnology-based biosensors and an increased demand for home-based Point-Of-Care (POC) devices according to the market research report from MarketsandMarkets™ [1].

Sensors based on optical fibre are of interest in healthcare applications due to their numerous advantages over conventional sensors. They usually have compact size and require physically small measurement volume; this offers greater geometric versatility and allows the application into arbitrary shapes. Optical fibres made of silica possess properties of being chemically inert, dielectric, and immune to electromagnetic interference (EMI). These properties provide the fibre optic sensor (FOS) with inherent advantages over conventional electrical and electronic sensors as they can be applied in harsh environments such as corrosive, high voltage, high EMI environment [2]. One example is the application in an MRI scanner, in which context electronic transducers are generally hazardous to the patient. The FOS has been used to monitor respiration in MRI scanners [3]. Moreover, they can be easily multiplexed so that such sensors can be made to measure multiple parameters or distributed measurement [4]. In addition, they are compatible with communication systems and capable of carrying out remote sensing for inaccessible sites. The numerous advantages of light over electronic systems have boosted their application in healthcare sectors [5-7]. The advantages render the potential and bright future of

FOS in the biosensor market as their capability of being a small, portable and wearable sensor.

Regarding biomedical application, FOSs that measure temperature, pressure and biomarkers have been investigated for supporting clinical diagnosis and monitoring in healthcare [4, 6, 8]. For example, FOS pressure sensors have been applied for the measurement of pressure and forces in *vivo* including cardiovascular, urologic and colonic diagnostic procedures, surgical procedures and monitoring of invasive treatments [9-11]. The FOS temperature sensor is utilised *ex vivo* to monitor the distributed temperature inside liver tissue during a radiofrequency ablation procedure [12]. Such sensors offer useful information for a clinician to adjust the treatment to the tissue undergoing ablation. The FOS biosensors are typically applied *in vitro* to detect the biomarkers such as pH [13], antibodies [14], antigen [15] related to specific diseases. Those sensors usually require an invasive process to sample body fluids such as blood or cerebrospinal fluid. However, for biomarkers such as gases, which are easy to sample, sensors can be non-invasive. Besides, the FOS biosensors has been found useful in the application of non-invasively monitoring physiological conditions such as respiration rate and heart rate [16] as well as blood flow measurement [17].

1.1 Aims and objectives

This research study aims to investigate whether FOS can be turned into a biosensor that detects a specific clinical parameter and be a useful diagnostic tool in the clinical POC. Different coatings are used/developed to measure some critical clinical parameters that include immunoglobulin M (IgM), CO_2, relative humidity (RH), NH_3 and fentanyl. The optical fibre sensing platforms includes Long-period grating (LPG) sensors and fibre-tip based reflection sensors. The possibility of sensing more than one parameter simultaneously by using an FOS is also investigated.

To achieve the aims mentioned above in terms of sensor development, the objectives should be met as follows:

- To develop an FOS that detects specifically human IgM with a minimum detectable concentration < 20 mg/dL that can be potentially used for the detection of IgM from blood sample.
- To develop an FOS that capable of measuring CO_2 and RH simultaneously with a detection range up to 5 % of CO_2 and 90 % of RH that is suitable for the breath gas measurement in supporting endotracheal intubation.
- To develop an FOS that can measure CO_2 and NH_3 simultaneously for the potential application in breath gas analysis.
- To investigate the possibility of detecting fentanyl or fentanyl analogues by using an FOS.

1.2 The structure of the thesis

This thesis composes of 10 Chapters that describe the work conducted during the PhD study focused on development of FOS for the detection of antibodies (IgM), anaesthetic drug (fentanyl) and body exhausted gases (CO_2, RH and NH_3) with the aim of applications in healthcare.

Chapter 1 introduces the background and motivation of the work; describes the clinical significance of the target biomarkers (IgM, CO_2, RH, NH_3 and fentanyl) as well as the review of current technology applied in commercial products and the development of FOS for their detection.

Chapter 2 consists of an introduction and literature review of the FOS technology including typical sensor configuration, coating film preparation. Different types of FOS platforms including long period grating (LPG) sensor, tip-based sensor and other evanescent field sensors, which are typically used for chemical sensing are introduced.

Chapter 3 explains the theoretical background of an LPG sensor, covers the simulation and experimental results of fabrication and characterisation of an LPG sensor.

The content of Chapter 4 describes the synthesis of nanoparticles for the LPG-biosensor application. Two types of nanoparticles which are silica nanoparticles (SiNPs) and gold nanoparticles (AuNPs) are prepared via chemical synthesis methods.

The two particles can form a composite nanoparticle with a silica core and gold shell that provides extinction property for the application in biosensing.

Chapter 5 summarises the fabrication and functionalisation processes of the FOSs developed during the PhD study, including (i) all the chemical materials, (ii) sensing film preparation and the coating of the film onto an optical fibre.

Chapter 6 demonstrates an LPG based biosensor fabricated by depositing the prepared nanoparticles and functionalised with relevant receptors for the detection of streptavidin and human IgM. The established IgM sensor is validated in the human blood serum.

In Chapter 7, the development of a fibre optic CO_2 sensor is presented by using a pH indicator, thymol blue. A hybrid sensor that combines Fabry–Pérot interferometer (FPI) and the colourimetric dye is reported for the simultaneous measurement of CO_2 and RH. The FPI sensor is successfully applied to measure the CO_2 and RH from human breath.

Chapter 8 describes an approach to integrate the two colourimetric dyes (thymol blue and TSPP) into one fibre detection system for measuring two gases, CO_2 and NH_3, simultaneously.

Chapter 9 demonstrates the progress achieved in developing fentanyl sensor based on LPG platform. An LPG array sensor is presented with one grating functionalised with molecularly imprinted polymer (MIP) nanoparticles for the detection of fentanyl and another bare LPG used as a reference sensor for compensating the temperature effect during the measurement. The sensor is demonetrated sensitivity to carboxyl-fentanyl in this chapter.

Chapter 10 includes the conclusion and discussion of the above chapters, a description regarding future work is done in this chapter.

1.3 Novelty statement

The thesis introduces 4 FOSs that were fabricated by incorporating different chemical coatings into an optical fibre sensing system for sensing one or multiple parameters.

The detection of human IgM by using an LPG sensor is for the first time reported in Chapter 6 in which the LPG was surface coated with anti-IgM anchored composite nanoparticles which are made of SiNPs surrounded by AuNPs forming shell structure. The developed sensor exhibits a high sensitivity, wide detection range and specificity to human IgM and is a useful tool in the diagnosis of IgM related diseases.

The previous work on CO_2 sensing with a pH dye was done by doping the dye into a matrix film and coating on a cladding-removed optical fibre sensing system. Such a sensor only measures one parameter. A novel FPI CO_2 sensor is presented in Chapter 6 by dip coating a pH dye (thymol blue) doped silica film prepared via a sol-gel method on the tip of an optical fibre. The tip-based sensor further reduced the volume of the sensor size and is more robust in the application, especially when the sample volume is small. Most importantly, the FPI sensor combines the colourimetric method and FPI technique and allows the measurement of CO_2 and RH simultaneously. For the first time to the best of my knowledge, multiple sensing by using a single film is reported, and it has potential to become the smallest sensor in the market that can measure both CO_2 and RH simultaneously. Such a sensor is successfully applied to measure CO_2 and RH from human breath.

An FOS that can simultaneously detect more than one gas species will enable a cheap, portable sensor to be applied on the breath gas analysis. A novel approach incorporates two sensitive dyes (TSPP and thymol blue) with different spectral information into one optical fibre detecting system to simultaneously detect CO_2 and NH_3 is described in Chapter 8.

There are limited papers published for the detection of drugs based on FOS. The FOS for detection of fentanyl or fentanyl analogues has not yet been reported. A carboxyl-fentanyl sensor based on LPG modified with MIP nanoparticles is presented in Chapter 9. It is configured with an LPG array sensor that contains two LPGs with one functionalised with MIP nanoparticles for the detection of carboxyl-fentanyl (molecularly similar to fentanyl with carboxyl group) and the second remains unmodified for compensating the temperature effect for the modified LPG. Such a sensor shows an encouraging result in detecting the carboxyl-fentanyl with the minimum detected concentration of 50 ng/mL.

1.4 Background and Related Work for the target biomarkers

1.4.1 The role of IgM in the body

Antibodies are important biomarkers in human body fluids. They participate in the humoral immune response and their levels increase during the immune system responses to pathogen infection. B cell is one type of lymphocytes cell that composes the immune system of the body, it has antibody molecules in cytoplasmic membranes and will secrete the molecules into the blood after exposure to appropriate antigen [18]. The level of antibody in the blood can be used as an indicator of infectious disease [19].

An antibody is also known as an immunoglobulin (Ig), and its isotypes or classes in blood named as IgA, lgD, lgE, lgG and lgM, respectively, depending on different types of heavy chains. The body has two types of immune responses to the invading of antigen, called primary and secondary immune response. The primary immune response occurs when a B cell sees an antigen for the first time. IgM is produced in the primary immune response and plays a significant role in fighting infection; it is the earliest antibody to appear in the course of an infection [20]. The secondary immune response occurs when the B cell sees an antigen a second time, and the predominant antibody produced in this stage is IgG. As IgM molecule does not contain the highly specific binding sites of the IgG molecule, this permits the B cells to produce IgM rapidly during a primary immune response, while the IgG molecule takes days to produce in quantity [18]. The pentameric structure of IgM (Fig 1.1) theoretically provides ten free antigen-binding sites and high avidity binding and can quickly clear antigens from the bloodstream during the initial stages of an infection.

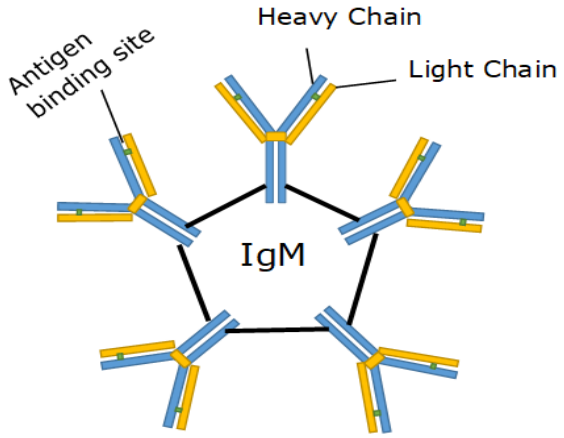


Fig 1.1 Schematic illustration of pentameric structure of IgM.

IgM is mainly found in blood and lymph fluid, and it is a very effective neutralising agent in the early stage of the disease. The level of IgM has significant clinical value in diagnosis of certain diseases. For example, because IgM antibody does not cross placenta, it can indicate recent infection or intrauterine infection when it appears in a neonate's serum [21, 22]. IgM also plays a vital role in rapid diagnosis of Dengue virus infection as it appears as the initial immune response to a primary infection a few days after the onset of Dengue fever [23]. In addition, IgM regulates autoimmunity and atherosclerosis and deficiency of IgM indicates increased susceptibility [24]. SIgMD is an immune disorder that is associated with serious infection. The deficiency of IgM in blood, usually < 20 mg/dL [25], can develop into prolonged or life-threatening infection to the patients (often infants and small children).

1.4.2 The detection of antibodies

The common method used in clinical practice for the detection of antigens or antibodies is based on the enzyme-linked immunosorbent assay (ELISA) [26]. Dependent on the exact method used, the technique usually involves multiple sequential incubations for long periods (60-90 mins each) and multiple wash steps, resulting ultimately in a colourimetric readout which is proportional to the level of the antigen or antibody present in the original sample. An example of such a process is illustrated in Fig 1.2.

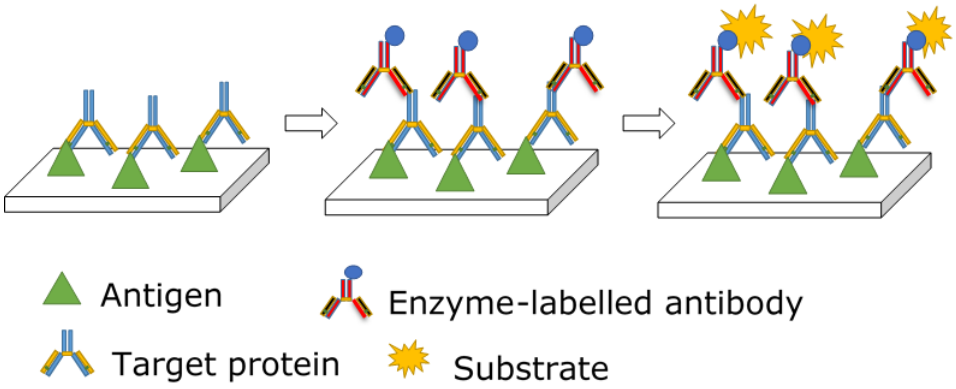


Fig 1.2 Schematic of a typical direct ELISA method; a target protein is immobilised on the surface of microplate wells and incubated with an enzyme-labelled antibody to the target protein (or specific antigen to the target antibody). After washing, the activity of the microplate well-bound enzyme is measured.

The readout requires a dedicated optical plate reader for translating the readings. Moreover, the multi-step nature of the procedure and requirement for enzyme-labelled antibodies is a significant weakness and does not allow real-time detection of target molecules. Fast and accurate detection of IgM in patients' serum would enable early screening of SIgMD and early intervention may help prevent some of the complications seen later in life. Some infections due to the deficiency of IgM in infants and small children such as bacteremia can be life-threatening.

To satisfy the need for real-time POC testing, researchers have focused on the development of different protein measurement methods in order to obtain accurate, fast sensors that would be able to replace the current ELISA method. Surface Plasmon Resonance (SPR) has been extensively used for quantitative measurement with a sensitivity of the order of µg/mL [27]. However, a drawback is the relatively high price and bulky optical system that usually limits its application to the clinical laboratory. Quartz crystal microbalance (QCM) [28] is also an important label-free method for the detection of antibodies. The shift of resonance frequency is induced by the mass change of crystal resonator after binding of antibodies. However, the viscosity of the analysed liquid also contributes to the frequency shift. To distinguish the mass-affected frequency shift with the contribution of liquid, a more expensive impedance analyser is required. Flow cytometry [29, 30] has been used for the detection of antibodies. The techniques can be used for detection of antibodies which are not be

detected by ELISA (e.g. glycospecific antibodies). However, the technique is not widely used due to the high cost compared with other alternatives. Planar waveguide sensors are also widely applied in detection of biomolecules [31]. The performance of this type of sensor strongly relies on the choice of substrate material and the quality of the deposited film. Fluorescence has been used for detection of nucleic acid on planar optical waveguides [32]. The use of fluorescent labels in the context of planar optical waveguide allows better specificity. The disadvantages of fluorescence detection include the rapid photobleaching of fluorescent dyes conjugated to the biomolecules of interest and the potential loss of activity of the biomolecules when chemically conjugated with fluorescent dyes. Microfluidic chips consist of micro-channels with sub-millimetre diameter have been applied in immunology and antibody screening [33]. The manufacture of such devices usually done in clean rooms using specialised lithography equipment [34], which are not accessible for non-specialist labs.

To satisfy the requirements of POC devices, it is not only sensitivity and response time that have to be taken into account, but also the size and simplicity of the sensor. In this regard, an FOS, due to its small size, provides an advantage in terms of application in POC devices used in the clinic or community. In addition, the optical fibre is immune to the interaction of electromagnetic field providing a robust response in environments containing electronic devices. There are diverse FOSs with different structures have been applied on sensing of proteins, table 1.1 lists some examples based on different sensing principle. Among those sensors, tapered, cladding removed, tip-based and grating-based sensor have been applied in combination of SPR, fluorescent sandwich and fluorescent competitive assay for the detection. An LPG biosensor is appealing in the detection of biomolecules because of the high sensitivity, label-free and real-time measurement.

Table 1.1 The application of FOSs in detection of biological molecules.

FOS	Target	Detection principle	LOD	Reference
Tapered fibre	Staphylococcus aureus Protein A	Fluorescent sandwich assay	1 ng/mL	[35]
Fibre SPR	Myoglobin	SPR	2.9 ng/mL	[36]
Tapered fibre	BSA	Intensity (RI)	10 fg/mL	[37]
Cladding removed fibre	BSA	Dye-protein complex absorption	2.5 µg/mL	[38]
Fibre tip	IgG	Fluorescent competitive assay	20 fM	[39]
LPG	*Escherichia coli* (*E. coli*)	RI	10^3 cfu/mL	[40]

1.4.3 The production of CO_2 in the body

CO_2 plays a vital role in the healthcare field. It is commonly used in the treatment procedure; for instance, in stimulating breathing in human neonates [41], in CO_2 cryotherapy for the treatment of Barrett's Esophagus and associated neoplasia [42]; as an insufflation gas for minimally invasive surgery [43] and during general anaesthesia to prevent postoperative atelectasis [44]. Besides these, it has a distinct position of diagnostic application in clinic intensive care units such as in detection of microbial growth during patient's blood culture for diagnosis of bacteremia [45, 46].

CO_2 in the human body is produced as a by-product of cell metabolism. The human body composes trillions of different functional cells and the cooperation between the working functional cells support the diverse activities of the human body. Each cell

requires ‘food’ to provide energy for maintaining its biological activities. The ‘food’ is obtained from the digestive system where the carbohydrate that is eaten is broken down into glucose ($C_6H_{12}O_6$) under the action of enzymes [47, 48]. The glucose is then undergoing oxidation in the cell and produces adenosine triphosphate (ATP) which is the energy required [49]. The chemical process can be explained using the following equation:

$$C_6H_{12}O_6 + 6\,O_2 \rightarrow 6\,CO_2 + 6H_2O + 25\,ATP \quad (1.1)$$

The oxidation process is also the cell breath process in which the cell consumes oxygen (O_2) and produce carbon dioxide (CO_2). The supply of O_2 and the release of CO_2 from the cell occur between blood in systemic capillaries and the cells. This process of gas exchange is also known as internal respiration. The direction of gas exchange is opposite for the two gases. O_2 moves rapidly out of the blood through the systemic capillary membrane into the cell, and at the same time CO_2 leaves the cells and enter the systemic capillary (illustrated in Fig 1.3). The movement of gases is a diffusion process, which is driven by the partial pressure differences of each gas. Systemic capillary has a higher partial pressure of O_2 (Po_2 100 mmHg) than that of the cells (Po_2 40 mmHg), and thus O_2 diffuses from the blood to the cells. On the other hand, the partial pressure of CO_2 in the cells (Pco_2 46 mmHg) is higher than that of the systemic capillary (Pco_2 40 mmHg) so that it moves from the cells to blood [50]. Meanwhile, part of the CO_2 produced by the skin tissue will diffuse through the skin barrier to the air under the drive of the partial pressure difference (the Pco_2 in the air is about 0.3 mmHg).

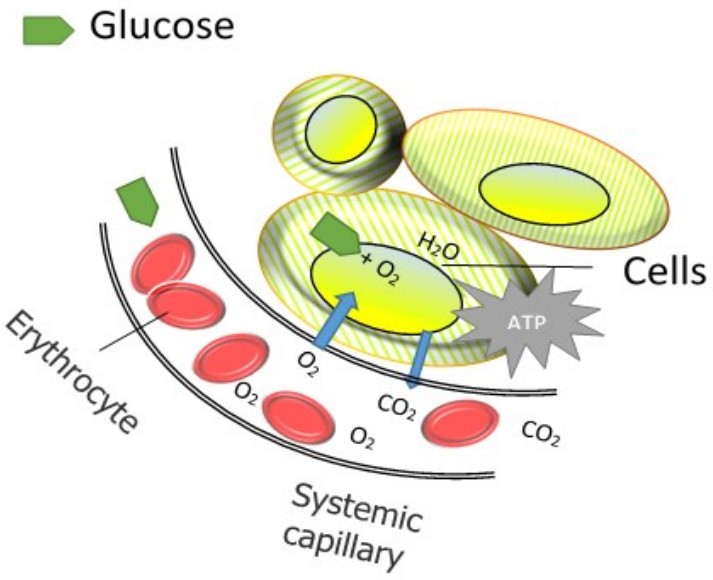


Fig 1.3 Internal respiration process; gases exchange between cells and systemic capillary.

CO_2 is carried in blood in three formats: dissolved (CO_2), as bicarbonate ions (HCO_3^-), and in combination with proteins as carbaminohaemoglobin, the majority of them (about 70 %) are transported in the format of bicarbonate ions [50]. The blood plasma that contains CO_2, also known as venous blood, flow to the lungs through the pulmonary circulation.

The produced CO_2 is ultimately expelled from the lungs through a gas exchange process called external respiration (Fig 1.5). As the venous blood arrives, the CO_2 starts to diffuse into the alveoli from the blood plasma under the drive of differential partial pressure (46 mmHg to 0.3 mmHg), and further moves from alveoli to out of mouth through the passageway of bronchioles to bronchi, trachea and mouth during the exhalation (illustrated in Fig 1.4). The O_2 is inhaled from mouth to alveoli through the passageway but in the opposite direction. It further passes through the capillary membrane into the bloodstream as the partial pressure in the air (Po_2 160 mmHg) is higher than it is in the blood (Po_2 40 mmHg). The blood that contains more O_2 after gas exchange will flow to the tissue of different parts of the body for supporting cell activities.

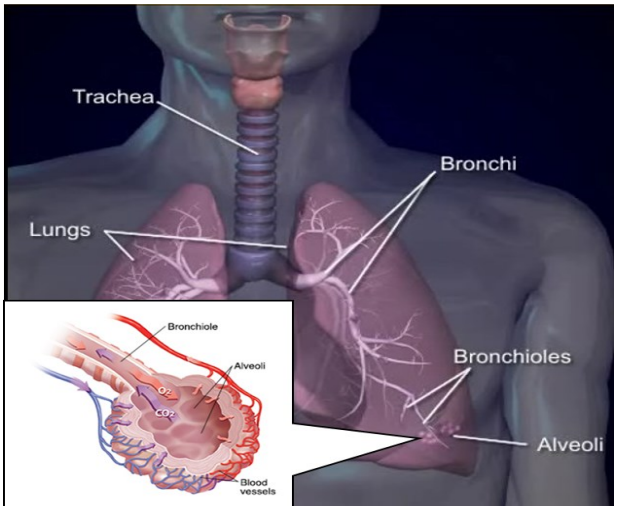


Fig 1.4 Schematic respiration system of the human body; Image is obtained from the publication of Thibodeau [50].

The internal and external respiration compose the respiration process of the body; the O_2 participates in the cell metabolism process and the produced CO_2 is transported out of the body as waste.

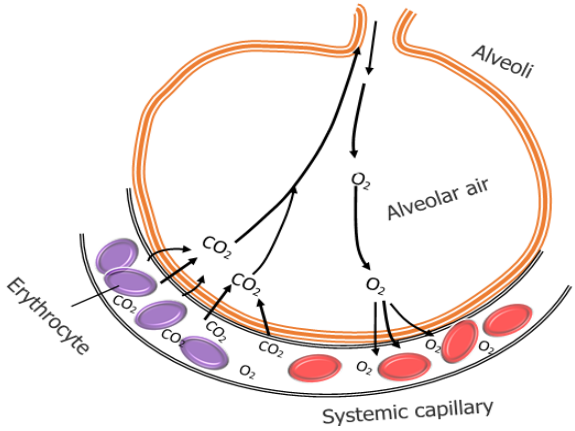


Fig 1.5 External respiration process; gas exchange occurs between systemic capillary and alveoli of the lung.

CO_2 dissolves in blood plasma, some of the CO_2 molecules associate with water (H_2O) to form carbonic acid (H_2CO_3). Once formed, some of the H_2CO_3 molecules dissociate to form hydrogen (H^+) and bicarbonate ion (HCO_3^-). The two processes are both reversible, and CO_2 molecules that enter the blood can continuously be removed from the blood. The above chemical activities can be summarised as:

$$CO_2 + H_2O \rightleftharpoons H_2CO_3 \rightleftharpoons H^+ + HCO_3^- \quad (1.2)$$

The transport of CO_2 plays an important and necessary role in regulating the pH of the blood [51]. In the healthy condition, the body has great control over its acid-base balance by altering alveolar ventilation and thus the elimination of CO_2. Normal pH has a range from about 7.38 to 7.42 [51]. However, in some pathological conditions such as asthma or chronic obstructive pulmonary disease (COPD), the functionality of lungs is affected and, as a result, the CO_2 cannot be fully released through breathing. The retention of CO_2 in blood will cause a lower pH of blood and lead to respiratory acidosis that can become life-threatening if left untreated [2].

End-tidal CO_2 ($ETCO_2$) is the partial pressure or maximal concentration of CO_2 at the end of an exhaled breath; it has been used to evaluate the status of pulmonary diseases such as COPD and asthma [52]. Moreover, $ETCO_2$ has been commonly used to verify the placement of breathing tubes in patients' lungs during endotracheal intubation and to detect inadvertent oesophageal intubation [53] during the procedure of assisted ventilation. CO_2 moves from the lungs and out through the tube if it is properly placed and so an absence of CO_2 can be used to indicate incorrect intubation.

The transcutaneous CO_2 ($tcCO_2$) is a measurement of CO_2 released from skin that has a good correlation with arterial carbon dioxide tension ($PaCO_2$) [54]. It allows a non-invasive measurement for determining the $PaCO_2$ for clinical application such as in monitoring the sleep of children [55], in monitoring ventilation [56], and in predicting the pressure ulcers in ischemic skin tissue [57]. As the tissue is underpressurised, the systemic capillary beneath the skin is occluded so that the gas exchange in Fig 1.3 is cut off resulting in the accumulation of CO_2 in the tissue. As a result, the $tcCO_2$ increase.

1.4.4 CO_2 measurement techniques

1.4.4.1 Non-dispersive infrared CO_2 sensor

Commercial CO_2 sensors such as non-dispersive infrared (NDIR) have been widely used at the POC to monitor patients' breath CO_2 level. NDIR relies on the strong absorption of CO_2 at specific wavelengths (2600 and 4300 nm) [58] and measures the gas density inside a sample chamber. Capnography is a type of NDIR sensor for the

measurement of CO_2 commonly applied for breath analysis as its fast response time enables the capture of CO_2 levels from breath-to-breath [59]. The commonest type of capnography device in clinical use is the "sidestream" design, in which expired gas is withdrawn from the breathing circuit and analysed in a distant chamber. This process has a number of limitations due to sampling rates, transfer times and different conditions in the chamber compared to the breathing circuit, which can lead to inaccuracies. "Mainstream" analysis is also available but requires relatively complex devices in the patient circuit. Both mainstream and sidestream types can only measure CO_2 in expired gas outside the patient when the true measure of interest is the concentration of CO_2 in alveolar gas. As such, measurement should ideally take place as close to the alveolus as possible, i.e. within the airways themselves. This is particularly true for neonates and infants. Current capnography devices generally are bulky and relatively expensive, which limits their use outside the operating room or intensive care environment. Many critically ill patients require CO_2 measurement either before arrival in hospital or during transfers and therefore a low-cost portable device would be beneficial.

1.4.4.2 Colourimetric CO_2 sensor

There are commercially available colourimetric sensors such as Easy Cap® detector (MedTree, UK), a disposable sensor for detecting $ETCO_2$ which is used to confirm correct tracheal intubation [60]. This type of sensor is cheap and portable and has been used by paramedics in emergencies to indicate correct tube placement. However, it only indicates CO_2 qualitatively or semi-quantitatively, and therefore cannot be used to help control CO_2 levels.

1.4.4.3 Semiconductor and Electrochemical CO_2 sensor

Semiconductor sensors comprise of metal oxide which absorbs CO_2 on its surface leading to a change of conductivity [61]. Due to the simplicity and scalability, such sensors are usually cheap but lack specificity since other gases such as water and volatile organic compounds may be absorbed on the oxide surface and provide false measurement.

The Severinghaus CO_2 electrode [62] is the most common electrochemical sensor which comprises a pH electrode in contact with a layer of bicarbonate solution encapsulated by a thin plastic CO_2 permeable membrane. CO_2 diffuses through the membrane and equilibrates with the inner bicarbonate layer leading to a change of pH that is then detected by the pH electrode. The probe is neither robust (slow response time, interference of acidic and basic gas samples, effects of osmotic pressure caused by the variable salt condition in the liquid sample) nor cheap.

1.4.4.4 FOS CO_2 sensor

The compact size of the FOS renders the ability to measure CO_2 as close to the alveolus as possible would provide an important advance of current standards of care. It would allow measuring CO_2 quantitatively that would be beneficial for clinicians in the diagnosis of tracheal intubation and assessment of pulmonary diseases. The current development of FOS for measuring of CO_2 utilises either the physical property or chemical property of CO_2; The physical property of CO_2 is that it strongly absorbs specific wavelengths of infra-red light [58]. The sensing mechanism of FOS using the physical property relies on the interaction of light that propagates inside of the optical fibre with the target gas, and the sensitivity depends on the absorption path length. The development of such sensor can be achieved by the direct interaction of light with CO_2 via a gas absorption cell such as White cells [63] or by evanescent field absorption such as a D-shape optical fibre [64]. The White cells provide multiple optical paths with a long absorption path length that offers a high sensitivity but are expensive and bulky. D-shape FOS suffers from low sensitivity due to the low power fraction of light in an evanescent field. Microstructure fibres have been used to develop such gas sensors as they provide sufficient interaction of the gas with light [65]. Hollow-core microstructured optical fibre allows the light directly to interact with the gas inside of fibre core for gas sensing. However, the response time is limited by the diffusion of gas into fibre core with the highest response time about 40 s [66]. Silica suspended-core photonic crystal fibre (PCF) has a large fraction of evanescent field and has been exploited for CO_2 gas sensing, the CO_2 in the air hole of optical fibre interacts with evanescent field leading to absorption change of light [67].

Regarding the chemical property of CO_2 for sensing purpose, it is an acid gas that dissolves in water forming carbonic acid which reduces the pH value of water. Based on the chemical property, the optical fibre sensors consists of pH-sensitive dyes such as thymol blue [68], phenol red [69] or fluorescent compounds such as 8-hydroxy-pyrene-1, 3, 6-trisulfonate (HPTS) [70] are reported (summarised in Table 1.2). The pH dyes or fluorescent compounds change their spectral properties according to the degree of the pH change induced by CO_2. In addition, amine functionalised silica has been applied as an adsorbent material for CO_2 sensing in which an LPG sensor was employed as the sensing platform to detect the RI change induced by CO_2 [71].

Table 1.2 The current development of FOS for CO_2 measurement based on the chemical method.

Sensing element		Optical Fibre platform	Range	LOD	Reference
pH indicator	thymol blue	cladding removed	0-100 %	> 0.1 %	[68]
	phenol red	cladding removed	0-100 %	0.03 %	[69]
	methyl red	cladding removed	0-100 %	0.01 %	[69]
	m-cresol purple	glass substrate	0-4 %	N/A	[72]
Fluorescent compound	HPTS	Tip-based	0.03-30 %	0.02 %	[70]
Adsorbent material	amine-modified nanoporous silica foams	LPG	10-90 %	0.75 %	[71]

The FOS based on the physical property of CO_2 has stable signal output, capability of long-term monitoring of signal and prolonged sensor lifespan. However, such an FOS requires a large sensing area to increase the signal to noise ratio, which is usually obtained by increasing the length of optical fibre, i.e. a few meters. The requirement

of a longer, specific wavelength of light, the corresponding detector and optical fibre increase the cost of such a sensor. On the other hand, for the chemical-based FOS, the colour change of dyes occurs at the visible wavelength range and the optic component and the chemicals required are relatively cheap. Crucially, the large absorbance change of the dye after interacting with CO_2 allows the fabrication of a thin film with small size. Such a film can be deposited on the optical fibre, for example on the tip to make a sensor probe with a compact sensing region. The drawbacks of such a chemical-based sensor are specificity and short lifespan (usually a week).

1.4.5 Relative humidity (RH) in healthcare

Humidity is important in a healthcare environment as not only does it affect the operation of expensive electrical equipment due to the static spark, but more importantly, affects the comfort and health of the patient [73]. RH is defined as the ratio of the water vapour in the atmosphere to the saturation value. An RH between 40 % and 60 % is recommended in the indoor air as it minimises the majority of adverse health effects caused by RH [74]. High RH level (> 60 %) causes discomfort to the human body that makes it overheated, easily exhausted and poses a potential danger to health. Low RH (< 40 %) in the atmosphere can cause breathing problems, headaches, sore throats and the situation is more severe in hospital environment. For example, the low RH of air in an operating theatre will draw moisture from body tissue exposed during operations and cause premature drying and promote the formation of a scab from coagulated blood during operations [75]. Low RH also has direct impact on the transmission of infectious disease from airborne infection [74]. Another example is monitoring the air delivery for a patient receiving mechanical ventilator support [76] and in managing the wound healing process as a moist microenvironment can accelerate the healing process by inhibiting the formation of solid, impenetrable scab [75, 77]. Moreover, exhaled humidity is also an important parameter that needs to be measured in spirometry method for diagnosis of pulmonary deficiencies [78, 79], especially in the determination of pulmonary oxygen uptake during anaesthesia [80].

The most popular commercially available RH sensors are electronic sensors that sense RH by the change of resistance, capacitance or conductivity of the active material

(usually thermoplastic polymer or thermoset polymer). Table 1.3 lists the current strategy in the development of RH sensor based on optical fibres. Different FOS platform and sensing materials have been explored for RH sensing. Among those developed sensors, fibre Bragg grating (FBG) based RH sensors exhibits an ability to measure multiple parameters, i.e. temperature and RH by multiplexing of two FBGs. The rest of the FOSs, however, are reported for sensing of RH only. The sensing of multiple parameters by using an FOS RH sensor will be of interest in applications where the parameters are significant and required to be detected, or where there is cross-talk in the sensor response due to RH. For example, a sensor that can measure CO_2 and RH simultaneously is useful in the clinical application for further reducing the complexity of measurement and the size of the instrument applied to patients.

Table 1.3 The typical development of RH sensor based on different FOS platform

Sensing material	Sensing platform	range	Sensitivity
Fluorescent dye [81]	Evanescent field plastic fibre sensor	20 %-80 %	N/A
Reduced graphene oxide [82]	Evanescent field side-polished fibre sensor	75 %-95 %	0.31 dB/%RH
Polymer coating (gelatin and poly (ethylene oxide)/cobalt) [83]	LPG	50 %-95 %	0.19 nm/%RH (for range 50%-77%) 0.33 nm/%RH (for range 77% -95%)
Thermoplastic polyimide / di-ureasil coating [84, 85]	Fibre Bragg gratings (FBG)	11 %-98 %	-0.000266 V/%RH 22.2 pm/%RH
PAH/SiNPs [77]	Evanescent field plastic fibre sensor	10 %-97 %	$-9.61X10^{-3}$ /%RH

Cellulose acetate butyrate film [86]	FPI	14 %-72 %	0.307 nm/%RH

1.4.6 The role of ammonia (NH_3) in healthcare

Ammonia (NH_3) is a colourless, highly irritating and corrosive gas with a pungent, suffocating odour. It is a harmful gas that produces adverse health effects once it is inhaled, ingested or contacted with eyes, the skin by the human body. Once contacting with available moisture in the skin, eyes, oral cavity, respiratory tract, and particularly mucous surfaces, it interacts immediately to form the very caustic ammonium hydroxide (NH_4OH) which could cause burning of respiratory tract, skin and eye damage [87]. Its workplace exposure limit is defined to 35 ppm (part per million) by the OSHA (Occupational Safety and Health Administration). However, the human perception for ammonia by smell is tabulated to be around 50 ppm [88], which means that the nose will fail to sense ammonia in a dangerous concentration (between 35 to 50 ppm). The monitoring of the atmospheric concentration of ammonia by using relevant sensors is of significance to the health of human, especially in places where NH_3 level could be over the safety threshold (35 ppm) (e.g. farmland, fertiliser factories).

Ammonia is also a normal constituent of the human body. It is produced internally via the breakdown of amino acids and used for the formation of Urea in the human body [89]. The production of Urea mainly occurs in the liver and is further released into the bloodstream. It ultimately travels to the kidneys and excreted in urine. Excess amounts of ammonia can be exhaled in the gaseous state. Besides, ammonia can also be produced by intestinal bacteria from either hydrolysis of urea or deamination of proteins and other nitrogenous substrates [90]. There is a great interest in the medical community in measuring ammonia levels in exhaled air for the diagnosis of certain diseases [91]. For example, it can be a fast diagnostic method for patients with disturbed urea balance, e.g. renal disease [92] or ulcers caused by bacterial stomach infection (e.g. Helicobacter pylori infection) [93]. Ammonia levels in the blood are also useful in sports medicine, in which the expired ammonia levels

increase exponentially with workload. The ammonia levels of interest in the expired air for breath analysis in diagnosis of a peptic ulcer are in the range of 50-2000 ppb [91] [93].

There are a variety of sensors that have been used for sensing of ammonia as listed in Table 1.4. The most widely applied and commercialised is electronic sensors in which the conductance of a metal oxide or a metal or a polymer changes due to the interaction of gas molecules to the sensing layer [94] [95] [96]. The selectivity of these sensors depends on metal properties (e.g. material, morphology) and operating temperature. The optical method to detect ammonia falls into two categories: spectrophotometric detection and optical absorption detection. The spectrophotometric detection relies on the colour change of a substance which chemically reacts with ammonia and changes its colour, for instance, the Nessler reaction [97]. And the latter is based on the distinguished optical absorption of ammonia gas molecules [98]. Optical absorbance analysers that measure multiple gases are commercially available but are costly (~£ 20k).

Table 1.4 A summary of different types of ammonia sensor and their characteristics [99].

Sensor type	LOD	Response time	Temperature range (℃)	Remarks
Metal-oxide (WO_3)	1ppm [95]	~5 mins	400	Low selectivity drift
Catalytic metal (Palladium)	1 ppm [94]	~1 min	Up to 600	Low selectivity
Conducting polymer (Polyaniline)	1ppm [96]	~3 mins	Up to 150	Irreversible reaction
Optical gas sensors: (Nessler) (Colourimetric) (Absorption spectroscopy)	90 ppb [97] 1 ppt [100] 1 ppb [98]	~1 min ~5 mins ~5 mins	37	expensive
Non-selective detectors (pH-transitions and EC detectors)	100 ppt [101]	~20 min	0-40	Fluidic system

FOSs have been reported to measure gaseous ammonia by using a pH indicator such as bromocresol purple [102, 103] and TSPP [104] and metal dioxide (e.g. SnO_2) [105]. Their sensing mechanism based on either change of the colour of the dye or the change of RI. Optical fibre based absorption spectroscopy for measuring of ammonia

is also demonstrated in [106]. However, in this configuration, the light beam leaves the optical fibre temporarily and travels in free space for a particular length (~60 cm) to interact with ammonia gas inside a sampling chamber. The integrated sampling chamber in the configuration increases the size and sensing area of the sensor and is less versatile compared to the chemical-based methods. The use of pH dye as the composition of FOS for ammonia sensing relies on the deprotonation of the dye as interacting with the ammonia molecule. It is generally believed that such sensors are susceptible to other pH-related gas such as CO_2, H_2S. Most such chemical-based FOS measure one single type of gas molecule. The simultaneously sensing of the two opposite pH gas species (i.e. NH_3 and CO_2) by using FOS composing of pH dyes has not been reported yet to the best of my knowledge. The multiple gas sensing for breath analysis is currently done by a gas analyser such as gas chromatography-mass spectrometry (GC-MS) or selected ion flow tube mass spectrometry (SIFT-MS) [107]. Despite the lower LOD (in a level of parts-per-trillion (ppt)), those devices are bulky and expensive. An FOS that is capable of measuring multiple breath biomarkers would allow a cheap and portable breath analyser to replace the current bulky equipment in some circumstance such as out of the laboratory.

1.4.7 Monitoring of fentanyl in healthcare

Survival in intensive care (IC) depends on having a comprehensive picture of a patient's condition. Accurate continuous monitoring of vital parameters such as gas exchange, blood pressures and heart rate, temperature, ventilatory mechanics, renal function, nutrition, and metabolism are available. However, continuous monitoring of drug levels is an unmet clinical need, solving of which would provide a step change in the IC practice and enable clinicians to provide optimised and individualised treatment of critically ill patients, with potential for reduced length of stay and adverse events.

Fentanyl is a series of opioids that is widely adopted as an analgesic agent in the POC [108]. The use of fentanyl helps to maintain anaesthesia in critically ill patients and those undergoing surgical procedures [109]. The dosage of fentanyl given is critical as unexpected lower dosage will not provide effective sedation and the patient could suffer from the pain caused by illness or surgical trauma. On the other hand,

overdose can cause unnecessary absorption which could increase adverse effects such as nausea, vomiting, pruritus and urinary retention as well as respiratory depression [108]. The overdose of fentanyl could be fatal and has been reported as being responsible for the jump in US overdose deaths involving synthetic opioids from 2013 through 2016 (overdose deaths from synthetic opioids (excluding methadone) increased from 3105 to approximately 20 000) [110]. Therefore, it is important to control the dosage of fentanyl given. Currently, in IC, many drugs are administered by continuous intravenous infusion devices which deliver a specified volume per minute or hour. The actual drug preparation and delivery rate itself are managed by clinicians. A sensor that can quantitatively detect fentanyl would allow more accurate and individualised management of drug administration. Monitoring of blood fentanyl concentration would also provide an error trap in the event of mistakes in the preparation or delivery of the drug. For a greater dose of potency, a low therapeutic blood concentration of approximately 0.6 to 3 ng/mL for anaesthesia is permitted [108, 111]. A mean blood fentanyl concentration of 26.4 ng/mL is deemed to be responsible for the intoxication death despite the unreliable prediction of antemortem dose from postmortem concentration [112].

The current methods that are used to measure the plasma fentanyl concentrations are radioimmunoassay [113] and gas-liquid chromatography [114]. The radioimmunoassay method can measure plasma fentanyl concentration as low as 0.06 ng/mL [113] but has limited reliability, the analysis can overestimate plasma fentanyl concentrations by as much as 29 to 100 % [115]. Compared with radioimmunoassay, gas-liquid chromatography produces comparable values in the spiked control and patient samples with a LOD of 0.25 ng/mL [116]. Both devices are bulky and laboratory-based, and cannot be placed in the IC bedside monitoring. FOS, thanks to its miniaturised size, remote sensing property and immunity to electromagnetic interference, have the potential to be a portable sensor applied in IC. Due to the lack of specific receptors, there are not many reports regarding drug detection by using FOS. The majority of FOSs for the detection of drug molecules is based on the fluorescent method as listed in Table 1.5. The molecular imprinting technique is the popular method to create the receptor. A vancomycin sensor based on LPG modified with molecularly imprinted polymer (MIP) is reported [117], which

detects vancomycin via the RI change. There is no FOS currently reported for the detection of fentanyl to the best of my knowledge.

Table 1.5 The reported FOS for the detection of drugs

Platform	Sensing material	Target drug	Sensing principle	Detection range	LOD
Tip based sensor [118]	Molecularly imprinted polymer (MIP)	Cocaine	Fluorescent	0 -500 µM	2 µM
LPG [117]	MIP nanoparticles	Vancomycin	RI	0.01 -700 µM	2.5 pM
Tip based sensor [119]	D-70 Dye	Adriamycin	Fluorescent	0.01-10 µg/mL	0.057 µg/mL
Fibre tip collection [120]	MIP	Propofol	Fluorescent	0.1-15 mg/mL	N/A

Chapter 2 Introduction of fibre optic sensor

The previous Chapter has discussed the advantages and prospect of FOS in the healthcare application. This Chapter will give an explicit introduction to the technical background of FOS and sensing film deposition techniques. As the majority of research in this study is about sensing of chemical species which chemically interact to sensing element in the way of change optical properties such as RI and colour, this chapter mainly focuses on discussing FOS bio-/chemical sensor and their popular configurations. Two thin film preparation techniques: layer-by-layer (LBL) and sol-gel used in later chapters (Chapter 6, 7 & 8) for detection of antibody and measurement of CO_2 are explained.

2.1 Introduction

Despite the fact that FOS has been used for a considerable period, they are still an exciting and dynamic research field with a wide range of new emerging techniques and applications. For example, fibre Bragg gratings (FBG) as a strain sensor has been widely used in application such as real-time monitoring of the structural health of bridges [121]. A bioresorbable FBG is recently reported by inscribing FBG in a water dissolvable glass fibre [122], which allows it to be implanted inside of human body for the application such as monitoring bone fracture healing. The sensor can break down inside of human body and is safer for patients in the case of the breaking of the fibre than conventional FBGs.

FOSs can be classified into two major types: physical sensors and chemical sensors depending on the type of measurands. Physical sensors measure physical, mechanical (such as strain and pressure) and electromagnetic parameters, and chemical sensors measure chemical, environmental, biological and physiological parameters such as pH or a chemical species. There are also other different classification methods: depending on sensor location, they can be classified as intrinsic and extrinsic; based on operating principles, there are intensity, phase, frequency, polarization-based sensors [123].

A typical FOS system is illustrated in Fig 2.1. It comprises an optical source, a detector and various optical components between them such as an optical fibre or optical fibre coupler. Light is electromagnetic radiation that has properties of waves, i.e. amplitude, frequency and phase. It can be polarised by constraining the vibration of light in only one plane. Such properties of light can be altered by the change of environmental factors such as the propagation medium. The optical fibre is the waveguide for the light transmitting from light source to the photodetector. The measurand is the external perturbation working on the fibre transducer that affects the light propagating in the fibre. The transducer is the sensor that converts the external measurand into a change of the properties of the light propagating in the fibre. The detector detects the change of optical signal induced by the measurand; this can be amplitude and frequency change, phase shift or the change of polarization status. By comparing the modulated signal with the original light signal, the measurand can be quantitatively identified with a pre-calibrated optical fibre sensor.

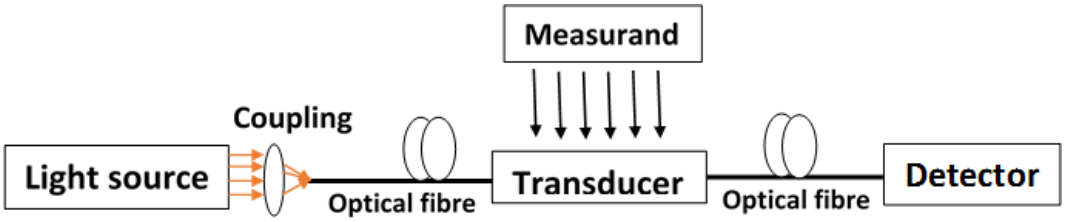


Fig 2.1 Fibre optic sensor platform component.

The optical fibre-based bio/chemical sensor is typically incorporated with recognition materials whose optical properties change under exposure to the measurand. Under this circumstance, material preparation and incorporation with optical fibres becomes an important technique in developing FOS.

2.2 Optical fibre sensor components

2.2.1 Optical fibres

Optical fibres are the waveguide for transmitting the optical signal in the sensing platform as well as part of the transducer for sensing the measurand. Light propagation along an optical fibre is governed by total internal reflection where light is trapped inside the fibre. The choice of optical fibre is important in designing the

sensing platform as it determines the property of the light being delivered to the transducer, efficiency in transmitting, collecting and maintaining the optical signal induced by the measurand. The typical parameters of optical fibre to consider are materials, geometrical diameters (including core and cladding), RI, numerical aperture (NA), cut-off wavelength, operating wavelength and attenuation. The selected optical fibres for the sensing platform needs to ensure that the optical fibre is compatible with the sensing measurand. For example, the optical fibre needs to have high heat-resistance for measuring high temperature; have strong mechanical properties for measurement of pressure, strain; have chemical resistance when used in chemical sensing.

2.2.1.1 Waveguide by total internal reflection

Light travels in an isotropic medium with a constant speed and direction, when light passes from one isotropic medium to another with different RI, the speed and direction of light propagation will be altered. The speed of light in a medium is given by:

$$v = \frac{c}{n} \tag{2.1}$$

Where v is the speed of light propagation in the medium, c is the speed of light in vacuum and n is the RI of the medium.

Snell's law, also known as the law of refraction, describes the relationship between the angle of incidence and refraction when referring to light passing through a boundary between two isotropic media with differential RI.

$$n_1 sin\theta_1 = n_2 sin\theta_2 \tag{2.2}$$

Where θ_1 is the angle of incidence and θ_2 is the refracted angle. When light goes from a higher RI medium into a lower one, $n_1 > n_2$, and the refracted angle θ_2 is bigger than the incident angle. The refracted angle increases with increase of incident angle. However, there is a critical angle for the incident beam when the refracted angle reaches 90 degrees. In this case the refracted light will propagate along the boundary of two media and further increase of the incident angle will result in total internal

reflection (illustrated in Fig 2.2). The incident angle when the refraction angle equals 90 degree is called critical angle and can be calculated as:

$$\theta_c = arcsin\ (\frac{n_2}{n_1 sin\theta_2}) \quad (2.3)$$

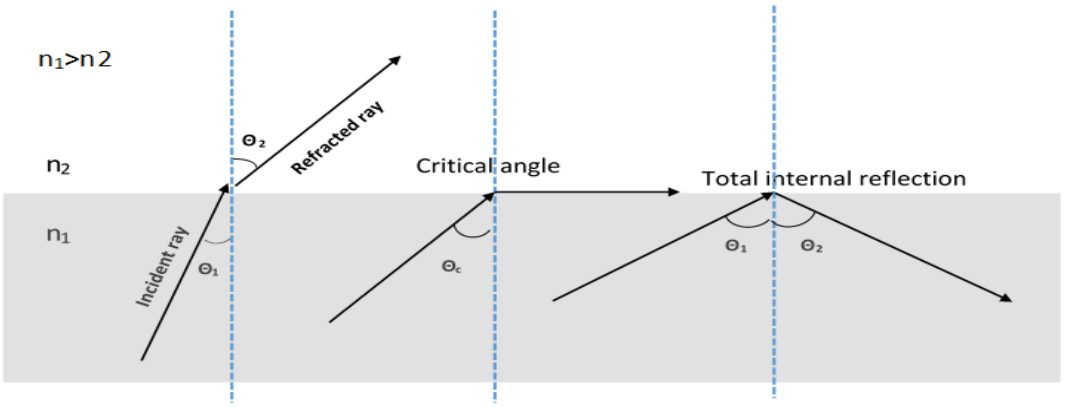


Fig 2.2 Refraction of light at the boundary of two media.

An optical fibre is made by creating differential RI media where the light is constrained in the higher RI medium based on total internal reflection. This can be achieved for silica optical fibre either by doping the core with elements like Germanium which increases the RI or by doping the cladding with elements like Fluorine which lowers the RI. The most common processes to produce the glass rod also called glass preform of an optical fibre are modified chemical vapour deposition (MCVD), outside vapour deposition (OVD) and vapour axial deposition (VAD), in which applied mixture gases are fused into solid glass under heating forming glass preform. The glass preform is then fed to a draw tower which comprises of a furnace, measurement devices and a coating apparatus to produce optical fibres by controlling the drawing speed of the process. An optical fibre can be classified as single mode optical fibre and multimode optical fibre depends on the number of modes it supports. A single mode optical fibre is designed to carry light only directly down the fibre and allows only one mode of light propagate through. The typical structure of an single mode optical fibre (Fig 2.3) consists of (i) fibre core which has diameter about 5 -10 µm, (ii) fibre cladding with a diameter of 125 µm, (iii) protective coating, which is usually made of acrylate, fluoroacrylate, polyurethane, polyamide or carbon to protect the optical fibre from mechanical damage with a typical thickness of ~245 µm.

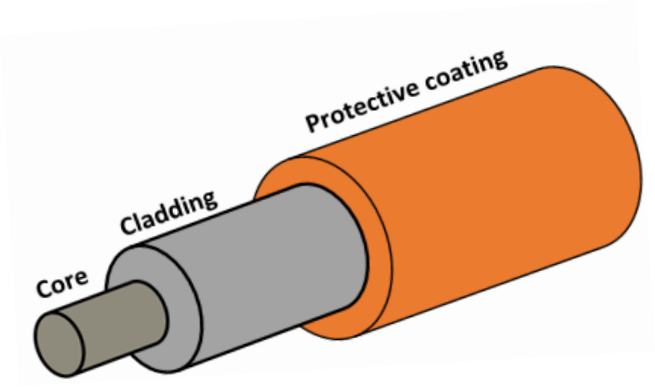


Fig 2.3 Structure of an optical fibre.

Light can be coupled into an optical fibre by using an optical lens to focus light into fibre core or by using optical fibre connectors such as SMA connectors which fix the optical fibre closely to the light source. Light is guided inside the core due to the total internal reflection. The advantage of having a two-layer structure (core and cladding) over simple version (core only) is the fibre surface, the boundary between cladding and outer environment is no longer involved in the light-guiding system. The transmission of light is therefore not affected by the external environment. The fibre can be buried in soil or under water without loss of function. The core only fibre, in contact with an external medium, may suffer enormous losses.

2.2.1.2 Numerical aperture

NA is the property of the optical fibre usually used to specify the acceptance angle. Fig 2.4 illustrates a light ray illuminating the end face of an optical fibre. There are different RI between fibre core, cladding and outer air, with a relationship of:

$$n_1 > n_2 > n_3$$

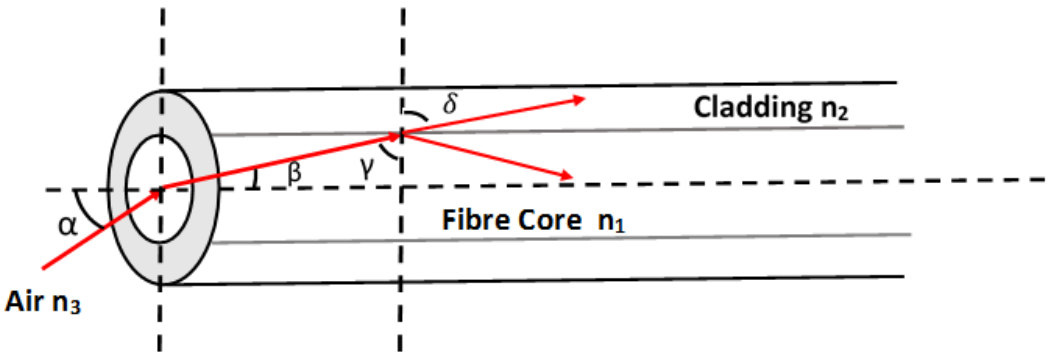


Fig 2.4 Total internal reflection demonstrating NA; the optical fibre is considered as a step-index optical fibre

Where n_1, n_2, n_3 represent the RI of the fibre core, cladding and air respectively.

According to Snell's law:

$$n_3 sin\alpha = n_1 sin\beta \tag{2.4}$$

$$n_1 sin\gamma = n_2 sin\delta \tag{2.5}$$

Considering a step index fibre, the RI of the fibre core is homogeneous. β + γ=∏/2 and hence $sin\beta$ =cosγ . Then

$$sin\beta = \sqrt{1 - sin^2\gamma} \tag{2.6}$$

The limit angle for total internal reflection is defined by $\sin^2\delta$ =1, thus

$$sin\gamma_{min} = \frac{n_2}{n_1} \tag{2.7}$$

Inserting Eq 2.7 in Eq 2.6 and that in Eq 2.4, we have

$$n_3 sin\alpha_{max} = n_1\sqrt{1 - \left(\frac{n_2}{n_1}\right)^2} = \sqrt{n_1^2 - n_2^2} \tag{2.8}$$

Assuming the light was sent from air into an optical fibre, then we have n_3=1. The limit angle α_{max} for rays to be guided into the fibre is

$$\alpha_{max} = arcsin\sqrt{n_1^2 - n_2^2} \tag{2.9}$$

NA is a measure that depends on the relative RI of the core and cladding:

$$NA = \sqrt{n_1^2 - n_2^2} \tag{2.10}$$

The largest acceptance angle for rays hitting the fibre face is given by:

$$sin\alpha_{max} = NA \tag{2.11}$$

For instance, for a single mode optical fibre, the RI of core and cladding are known as 1.450 and 1.444 respectively. The NA is then calculated as NA=0.13; the acceptance angle is about ± 7.4°. Rays illuminating the fibre face within this angle will be guided and those at larger angles will leave the core and propagate in the cladding and move away from the axis. The propagating light in the cladding will eventually reach the protective coating which usually has strong optical loss.

2.2.1.3 Propagation modes in optical fibre and V number

Optical fibres can be classified based on their RI profile: step-index fibre and graded-index fibre. The index properties of these two fibres are shown in Fig 2.5. In a step-index fibre, the RI of core is uniform and there is a sharp decrease of RI at the core-cladding interface. Light bounces back and forth which forms guided modes propagating in the longitudinal direction. On the other hand, with the graded-index fibre, the RI in the core gradually reduces its value along the radius. The light transmits in the continual index profile of core will always bend towards higher RI areas, creating a self-focus effect within the fibre core to form an optical waveguide.

For multimode fibre of these two categories, the graded-index fibre (parabolic index profile) are superior over the step-index fibre in dealing with signal delay distortion caused by path length differences among the possible propagation directions as the path length differences in the graded-index fibre are compensated by velocity variations across the core region [124].

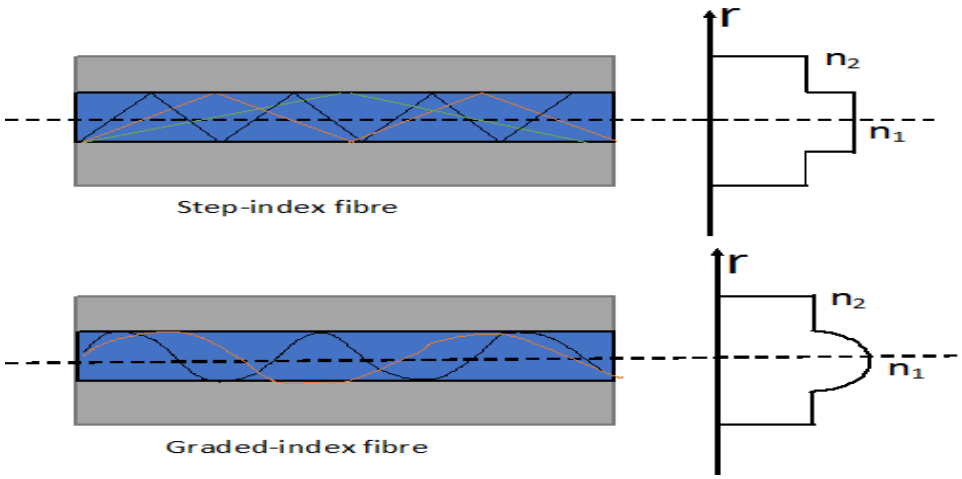


Fig 2.5 Illustration of step and graded index fibre with its RI profile; n_1 is RI of fibre core and n_2 is RI of cladding.

Propagation modes in optical fibres can be rigorously explained by wave optics as light is an electromagnetic wave. A mode can be defined as the distribution of an electromagnetic field in a transverse plane propagating through the optical fibre without changing its amplitude [125]. The V-number is an important parameter of a fibre that is used to estimate the number of modes propagate in the fibre:

$$V = \left(\frac{2\pi a}{\lambda}\right)\sqrt{n_1^2 - n_2^2} = \left(\frac{2\pi a}{\lambda}\right) NA \quad (2.12)$$

Where a is the diameter of fibre core, n_1 and n_2 are the RI of fibre core and cladding. λ is the wavelength of light. The total number of guided modes in a fibre is approximately equal to N≈ $V^2/2$ [126]. For an optical fibre with large core diameter and large NA, it will support a large number of propagation modes. The number 2.405 is the solution of the first zero of the Bessel function of the wave equation [127], which defines the criterion of the mode cut-off condition. For an optical fibre with V< 2.405, only one mode is supported, while for V–number is greater than the number of supported modes increases. A fibre with parameter V < 2.405 is called single mode fibre and that with V>2.405 is called multi-mode.

2.2.1.4 Cut-off wavelength

The cut-off wavelength is defined as the maximum wavelength at which a mode will propagate. The operation wavelength must be greater than the cut-off wavelength to operate the fibre in a single mode regime. For example, if a single-mode optical fibre is characterised by a cut-off wavelength of 670 nm, then wavelengths of light longer than 670 nm only have one fundamental mode inside the fibre. On the contrary, for a wavelength below the cut-off wavelength, the light propagation will be multi-mode. Applying the criterion V=2.405 to Eq 2.12, the cut-off wavelength can be calculated as:

$$\lambda_{cutoff} = \left(\frac{2\pi a}{2.405}\right) NA = \left(\frac{2\pi a}{2.405}\right)\sqrt{n_1^2 - n_2^2} \quad (2.13)$$

2.2.1.5 Evanescent field

When total internal reflection takes place at the boundary of core and cladding as shown in Fig 2.6, there is a portion of the energy in the electric field that penetrates the cladding which is called the evanescent field. The evanescent field penetrates from the fibre core-cladding boundary heading away from the core with an exponential decay in energy.

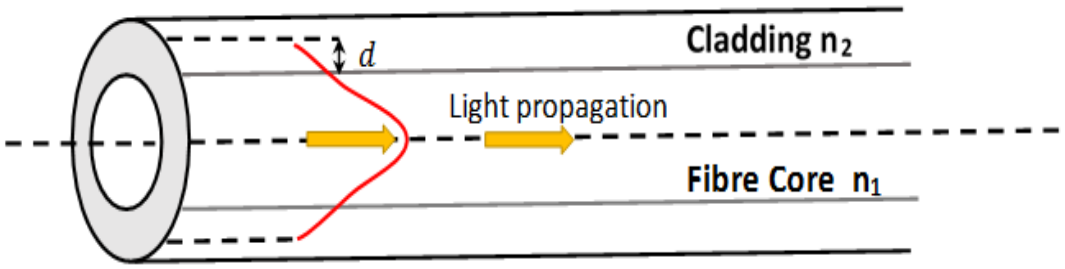


Fig 2.6 Evanescent field and penetration depth of an optical fibre.

The energy wave propagates along the interface, the same direction as the light propagating within the core. The penetration depth (d) is given as:

$$d = \frac{\lambda}{2\pi\sqrt{n_1^2 \sin^2\gamma - n_2^2}} \tag{2.14}$$

Where n_1, n_2 is the RI of fibre core and cladding, respectively; λ is the wavelength of light; γ is the incident angle from fibre core to cladding.

2.2.1.6 Mode Coupling and partition noise

The distribution of power at different modes in a multimode optical fibre is not necessarily maintained as the light propagates along the fibre. There will be coupling between each mode whenever the fibre is strongly bent. Mode coupling is generally caused by impurities or inhomogeneities introduced during the manufacturing process. These imperfections are microscopic bends, diameter variations, irregularity of the core-cladding boundary and RI distribution fluctuations [128]. Mode coupling can occur between the fundamental mode to higher-order propagation modes or even cladding modes and coupling between different polarization states. Any motion of fibre or even just small temperature fluctuations can lead to a change of power distribution between the modes. This does not affect the output of the fibre as long as the detector measures the sum of all partial powers. However, in practice, detectors are not necessarily uniformly sensitive across their surface and, as a result, some modes are registered stronger than others. Then the random changes of the mode partition will be reflected as the random change of received power. This phenomenon is called mode partition noise.

2.2.1.7 Loss and attenuation

Attenuation is one of the most important parameters for an optical fibre, it determines how far the light signal can be delivered with a detectable signal strength. The attenuation of an optical fibre is mainly attributed by the material absorption which is caused by the molecular vibrations or impurities such as OH^- , or metal ions during the fabrication process; by Rayleigh scattering which is caused by the structural inhomogeneities of the optical fibre. These losses are intrinsic loss of an optical fibre. The attenuation of an optical fibre (a_{dB}) is defined as:

$$a_{dB} = \frac{1}{L} 10\, log \left[\frac{P0}{P(L)}\right] \tag{2.15}$$

Where $P0$ is the light input power into the optical fibre, and $P(L)$ is the power output that is detected at a transmission distance of L. The attenuation of an optical fibre is usually around 0.2 dB/km.

In most applications considered in this thesis the length of the fibre is short (a few metres) and so the intrinsic attenuation of the optical fibre is not usually of concern. However, certain materials, may have massive attenuation at specific wavelengths. For example, plastic optical fibres usually operate at shorter wavelengths (e.g. red light) compared to that of silica and have high attenuation when the wavelength is above 1 µm [129] which means that the light detected may be insufficient for sensing.

Optical fibre exhibits an additional transmission loss when it is bent. The loss rises very quickly once a certain critical bend radius is reached. This needs to be considered during the optical fibre sensing as it may simulate an optical signal same as when the measurand is presented.

Additional losses can occur when two fibres are connected. These losses depend on the type of fibre, the extent of separation and degree to which two fibres are aligned. In practice, such coupling losses can be minimised by using RI matching gel or by using ball lenses between fibres. Two fibres are also can be tightly joined together with highly efficient coupling. This joint connection can be achieved by mechanical splicing in which two fibres are tightly held together with cores well aligned via mechanical means; by fusion splicing where the two fibres are fused together using

an electrical arc. Fusion splicing provides permanent connection of two fibres with low insertion loss. The fusion splicing or mechanical splicing usually works well with low coupling loss unless there are: (a) mismatch of core size, (b) deviation between the fibre axis directions, (c) angular misalignment, (d) air gap between two fibres. (illustrated in Fig 2.7).

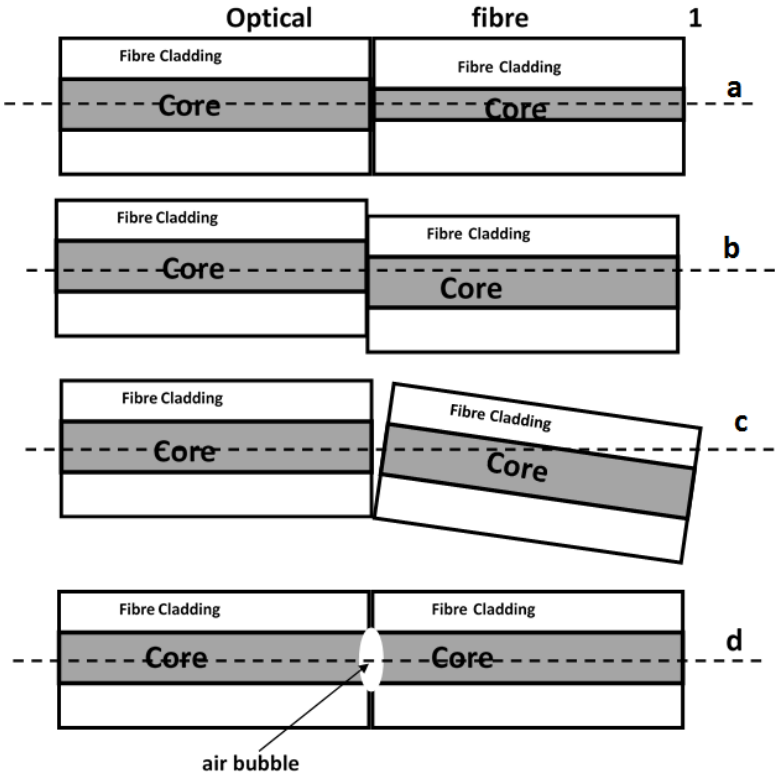


Fig 2.7 The loss introduced by fibre connection between two fibres: (a) mismatch of core size, (b) lateral misalignment, (c) angular misalignment, (d) air gap.

2.2.1.8 Optical fibre coupler

An evanescent field exists at the core-cladding interface and energy can leak from the fibre into another fibre depending on the proximity (d) of two fibres. A fused optical fibre coupler generally consists of two or more parallel optical fibres that have been twisted, stretched and fused together so that their cores are very close to each other (illustrated in Fig 2.8). This forms a coupling region where the power of light from one optical fibre into the second or more optical fibres. The coupling ratio of an optical fibre coupler is determined by the coupling length (L) and the distance between two fibres (d). A typical 50:50 or 3 dB 2×2 coupler has two inputs and two

outputs; the input power (P_{in}) is equally split at the coupling region to the two outputs (P_{out}). A 3dB 1×2 coupler has the same coupling ratio with the 2×2 coupler but with one output arm cut short, crushed and tucked away inside the housing of coupler so that the reflection from the facet is neglected .

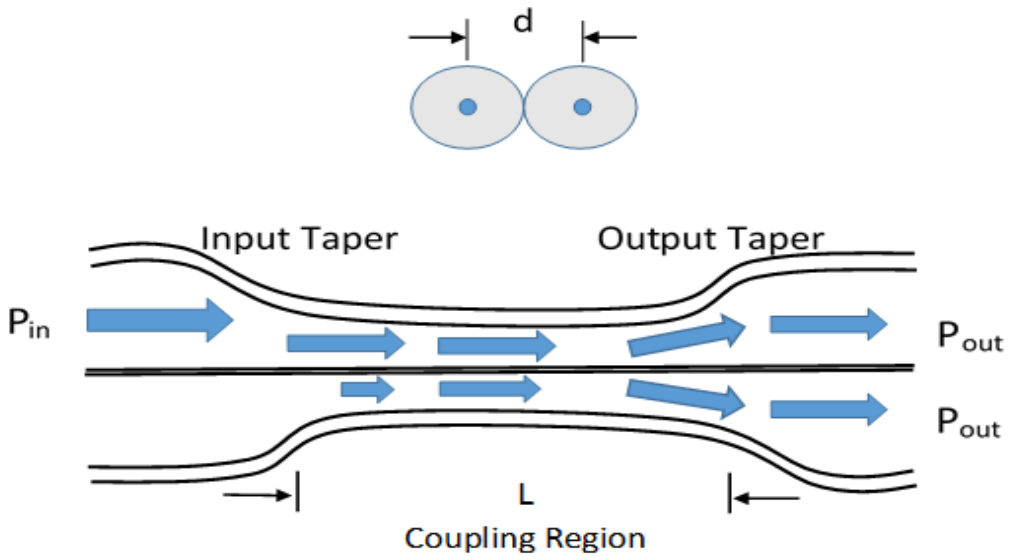


Fig 2.8 Schematic image of the light coupling in an optical fibre coupler.

2.2.2 Light sources

An appropriate light source is essential for the FOS. The general considerations in choosing the light source when designing an FOS are operating wavelength, optical output power, output stability, power consumption and lifetime. The operating wavelength should cover or match to the designed wavelength of the transducer as a mismatch of wavelength could cause nonresponse or lower sensitivity of transducer to the measurand. The output power is especially important for an optical biosensor or chemical sensors as lower output power may lead to an insufficient interaction of light with the sample leading to a small magnitude of the induced optical signal, whereas high power of light will cause damage of a biological sample [130] or photo-bleaching of some colour chemicals (e.g. fluorophore) [131]. Light emission angle of a light source also needs to be taken into account as it (along with the NA of the fibre) determines the coupling efficiency of light into the optical fibre. There is a vast variety of light sources in the market that can be generally classified as incandescent lamps, discharge lamps, semiconductor source and lasers.

Each type of light source has its advantages and disadvantages. Depending on the technology requirement and limitation of optical fibre sensing techniques, different light sources can be chosen to meet the requirement and be cost-effective. For example, laser light has high coherence and can be easily coupled into fibres; it is usually applied in the optical fibre interferometer sensor as it has long coherence length and it is easy to obtain interference fringes. Compared with the laser source that has a narrow bandwidth, incandescent light can have a broader wavelength range of white light (e.g. Halogen lamps). The white light source is commonly exploited when measuring the absorption of a dye compound or fluorescent molecular based on the fact that those chemical molecules usually work in the visible wavelength range. Semiconductor sources such as light emitting diodes (LEDs) are also popular in designing FOS thanks to their high stability, low power consumption and multiple selections of wavelength in the range from 240 nm to 900 nm [132].

2.2.3 Detectors

Photodiodes are the most common detectors that are exploited for precise measurement of the intensity of light in science and industry. They are devices that convert the optical energy into electrical signals by producing photocurrent through a p-n junction after absorbing photoenergy and used for detecting the intensity modulated optical signal of an FOS. The absorption of photoenergy in the depletion region of a p-n junction creates electron-hole pairs; these hole pairs are swept from the junction due to the built-in electric field resulting in the movement of electrons toward the cathode and production of photocurrent. Photodiodes generally have an enhanced, more linear response to the detected light than photoconductors. They usually have a compact size, low noise and wide spectral response. Depending on the material, each photodiode has its specification that only detects the wavelength of light located in the spectral range. For example, a photodiode made from silicon usually has a spectral response range of 190 -1100 nm, 400-1700 nm when it is made with germanium, 800-2600 for indium gallium arsenide and <1000-3500 nm for Lead(ll) sulphide [133]. The wavelength detection range of the photodiode for designing the FOS needs to match the wavelength of the light source or optical signal induced by the transducer to ensure the optical signal can be properly detected.

Charge-coupled devices (CCDs) are also commonly used for FOS measurement when spectral information is required. CCD detectors consist of a two-dimensional detector array built on a single strip of silicon (labelled as 7 in Fig 2.9). The pixels accumulate light intensity information until they are read out and a new exposure starts. The available response range of CCDs is from 200 nm (with UV enhancement) to 1000 nm. As illustrated in Fig 2.9, light from an optical fibre enters the CCD spectrometer, it passes through the entrance slit and undergoes reflection at collimating mirrors (labelled 4) and diffraction at a fixed grating (labelled 5), the light is then decomposed into multiple wavelengths with different optical path. All the wavelengths arrive ultimately at the detector array (labelled 8) after being reflected by a focusing mirror (labelled 6). The spectral output of CCDs has an advantage in the application of FOS which provides two-dimensional information with wavelength and intensity. However, this type of device is usually expensive and bulky compared with photodiodes.

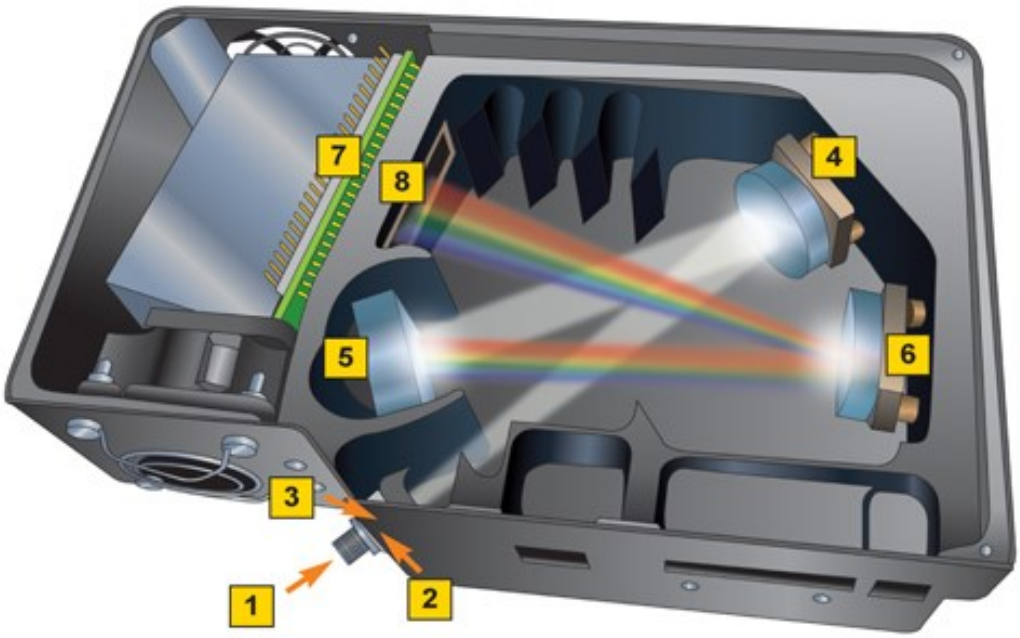


Fig 2.9 Schematic of optical spectrometer. The graph is from Ocean Optics [134]. 1,SMA connector; 2,slit; 3, filter; 4, collimating mirror; 5, diffraction grating; 6, focusing mirror; 7, cooling set; 8, detector array.

2.3 Classification of FOSs

FOSs have numerous configurations depending on the way of the light interacts with the measurand. They can be classified into two categories based on the configuration of the transducer: intrinsic and extrinsic. An intrinsic FOS directly uses the optical fibre itself as a transducer, this can be done by a micromachining process (e.g. laser processing, arc discharge, chemical etching) to produce fibre gratings [135], interference cavity [136], cladding removed fibre [137], U-shape fibre [138] or microchanneled optical fibre [139] for sensing. These types of FOSs are commonly used for the sensing of physical parameters such as temperature, pressure, strain and RI. For the extrinsic FOS, light leaks from the optical fibre and interacts with an external functional material or structure that is incorporated with an optical fibre. In this case, the external material or structure is the sensor transducer. This configuration is usually used in sensing of chemicals or biological samples by determining the type of functional material. The functional materials convert the biochemical change caused by the measurand into a measurable optical signal from a change in its optical properties (e.g. absorbance, RI, fluorescent status).

2.3.1 Configuration of extrinsic FOS

There are various configurations of FOS reported that are incorporated with sensing materials for detection of absorbance, RI or fluorescent signal change. A cladding removed FOS (Fig 2.10a) is fabricated by removing the cladding of an optical fibre to expose the evanescent field to the environment of interest. For fibres with a silica core and a polymer cladding (e.g. urethane acrylate, polyamide, poly methyl methacrylate), this can be done by removing the plastic coating with a burner, using a mechanical fibre stripper, or by plasma processing. For fibres whose core and cladding are silica, chemical etching with hydrofluoric acid (HF) can be used but the reaction time needs to be precisely controlled [140]. By replacing the cladding with sensitive functional materials, the cladding removed FOS has been used to measure ammonia gas [141], carbon dioxide [69] based on the absorption change of sensing material, volatile organic compounds such as methanol, ethanol by detecting the RI change of a coated material [142]. An SPR sensor can also be made by using this

configuration for the detection of a biological sample, i.e. proteins [143]. A tapered FOS (Fig 2.10b) is made by heating a section of the single mode optical fibre and pulling both ends in the opposite direction either using a constant speed, force or tension. Depending on the pulling condition, the tapered fibre can be fabricated with different shapes and properties. Fibre tapers are of two distinct types: adiabatic and non-adiabatic depending on the taper angle. An adiabatic fibre taper has a small taper angle so that there is a smooth mode conversion without significant losses in the transmitted signal [144]. The light remains in the fundamental mode as it propagates along the taper. The working principle of an adiabatic taper is similar to the cladding removed fibre as the aim of both procedures is to expose the evanescent field outside the fibre. On the other hand, non-adiabatic fibre tapers have an abrupt taper angle so that more than one mode exists when the light propagates along the taper region due to the large RI difference between air and glass [145]. The multiple modes of the taper will interact with the fundamental mode of the unpulled fibre creating an interference peak which acts as an interferometer. This non-adiabatic tapered sensor configuration has been exploited for measurement of RI and as a biosensor for detecting of amino acids [146]. As a specific type of cladding removed FOS, a U-shape fibre sensor (Fig 2.10c) is favoured as it exhibits a higher sensitivity to the surrounding RI than the straight fibre sensor due to the extended evanescent field caused by the bending [147]. The sensitivity of such sensors varies for different bending radius [138]. There are also other types of cladding removed fibre sensors such as D-shape or side-polished optical fibre sensors that have been utilised for chemical sensing [148, 149]. The use of an optical fibre coupler allows the fabrication of FOS in reflection mode (Fig 2.10d). A sensing film is coated on the tip which provides direct interaction of light with sensing materials. Such a sensor configuration has a miniaturised area compared with others. Depending on the properties of the coated film, such a configuration can be constructed as a FPI sensor for chemical sensing [150] based on the interference between the reflected beam from two interfaces of the film. The visibility of interference fringes depends on the reflectivity of two interfaces, optical path length difference of two interference beams and the light source. To obtain the interference, the optical path length difference should be less than the coherence length of the light source. Moreover, coating fluorescent dye on the tip of the optical fibre allows

excitation of the fluorophore and collection of the fluorescent signal in the same fibre [70].

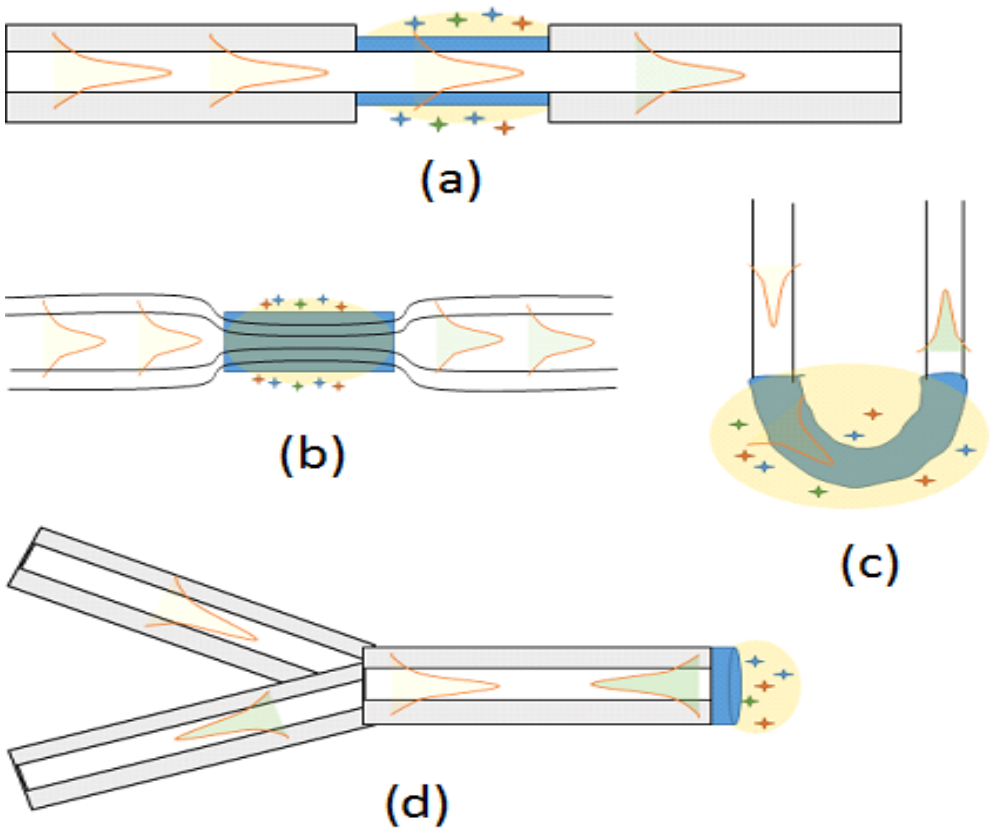


Fig 2.10 The configuration of extrinsic FOS. (a) Cladding removed FOS; (b) Tapered FOS; (c) U-shape FOS; (d) Tip based FOS.

2.3.2 Grating-based optical fibre sensor

A grating is fabricated by introducing a periodic RI modulation inside the optical fibre core (Fig 2.11). The light that propagates along the longitudinal direction (z-direction) undergoes diffraction due to the grating. Depending on the grating period, the diffraction of light can either have a backward mode with all light trapped inside the core (grating period < 1µm) or a cladding forward mode where light propagates in the cladding (grating period> 100 µm). These are called Fibre Bragg grating (FBG) sensor and Long period grating (LPG), respectively. The wavelengths of light for

forward or backward propagations are determined by the grating period, they can occur at visible wavelength range or infrared range.

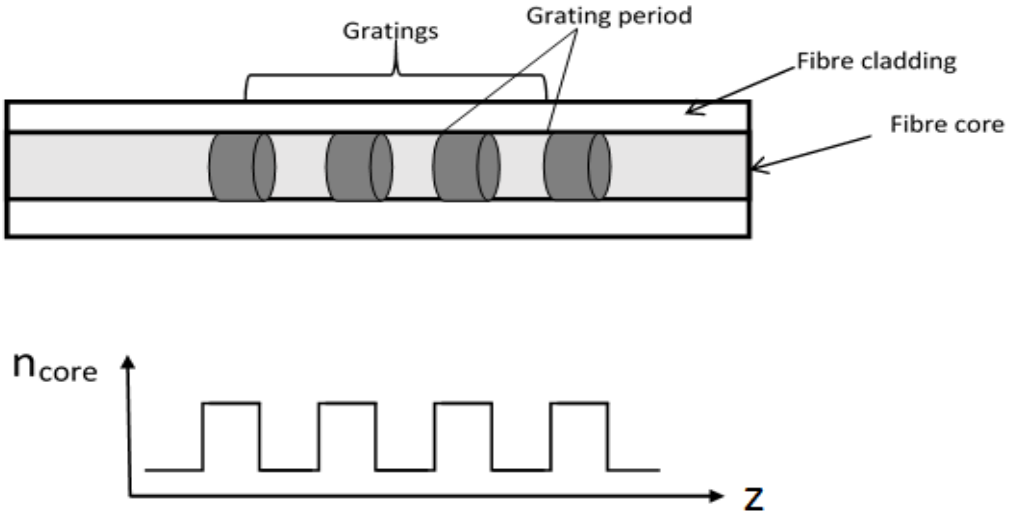


Fig 2.11 Schematic of a grating-based FOS; the RI of fibre core has a periodic modulation due to the existing of the fibre grating.

The typical way to fabricate a grating sensor is to apply a periodic ultraviolet (UV) light pattern on a photosensitive optical fibre [151]. The photosensitive optical fibre changes locally its RI when irradiated by UV light. An optical fibre can be photosensitive after doping materials such as germanium (Ge), cerium and europium during the fabrication process. Although the photosensitivity of fibres doped with cerium and europium have been reported, the Ge-doped optical fibre has been demonstrated to have the maximum RI change [152, 153]. The Ge-doped optical fibre changes its RI after absorbing the UV radiation and the biggest RI modulation is obtained when the incident UV radiation matches the absorption wavelength of the germanium-oxygen deficiency centre (GODC) [154]. The magnitude of photosensitivity is also proportional to the amount of Ge doped in the fibre and the RI change induced for standard single mode fibres with 3 % Germania is approximately 3×10^{-5} [155]. The RI change can be enhanced about two orders of magnitude with the help of molecular hydrogen or deuterium [156]. The hydrogen-loading of Ge-doped fibre can be practically achieved by high-pressure loading. The addition of hydrogen to Ge-doped glass leads to the breakdown of the Si-O-Ge bonds resulting in the formation of Si-OH bonds and GODC, both contribute to the increase

of RI [156]. The UV irradiation method to fabricate a grating on a photosensitive fibre requires removal of the plastic outer layer of the optical fibre which could have absorption and scattering effects on the UV light and affect the interaction of light with the fibre. In recent decades, femtosecond lasers have been of interest in the fabrication of grating [157]. The ultrahigh peak power radiation generated by the pulse laser can induce an RI change through multiphoton absorption and ionisation processes that result in material compaction or defect formation depending on the intensity of exposure. This method eliminates the use of expensive photosensitive optical fibre for fabrication and reduces the fabrication cost per grating. Moreover, it removes the need for removing plastic protection coating and keeps the mechanical integrity of the grating sensor.

2.3.2.1 Fibre Bragg grating sensor

An FBG sensor is probably the most popular grating-based sensor and is widely explored and commercialised. For example, it has been used as a sensor for stress monitoring [158], temperature monitoring [159] and structural health monitoring [159]. A conventional FBG is fabricated by introducing a short period of RI modulation using a laser with a point-by-point exposure [160] or multi-beam interference using a phase mask [161]. An FBG is characterised by a backward propagation of light at a specific wavelength while transmitting all others. The reflected wavelength is defined by [162]:

$$\lambda = 2n_{eff}\Lambda \tag{2.16}$$

Where n_{eff} is the effective RI of the fibre core and Λ is the grating period. As all light propagates inside the fibre core, the conventional FBG is free from the surrounding perturbation of RI. FBG sensors are commonly used for sensing of physical parameters such as temperature and strain. Typically, FBGs have a length of 5 mm with a temperature sensitivity of 10 pm/°C and strain sensitivity of 1 pm/με (με =microstrain) while operating at 1500 nm [163]. Special techniques have been exploited for FBG fabrication or post-treatment in order to incorporate the FBG with functional material for chemical sensing, these include fabricating the tilted FBG [164], etched or side-polished FBG [165]. By etching or side-polishing the fibre

cladding around grating, the evanescent field of the guided mode is accessed. An RI change under the evanescent field will change the effective RI of the guided mode resulting in a shift of the Bragg resonance wavelength. The major drawback is the requirement of an expensive high-resolution spectrum analyser due to the small strain or temperature-induced wavelength shift (1 pm/με and 10 pm/℃, respectively). A bi-cell detector that has two photo detectors located closely to each other may be used to detect the intensity change induced by the small shift of the wavelength and will be a low-cost detector for the FBG sensor.

2.3.2.2 Long period grating sensor

An LPG sensor couples the energy of the fundamental core mode to discrete, forward-propagating cladding modes (Fig 2.12). The cladding modes are quickly attenuated resulting in the transmission spectrum of the fibre containing a series of attenuation bands with discrete wavelengths. Each wavelength of the attenuation band corresponds to the coupling of a different cladding mode. The central wavelength of the attenuation band depends on the grating period, and the external environment perturbations such as temperature, strain and RI of the surrounding medium [166]. Due to the capability of responding to the surrounding RI, LPG sensors have been demonstrated as biosensors for detection of biological molecules such as RNA [167], antibodies [168] and bacteria [40].

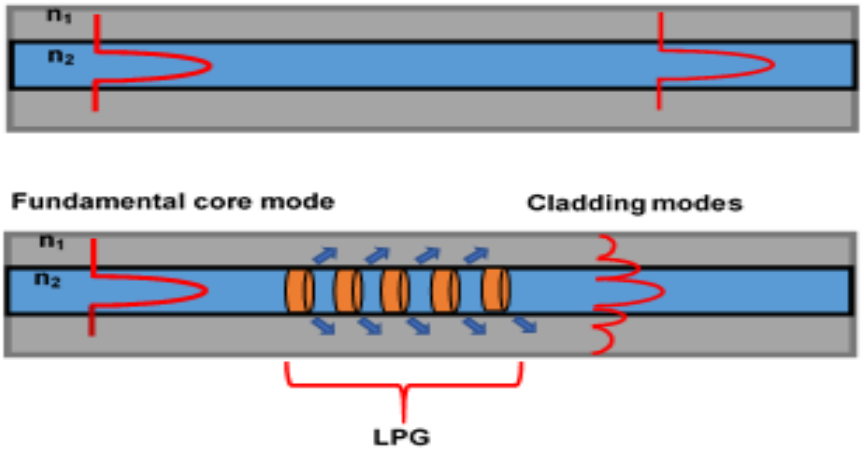


Fig 2.12 Waveguide of a standard optical fibre (top) and an LPG sensor (bottom).

2.3.2.2.1 LPG sensor fabrication

The inscription of a grating with long period in an optical fibre is the generation of periodical perturbation of RI in the core. Different physical properties and variable structure of optical fibre have been used to produce such perturbation. UV laser radiation is the most commonly used method to produce LPGs. The electric arc technique is a simple, flexible and low cost thermal induced method to fabricate the grating [169]. The heating processed by an electric arc in an optical fibre alters the viscosity, and as a result, the RI and symmetry is slightly modified. The method can be applied in any type of optical fibre but with a limit of fabricating grating periods below 200 µm [170]. Due to the photo-elastic property of glass, the RI of glass can be modulated when the glass is exposed to stress. Thus, LPG sensors have been successfully fabricated by applying mechanical stress to induce periodical microbending or pressure points [171]. Another way, but not popular, is etching induced RI modulation. The RI modulation is introduced by periodically removing the cladding region of the optical fibre via chemical etching using HF. This method suffers low repeatability and difficulty in controlling the structures.

2.3.2.2.2 LPG theory

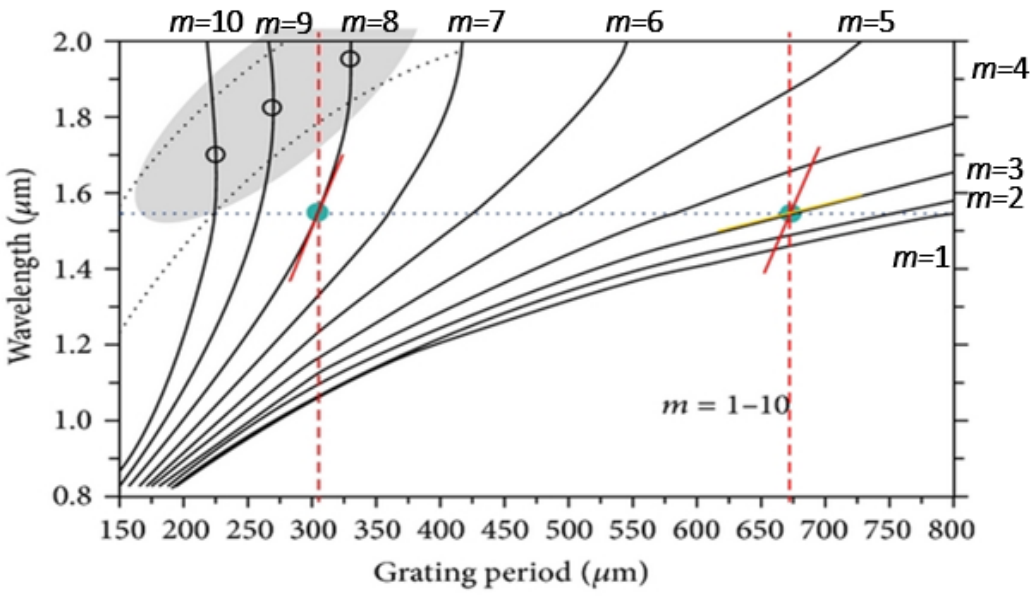
The wavelengths of discrete attenuation bands appearing at the transmission spectrum of an LPG sensor are governed by [172]:

$$\lambda_{res} = (n_{co}^{eff} - n_{cl,m}^{eff})\Lambda \tag{2.17}$$

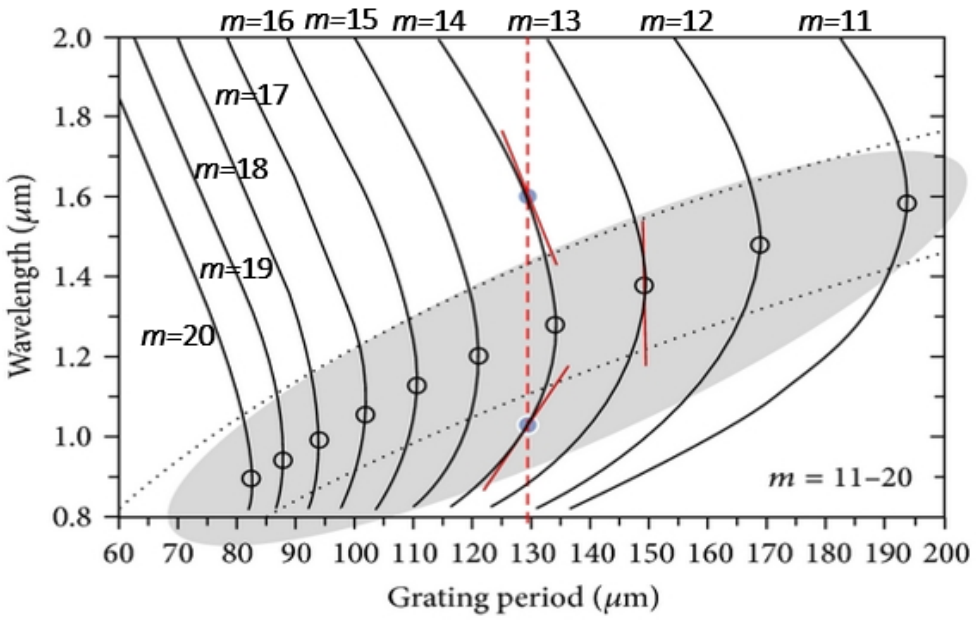
that illustrates the relationship of resonance bands (λ_{res}) with the intrinsic properties of the LPG (grating period (Λ) , effective RI of the fibre core n_{co}^{eff} , extrinsic variation $n_{cl,m}^{eff}$). According to the three layer theory from Erdogan [172], the effective RI of the fibre core is determined by the RI of the core and the cladding; whereas the effective RI of the cladding is regulated by the RI of the core, the RI of the cladding as well as the RI of the external environment surrounding the cladding. Changing the RI of the medium surrounding the cladding alters the effective RI of the cladding mode leading to a wavelength shift of the resonance bands.

2.3.2.2.3 Phase matching turning point

An LPG sensor is intrinsically sensitive to the surrounding RI and the sensitivity depends on the interaction of cladding modes with the surrounding RI. The sensitivity reaches its maximum close to the phase matching turning point (PMTP) [173]. Fig 2.13 illustrates the phase matching curve that is achieved from Eq 2.17 via calculating the effective RI of core and effective RI of cladding for each coupled mode, shows the resonance wavelengths of an LPG as a function of grating period for the first 20 cladding modes between wavelengths of 0.8-2 μm. The PMTP is defined as the region where the slope of the phase matching curve changes from positive to negative. Beyond the PMTP, for each grating period, there are two wavelengths corresponding to the coupling to the same cladding mode (Fig 2.13). Therefore, for a given grating period, there will be dual resonance peaks appearing in the transmission spectrum when the monitored cladding modes are beyond the PMTP. The PMTP is located at longer wavelengths for lower cladding modes and shifts to shorter wavelengths as the mode number increases. Theoretically, a PMTP exists for each mode provided that the observed wavelength range is large enough. The maximum sensitivity condition of each cladding mode is determined at the PMTP, and thus an LPG sensor can be designed to have the highest sensitivity for particular wavelength by selecting a cladding mode and grating period at or close to the PMTP.



(a)



(b)

Fig 2.13 Phase-matching curves of the first 20 cladding modes in the wavelength range of 0.8 to 2 µm: (a) cladding modes 1-10; (b) cladding modes 11- 20. PMTP are illustrated for each cladding mode. The graphs are modified from the work published by Shu, et al., [173] and Rego, et al. [174].

2.3.2.2.4 RI sensitivity

The sensitivity of an LPG sensor for surrounding RI can be understood by the following equations [173]:

$$\frac{d\lambda_{res}}{dn_{sur}} = \lambda_{res}\Upsilon\,\Gamma_{sur} \tag{2.18}$$

Where Υ is the waveguide dispersion and defined by:

$$\Upsilon = \frac{\frac{d\lambda_{res}}{d\Lambda}}{n_{co}^{eff} - n_{cl,m}^{eff}} \tag{2.19}$$

Where $d\lambda_{res}/d\Lambda$ represents the slope of the dispersion curve. Γ_{sur} is the surrounding RI dependences of the waveguide dispersion, expressed as:

$$\Gamma_{sur} = -\frac{u_m^2 \lambda_{res}^3 n_{sur}}{8\pi r_{cl}^3 n_{cl}\left(n_{co}^{eff} - n_{cl,m}^{eff}\right)\left(n_{cl}^2 - n_{sur}^2\right)^{\frac{3}{2}}} \tag{2.20}$$

The term u_m is the mth root of the zero-order Bessel function; n_{cl} and r_{cl} are the RI and radius of the fibre cladding, respectively.

From Eq 2.18 and Eq 2.19, it is clear that the sensitivity increases with the slope of dispersion curves. Combining with the phase matching curve (Fig 2.13), this shows that the higher cladding mode is more sensitive which can also be verified from the energy distribution of modes as higher cladding modes couple more energy than lower ones. For a particular mode, the resonance wavelengths beyond the PMTP exhibit higher sensitivity. Eq 2.20 also shows that the sensitivity increases as the surrounding RI approaches that of the cladding. In this case, the evanescent field extends further into the surrounding medium leading to a higher interaction. The phenomenon of RI sensitivity transition has been experimentally demonstrated by G .Rego [175]. As illustrated in Fig 2.14, the magnitude of the resonance wavelength shift increases as the RI gets close to ~1.46 (which is very close to the RI of the cladding). The transmission value, on the other hand, exhibits an increase while the RI reaches ~1.46. The attenuation band disappears as the RI matches the RI of the fibre cladding. When the RI rises above that point, the attenuation band appears but with the wavelength shifting to opposite direction. In this case, the modes are propagating by Fresnel reflection and not by total internal reflection ($n_{sur} > n_{cl}$), and they lose part of the energy at each reflection interface and are known as lossy modes. The resonance wavelength, in this case, is no longer sensitive to the further increase of the RI. This is because the phase of the partially reflected field at the surrounding-cladding interface does not change with the external medium [176].

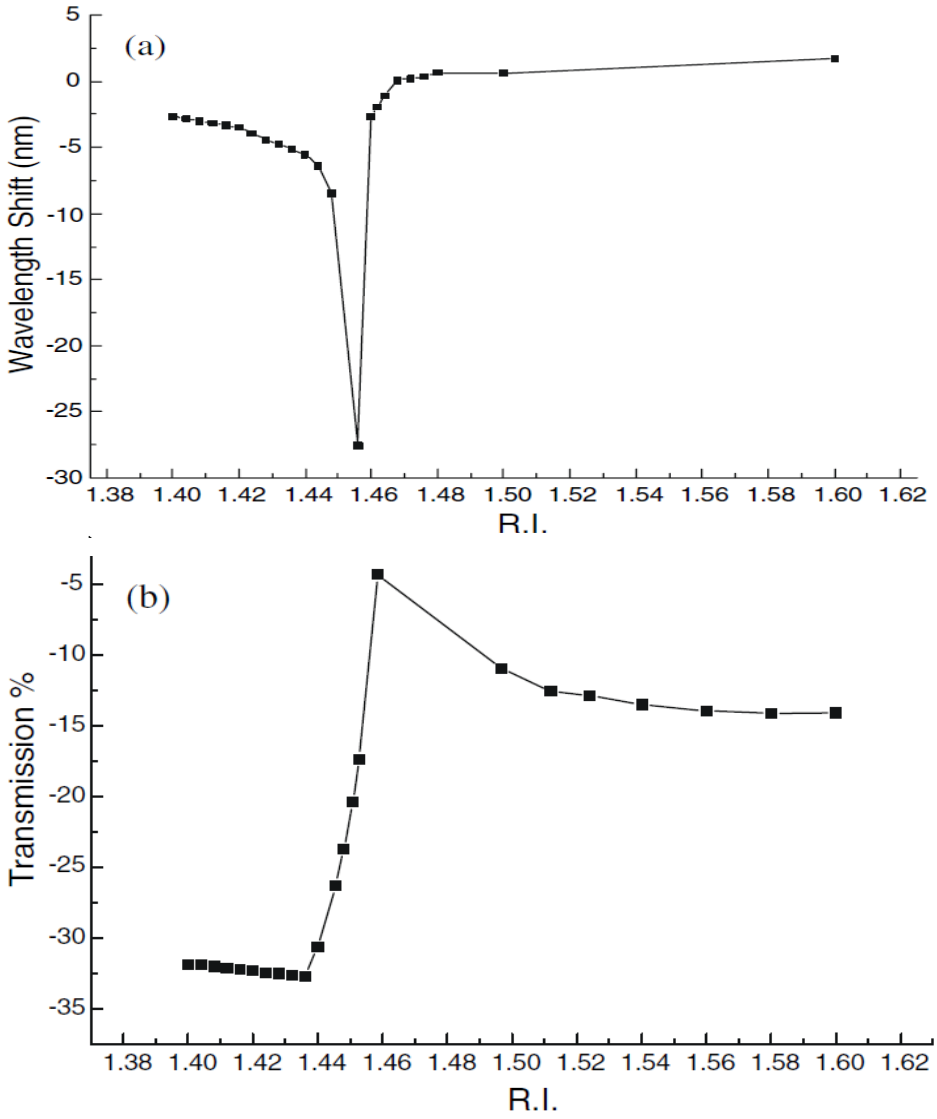


Fig 2.14 Plot of wavelength shift (a) and transmission value (b) of the attenuation band in response to the surrounding RI. The central wavelength of the attenuation band is corresponding to the fifth cladding mode of an LPG sensor with a grating period of 400 µm. The image is obtained from the publication of Rego [175].

2.3.2.2.5 Temperature sensitivity

The temperature sensitivity of an LPG can be expressed as following equation [173]:

$$\frac{d\lambda_{res}}{dT} = \lambda_{res}\Upsilon(\mathcal{T} + \Gamma_{temp}) \tag{2.21}$$

$\mathcal{T}$ is the thermal expansion coefficient of the fibre. Υ decribes the waveguide dispersion as introduced in Eq 2.19 and Γ_{temp} is the temperature dependence sensitivity factor.

$$\Gamma_{\mathrm{temp}} = \frac{\xi_{\mathrm{co}} n_{\mathrm{co}}^{\mathrm{eff}} - \xi_{\mathrm{cl}} n_{\mathrm{cl,m}}^{\mathrm{eff}}}{n_{\mathrm{co}}^{\mathrm{eff}} - n_{\mathrm{cl,m}}^{\mathrm{eff}}} \tag{2.22}$$

ξ_{co} and ξ_{cl} are the thermooptic coefficients of the core and cladding, respectively.

In Eq 2.22, the temperature sensitivity factor depends on the fibre materials which contribute to the thermooptic coefficients. The thermooptic coefficient of the pure silica (the material of fibre cladding) is 7.8×10^{-6} according to [173]. Therefore, for a given value of ξ_{co}, the absolute value of temperature sensitivity factor Γ_{temp} decreases for higher cladding modes because the $n_{\mathrm{co}}^{\mathrm{eff}} - n_{\mathrm{cl,m}}^{\mathrm{eff}}$ is larger. The Γ_{temp} increases as the thermooptic coefficient difference between fibre core and cladding material increases. Therefore, the Γ_{temp} can be either positive or negative depends on the fibre materials. In general, for a silica-based fibre, thermal expansion coefficient $\mathcal{T}$ in Eq 2.21 is 4.1×10^{-7} and is far smaller than Γ_{temp}. Then the temperature sensitivity is determined predominately by the product of $\Upsilon\,\Gamma_{\mathrm{temp}}$. Based on this phenomenon, it is possible to fabricate an LPG that is temperature insensitive [177]. For example, when $a = -\Gamma_{\mathrm{temp}}$.

2.3.2.2.6 Strain sensitivity

The axial strain sensitivity of LPGs can be expressed as:

$$\frac{d\lambda_{res}}{d\varepsilon} = \lambda_{res}\Upsilon(1 + \Gamma_{strain}) \tag{2.23}$$

Υ describes the waveguide dispersion as introduced in Eq 2.19 and Γ_{strain} is the strain dependent sensitivity factor.

$$\Gamma_{strain} = \frac{\eta_{co} n_{co}^{eff} - \eta_{cl} n_{cl,m}^{eff}}{n_{co}^{eff} - n_{cl,m}^{eff}} \quad (2.24)$$

Where η_{co} and η_{cl} are the elastoopitc coefficients of the core and cladding, respectively. The strain sensitivity factor Γ_{strain} is determined by the elastoopitc coefficients of the fibre materials as well as mode number. As shown in Eq 2.23, the strain sensitivity, $\frac{d\lambda_{res}}{d\varepsilon}$, depends on the value of strain sensitivity factor Γ_{strain}. Similar to temperature sensitivity, the strain sensitivity can be either positive or negative or to fabricate the strain insensitivity sensor if Γ_{strain} = -1.

2.4 Functional film deposition techniques

Optical fibres are usually made of substrates that are chemically inert (e.g. silica) and do not make direct interaction with chemical species or biological molecules for sensing. Fibre optic bio-/chemical sensors are configured by functionalizing optical fibre with materials that respond to sensing targets and change their optical properties correspondingly. How to incorporate such functional materials with optical fibre is the key step in the development of FOS bio-/chemical sensors. The film deposition techniques fall into two categories: chemical deposition and physical deposition. There are no strict boundaries between the two categories; the classification depends on whether the primary principle is closer to which side. Chemical deposition techniques require the depositing molecules having specific chemical properties. For example, the Langmuir-Blodgett method requires depositing molecules that are amphiphilic with a hydrophilic head and a hydrophobic tail [178]. Chemical vapour deposition (CVD) require the depositing element is halide or hydride. Physical deposition techniques usually occur at an energetic, entropic environment and require expensive instruments; these include electron beam evaporator, sputtering and cathodic arc deposition.

2.4.1 LBL deposition technique

LBL technique is used in later Chapter (Chapter 6) as part of the functionalisation process for LPG IgM sensor. The following content provides a brief introduction and review for the application of such a technique. LBL assembly is a thin film deposition

technique that has developed as a group of versatile and convenient methods for constructing composite films with precise control of film structures and composition. It has been of great interest because of its ability to control the film thickness in nanometre scales and its inexpensive choice of usable materials for coating planar and particulate substrates. The fabrication can be accomplished by using various techniques such as immersion, spin, spray, electromagnetism or fluidics [179] in which automation or robotics can be applied. There are diverse driving forces for LBL film fabrication such as electrostatic interaction, hydrogen-bond, halogen-bond, coordination-bond and cation-dipole interaction. The LBL-deposition techniques have been utilised for fabrication of antireflection coatings [180], controlled releasing coating in drug delivery [181], biosensors [182] [183], solar-energy conversion [184] and separation membranes [185]. With the development of material science, the extension of materials for LBL film fabrication will certainly enrich the structures and the functionality of LBL-deposited film materials. The films are usually formed by alternately depositing oppositely charged materials with wash steps in between. When immersed in a solution with positively charged polyelectrolytes, the negatively charged surface become positive due to the overcompensation by the surface adsorbed of positive polyelectrolytes. Typical immersion coating steps are illustrated in Fig 2.15.

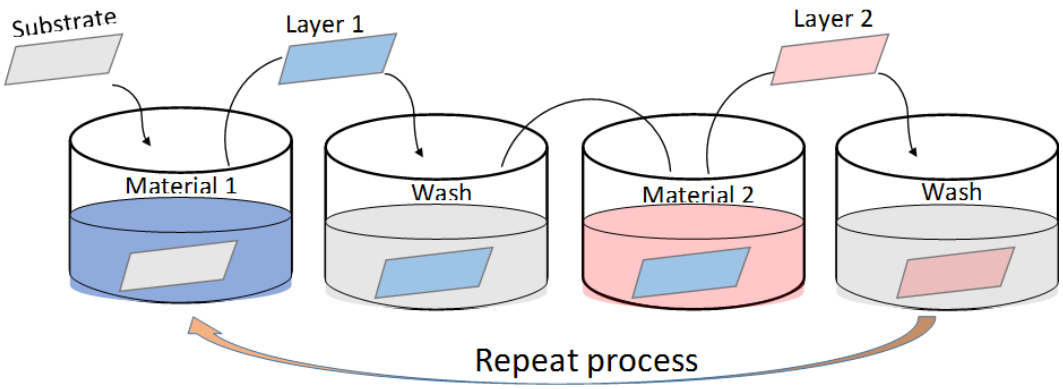


Fig 2.15 An immersion LBL deposition process.

The materials (e.g., particles in colloid or polymers) with opposite charge to the immersed substrate are driven by electrostatic force and attach on the substrate

surface. Multiple layers of film can be produced by repeating the deposition cycle. The LBL technique is not only applicable to polyelectrolyte systems but also for almost any type of charged species including inorganic molecules, nanoparticles, nanotube and nanowires, proteins, nucleic acids and DNA, and viruses. Table 2.1 lists the combination of positively charged materials with negatively charged materials that are found in the literature for LBL fabrication of thin films. There is also some cross combination between polycations and negatively charged materials such as PDDA/SiNPs, PAH/PSS that are not listed.

Table 2.1 A review of LBL thin film fabrication and their application.

Polycations / Positive charge	Polyanions/ negative charged particles	Intended use
Poly (diallyldimethylammonium chloride) (PDDA)	Poly (acrylic acid) (PAA)	Anti-corrosion and self-heal coating [186]
Poly (allylamine hydrochloride) (PAH)	Poly (acrylic acid) (PAA)	Matrix for pH sensing [187]
Poly-L-lysine (PLL)	Polystyrenesulfonate (PSS)	Biofunctionalisation of electronic devices [188]
poly(allyamine hydrochloride) (PAH)	Ethylenediaminetetraacetic acid (EDTA)	Switchable materials in bioanalysis and bioseparation [189]
Poly (diallyldimethylammonium chloride) (PDDA)	CdTe nanocrystals	Selectively deposition on working electrode [190]

Poly-L-lysine (PLL)	Dextran sulfate (DS)	Film formation kinetics study [191]
Poly-L-lysine (PLL)	DNA	Film property investigation [192]
Poly-L-lysine (PLL)	Heparin (HEP)	Drug delivery [193]
Poly-L-lysine (PLL)	Hyaluronic acid (HA)	Drug releasing systems [194]
Poly(ethyleneimide) (PEI)	Avidin	Disintegration study [195]
Poly (allylamine hydrochloride) (PAH)	SiNPs	Biosensors, chemical sensor [183, 196]
Poly (diallyldimethylammonium chloride) (PDDA)	tetrakis(4-sulfophenyl)porphine (TSPP)	Ammonia sensing [197]
poly(allyamine hydrochloride) (PAH)	platinum tetrakis pentrafluorophenyporphine (PtTFPP)	Sensor for detection of O_2 [198]

2.4.2 Sol-gel technique

Sol-gel is a method to produce a solid material from monomer molecules. It is a process that the phase of an aqueous system transits from a liquid to a diphasic system which contains both a liquid and solid phase, or to a solid phase. The method is employed in Chapter 4 for the synthesis of SiNPs and in Chapter 7&8 for the production of a matrix film that encapsulates colourimetric dyes for the measuring of CO_2. The sol-gel process is used to fabricate glassy and ceramic materials. A typical

example of the process is the polymerisation of metal alkoxides to form a metal oxide network structure. A popular choice used in the preparation of silica-based gels are tetramethoxysilane, $Si(OCH_3)_4$, and tetraethoxysilane, $Si(OC_2H_5)_4$, known as TMOS and TEOS, respectively. In the process, there are two distinct reactions: hydrolysis and polycondensation. The liquid silicon alkoxide precursor ($Si(OR)_4$) initially undergoes hydrolysis (Eq 2.25) by reacting with water forming silanols (Si-OH) group. As water and silicon alkoxide are immiscible, this requires a solvent which can dissolve the both to make the reaction more efficient. Hydrolysis occurs very fast once the silicon alkoxide makes contact with water, the reaction speed depends on the concentration ratio of both reactants. Depending on the amount of water present, the hydrolysis may go to completion or stop while the metal is only partially hydrolysed. Complete hydrolysis often requires an excess of water and the use of a catalyst. In this stage, a liquid medium containing numerous small particles is referred as the Sol.

$$Si(OR)_4 + 4\,H_2O \xrightarrow{H^+ or\ OH^-} Si(OH)_4 + 4\,R(OH) \qquad (2.25)$$

During hydrolysis, a polycondensation process occurs simultaneously to form a 3-D entangled network of the corresponding inorganic oxide. The hydrolysed product, silanol groups, are cross-linked by forming siloxane bonds (Si-O-Si) as illustrated in Fig 2.16. The Sol is converted into a gel in this stage.

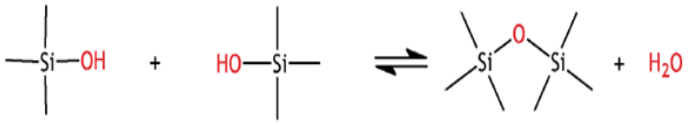


Fig 2.16 Condensation process between silanol groups.

Therefore, the total reaction of the sol-gel process is:

$$Si(OR)_4 + 2\,H_2O \xrightarrow{H^+ or\ OH^-} SiO_2 + 4\,R(OH) \qquad (2.26)$$

Hydrolysis and polycondensation can be accelerated by adding an appropriate acid or base catalyst. Catalyst plays an important role in determining the structure of the silica dioxide network as it affects the ionic charge of the silica particles that directly affect the polycondensation rate. At low pH (acidic condition), the silica particles bear

very little ionic charge and thus can collide and aggregate into chains, forming linear molecules that are occasionally cross-linked resulting in polymeric structure [199]. Under high pH (basic condition), there is a faster hydrolysis speed that forms more highly branched clusters that behave as discrete species [199]. The silica particles aggregate and attach to each other forming a mesoporous structure. A xerogel film can be prepared by coating the sol solution on a substrate via a dip-coating or spin-coating method and drying the wet film under mild conditions (low temperature 25-100 ℃). The film usually undergoes a shrinkage after the liquid inside of the pore has been removed by evaporation. A process of the sol-gel technique is illustrated in Fig 2.17. Inside the silica film, there are three types of chemical groups: siloxane bridges (≡Si-O-Si≡), hydroxyl groups (-OH) and unsaturated Si atoms. The siloxane bridges are hydrophobic whereas the hydroxyl groups and unsaturated Si are hydrophilic so that water molecules can absorb on the film surface by physisorption. The hydrophobicity of such silica film is determined by the number of hydroxyl groups presented. Sintering of film at high temperature (above 200 ℃) can reduce the number of hydroxyl groups and increase the hydrophobicity of film [200]. Another way to increase the hydrophobicity is to substitute the hydroxyl groups with some organic [201] or inorganic groups [202] via chemical modification.

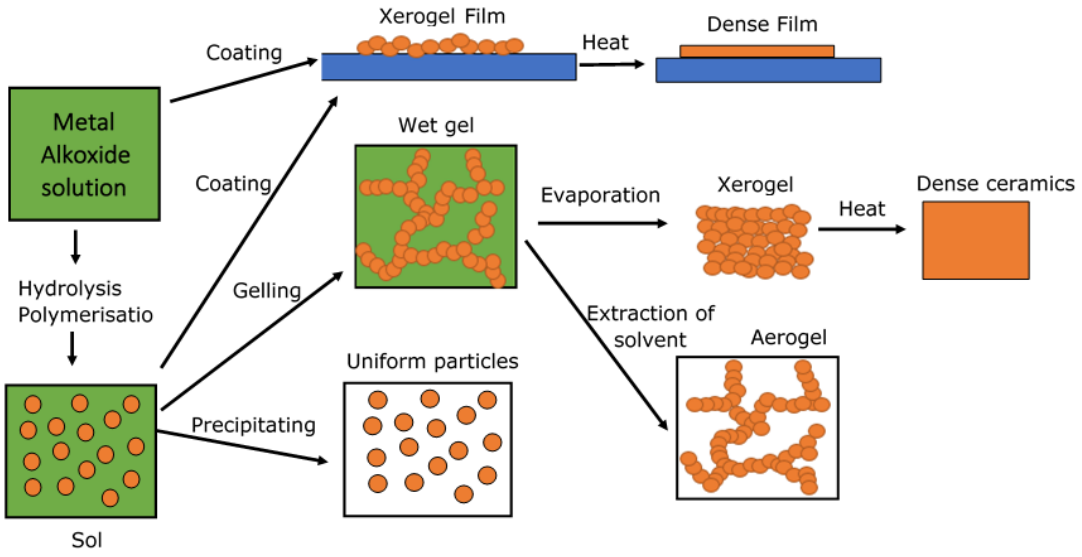


Fig 2.17 Schematic representation of the different stages and routes of the sol-gel technology.

The fabrication of sol-gel xerogel film has been applied in doping with sensing elements such as fluorescent dyes, a pH indicator for chemical sensing [70, 203-206]. The mesoporous silica structure provides the cage-like structure to physically or chemically entrap the sensing element inside the film and meanwhile, allows the analytes to diffuse into the pores and interact with the sensing element. The formed porous silica matrix is transparent with lower light adsorption; it is chemically inert and the most important feature is that it is easy to entrap active species. The physical entrapment allows the gel matrix to entrap any species from small molecules to big compounds, from liquid phase to solid phase.

Compared to aerogel film described above, an aerogel film can be obtained by drying the wet sol-gel film under supercritical condition (e.g. high pressure, high temperature) so that the liquid inside the pore is replaced by air; such film bears less shrinkage with higher porosity (~30-99 %) [207]. However, this film is almost impossible to obtain in ambient conditions.

Apart from making ceramic films, the sol-gel process has also been widely used to fabricate spherical SiNPs [208, 209] that offers a straightforward, scalable and controllable method to produce variable sizes (Fig 2.17). The SiNPs have a regular porous structure with uniform pore size, large surface area and superior thermal stability. They are suitable for a variety of application in diverse fields such as drug delivery, biosensors and molecular separations.

2.5 Gas diffusion through the porous silica film

Gases can pass through the porous silica film and their diffusion rate largely depends on the characteristic of the diffusion gas (e.g. diameter, polarity), membrane characteristics (e.g. pore size, thickness and chemical groups on the surface) and operating condition (e.g. pressure, temperature). The gas permeation of such silica film is usually classified as Knudsen diffusion due to the small size of pore (average diameter of a few nanometres) approximately equal to the mean free path of a gas molecule [210]. According to Fick's first law of diffusion, the diffusive flux (J) in a given direction is related to the gradient of the concentration (C_{gas}) as it is expressed in Eq 2.27:

$$J = -D\frac{dC_{gas}}{dx} \tag{2.27}$$

Where x is thickness of the silica film and D is diffusion coefficient which can be expressed as Eq 2.28 for Knudsen diffusion [211].

$$D = \frac{d_p}{3}\sqrt{\frac{8RT}{\pi M}} \tag{2.28}$$

Where R is gas constant value, M represents the molecular weights of gas and d_p is the mean pore size of the silica film. Considering the ideal gas relation in which the correlation of gas concentration with gas pressure (P) and temperature (T):

$$\mathrm{C_{gas}} = \frac{\mathrm{P}}{\mathrm{RT}} \tag{2.29}$$

The Eq (2.27) can be rewritten as Eq (2.30) by substituting Eq (2.28), Eq(2.29) into Eq (2.29):

$$\mathrm{J} = -\frac{\mathrm{d_p}}{3}\sqrt{\frac{8\mathrm{RT}}{\pi\,\mathrm{M}}}\frac{\mathrm{dC_{gas}}}{\mathrm{dx}} = -\frac{\mathrm{d_p}}{3}\sqrt{\frac{8}{\pi\,\mathrm{MRT}}}\frac{\Delta\,\mathrm{P}}{\mathrm{L}} \tag{2.30}$$

Where ΔP is the pressure drop as the driving force for diffusion across the diffusion length L or the thickness of the silica film. Therefore, the diffusion flux of a specific gas in a porous silica film depends on the geometry of the film (pore size and thickness) as well as gas pressure and temperature. It has a higher diffusion rate for gases with small molecular weight. The theoretical gas diffusion mode is not taken into account of the chemical interaction of gases with film, for example, the silica film contains silanol groups (-OH) which can produce strong interaction with polar gases (e.g. NH_3) affecting the flux of gases.

2.6 Summary

FOSs have been widely applied for sensing of physical and chemical parameters. A typical FOS comprises of a light source, optical fibre transducer and photodetector. The choice of the three components should consider many factors, for example, operating wavelength of light source, the attenuation of light in optical fibre and the sensitivity of photodetector while designing the sensor for a specific application. FOS bio-/chemical sensor can have various fibre configurations to create interaction of light with the sensing material around it. The determination of the configuration

relies on the change of sensing materials after interacting with target molecules. LPG sensor is sensitive to surrounding RI and is an elegant platform for biosensing.

LBL method provides a precisely controlled thickness to build up film via molecular interaction between each layer. Sol-gel method is used to prepare porous silica film and is versatile for sensor fabrication as it can dope different sensing elements such as pH dyes and easy to deposit on the optical fibre. The mesoporous structure of silica film allows gas exchange between the inside and outside of the film.

Chapter 3 LPG sensor fabrication and characterisation

3.1 Introduction

As discussed in the previous chapter, LPG sensors are sensitive to RI (RI), temperature and strain. Their sensitivity to perturbations in these parameters reaches a maximum at the PMTP of each mode [173, 212]. We are interested in fabricating LPGs with a period around 110 µm which couples to higher cladding modes and the PMTP is observed at wavelengths located closer to the visible light range (850 nm). This renders a higher sensitivity than that of lower cladding modes as explained in Section 2.3.2, Chapter 2. Besides, the shorter wavelength range allows the use of a visible-near-infrared range optical spectrometer and a cheap halogen light source rather than an expensive optical spectrum analyser and light source.

In this chapter, the system set-up and process for fabrication of LPGs by using UV irradiation are introduced. The fabricated LPGs have phase matching dual bands centred at around 850 nm in their transmission spectrum. Simulation of an LPG transmission spectrum is demonstrated by using *OptiGrating*. Characterisation of such an LPG sensor was conducted experimentally in terms of sensitivity to temperature, strain and RI. The chapter describes two LPG fabrication methods which are the point-by-point method and the amplitude mask method. The point-by-point method has flexibility in the fabrication of various grating periods of an LPG compared with the amplitude mask method, in which each mask can only fabricate one fixed period of LPG sensor. However, the latter has a short fabrication time and will be used if the desired grating period matches the amplitude mask.

3.1 Fabrication of LPG sensor

The fabrication system used is illustrated in Fig 3.1 [151]. The system comprises (i) a UV laser which is a frequency-quadrupled Nd:YAG laser (Continuum Minilite-10, USA) operating at a wavelength of 266 nm, the output power (measured with laser power meter from Coherent Ultima Labmaster) of the laser is about 7 mW, (ii) A cylindrical

lens with a focal length of 100 mm was exploited to focus the laser beam, (iii) translation stage (Physik Instrumente, Germany) with a resolution of 1 µm that is used to move the fibre to a new position, (iv) A slit or amplitude mask that constrains the size of laser beam illuminating the optical fibre, or projects a grating pattern onto the optical fibre, respectively. Boron-germanium photosensitive optical fibre (PS750, Fibrecore, UK) with a cut-off wavelength of 750 nm was placed into V-grooves that are mounted on either side of the translation stage. The fibre was stretched in taut and fixed with two strong magnets to the V-grooves during the laser irradiation process. Before placing on the V-grooves, the optical fibre was initially stripped mechanically (~3 cm length in the mid-section) using an optical fibre stripper and cleaned with isopropyl alcohol to remove any debris that could become a hot spot and damage the fibre.

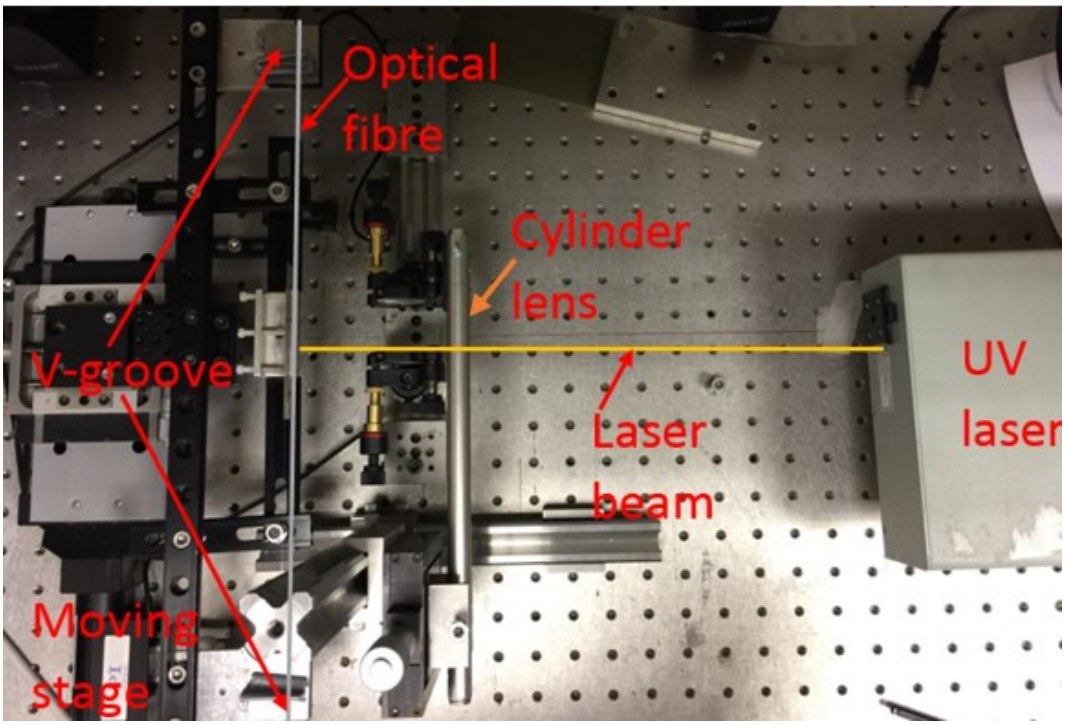


Fig 3.1 Laser system set-up for fabrication of LPG sensors.

Before starting to fabricate LPGs, it is necessary to predict the desired grating period according to transmission spectrum of the users' requirement. This can be done from the phase matching curve explained in Fig 2.13 or from simulation by using commercial software such as *Optigrating*. It has to be noted that the phase matching curve varies for the fibres with different RI profile. As described in section 2.3.2, UV

laser irradiation is used to introduce RI modulation to a photosensitive optical fibre by the absorption of the germanium-oxygen deficiency centre (GODC) to UV radiation. The determination of grating profiles including grating period, grating length, duty cycle, on the other hand, is decided by the specific methods that are introduced below.

3.1.1 Point-by-point method

The point-by-point method is used when the amplitude mask failed to match the desired grating period which is usually defined as the grating period at optimal sensitivity. It was conducted by exploiting a size controllable metal slit in front of the UV laser beam (illustrated in Fig 3.2) to control the area of illumination on the optical fibre. After a certain exposure time (approximately 30s), the fibre was then moved to the next position by the translation stage. During the exposure time, the region that was under UV radiation obtains an increased RI value change than that of the surroundings due to the absorption of UV light. The distance between each translation stage position equals the size of slit in order to fabricate an LPG sensor with duty cycle of 50/50 (the gap is half of grating period length). For example, in order to fabricate a grating period of 109 µm, the slit size should be set to 54.5 µm and the moving step is 109 µm. It has been demonstrated that the duty cycle of an LPG determines the properties of loss bands and a duty cycle of 50/50 has the strongest attenuation [213, 214].

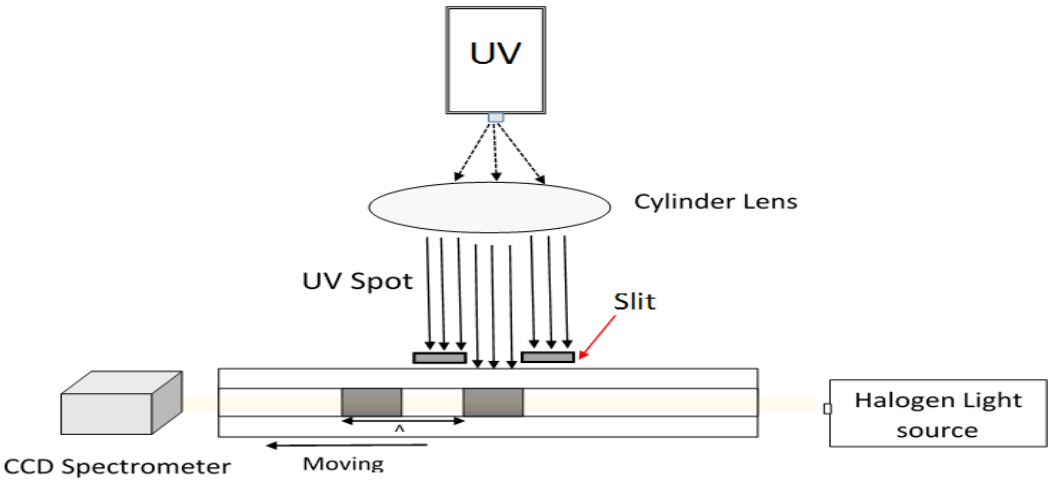


Fig 3.2 Point-by-point fabrication of LPGs. The top is the UV laser source. The specification of the laser, lens and moving stage have been described above for Fig 3.1.

The evolution of the attenuation bands of an LPG can be monitored during the fabrication process by visualizing the transmission spectrum of the optical fibres. As illustrated in Fig 3.2, a halogen light source (Ocean optics, HL-2000, UK) is exploited to send light into the optical fibre and a CCD spectrometer (Ocean optics, USB2000, UK) connected to the distal end of the optical fibre to detect the transmission spectrum. This allows the real-time monitoring of LPG fabrication.

Fig 3.3 illustrates the transmission spectrum of an LPG at different timestamps after starting point-by-point fabrication of a 3cm LPG with a period of 108.8 µm. It shows that the cladding mode LP_{018} starts to appear at a wavelength of 684 nm after about 0.75 cm long grating, 2000s after starting the fabrication and then the attenuation becomes stronger along with the coupling to the cladding mode LP_{019}. The attenuation band at LP_{019} has two coupled bands centred at about 850 nm. This observation matches the theoretical result based on the phase matching curve reported by James, et al. [215]. The overall time for fabricating this 3 cm of LPG is more than 2 hours.

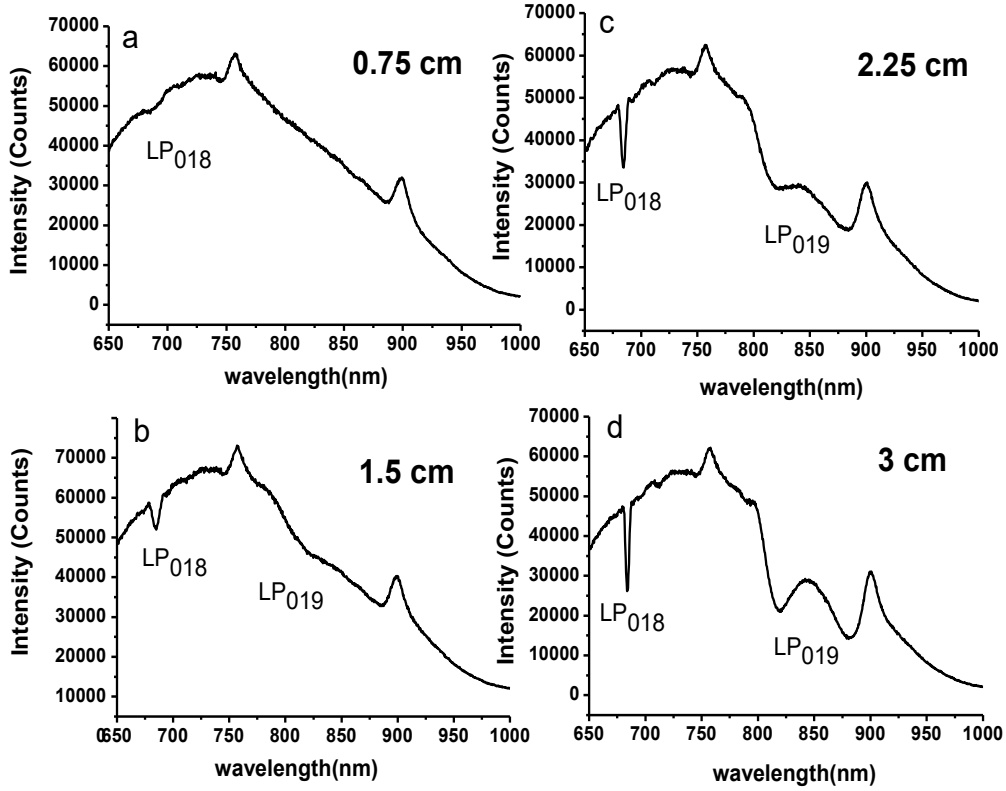


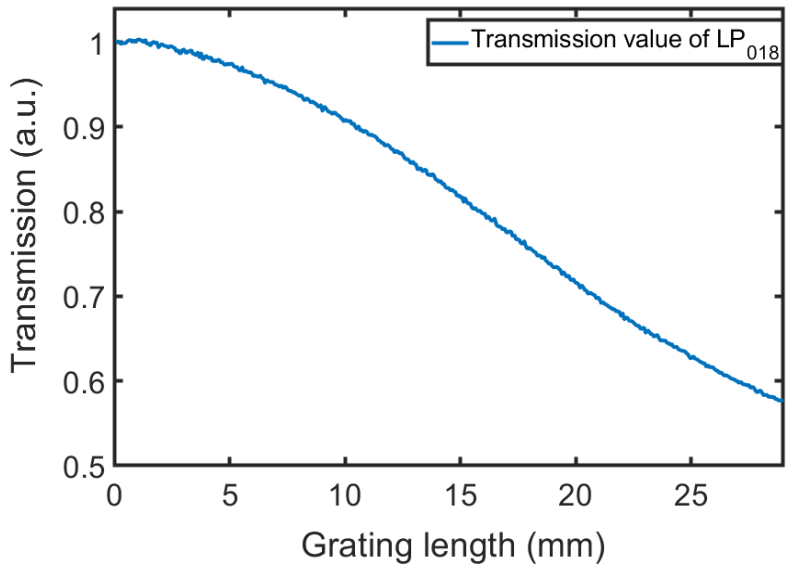
Fig 3.3 Transmission spectrum of different grating length after starting point-by-point fabrication process: (a) 0.75 cm ; (b) 1.5 cm; (c) 2.25 cm; (d) 3cm.

The grating length is defined as the total length of the written region, which increases as a function of time during the fabrication. Fig 3.4 illustrates the transmission value and central wavelength of the LP_{018} mode as a function of grating length. It is observed that the transmission value of LP_{018} decreases with increase of grating length. This result is explained from the theoretical expression of [215]:

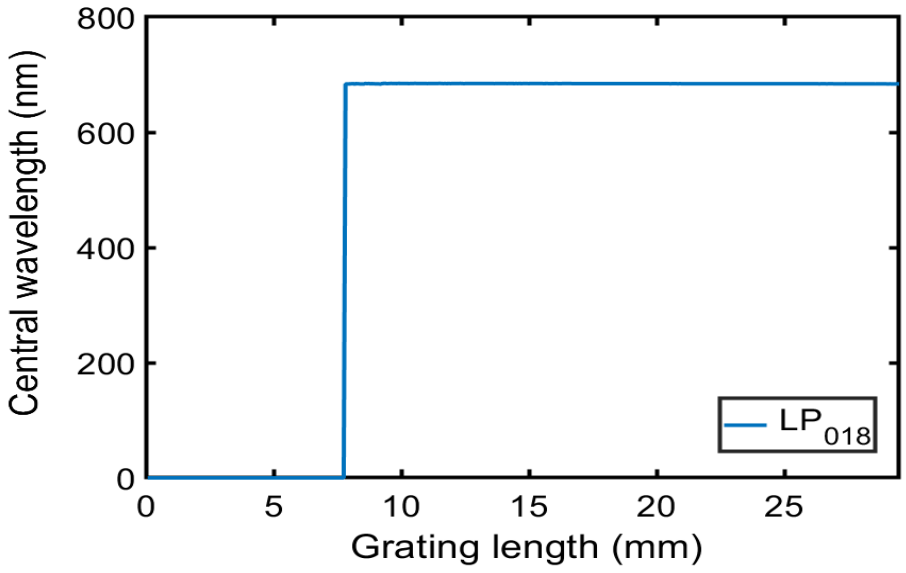
$$T_i = 1 - \sin^2(k_i L) \tag{3.1}$$

Where T_i is the transmission value of the i^{th} attenuation band, L is the length of grating and k_i is the corresponding coupling coefficient. According to this equation, a longer grating provides a lower transmission value, in the other words, a deeper attenuation band. However, this isn't always true considering the sine function is a periodical wave and the transmission value is expected to bounce back and increase after certain length of grating.

The central wavelength, on the other hand, shows a stable value (684.29± 0.24 nm) after evolving as the grating length increases. For the first 7 mm, the attenuation band is too small to be tracked.



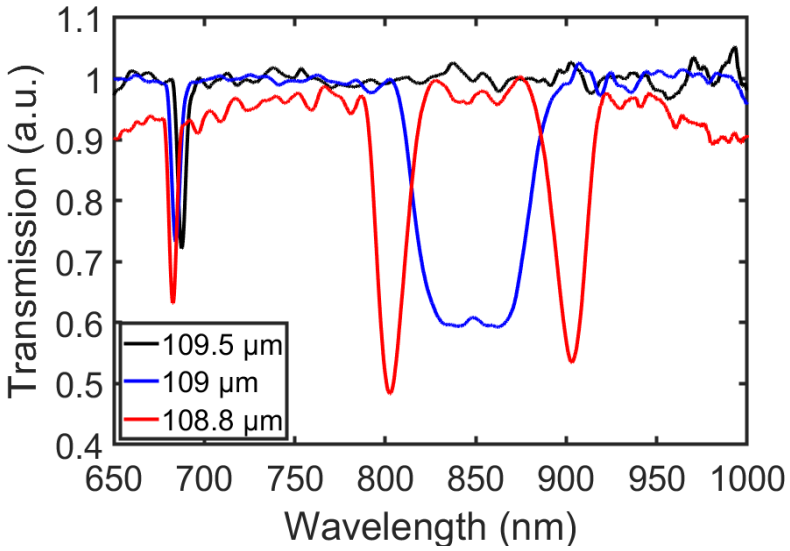
(a)



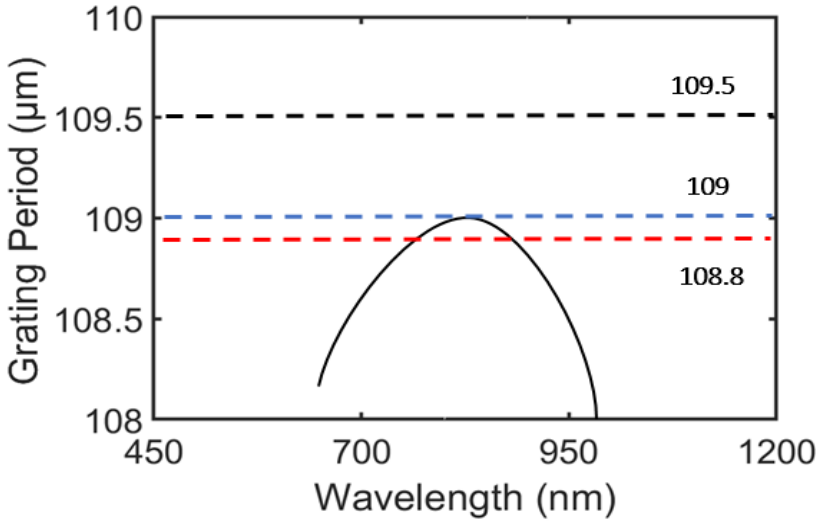
(b)

Fig 3.4 Transmission value (a) and central wavelength (b) of LP_{018} against the grating length.

LPGs with different grating periods around 109 µm were fabricated by using point-by-point method in order to investigate the attenuation band close to the PMTP (illustrated in Fig 3.5a). It is clear that the phase matching condition of LP_{019} appears as one big attenuation band when the grating period is 109 µm. A shorter grating period (108.8 µm) leads to a split of attenuation band at the PMTP (LP_{019}) and a longer grating period (109.5 µm) causes no attenuation band at a wavelength of 850nm. This phenomenon can be explained from Fig 3.5b where the phase matching curve of LP_{019} has one intersection point when the grating period was 109 µm, two intersections with grating period of 108.8 µm and no intersection with 109.5 µm.



(a)



(b)

Fig 3.5 (a) Normalised transmission spectra of LPGs that were fabricated with grating periods of 108.8, 109 and 109.5 μm, respectively. (b) Schematic explanation of resonance band behaviour at LP_{019} for different grating periods. The curve in the graph mimics the phase matching curve of LP_{019}.

3.1.2 Amplitude mask method

The point-by-point fabrication method allows the flexible fabrication of an LPG with the variable grating periods. However, this method takes a very long time (~2 hours) to fabricate one single 3 cm long LPG for same laser power. An alternative method

applied in this thesis is an amplitude mask method in which the slit was replaced with an amplitude mask (Fig 3.6) which has periodical slots. The amplitude mask itself determines the grating period and duty cycle of an LPG. The mask is placed in proximity in front of the optical fibre and facing the laser beam (illustrated in Fig 3.7). It is mounted on the translation stage and moves in synchronisation with the optical fibre. The UV laser beam passes through the mask and projects a periodic UV light pattern on the optical fibre. The size of the light pattern is equal to the beam size (3 mm). During the fabrication, the translation stage moves at a constant speed (0.02 mm/s) so that the UV beam continuously projects a periodical UV pattern through the amplitude mask onto the optical fibre. Apart from the start and end position of the grating, every single point of the grating will have enough exposure time (150s) that ensures a periodic increase in RI.

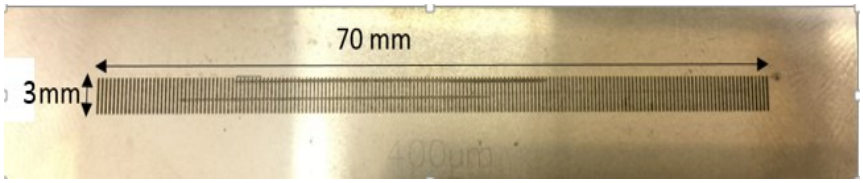


Fig 3.6 Amplitude mask. The mask was made of steel (1Cr18Ni9Ti) and produced by Suzhou Sunshine Laser Technology Co, Ltd, China. The length of the grating region is 70 mm, and the width is 3 mm.

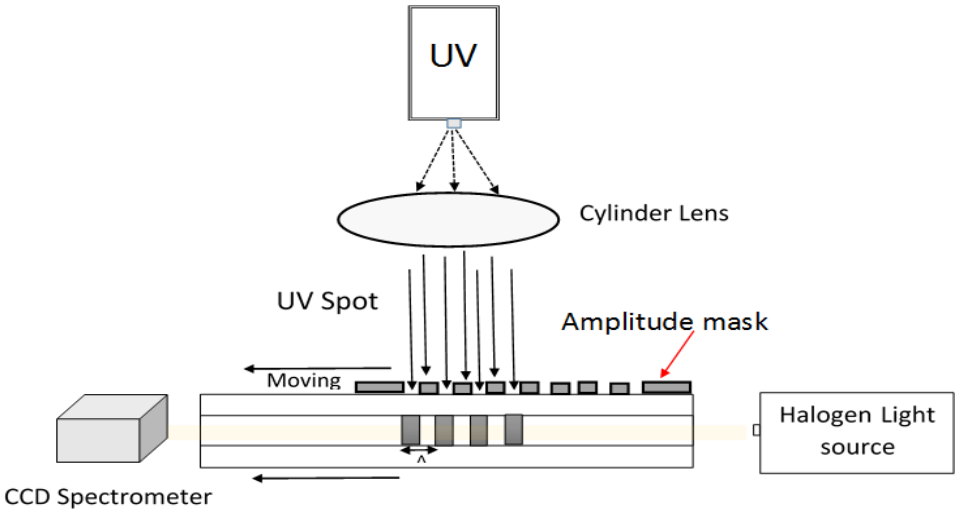


Fig 3.7 Amplitude mask method to fabricate an LPG sensor. The top is the UV laser source and the fibre and amplitude mask was fixed in the same moving stage so that they move together.

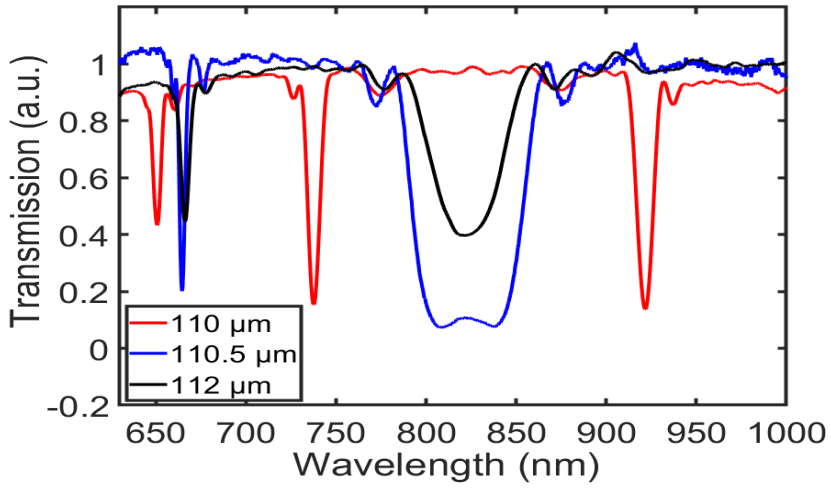


Fig 3.8 The normalised transmission spectrum of LPGs fabricated by using the amplitude mask method with grating period of 110, 110.5 and 112 µm.

Fig 3.8 illustrates the normalised transmission spectrum of three LPGs at phase matching condition. The corresponding grating period of the PMTP is larger than that of the point-by-point method (112 µm compared to 109 µm). The difference is not due to the fabrication method but the optical fibre. The two LPGs were fabricated from two batches of optical fibre which may have different RI profile resulting in different phase matching condition of the fabricated LPG. The grating period of PMTP remains the same for the same batch of optical fibre.

The amplitude mask method takes approximately 25 mins to write a typical 3 cm long LPG at the laser power around 7 mW. It significantly reduces the time it takes compared to the point-by-point method (2 hours). The grating quality (perhaps defined by the depth of attenuation bands) is higher using amplitude masks compared to the point-to-point. Its transmission loss of attenuation band is about 0.9 which is almost double that of the point-by-point method (~0.5).

Despite the advantage of the amplitude mask method over the point-by-point method, it is not as flexible as the grating period is fixed and one amplitude mask can only produce one period of LPG. Besides, it is also a technical challenge to manufacture such an amplitude mask with small grating period variation (e.g. 0.1 µm).

3.2 LPG simulation using *Optigrating*

The characteristics of cladding modes and the transmission spectrum of an LPG can be simulated using Coupled Mode Theory [172, 216]. Coupled Mode Theory is a method to analyse the light propagation in weakly coupled waveguides. It assumes that the field of coupled structures is sufficiently represented by a linear superposition of the modes of the uncoupled structure [217]. The basic idea of Coupled Mode Theory is that the modes of uncoupled structures are defined and solved first. Then a linear combination of these modes is used as a trial solution for Maxwell's equations for coupled structures. After that, the derived coupled mode equations can be solved analytically or by numerical method.

There are two approaches to conduct the theory which are a two-layer method [218] and a three-layer method [172, 216]. Both methods employ a weakly guided approximation to find the effective RI of the fundamental core mode. In the weakly guided approximation, the normalised core-cladding RI difference is considered very low (<<1) or the RI difference between core and cladding is very small [172]. This allows the simpler solution of the characteristic equation resulting in linearly polarised (LP) modes because the waves constructed from these simplified solutions propagate at small angles to the fibre axis and are essentially polarised in a single direction. The main difference between these two approaches is the representation of the fibre geometry, mode field profiles, intensity distributions and coupling coefficients. The two-layer method considers a fibre cladding surrounded by a homogeneous of ambient material, which ignores the core-cladding interface in calculating the effective RI of the cladding modes. However, the three-layer method considers the core-cladding interface. It has been shown that the three-layer fibre geometry is a more accurate method for theoretically simulating LPG but with a greater mathematical complexity compared to the two-layer method [216].

The Coupled Mode equation helps to solve the component of the electric and magnetic fields vector of a mode in the fibre core, fibre cladding and external media, respectively. The transmission spectrum of an LPG sensor can be then obtained. There are three common methods to calculate the transmission spectrum of the LPG,

which are the integral method [219], formula method [220] and transfer matrix method [221]. The integral method is capable of providing a multi-mode transition spectrum in a wide range of wavelengths but requires complicated computation process. The formula method is convenient for calculation but can only solve a single mode transition spectrum in a narrow wavelength range. The transfer matrix method is used to calculate the transmission spectrum of a non-uniform fibre grating and offers high accuracy and fast speed [222].

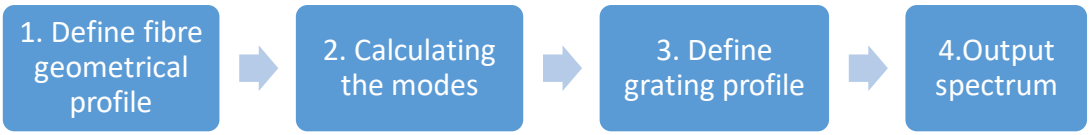
Optigrating is a commercially available user-friendly software for modelling grating assisted devices such as LPG and FBG. It helps to design and analyse a grating assisted devices by calculating light propagation, reflection and transmission spectra based on the input profile of the optical fibre and the profile of the grating.

Table 3.1 illustrates the parameters of optical fibre PS 750 that were used to simulate the LPG transmission spectrum based on *Optigrating* (version 4.2.3).

Table 3.1 Datasheet of PS750

Fibre type	PS 750
RI of core	1.4584
Radius of core (µm)	2.14
RI of cladding	1.4533
Radius of cladding (µm)	62.6
External RI	1

The use of the software can be summarised as the following flow chart:



The first step is to define the optical fibre profile; a three-layer cylinder structure was built and followed by inputting parameters such as width, RI and material dispersion for each layer. The first two layers are the fibre core and cladding. The third layer is the external environment, this can be air, water or another RI medium. In this case, air was defined as the third layer. The second step is then defining the propagation modes and calculating the effective RI of the cladding of each different cladding modes. The third step is to define the fibre grating profile in which the shape, length and RI modulation can be defined. After that, the transmission spectrum of the defined LPG can be achieved.

The transmission spectrum of an LPG with a grating period of 111.5 µm is simulated and illustrated in Fig 3.9. It shows the PMTP of the attenuation band with central wavelength at 830 nm. An LPG sensor is fabricated with the same grating period by using the amplitude mask method described in the previous section and its transmission spectrum is plotted in Fig 3.9 for comparison. There is a wavelength difference (~7 nm for PMTP) compared to the simulated result, which may be attributed to the deviation of the modelling method to the real scenario or the grating isn't a true binary grating. As the PMTP is extremely sensitive to the grating period, it is difficult to achieve the PMTP without knowing the exact period. The simulation will benefit in finding the correct grating period of PMTP.

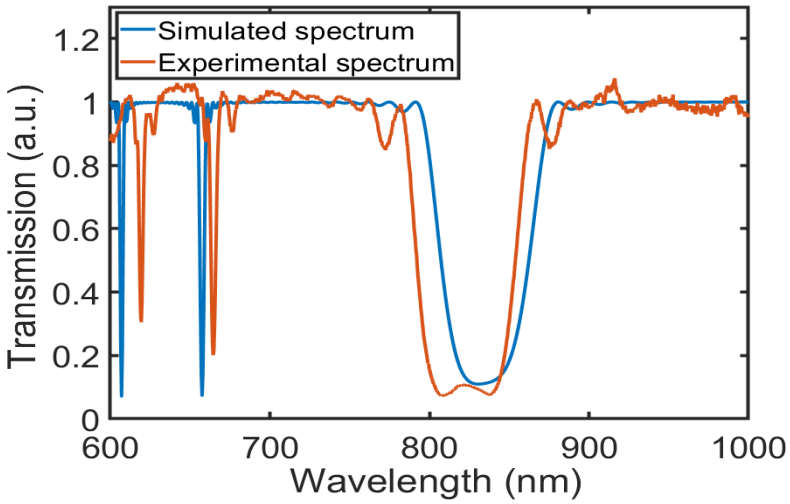
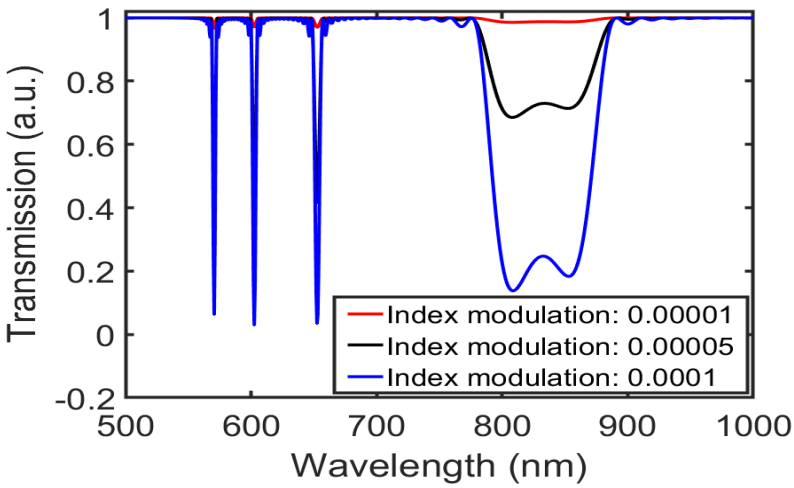
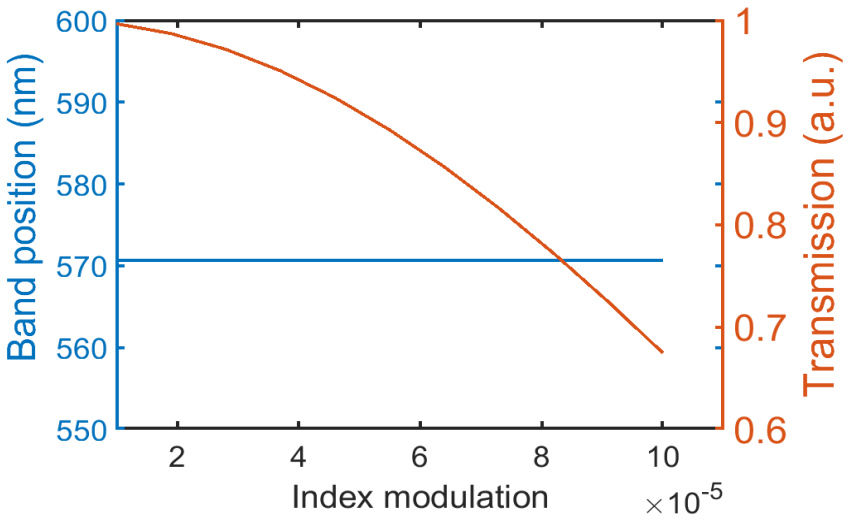


Fig 3.9 Transmission spectra of LPGs with a grating period of 111.5 µm, length of 3 cm that are achieved by simulation and experiment; the simulation is done by using of *Optigrating*, and the fabrication is completed by using the amplitude mask method.

The effect of the amplitude of the modulation index to the LPG's transmission spectrum is investigated by varying the value of the modulation index in *Optigrating* and keeping the other parameters the same. The results are shown in Fig 3.10 where the transmission value of the attenuation band decreases with increasing modulation index and the wavelength of the attenuation band remains constant. This can be explained in Eq 3.1 as the higher modulation index enhances the coupling coefficiency and results in a lower transmission value and a deep attenuation band.



(a)



(b)

Fig 3.10 (a) Simulated transmission spectrum of an LPG (grating period: 111.2 µm) with different RI modulation. (b) Attenuation band position and transmission value of attenuation band as a function of index modulation. The band with the central wavelength of 0.57 µm was selected.

When fabricating an LPG, the amplitude of RI modulation is determined by the output power of the UV laser, the power density of the UV light over the fibre region (focusing of UV beam to optical fibre), the exposure time of each grating point and the photosensitive dopants of the optical fibre. All the above factors contribute to the transmission loss of an LPG.

3.3 LPG temperature measurement

An LPG that is fabricated using the amplitude mask method described in the previous section with a grating period of 109 µm was used to calibrate the temperature sensitivity by using the set-up illustrated in Fig 3.11.

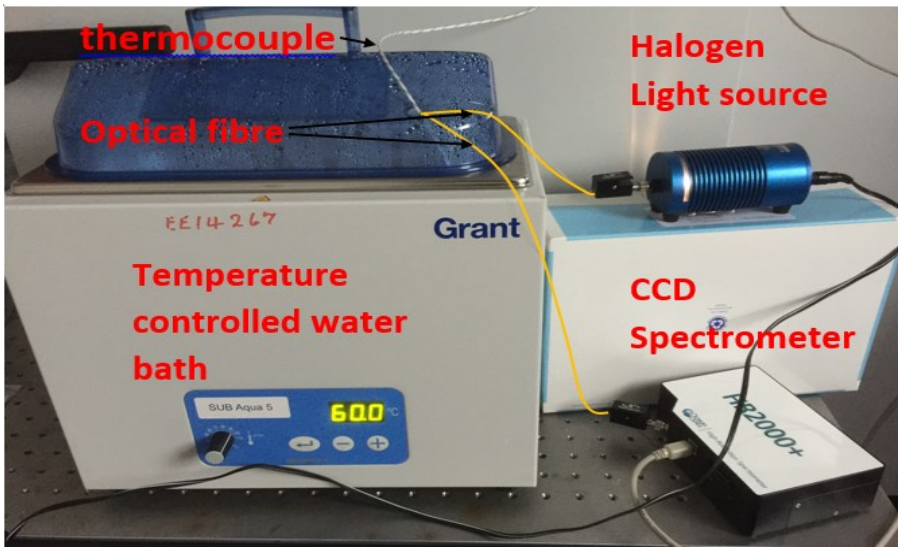
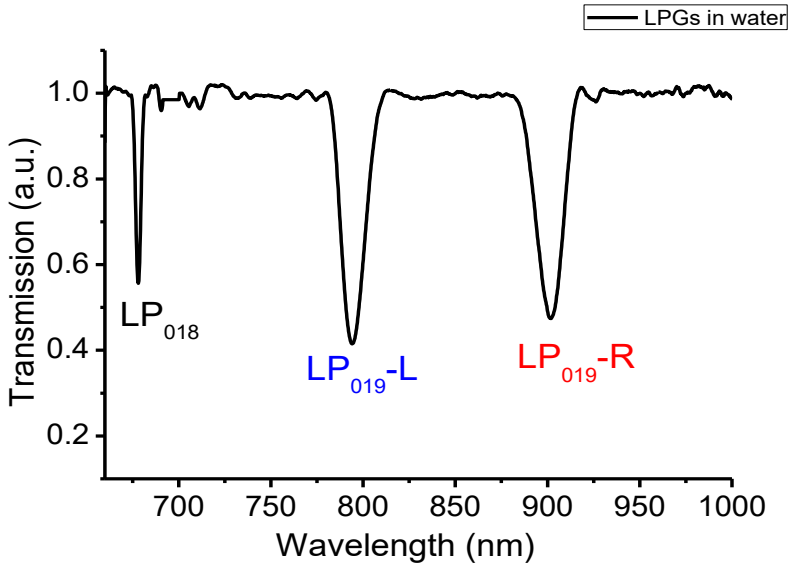
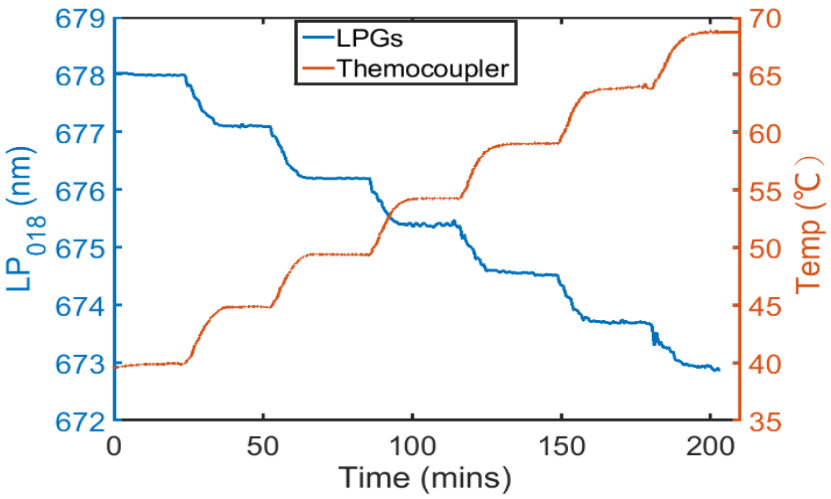


Fig 3.11 Set-up for calibrating the LPG in a temperature regulated water bath (Grant Aqua Plus, UK); The LPG with a grating period of 109 µm was fixed by a Teflon holder with two clamps and immersed in the water bath. A thermocouple type K, connected to a thermocouple logger (TC-O8, Pico Technology, UK) is placed close to the LPG to simultaneously record temperature. A halogen light source (Ocean Optics, HL-2000, UK) and CCD spectrometer (HR 2000+, Ocean Optics, UK) were used to characterise the LPG.

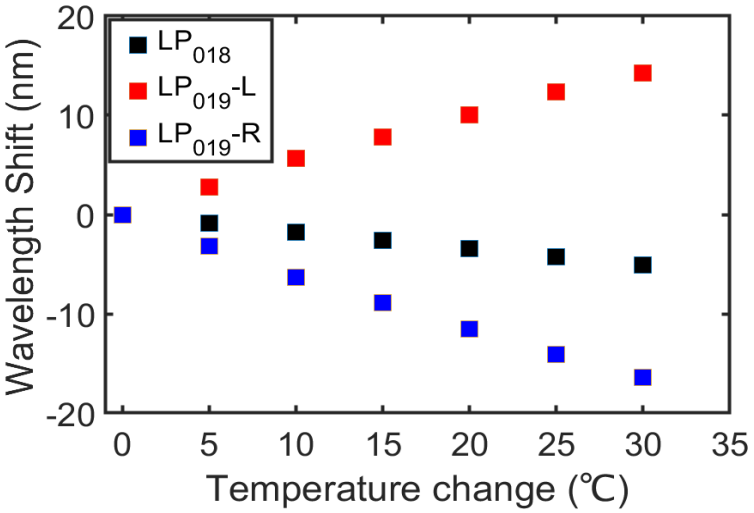
The transmission spectrum of the LPG in water (40 ℃) is illustrated in Fig 3.12a in which the cladding mode LP_{019} is at the phase match condition with split dual attenuation bands. The wavelength shift of the attenuation bands match well with the temperature change as it is illustrated in Fig 3.12b. The wavelength of attenuation band of LP_{018} progressively decreases as the temperature progressively increases from about 40 ℃ to 70 ℃. The wavelength shift of the attenuation bands is plotted against the temperature change in Fig 3.12c. It can be observed that the wavelength shift of the left hand attenuation band of LP_{019} , abbreviated as LP_{019}-L, has the same direction of wavelength shift as LP_{018} but with larger magnitude. The attenuation band of LP_{019}-R, on the other hand, undergoes an opposite wavelength shift with increase of temperature. Because the dual attenuation bands of LP_{019} are coupled from one mode, the two bands can be treated as one signal. Therefore, the wavelength separation between LP_{019}-L and LP_{019}-R is considered as the response of LP_{019} to external perturbation. Fig 3.12d illustrates the separation of dual-bands at LP_{019} as a function of temperature. It shows that the attenuation bands of LP_{019} linearly fit to the temperature change with a sensitivity of ~1 nm/℃.


LPGs in water
Transmission (a.u.)
1.0
0.8
0.6
0.4
0.2
LP018
LP019-L
LP019-R
700
750
800
850
900
950
1000
Wavelength (nm)

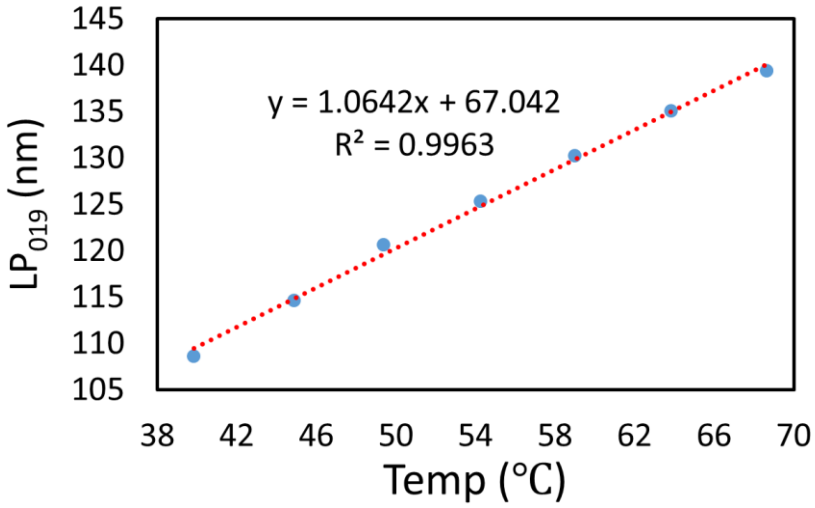
(a)


LPGs
Themocoupler
LP018 (nm)
679
678
677
676
675
674
673
672
Temp (℃)
70
65
60
55
50
45
40
35
0
50
100
150
200
Time (mins)

(b)



(c)



(d)

Fig 3.12 (a) Transmission spectrum of the LPG in water at a temperature of 40 ℃. (b) The wavelength of LP_{018} response to temperature. (c) Wavelength shift of attenuation bands against the temperature change. (d) Separation of dual bands at LP_{019} as a function of temperature. Error bar is less than the marker size.

In some applications, such as the measurement of RI, the temperature sensitivity of an LPG is something that needs to be compensated for. A typical action is to place the LPG in a thermostatic environment (such as an incubator) where the temperature is stable during the measurement. This can remove the temperature effect but also increases the marginal cost of the sensor set-up. The second way is to design

temperature insensitive LPGs based on the above theory. This requires the special composition of optical fibre so that the thermal expansion contribution of fibre glass cancels out the thermooptic factors. The third method is by applying a reference LPG.

Fig 3.14 illustrates the transmission spectrum of an LPG array which contains two LPGs that were fabricated sequentially by the amplitude mask method with different grating periods (109 µm and 110.5 µm) in a single optical fibre (illustrated in Fig 3.13). Let us consider the first LPG (109 µm) as the target LPG (LPG1) and the latter (110.5 µm) as reference LPG (Ref-LPG). The Ref-LPG was fabricated approximately 30 cm away from the LPG1. The choosing of grating period of Ref-LPG is important as it determines the position of attenuation bands. The overlapping of attenuation bands of two LPGs may make it difficult to resolve two attenuation bands. In Fig 3.14, two attenuation bands belong to one cladding mode (LP_{018}) of two different LPGs. The wavelength of attenuation band in LPG1 is shorter than the Ref-LPG due to the small grating period. Both LPGs were tested to the temperature sensitivity by the means of set-up in Fig 3.14.

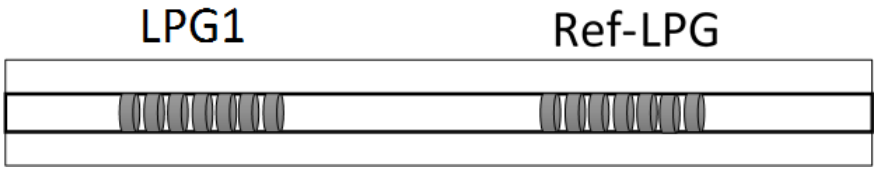


Fig 3.13 Schematic of an LPG array sensor.

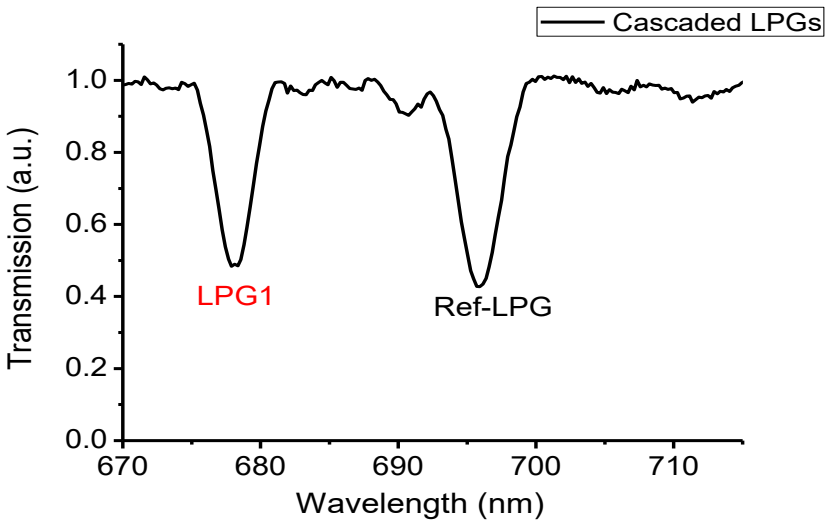


Fig 3.14 Transmission spectrum of an LPG array. The attenuation bands in the graph belong to cladding mode LP_{018} of the two LPGs. LPG1 and Ref-LPG are the LPG with grating period of 109 µm and 110.5 µm, respectively.

Fig 3.15 demonstrates that the wavelength of attenuation bands in Fig 3.14 linearly fits to temperature. The attenuation band from the two LPGs shifts to a lower wavelength with increase of temperature. The Ref-LPG exhibits a sensitivity of 0.196 nm/°C which is slightly higher than that of LPG1 (0.177 nm/°C) as it is closer to the PMTP of the cladding mode. The sensitivity difference between two LPGs is observed as ~0.02 nm/°C. Considering the resolution of the spectrometer (0.17 nm), this difference can only be detected while the temperature changes above 9 °C. This range covers almost all the general condition of the laboratory test and therefore, the reference LPG method is possible to be used to eliminate the unwanted temperature cross-sensitivity by subtracting the wavelength shift of the reference LPG from the detection LPG.

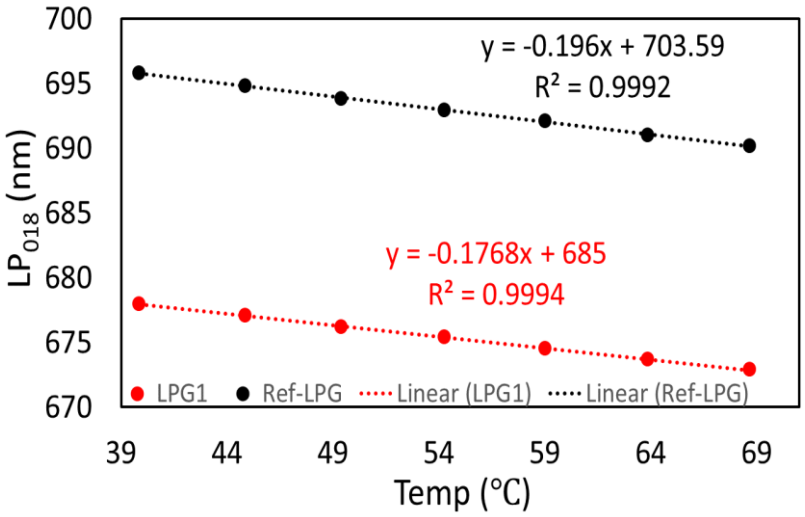


Fig 3.15 Temperature calibration of the LPG array sensor. Error bar is smaller than the marker size.

For the temperature variation above 9 °C, a weight factor can be applied to either LPG to eliminate the sensitivity difference. The weight factor is defined as the sensitivity ratio of two LPGs, and in this case is 1.1086 (0.196/0.1768). The wavelength shift of LPG1 will be weighted by multiplying the weight factor so that the wavelength shift induced by temperature will be same as the reference LPG, and

the subtracted result will be always close to zero if there are no additional perturbations such as RI change. It is shown in Fig 3.16 that the Ref-LPG undergoes a bigger wavelength shift than LPG1 as the temperature increase, this difference gets bigger as increasing the magnitude of temperature change. After applying the weight factor, the difference is maintained as the temperature increases.

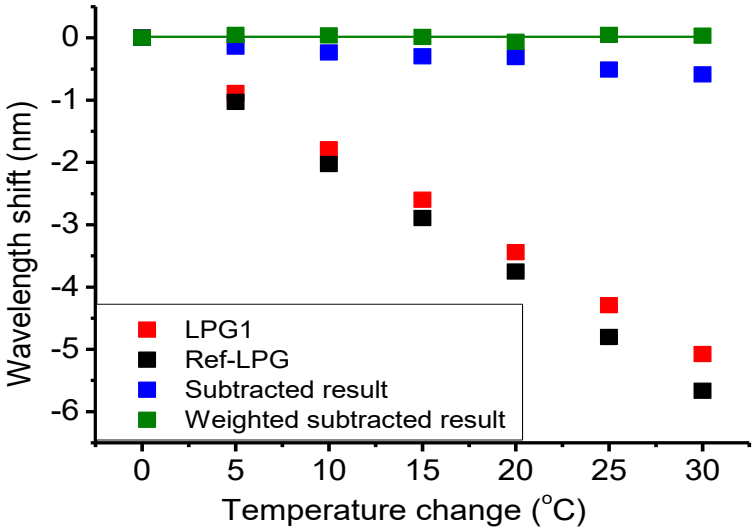


Fig 3.16 Wavelength shift of the LPG array sensor against the temperature change.

As the Ref-LPG has a larger grating period than that of phase matching condition, the subtracted result of the phase matching cladding mode LP_{019} is not shown in this case. The same way of referencing can be done by choosing a short grating period of a reference LPG which has two separate bands at PMTP that are separated from the detection LPG.

3.4 LPG strain measurement

Strain is defined as extension per unit length with:

$$\varepsilon = \frac{e}{L0} = \frac{L-L0}{L0} = \frac{L}{L0} - 1 \qquad (3.2)$$

Where e is the extension length, $L0$ is the original length and L is the stretched length.

The strain sensitivity of an LPG at the PMTP of LP_{019} has been experimentally determined by using the set-up in Fig 3.17. The optical fibre was stretched and fixed

on a platform comprising of two groove fibre holders. One of the holders is mounted on a translation stage (resolution: 0.01 mm) (Micro Control, France) which allows the adjustment of the distance between two stages. Two points of fibre on either side of the LPG were glued on the two V-grooves of the platform. The two points of fibre were stripped to remove the plastic jacket prior to the fixing on the V-groove. This guarantees the tight fixing of silica fibre on stages rather than the plastic jacket and avoids the potentially inaccurate measurement induced by the internal movement of silica fibre inside of jacket under the application of strain. The initial distance between two points was measured as 30.2 cm. The translation stage was controlled by the graduated rolling screw and gradually increased the separation distance of two glued points step by step (each step was set to 0.1 mm). The transmission signal of LPGs was recorded simultaneously with a frequency of 1 Hz.

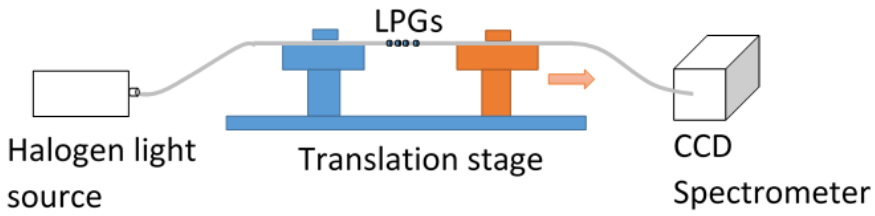


Fig 3.17 Set-up of strain measurement of LPGs. Blue is the v-groove stand that is fixed on the platform. Orange is the v-groove stand that is mounted on a translation stage for modulating the strain applied on the LPG.

The axial strain applied on the optical fibre by the increased distance of two glued points are converted from Eq 3.2. The transmission spectra of the LPG at LP_{019} under different axial strain are illustrated in Fig 3.18. With increasing strain from 0 to 0.0165 Ɛ, the dual attenuation bands of LP_{019} move towards each other, and the transmission value at 850 nm decreases. The dynamic change of the separation of dual bands and the transmission value are displayed in Fig 3.19a. Both separation of dual bands and transmission of 850 nm exhibit linear correlation to applied axial strain with a sensitivity of -2246.5 nm/Ɛ for wavelength shift and -17.284 /Ɛ for transmission change (Fig 3.19b).

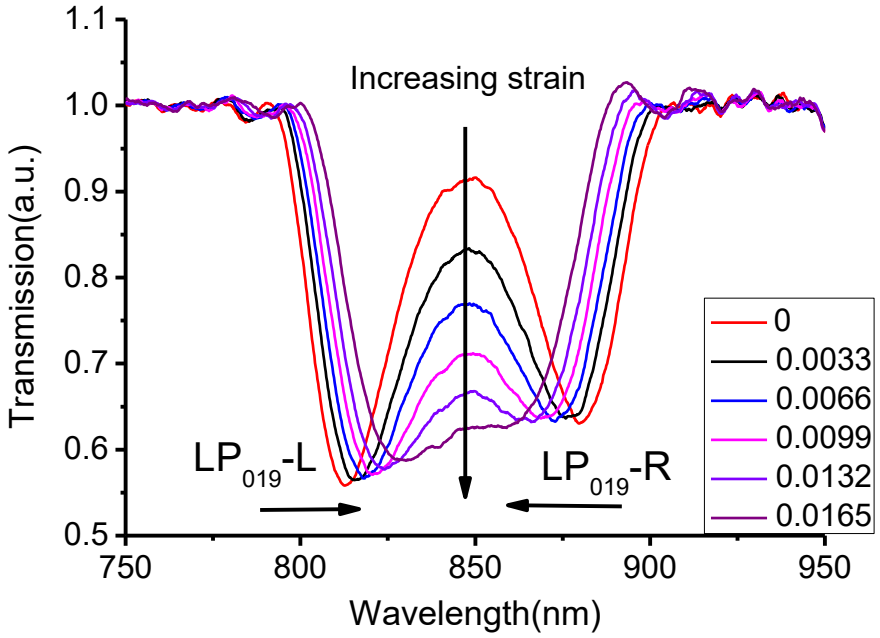
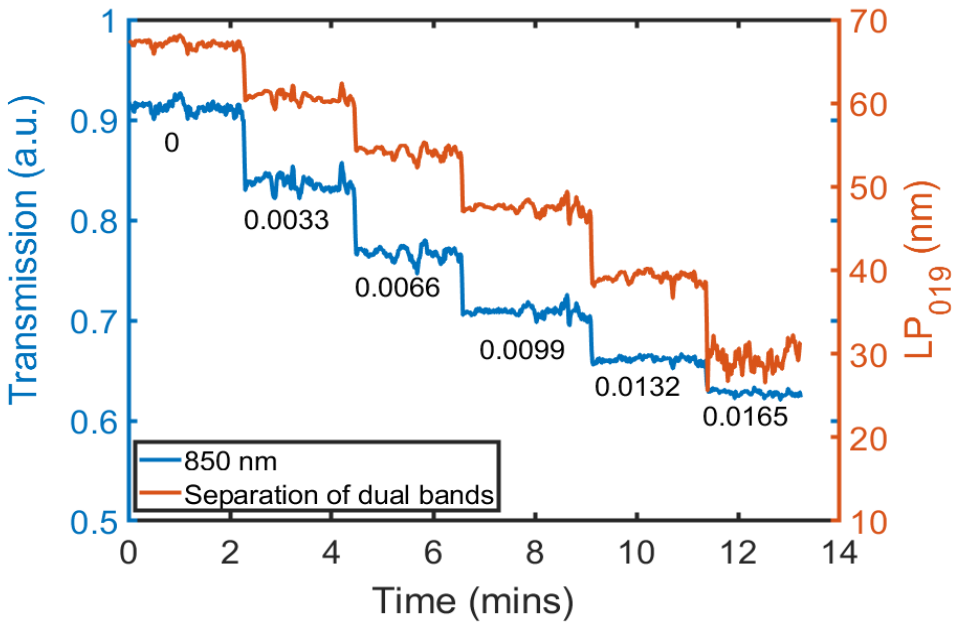
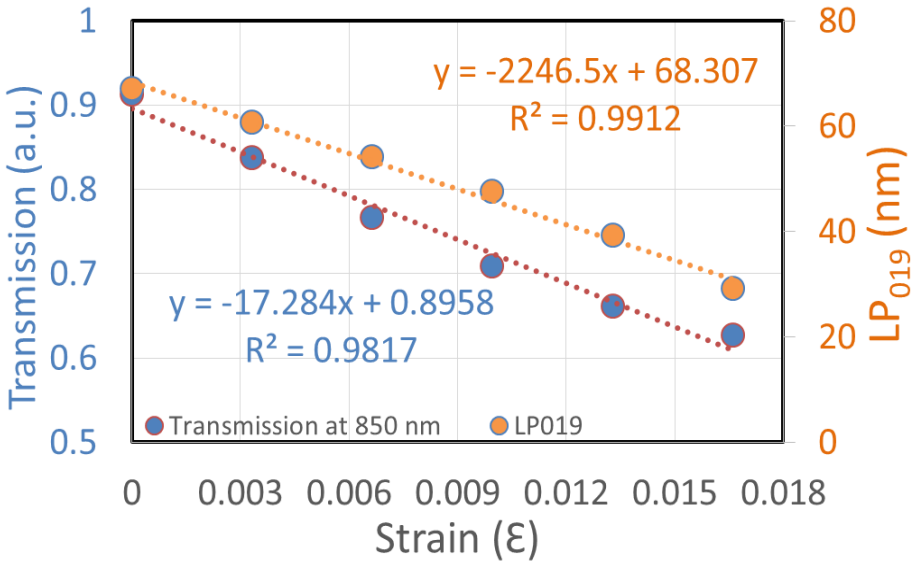


Fig 3.18 Transmission spectra of LPGs at LP_{019} under different applied axial strain.



(a)



(b)

Fig 3.19 (a) The separation of dual bands at LP_{019} and transmission at 850 nm versus time while applying different axial strains. (b) Linear fitting of transmission and wavelength as a function of axial strain. Error bars are smaller than the sizes of markers.

3.5 LPGs RI measurement

The RI sensitivity of the LPG was measured by immersing the LPG into prepared RI medium by using the set-up illustrated in Fig 3.20.

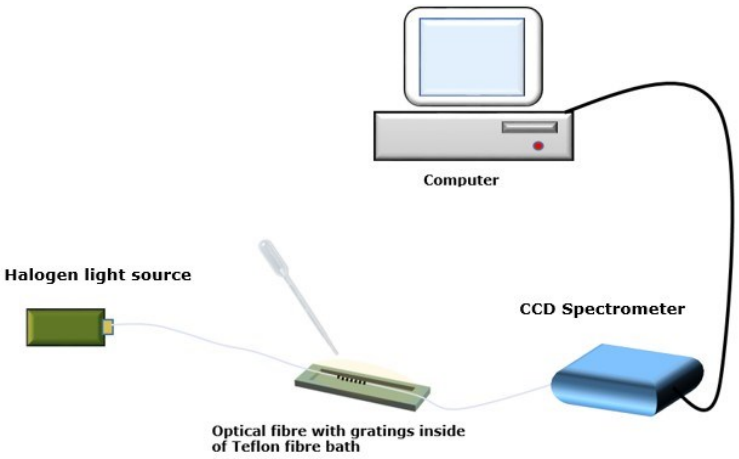


Fig 3.20 Set-up for RI measurement of the LPG. An LPG was placed inside a Teflon fibre bath, light was sent from a halogen light source and captured by a CCD spectrometer. The experiment was conducted in a temperature regulated laboratory with the temperature around 22 ℃ and the LPG was stretched in taut with two ends fixed to avoid the strain change during measurement.

The RI liquid media were prepared by mixing distilled water with isopropyl alcohol (IPA) with different volume ratio. The value in each concentration was measured by using a digital refractometer (Reichert 13940000). Its correlation to the volume percentage of IPA is illustrated in Fig 3.21, which exhibits a polynomial regression to volume percentage of IPA from the minimum value of 1.3328 (RI of water) to the maximum value of 1.3761 (RI of IPA).

The spectral response of the LPG for different RI medium is illustrated in Fig 3.22a, where the left-hand attenuation bands of LP_{019} shifts to a shorter wavelength with increasing RI and the right-hand attenuation band, on the other hand, shifts to a longer wavelength. The wavelength separation of the dual bands increases with increasing of RI and it linearly fits the RI with a sensitivity of 407 nm/RIU (Fig 3.22b). The sensitivity is higher than that of the typical LPG which is about 50 nm/RIU with the attenuation band at 1563 nm [223]. The higher sensitivity is attributed to the higher cladding mode of PMTP of the lower wavelength.

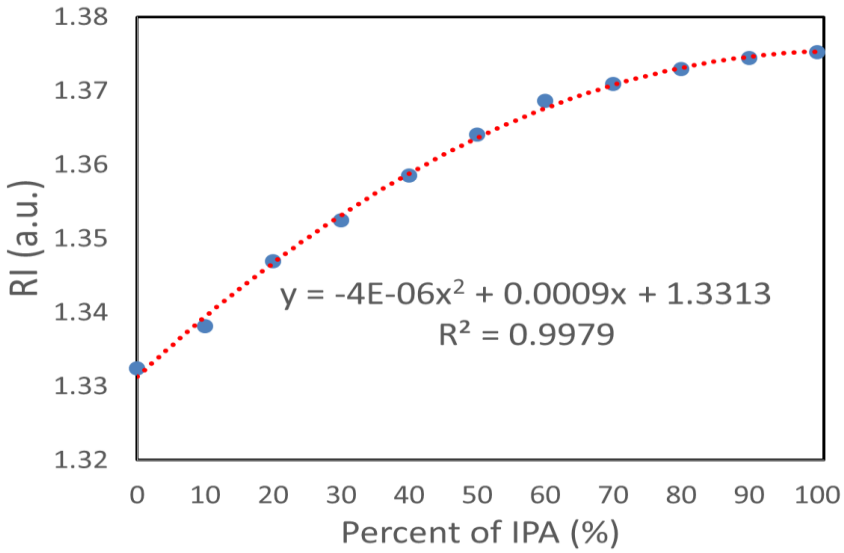
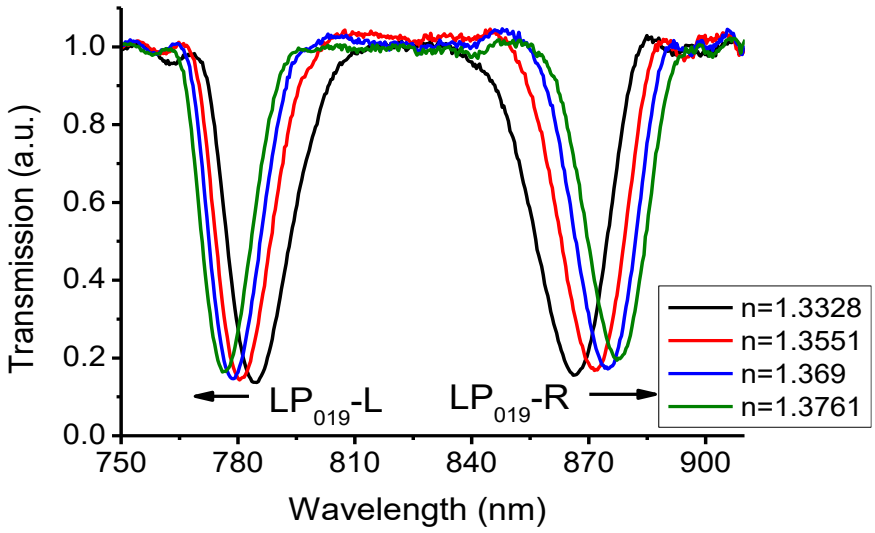
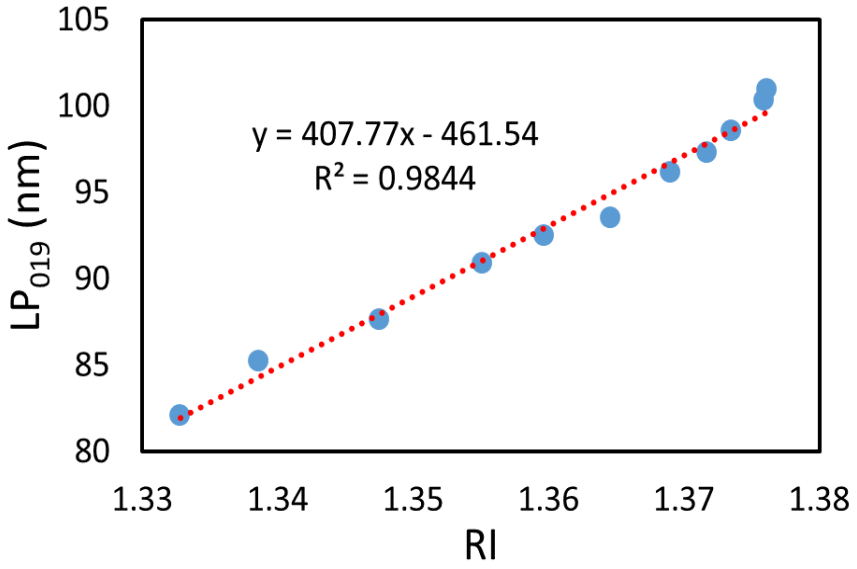


Fig 3.21 The correlation of RI value to volume percentage of IPA to water.



(a)



(b)

Fig 3.22 (a) Transmission spectrum of LPGs at LP_{019} for different RI medium. (b) Linear fitting of separation of dual bands at LP_{019} to RI.

3.6 Preparation of reflection LPGs

A reflection mode LPG can be prepared by changing the configuration of the LPG from the middle of the fibre into a tip probe. It provides advantages such as compact size and the ability to use as a single-ended probe. The reflection mode LPG is usually done by coating one end of the fibre containing the LPG with a metal mirror such as

gold. The coating of metal on the optical fibre tip can be accomplished by using a sputter coater [224] or by using a chemical method [225]. The sputtering method has better thickness control than the chemical formation but requires expensive devices and bulky set-up to create a vacuum environment.

3.6.1 The formation of silver mirrors via chemical reaction

A silver mirror can be formed by mixing Tollens' reagent with an aldehyde [226]. The Tollens' reagent reacts with an aldehyde to produce element silver and forms a characteristic 'silver mirror' on the inner surface of the reaction vessel. The preparation of Tollens' reagent can be summarised as following two-step:

Step 1: Silver nitrate ($AgNO_3$) is precipitated and converted into silver oxide (Ag_2O) from solution in the presence of OH^- ions. In this step, a clear silver nitrate solution will appear with brown solid precipitation. The reaction can be explained as:

$$2AgNO_3 + 2OH^- \rightarrow Ag_2O + 2NO_3^- + H_2O \quad (3.3)$$

Step 2: Aqueous ammonia is added to dissolve the brown precipitation. The solution in this case returns to clear. Reaction in this step is:

$$Ag_2O + 4NH_3 + 2NO_3^- + H_2O \rightarrow 2[Ag(NH_3)_2]NO_3 + 2OH^- \quad (3.4)$$

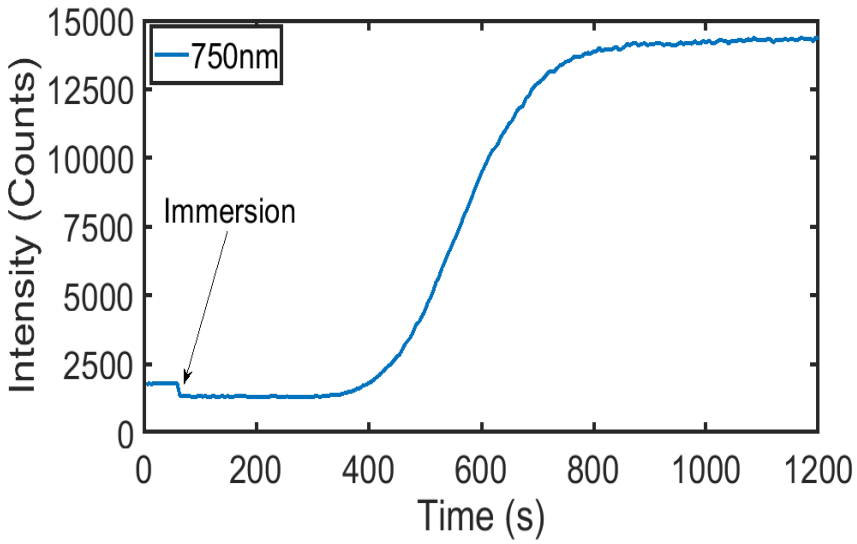
The Tollens' reagents will oxidise the aldehyde (RCHO) to a carboxylate ion ($COOH^-$) and itself is reduced to a silver element. The elemental silver precipitates out of solution and assembles on the surface forming a mirror.

$$[Ag(NH_3)_2]^- + RCHO + H_2O \rightarrow 2Ag(s) + 4NH_3 + RCOOH + 2H^+ \quad (3.5)$$

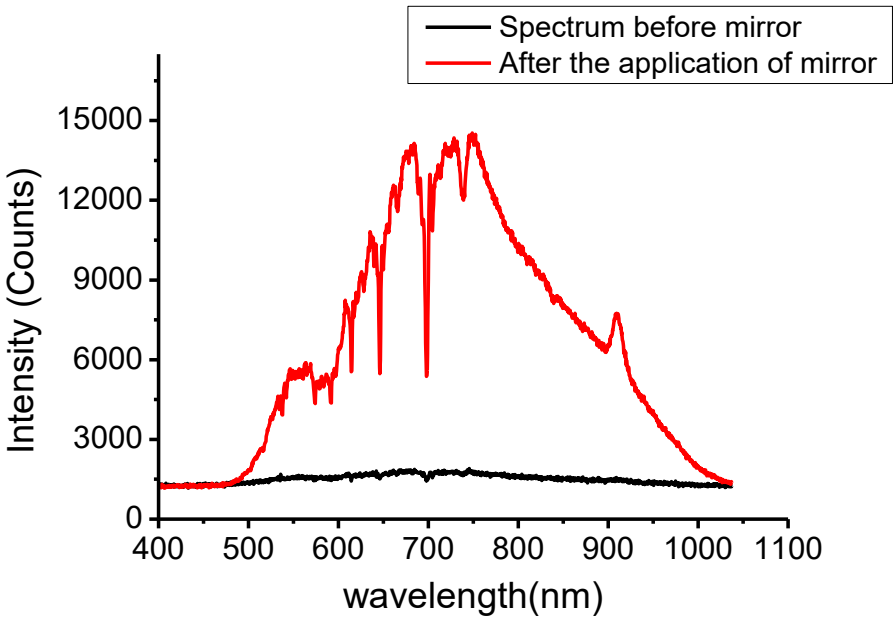
3.6.2 The fabrication of reflection LPGs

A 1.5 cm length LPG with a grating period of 110 µm was fabricated by using the amplitude mask method described in the previous section. During fabrication, the fibre was stripped of its jacket for 1.5 cm so that the edge of the LPG is located exactly on the end of the stripped region and can be easily identified. One end of LPGs was spliced with a single mode optical fibre coupler (working wavelength: 850 ± 100 nm, Throlabs, UK) and the second end is cleaved so that only 1.5 cm of the LPG remains.

A mirror coating solution was prepared by adding 640 µL of 0.1 M $AgNO_3$ into a 1.5 mL vial, followed by 440 µL of 0.8M KOH and 50 µL of 28 % NH_4OH; then 64 µL of 0.25M dextrose into the prepared solution was added and mixed. The tip of the LPG with 90 degree cleaved end is then immersed into the mixed solution with the length of ~0.1 cm (this process can be controlled by monitoring the intensity value reflected from the fibre tip, a significant drop of intensity will be observed as the fibre tip enters the liquid interface). As illustrated in Fig 3.23a, the intensity of light (750 nm was selected) that is reflected from the tip decreases when the tip was immersed into the liquid solution because of the lower reflectivity from fibre liquid interface induced by the low RI difference. With the reduction reaction occurring in the liquid solution, the silver particles start to form and attach on the fibre tip. As a result, the intensity value significantly increases with time until it is saturated. Then the mirror is formed, and the fibre can be taken out from the liquid. The coating process takes less than 20 mins, and there is no intensity change after removing the fibre tip from liquid to air as the light from the tip reflected by the silver mirror does not interfere with the external environment. The reflection spectrum of the LPG shows a significant increase in intensity value compared with that before coating (Fig 3.23b). The mirror on optical fibre can be visually identified. An SEM image of an optical fibre that is partially coated with silver mirror confirms the formation silver mirror as illustrated in Fig 3.24.



(a)



(b)

Fig 3.23 (a) The intensity at the wavelength of 750 nm changes with time during the mirror coating. (b) Reflection spectrum before and after application of silver mirror. The integration time for both spectra is the same (200 ms).

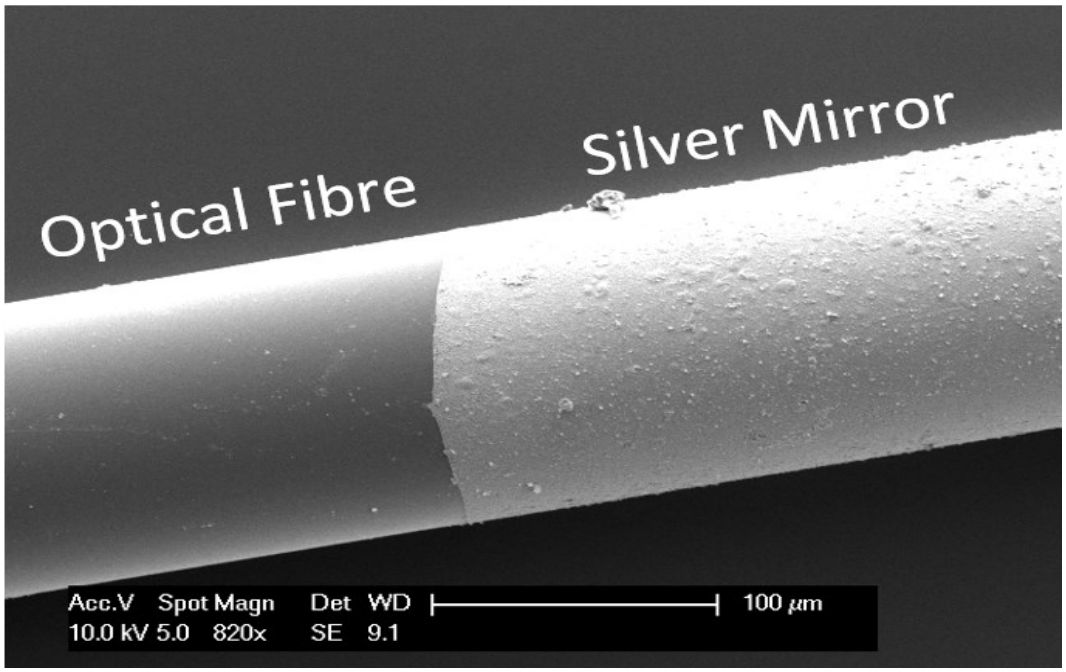


Fig 3.24 SEM image of an opitcal fibre that was partially coated with silver mirror. The image was taken by using the SEM intrument (JEOL 7100F, UK). Scale bar=100 µm.

Another advantage of a reflection LPG is that it enhances the loss of attenuation bands and can potentially reduce the length of gratings which is typically 3 cm for

transmission LPGs. The propagation light passing through the LPG twice in a reflection LPG can halve the length used. As illustrated in Fig 3.25, the loss of attenuation bands is approximately 0.3 (30 %) when measured in transmission mode. After coating with silver mirror and taking a measurement in reflection mode, the loss of attenuation bands becomes 0.55 (55 %) and almost doubling of the loss in transmission mode.

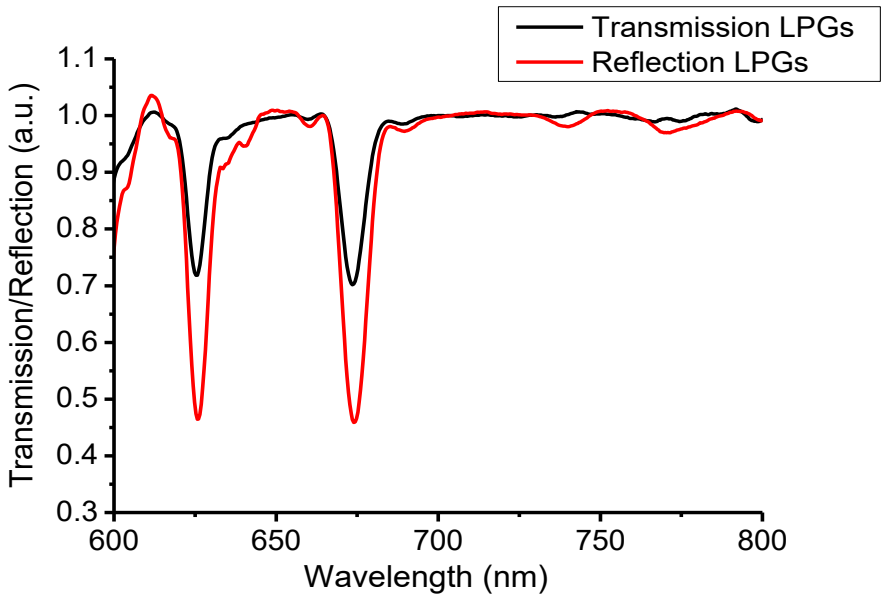


Fig 3.25 Spectrum comparison of a 1.5 cm LPG with the grating period of 110 µm in transmission and reflection mode (mirror applied).

3.7 Conclusion

The fabrication process of an LPG by using UV irradiation was introduced with two methods which are point-by-point and amplitude masks, respectively. The amplitude mask obtains a significantly shorter fabrication time and a better quality of attenuation bands compared with the point-by-point. However, the latter has better flexibility in fabricating of a variety of grating period as one amplitude mask can only produce a fixed grating period. The amplitude mask method is preferred if the grating period is known.

The transmission spectrum of an LPG was simulated by using *OptiGrating* software. The simulated spectrum shows a comparable result to that of experimental data, indicating the usefulness of such a tool in predicting the transmission spectrum of

LPG at PMTP. The factors such as the grating period, grating length and RI modulation in determining the property of attenuation bands of an LPG were investigated theoretically and experimentally. Longer grating length, higher RI modulation will render a higher attenuation of the LPG rejection bands. The fabricated LPG at phase matching condition of cladding mode LP_{019} was achieved at the grating period around 109 µm (112 µm for the different fibre batch). It exhibits a sensitivity of ~1 nm/℃ for temperature, -2.2 X 10^{-3} nm/µε for microstrain and 407 nm/RIU for RI respectively. A reflection mode LPG is proposed by depositing a silver mirror on one end of an LPG that has more compact size than conventional LPGs and is able to use as a fibre probe.

Chapter 4 Synthesis of nanoparticles for LPG biosensor development

4.1 Introduction

Nanotechnology has become very popular in the field of bioanalysis. A variety of nanomaterials, especially nanoparticles have been found in many applications in variable analytical methods of bioanalysis [227]. Nanoparticles (NPs), thanks to the small size (usually ranging from few to a hundred of nanometres), show unique physical, chemical and electronic properties that are different from those of bulk materials and can be used to configure and improve sensing devices, for example electrochemical and optical measurements in biosensing [228]. In optical sensing, they can overcome many of the significant chemical and spectral limitations of molecular fluorophores and can be used as quantitation tags in biological assays that eliminate the need for either organic fluorophores or radioactive labelling [227, 229]. They can also act as signal transducers and show promise in diagnostic assays, which reduces the need of tag labelling making diagnostic tests potentially more robust and less expensive [230]. Moreover, they can also be used as substrates for multiplexed biological assays in solution which provide greater flexibility, more rapid assay times and greater reproducibility than microarray-based methods [231].

Nanoparticles, depending on the chemical constitution, can have different types such as polymer NPs, metallic NPs and metal oxide NPs. Particles made of a composite have been presented for bioanalysis, which reveals distinct properties compared to that of a single composition. For example, Hirsch et al. have used gold nanoshells which are spherical nanoparticles made up of a dielectric core (silica) and surrounded by a thin gold shell to detect immunoglobulins in whole blood [232]. Such particles possess a tunable plasmon resonant response that gives rise to intense optical absorption and scattering [233]. The plasmon resonance frequency can be varied systematically from the visible to the mid-infrared regions of the spectrum by modifying the relative dimensions of the core and the shell layers [234]. They can also have various shapes such as nanotube, nanosphere and nanorods.

Among those NPs, metallic nanoparticles especially AuNPs due to their distinct optical and electrical properties have been widely used in bioanalysis application using gold-based aggregation assay [232, 235, 236] and for construction of biosensors [237, 238]. They are good candidates for developing optically based biosensors because of their strong interaction with visible light. During the interaction, the free electrons in gold atoms are excited leading to a state of collective oscillations called surface plasmon resonance (SPR) that provides gold with the ability to absorb and scatter visible light depending on its size, shape and agglomeration state [239, 240]. Moreover, biological molecules such as antibodies are readily conjugated to the gold surface via either chemical or physical interaction [241]. AuNPs are chemically inert and considered as a biocompatible device for biomedical applications [242, 243].

SiNPs show promise in biomedical application owing to their excellent biocompatibility, low toxicity, and thermal stability, easy and large-scale synthetic availability [244]. Their particle size, shape and porosity can be precisely manipulated that enables various applications. For example, the most appropriate size can be chosen depending on the wavelength of light to enhance Mie scattering in detecting fluorescent signals [245]; the spherical shape has a large surface to volume ratio, and the surface can be further modified or functionalised for biomedical application such as in drug delivery and detection of antibodies [246-248]. They can be incorporated into the coating film of an LPG and significantly raise its RI sensitivity [249].

In this chapter, the method of synthesis of SiNPs and AuNPs is introduced and presented. The samples that are prepared and characterised in this chapter are used in Chapter 6 for the fabrication of LPG based biosensors.

4.1 Synthesis of SiNPs

SiNPs can be synthesised by using the Stöber method [209] based on the fact that they can be produced by the chemical reaction of sol-gel (as described in Chapter 2). Their formation can be divided into two stages: nucleation and growth. The nucleation process describes the stochastic and dynamic association of the hydrolysed silicon alkoxide molecule forming initial nuclei. There are two models to

explain the growth stage, which are monomer addition [250] and controlled aggregation [251]. The monomer addition model describes that the particles start to grow after adding the additional hydrolysed monomers to the burst of nucleation. Whereas the aggregation model elaborates that nucleation occurs continuously during the reaction and the resulting nuclei will aggregate together to form dimer, trimer and large particles. Both models lead to the formation of either a spherical or gel network depending on the reaction condition.

The size of SiNPs is determined by the rate of polycondensation reaction which is adjustable through manipulation of reaction parameters such as the concentration of silicon alkoxide, the amount of base catalyst and the concentration ratio of water to silicon alkoxide [251, 252]. Efforts were conducted in the experiment for the synthesis of SiNPs with different size by manipulating the concentration ratio of tetraethyl orthosilicate (TEOS). The experiment details and result are demonstrated below.

4.1.1 Materials and Methods

4.1.1.1 Materials

Tetraethyl Orthosilicate (TEOS), Ethanol, ammonia hydroxide (NH_4OH) (28 %) were purchased from Sigma-Aldrich, UK.

4.1.1.2 Synthesis of SiNPs

Different volumes of TEOS (10, 20, 40, 80 µL) were first added into four glass vials (volume of 10 mL). Adding 7 mL of ethanol to each vial, then later adding 3 mL of NH_4OH in each vial. The vials were then capped and placed into an ultrasonic bath (U 50, Ultrawave Limited, UK) for sonication of 15 mins. The prepared solutions are named as sample 1 to 4 based on the addition of TEOS. (Samples 1 to 4 are with TEOS of 80, 40, 20 and 10 µL, respectively) (Illustrated in Fig 4.1).

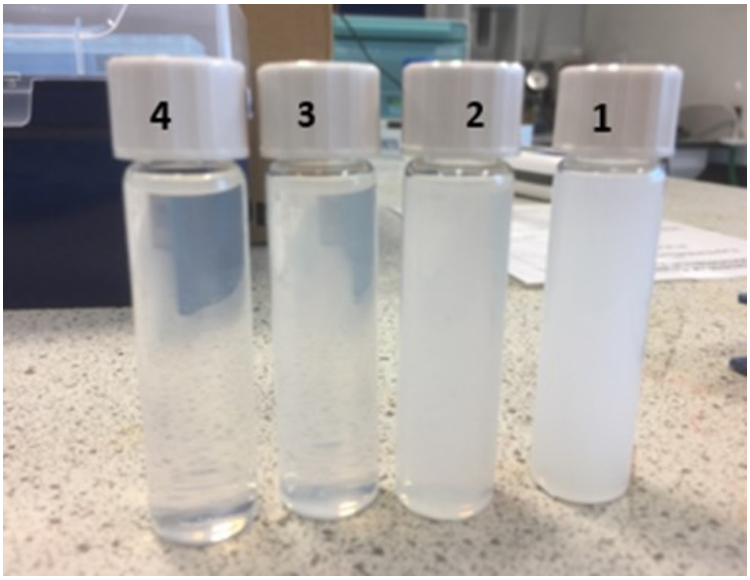


Fig 4.1 The prepared SiNPs sample solution.

The obtained solutions were then placed into a centrifugal machine (Rotofix 32A, Hettich, UK) with a rotation speed of 40 000 rotation per min (RPM) for 30 mins. After centrifugation, the liquid was carefully poured out and the remaining precipitate (pellet) was placed into an oven (50 °C) overnight to dry. The dried SiNPs powders were stored in ambient conditions before use.

4.1.1.3 Characteristics of synthesised nanoparticles

Dynamic light scattering (DLS) is an analytical technique to measure size and size distribution of particles with diameters ranging from a few nanometers to a few of micrometres. The measurement is based on the random changes in the intensity of scattered light from a sample suspension [253]. Particles in suspension undergo random thermal motion, known as Brownian motion. The Brownian motion can be modelled by the Stokes-Einstein equation [254]:

$$D_h = \frac{k_B T}{3\pi\eta D_t} \tag{4.1}$$

Where D_h is the hydrodynamic diameter, K_B is Boltzmann's constant; T is temperature, η is dynamic viscosity and D_t is the translational diffusion coefficient.

According to the above equation, the hydrodynamic diameter (correlated to particle size) is a function of the translational diffusion coefficient as other environmental parameters are known. DLS measures light intensity fluctuation and applies an

autocorrelation function to calculate the translational diffusion coefficient and produce the hydrodynamic diameter based on the Stokes-Einstein equation [255].

Modern commercial DLS instruments are relatively low cost, easy to operate and directly output data from measurement without the needs for further mathematical processing. DLS outputs Z-Average size of the testing sample that is the intensity-weighted mean diameter derived from the cumulants analysis. The Z-Average Mean is recognised as the best value to report when used in a quality control setting as defined in ISO13321 [256]. The polydispersity index (PDI) is a width parameter measured from DLS, is calculated as the square of the standard deviation divided by the square of the mean size. Higher PDI (> 0.7) indicates that the sample has a very broad size distribution and is probably not suitable for the DLS analysis [257].

Four harvested SiNPs samples were dispersed into distilled water to prepare solutions of particles with concentration of 0.5 wt%. The samples were sonicated for three minutes before the measurement. A disposable cuvette containing 1mL of the sonicated suspension was mounted into Malvern Zetasizer Nano-ZS (Malvern Instruments, UK) for measuring the size distribution of SiNPs RI.

Morphological examination of SiNPs was conducted using scanning electron microscopy (SEM) (JEOL 7100F, UK). A drop of prepared SiNPs solution was spread evenly on a piece of glass substrate. After drying in air, the substrates were coated with ~ 6 nm of iridium for increasing the conductivity of electrostatic discharge using a sputter coater (Q150V, Quorum, UK) before SEM.

4.1.2 Result and discussion

Table 4.1 illustrates the four samples prepared by varying the amount of TEOS in reactants and their Z-Average size measured by DLS. The average particle size decreases from about 300 nm to 220 nm with decreasing amount of TEOS. The size distribution for sample 1 to 4 is illustrated in Fig 4.2. The mode diameter value of each curve reduces in size as the amount of TEOS decreases. The four samples all have a very small value of PDI (< 0.1) indicating the samples qualify for DLS analysis and have narrow size distribution.

Table 4.1 Samples that are made with different volume of TEOS and their Z-average size measured by DLS. The value displayed in Z-Average size is taken as the average value of the Z-Average size of three times measurement.

Sample number	TEOS	Ethanol	NH_4OH (28 %)	Z-Average Size	PDI
1	80 µL	7 mL	3 mL	308 ± 10 nm	0.025
2	40 µL	7 mL	3 mL	262 ± 6 nm	0.004
3	20 µL	7 mL	3 mL	246 ± 1 nm	0.09
4	10 µL	7 mL	3 mL	218± 3 nm	0.037

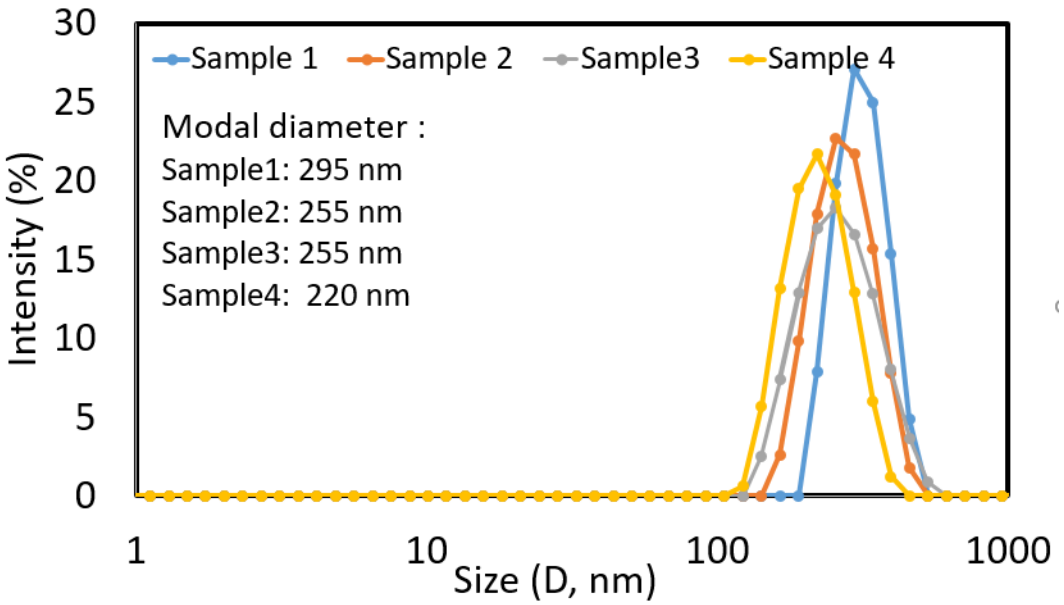
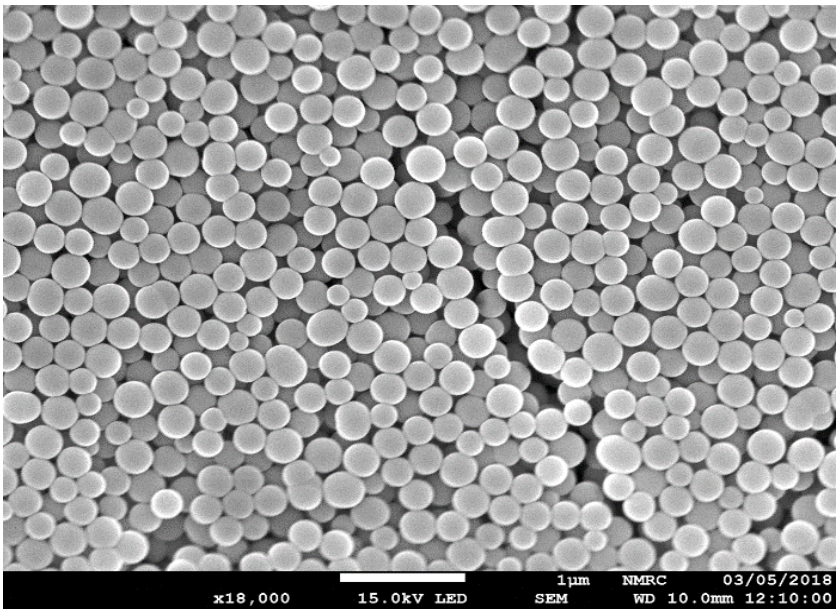


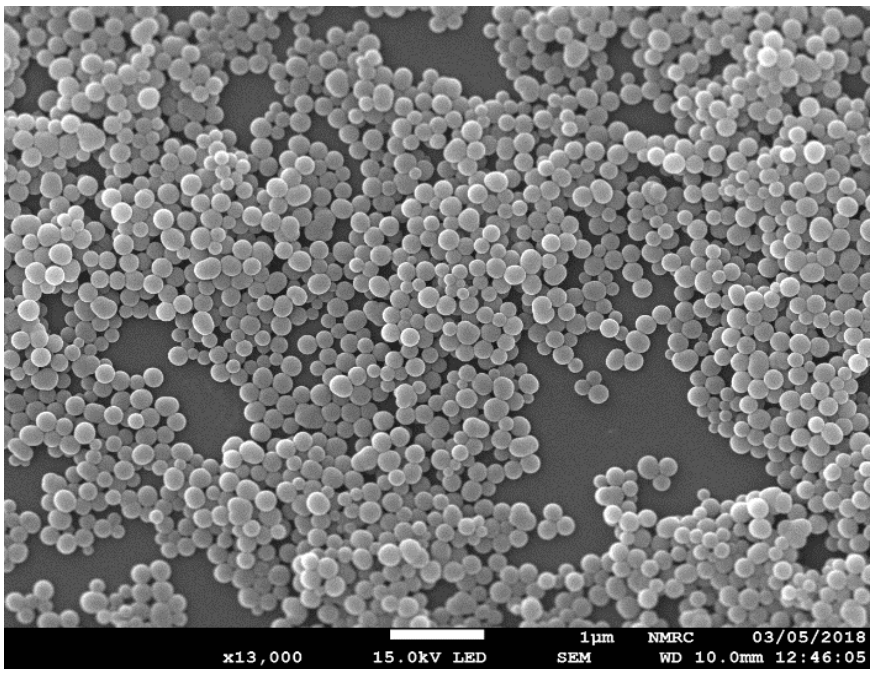
Fig 4.2 Size distribution of samples that are measured from DLS.

Fig 4.3 illustrates the SEM image of SiNPs of sample 1 and 4. The image confirms the synthesised particles have a uniform spherical shape. The size can also be measured based on the image (illustrated in Fig 4.3c) by using image-processing software (*ImageJ*). The total number of 100 nanoparticles were measured in diameter individually, and the size distribution curve is achieved by fitting the histogram of particle size with a normal distribution shown in Fig 4.4. Descriptive statistics were

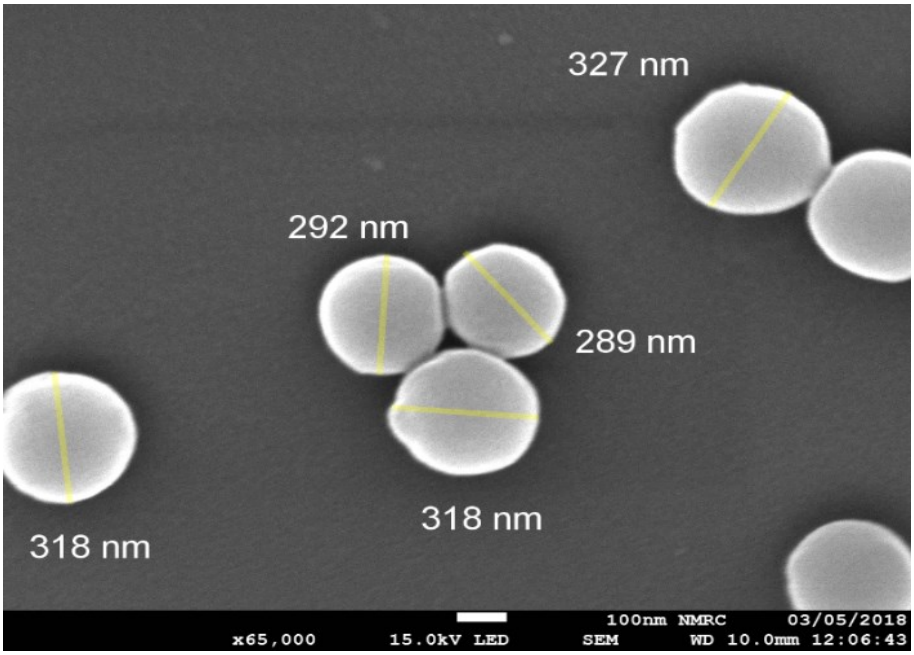
performed for analysing the data, and an average value of 289.4 ± 31.2 (mean+ standard deviation (SD)) and a median value of 290.8 nm are obtained. The mean value measured is close to the Z-average size of DLS measurement (308 ± 10 nm) that confirms the comparable result of DLS measurement to SEM measurement. In above statistical analysis, only the sample 1 was used to calculate the mean size from the SEM images for demonstrating the variation of two measurement methods.



(a)



(b)



(c)

Fig 4.3 SEM image of SiNPs which is synthesised by using method above (a) sample 1, scale bar= 1 µm; (b) Sample 4, scale bar=1 µm; (c) The measurement of the diameter of SiNPs (sample 1), scale bar= 100 nm.

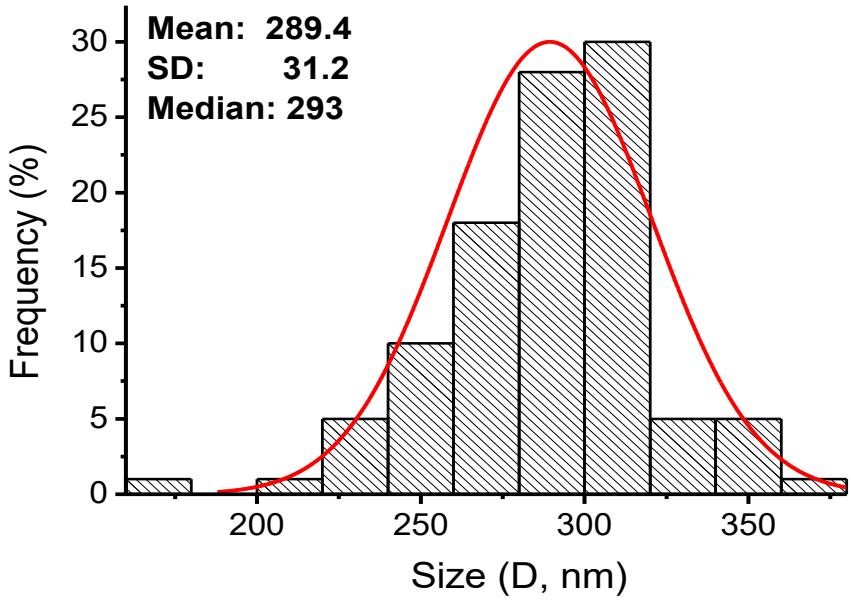


Fig 4.4 Size frequency distribution of SiNPs based on the measurement of SEM image. The total number of 100 nanoparticles were counted from sample 1.

4.2 Synthesis of AuNPs

AuNPs can be prepared with various materials using a relatively simple method. Generally speaking, there are two kinds of approaches that were used to prepare AuNPs: breaking bulk material into nanoparticles via physical methods such as laser ablation [258] and building up nanoparticles from atomic level via chemical methods [259]. Chemical methods are considered as a simple way to prepare such particles due to a simplified synthesis process and do not require bulky, expensive instrument to trigger the reaction. There are various chemical methods in the preparation by reducing chloroauric acid ($HAuCl_4$) to spheroidal AuNPs [260-262]. The Turkevich method [263] is the most applied chemical procedure in which sodium citrate was used as a reducing agent to reduce $[AuCl_4]^-$ into gold. The chemical reaction is illustrated as:

$$2[AuCl_4]^- + Ctr^{3-} + 2H_2O \xrightarrow{100\ ^\circ C} 2\,Au + 3CH_2O + 3CO_2 + 8Cl^- + 3H^+ \quad (4.2)$$

The Au^{3+} will be reduced into Au^0 by the citrate ion (Ctr^{3-} or $(C_6H_5O_7)^{3-}$) at the boiling temperature of water. The reduced Au^0 atom will undergo nucleation process and grow into nanoparticles as illustrated in Fig 4.5. The abundant citrate anions in solution are then absorbed on the surface of AuNPs, providing an overall negative charge. The negative charge surface produces a repulsive force between each nanoparticle to prevent the aggregation.



Fig 4.5 Schematic of the growth of AuNPs.

The size and geometry of AuNPs are determined by factors such as the concentration of $HAuCl_4$, reducing agent, reaction temperature and pH [262, 264]. In general, the greater the power and concentration of the reducing agent, the smaller the resultant particles will be. The Turkevich method is normally used to prepare a relatively large size in a range of about 9 nm to 120 nm depending on the concentration of citrate

[265]. A smaller size (<5 nm) can be prepared by using the method proposed by Bonnard et al. [266], in which sodium borohydride ($NaBH_4$) is used as a reducing agent and capping agent for stabilizing the AuNPs colloid at very low temperature (~0 ℃). The chemical process is illustrated as:

$$[AuCl_4]^- + [BH_4]^- \xrightarrow{0\ ℃} Au + B(OH)_3 + Cl^- + H^+ \quad (4.3)$$

Both methods are utilised to prepare AuNPs in the following content, but only the sample that prepared via the Bonnard method is used later in Chapter for the preparation of the LPG biosensor as it produces smaller size of particles that easily diffuse into the inner layer of the multi-layer of PAH/SiNPs film forming shell structure. Besides, the small size of particles also reduces the space constraint of the porous structure.

4.2.1 Materials and method

4.2.1.1 Material

Chloroauric acid ($HAuCl_4$), Sodium citrate dihydrate ($Na_3C_6H_5O_7$), Sodium borohydride ($NaBH_4$), Potassium carbonate (K_2CO_3) were purchased from Sigma-Aldrich, UK.

4.2.1.2 Synthesis of AuNPs

Turkevich method (Prepare AuNPs: 14~25 nm):

1 mM of the $HAuCl_4$ solution and 38.8 mM of $Na_3C_6H_5O_7$ stock were prepared separately in advance by dissolving the powder into distilled water. 20 mL of the prepared $HAuCl_4$ solution was poured into a clean glass beaker (50 mL) and heated to boil on a stir/hot plate while stirring with a magnetic stir bar. Then rapidly pouring the sodium citrate solution (volume: 0.1-5 mL) into boiled $HAuCl_4$ solution, continue to boil and stir until the colour of liquid turns into deep red (about 5-10 mins) and then move the solution to ambient temperature for cooling. The prepared solution was then stored in the fridge (~4 ℃) for use.

Bonnard method (Prepare AuNPs < 5 nm):

1 mM of $HAuCl_4$ solution, 0.2M K_2CO_3 and 13 mM $NaBH_4$ were prepared by dissolving the powder in distilled water. A clean glass beaker (200 mL) filled with 100 mL of distilled water was placed into an ice bath that is seated on a stir plate while stirring with magnetic stir bar (set-up is illustrated in Fig 4.6). Then 375 µL of the prepared $HAuCl_4$ solution was added to 100 mL of distilled water and subsequently 500 µL of K_2CO_3 was added, mixing well for 2 mins. 1 mL of the $NaBH_4$ solution is quickly added into solution mixture for 5 times (avoiding large aggregation) while waiting for a few seconds before each addition. After that, wait for 5 mins before removing the solution back to ambient condition. The solution is then stored in ambient conditions for use.

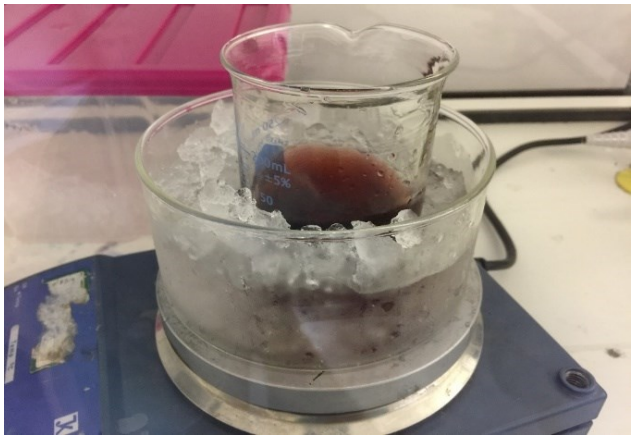


Fig 4.6 The experimental set-up for preparing AuNPs in an ice water bath (Bonnard method).

4.2.1.3 Characteristic of AuNPs

Transmission electron microscopy (TEM, JEOL 2100F, UK)) was used to image the prepared AuNPs sample. The statistics on the size of AuNPs were obtained from the TEM image. At least 100 spherical AuNPs were counted for each sample to achieve the size distribution curve and to calculate the average size. DLS analysis was also applied for measuring the size distribution. The prepared AuNPs solution was diluted about 20 times before the DLS analysis. The optical absorption spectra of the samples were measured using the set-up illustrated in Fig 4.7.

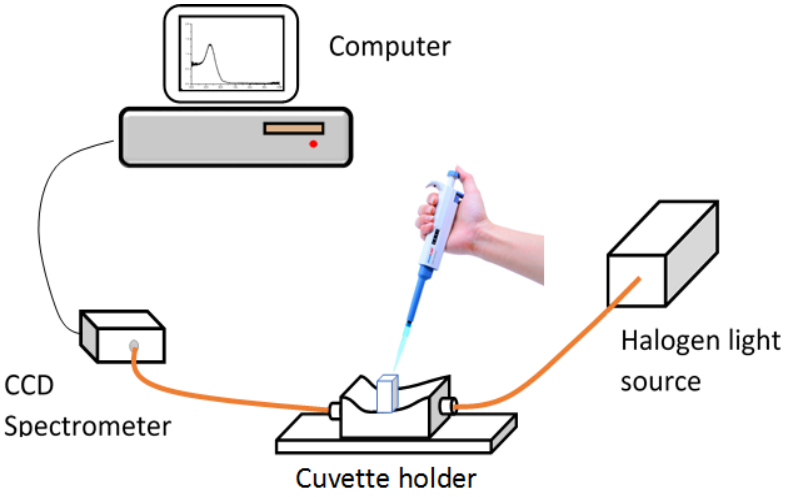


Fig 4.7 Set-up of absorption spectrometry. The orange line represents optical fibre. AuNPs solution was added into the cuvette that is mounted on the cuvette holder. The light emitted from the halogen light source passes through the sample and is detected by a CCD spectrometer (USB2000, Ocean Optics, UK).

4.2.2 Result and discussion

The colour of the AuNPs solution is size dependent. The prepared AuNPs colloid solution appears as red as illustrated in Fig 4.8 indicating the size of AuNPs is less than 100 nm [267].



Fig 4.8 Gold nanoparticle colloid prepared by using the Turkevich method.

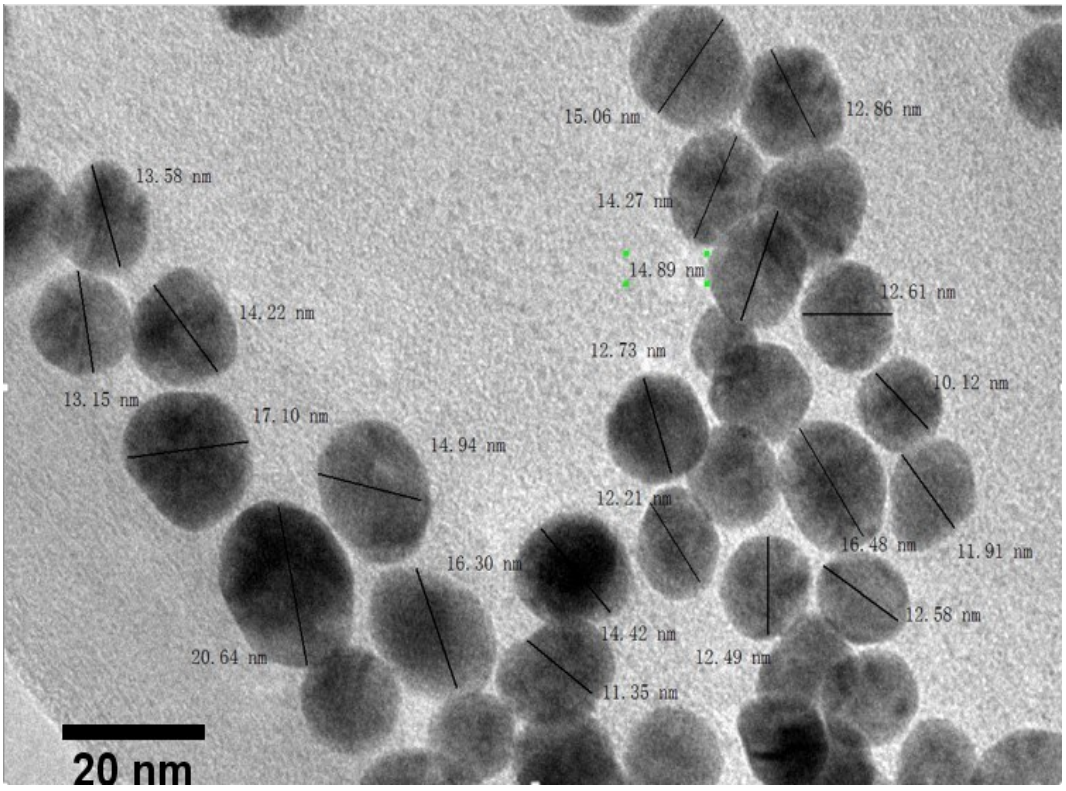
The table 4.2 lists different protocols of AuNPs preparation by using the Turkevich method and their average size that are calculated based on the measurement of TEM images (Fig 4.9a). All six samples from sample No.3 to 8 are observed to have a spherical shape based on TEM measurements. It appears that when the molar ratio

of sodium citrate to $HAuCl_4$ increases from about 1 to 10, the average size decreases. The size no longer decreases after the ratio >~2, and the average size is about 14 nm. The phenomenon is due to the limitation induced by reaction kinetics of the Turkevich method [38]. The average size of ~20 nm is achieved when the molar ratio is about 1. As the value reduces to ~0.4 nm (sample 2), the shape of AuNPs become arbitrary, and large particles are formed (Fig 4.10). The agglomeration of AuNPs causes the formation of large particles due to the insufficient stabiliser (sodium citrate) in the solution. It becomes more severe as the value further decreases to about 0.2 (sample 1), large particle clusters are found (Fig 4.11). In those cases, due to arbitrary size and shape, the quality of the samples is considered poor.

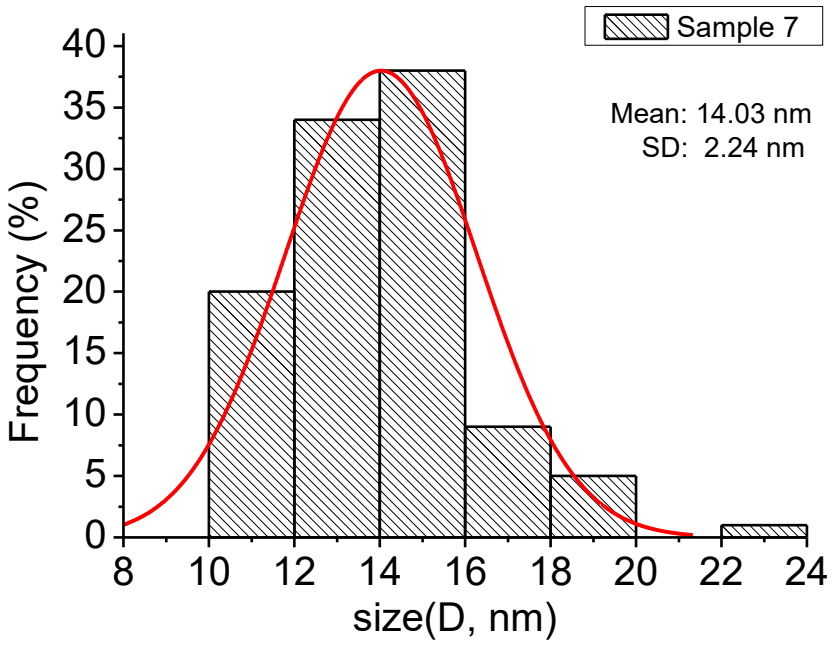
Table 4.2 AuNPs prepared by using the Turkevich method and their average size

Sample No.	$HAuCl_4$ 1 mM	Na_3ct 38.8 mM	Molar Ratio (Na_3ct :$HAuCl_4$)	Shape Of Particles	Sample Quality	Mean size ± SD (nm)
1	20 mL	0.1 mL	0.194	N/A	Massive Aggregated	N/A
2	10 mL	0.1 mL	0.389	N/A	Aggregated	N/A
3	20 mL	0.5 mL	0.97	Spherical	Qualified	23.64 ±2.65
4	20 mL	1 mL	1.94	Spherical	Qualified	15.28 ±4.72
5	20 mL	2 mL	3.88	Spherical	Qualified	16.24 ±3.20

6	20 mL	3 mL	5.82	Spherical	Qualified	14.68 ±3.23
7	20 mL	4 mL	7.76	Spherical	Qualified	14.03 ±2.24
8	20 mL	5 mL	9.7	Spherical	Qualified	14.91 ±3.10



(a)



(b)

Fig 4.9 (a) TEM image of AuNPs from the prepared sample 7, spherical AuNPs with size around 14 can be observed. (b) Size distribution of AuNPs from sample 7. The histogram is achieved by counting about 100 individual AuNPs from the TEM image. The red curve is the normal distribution of the histogram. The mean value and the SD are calculated as 14.03 ± 2.24 nm.

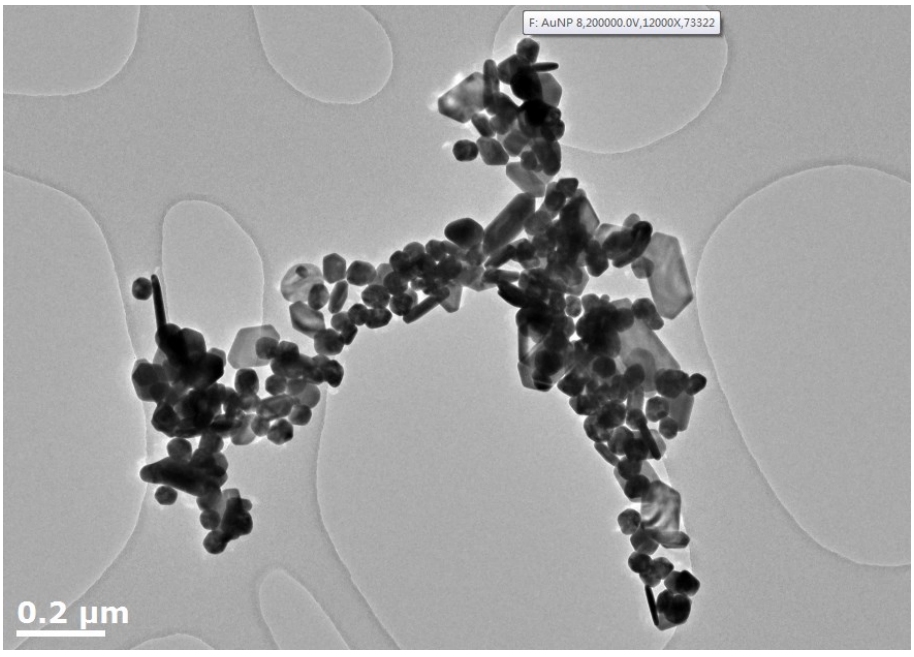


Fig 4.10 TEM image of AuNPs (sample 2). Non-uniform size and shape are observed.

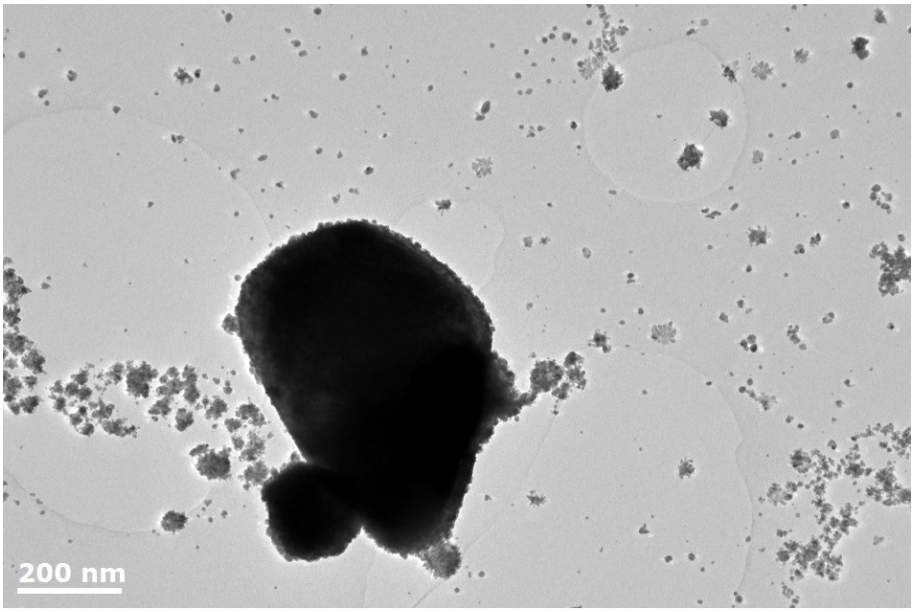


Fig 4.11 TEM image of AuNPs (Sample1). Clustered particles present.

Due to surface plasmon effects, AuNPs can cause absorption of a specific wavelength of light depending on particle size. The absorption wavelength shifts to a longer wavelength as the particle size increases [268]. The absorption spectra of the samples are illustrated in Fig 4.12. When the molar ratio of Na_3Ct to $HAuCl_4$ is 0.194, due to the massive agglomeration of the sample, no clear absorption peak can be observed. For the molar ratio of 0.389, the absorption spectrum shows absorption peaks at 546 nm and around 700 to 800 nm. The broad absorption band at the higher wavelength (> 700 nm) can be attributed to the agglomeration induced by the large size of AuNPs. The rest of the samples prepared with molar ratio from 0.97 to 9.7 exhibit a narrow absorption peak around 520 nm due to small and uniform size distribution.

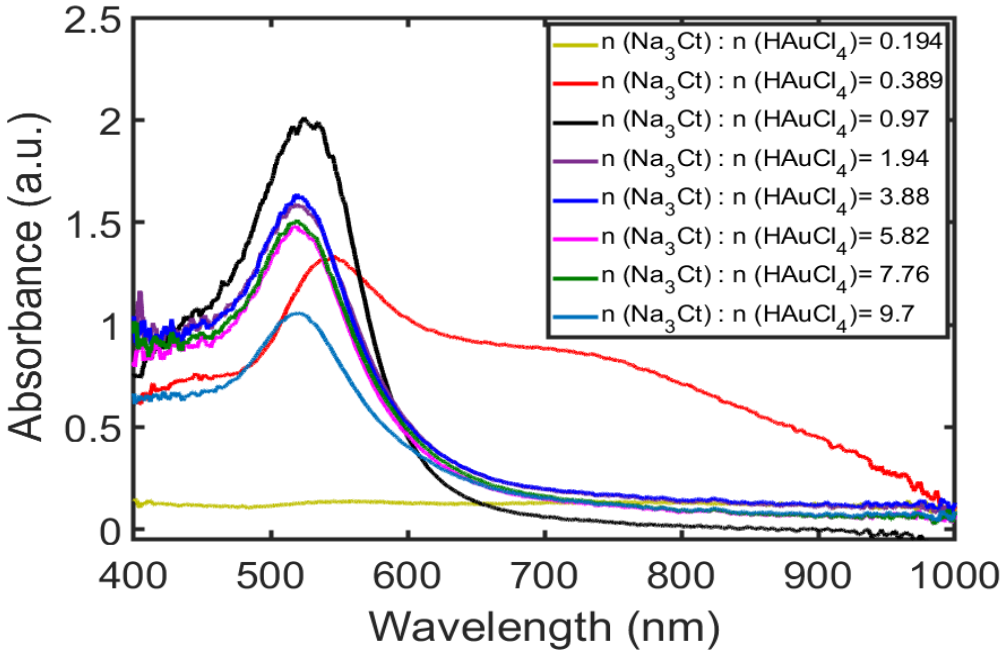


Fig 4.12 Absorption spectrum of each prepared SiNPs sample; absorbance value is calculated as Absorbance=2-$\log_{10}(I_0/I_1 \times 100\ \%)$, where I_0 is the intensity value detected at the spectrometer after AuNPs colloid solution was added into a cuvette and I_1 is the intensity while distilled water was added into the cuvette.

Due to the limitation of the Turkevich method in preparing small size AuNPs (diameter < 5nm), a reducing agent of sodium borohydride was used in this case. Addition of K_2CO_3 into the mixture of solution provides an alkaline pH environment for the particle growth that affects the size distribution [264]. The particles were expected to have spherical shape and diameter in the range 2-5nm based on [269]. The size distribution that is achieved by the DLS analysis is then illustrated in Fig 4.13. The average size is measured as 3.4 ± 1.08 nm and the result matches the expectation. The TEM image of the particles is presented in Fig 4.14, in which AuNPs are illustrated between two pointing arrows and the size is around 3nm.

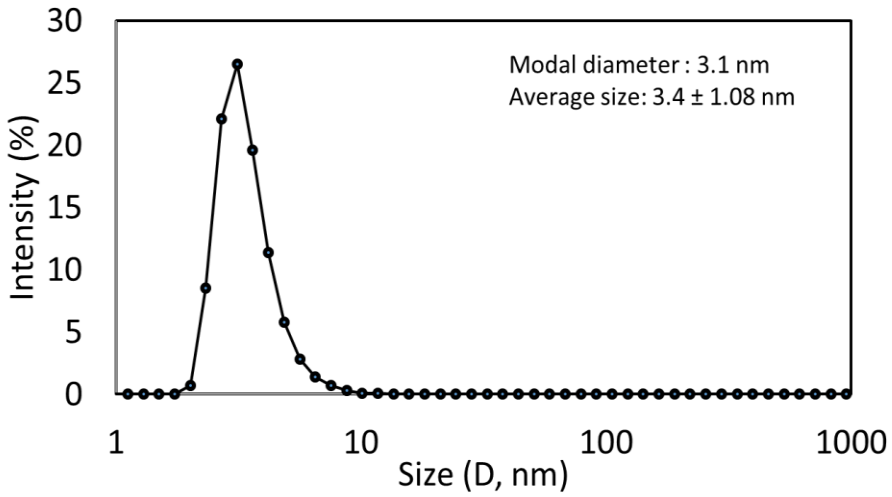


Fig 4.13 DLS size distribution of AuNPs that is prepared by using the Bonnard method.

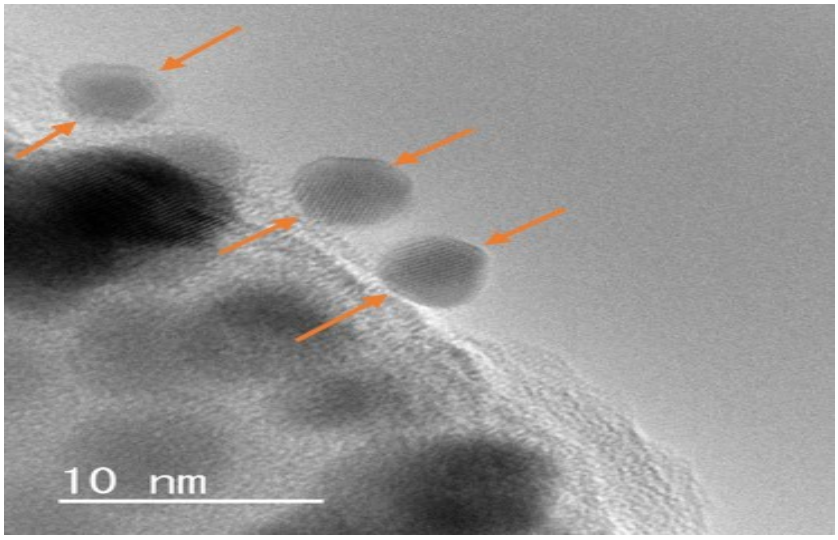


Fig 4.14 TEM image of AuNPs prepared by using the Bonnard method. Single particles are pointed out between two arrows.

4.3 Conclusion

Synthesis of SiNPs and AuNPs via chemical reaction are introduced in this chapter. SiNPs with the size of 200 to 300 nm are prepared based on the STÖBER method. The particles exhibit a uniform spherical shape, and their average size depends on the volume ratio of TEOS. The lower ratio leads to the smaller average size.

AuNPs are prepared using two methods based on two different reducing agents. The Turkevich method that uses sodium citrate as a reducing agent at boiling condition exhibits limitation in producing the small size of AuNPs (minimum size was achieved

as 14 nm). The average size is determined by the molar ratio of $Na_3ct/HAuCl_4$, and a lower ratio provides a larger size. When the ratio is less than 0.98, the arbitrary shape and agglomerated particles are observed due to the insufficient capping agent.

A smaller size of AuNPs (~3 nm) is made by means of the Bonnard method while using sodium borohydride at a lower temperature (~0 ℃) as a reducing agent. The prepared SiNPs (300 nm) and AuNPs (3 nm) will be used to form a silica core and gold shell structure on the optical fibre in Chapter 6 to configure the LPG based biosensors.

Chapter 5 Sensing film preparation for the fabrication of FOS

5.1 Introduction

This chapter introduces all the materials that were used in preparation of FOS, the sensing film preparation protocol and the coating process of the sensing film to the optical fibre for fabricating functional FOS to measure specific analytes of interest. It includes (i) the functionalisation of an LPG based biosensor that measures proteins, i.e. , streptavidin and human IgM, (ii) the fabrication of a fibre tip based CO_2 sensor, a Fabry–Pérot interferometer (FPI) sensor for the simultaneous measurement of CO_2 and RH, (iii) an integrated fibre sensor incorporated with two sensing films for measuring of CO_2 and NH_3 simultaneously, (iv) and an LPG sensor incorporated with Molecularly imprinted polymer (MIP) nanoparticles for the measuring of carboxyl-fentanyl.

5.2 Materials

Poly(allylamine hydrochloride) (Mw~58,000, PAH), (+)-Biotin N-hydroxysuccinimide ester (Mw: 341.38 g mol^{-1}), Streptavidin from Streptomyces avidinii (Mw: 60 kDa), 11-Mercaptoundecanoic acid (11-MUA), 3-Dimethylaminopropyl-N′-ethylcarbodiimide hydrochloride(EDC), N-hydroxysuccinimide (NHS) and 3-aminopropyltriethoxysilane (APTES), Cysteamine hydrochloride, Dimethyl sulfoxide, 2-(N-Morpholino)ethanesulfonic acid hydrate (MES hydrate), Sodium hydroxide, Potassium hydroxide, Sodium chloride, Tris hydrochloride, Potassium chloride, Sodium phosphate dibasic, Potassium phosphate monobasic, Sodium azide, Tetraethyl Orthosilicate (TEOS), Triethoxymethylsilane (MTEOS), Thymol blue, Ethanol and Tetramethylammonium hydroxide (TMAH) solution in water (10 wt%), Ethyl cellulose (EC) (48 % ethoxyl), Tributyl phosphate, Hydrogen chloride (HCl) solution, Sodium carbonate anhydrous, Sodium bicarbonate, Anti-Human IgM (µ-chain specific), IgM from human serum, Bovine Serum Albumin (BSA), Human serum (from male AB clotted whole blood) were purchased from Sigma-Aldrich, UK.

SiNPs (2.8 wt% in water, Diameter: ~300 nm) and the aqueous AuNPs (diameter 2-6nm) were prepared as described in Chapter 4.

SiNPs (Snowtex-ZL, 20 wt%, Diameter: 70-100nm), Tetrakis-(-4-sulfophenyl) porphine (TSPP) was purchased from Nissan Chemical, Japan.

Carbon dioxide (5 % in argon mixture) was purchased from Ryvalgas, UK. Nitrogen (oxygen-free) was purchased from BOC, UK.

5.3 LPG based biosensor for protein detection

5.3.1 LPG modification for biotin detection

For verifying the LBL coating method (described in Chapter 2), the PAH/SiNPs bilayer initially coated on a silicon substrate. The substrates were immersed into a 1 wt% ethanolic KOH (ethanol/water=3:2.v/v) solution for 30 mins in order to attach -OH groups on the surface of the substrates. After washing with distilled water (15 MΩ cm) and drying with N_2, the substrates were subsequently immersed into positively charged polymer poly(allylamine hydrochloride) (PAH) (0.17 wt%, pH=10 in water) and negatively charged SiNPs (concentration range: 0.5 wt% - 20 wt%) (diameter: 70-100 nm) for 15 mins in each solution. Washing with distilled water and drying with N_2 gas were applied between each immersion (illustrated in Fig 5.1). Repeating the coating process for up to 4 times. Each SiNPs solution was sonicated for 15 mins prior to use.

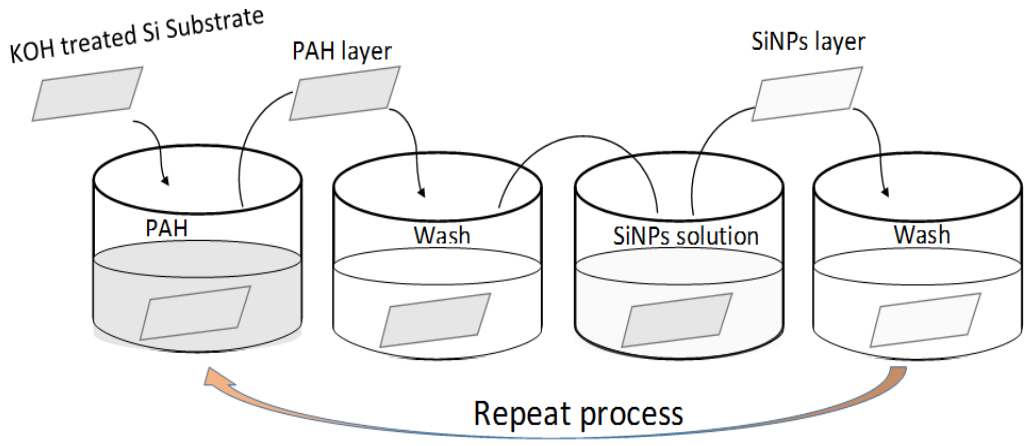


Fig 5.1 LBL deposition of PAH/SiNPs bilayers on silicon substrates

A bare LPG (grating period: 110 µm, grating length: 3 cm) was prepared to deposit the PAH/SiNPs bilayer via the LBL method (Fig 5.2a). The KOH etched LPG was later immersed into the PAH and the sonicated SiNPs solution (20 wt%) for alternately depositing positive charged PAH polymer and negative charged SiNPs on the LPG surface. The sample was washed with distilled water and dried with N_2 between each step. This process is repeated to build up to 6 layers to find out the optimal thickness which renders the highest sensitivity of the LPG sensor. An LPG is coated with the three layers PAH/SiNPs for further modification. A second bare LPG is coated with three layers of PAH/SiNPs by following same coating process but replacing 20 wt% of SiNPs (diameter: 70-100 nm) with 2.8 wt% of SiNPs (diameter: 300 nm, prepared in Chapter 4 (section 4.2)).

The three-layer PAH/SiNPs coated LPG was then immersed into 5 % v/v APTES solution (5% APTES and 5% water in 90% absolute ethanol) for 30 mins followed by washing with ethanol and water seven times each. The LPG was then dried and left at room temperature overnight for approximately 17 hours to condense the silanols group and stabilise the linker.

An aqueous gold nanoparticle (diameter: 3.4 ±1.08 nm) solution was prepared in Chapter 4 (section 4.3), and then added to the LPG fibre bath in which the coated LPG sensor was placed for 1 hour. The LPG was subsequently washed and dried.

The silica-Au modified LPG was immersed into 0.1 M cysteamine hydrochloride solution in water for 30 mins to provide amine group termination. The fibre is then ready to bind with NHS-ester modified biotin as illustrated in Fig 5.2b.

A biotin solution 1 mg/mL was made by dissolving biotin in dimethyl sulfoxide and deionised water with a volume ratio 2:3; and was then added into LPG fibre bath for 1 hour followed by washing and drying process.

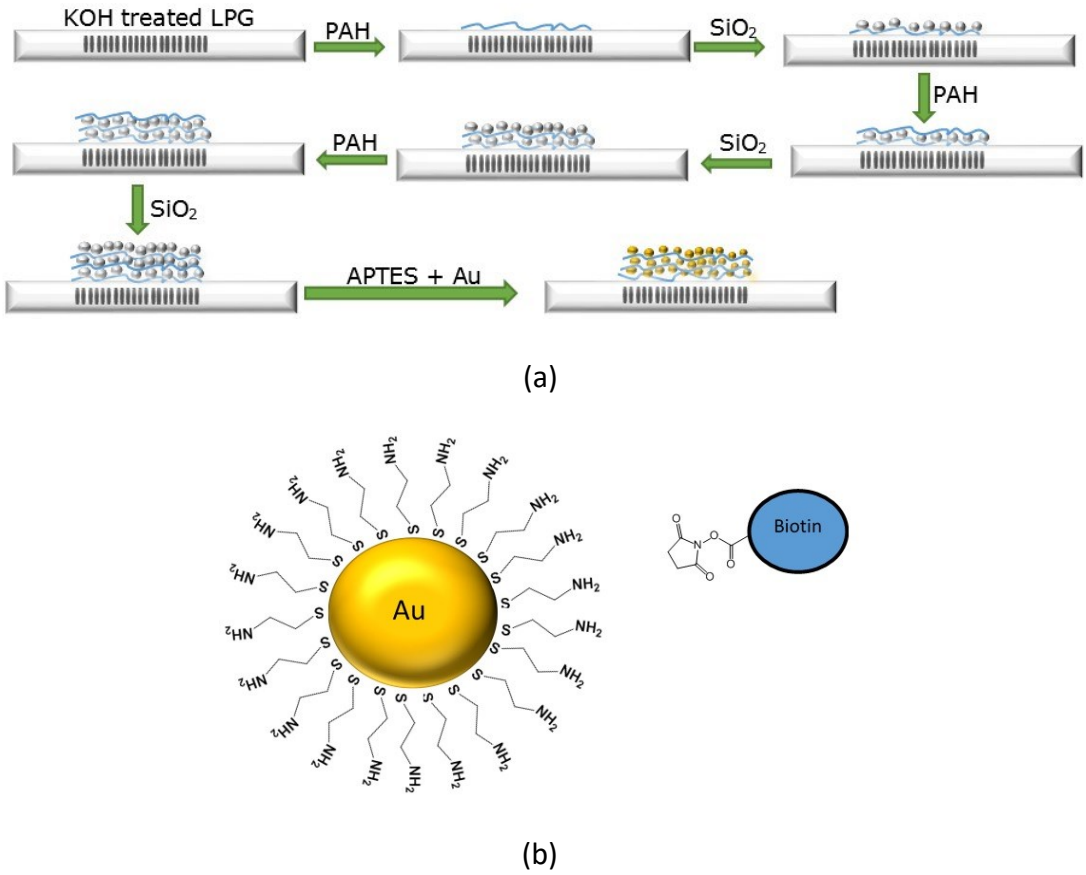


Fig 5.2 (a) Schematic diagram of the LBL modification of LPG. The bare LPG was initially treated with KOH to etch –OH group and then followed by subsequently adding polycations (PAH) and negatively charged SiNPs to build up the film LBL. The functionalisation of SiNPs was achieved by APTES with a silanisation process for attachment of AuNPs forming a shell structure. (b) Gold nanoparticle chemically decorated with amine groups to attach biotin.

5.3.2 LPG modification for IgM detection

A three-layer silica-Au coated LPG was fabricated using the assembly method described in section 5.3.1. It was immersed into 20 mM 11-Mercaptoundecanoic acid (11-MUA) solution in ethanol for 30 mins. The self-assembled monolayer of the thiol linkers in 11-MUA solution made a continuous binding to the gold surface leading to a termination of –COOH group. The LPG was then immersed into 25 mM EDC solution in MES buffer (0.1 M pH=5.6, with 0.9 % NaCl) for 20 mins followed by immediate immersion in 60 mM NHS solution (0.1 M PBS buffer, pH=7.4) for another 20 mins. After brief washing with deionised water, the LPG was immersed into a solution that contains 1 mg/mL anti-IgM in PBS buffer for 1 hour at room

temperature (temperature regulated at 26 ℃). The schematic of the modification is illustrated in Fig 5.3.

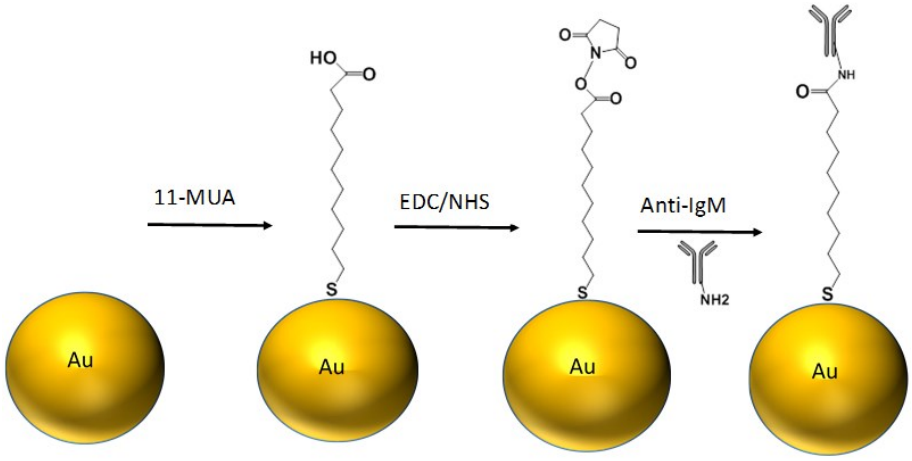


Fig 5.3 The modification of LPG for the detection of IgM. The LPG has been coated with three-layer PAH/SiNPs-Au in advance as illustrated as Fig 5.1 a. Then an EDC/NHS linker is activated and linked on the surface of gold via a two-step procedure. The primary amine group of anti-IgM covalently binds to the activated NHS esters leading to the immobilisation of anti-IgM on the LPG sensor

After washing with deionised water, the anti-IgM functionalised sensor was then immersed into 1mg/mL BSA for incubation of 1 hour in room temperature followed by washing with deionised water to remove excess unbound proteins.

5.4 Reflection mode fibre optic CO_2 sensor

5.4.1 Sol-gel based sensing film preparation

Organically modified silica (Ormosil) was produced by mixing 200 µL of TEOS with 1.8 mL of MTEOS in a 20 mL volume of vial under stirring for 10 mins, subsequently adding 5 mL of ethanol and stirring for another 10mins. Six concentrations of solution mixture were made by adding 12/17/22/27/32 mg thymol blue into prepared Ormosil solutions and stirring for 15 mins. Different concentrations were used in order to evaluate the association of concentration to sensitivity and find out the optimal concentration. 500 µL of TMAH solution was dropwise added to each solution mixture, the vials are capped and stirred for 1.5 hours prior to dip-coating. The final coating solutions that are prepared have dye (thymol blue) concentrations of 1.6/2.3/2.9/3.6/4.2 mg/mL.

5.4.2 Polymer-based sensing film preparation

The preparation of EC coating solution is done by dissolving 32 mg of thymol blue into 10 mL of 9 wt% ethyl cellulose solution and adding additives of TMAH and tributyl phosphate each for 500 µL (final dye concentration: 2.9 mg/mL). 900 mg ethyl cellulose powder is dissolved into 10 mL of ethanol in advance for mixing of 2-3 hours under stirring (clear viscous solution is obtained). Thymol blue (32 mg) is added into the solution for mixing of 30 mins, then adding 500 µL of TMAH and 500 µL of tributyl phosphate into the solution mixture. Keep the vials capped and under stirring for overnight (~10 hours).

5.4.3 The coating of the sensing film on the optical fibre

The tip of a 2×1 multimode optical fibre coupler (3dB, F-CPL-M12855, Newport, UK) cleaved at 90° was dip coated with the sol-gel solution by using an in-house made dip coater with withdrawal speed of 6mm/s. The coating set-up is illustrated in Fig 5.4, in which the optical fibre is mounted vertically with the tip facing downward on the translation stage (M126, Physik Instrumente, Germany). The prepared coating solution is placed underneath the optical fibre. The two distal ends of the coupler are connected to a halogen light source (HL-2000, Ocean Optics, UK) and a CCD spectrometer (USB 2000, Ocean Optics, UK) respectively, and a computer is connected to the spectrometer for displaying and recording the spectrum during the coating process. The coating procedure was repeated four times and a drying period of 2 mins between each coating was allowed. The coated fibres were left in ambient air for drying for 24 hours before use. The fibre that was dip-coated with the prepared EC coating solution with same coating speed (1 time) was placed inside of a pre-heated oven (70 ℃) for coalescence 4 hours before use.

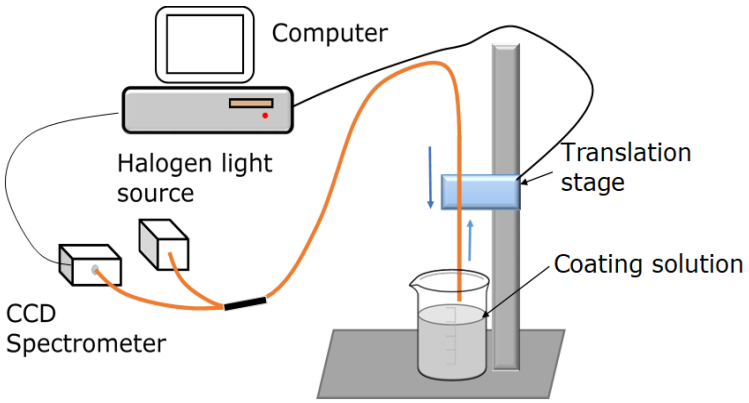


Fig 5.4 Schematic of the dip coating process for coating the sensing film on the tip of an optical fibre.

5.4.4 The coating of the CO_2 sensitive film for fabricating of Fabry–Pérot interferometer (FPI) sensor

The tip of the same optical fibre coupler in section 5.4.3 was cleaved at 90°, and then dip coated with the sol-gel coating solution prepared above at the dye concentration of 2.9 mg/mL (this is the optimal concentration that found from the experiment) by using the in-house made dip coating with withdrawal speed of 0.5 mm/s (set-up illustrated in Fig 5.4). The coating process was repeated up to four times and a drying period of 2 mins is allowed between each coating. The coated optical fibre is inserted into a Tedlar bag filled up with 100 % N_2 (humidity free) for drying about 24 hours before use. Three sensors with different layer numbers from 1 to 3 are prepared and exposed in ambient in order to investigate the longevity in air.

5.5 Preparation of FOS for NH_3 and CO_2 sensing

5.5.1 CO_2 sensing film preparation

The CO_2 sensing coating solution is made by doping the thymol blue and TMAH into a sol-gel film by following the protocol described above.

5.5.2 NH_3 sensing film preparation

The NH_3 sensing coating solution is prepared by first adding 100 mg of EC into 10 mL of ethanol for stirring of 2 hours until all the powder is dissolved and the solution turns to clear. 12 mg of TSPP is then added into the solution for stirring of another 15 hours. Finally, adding 500 µL tributyl phosphate for mixing of 2 hours.

5.5.3 Coating of the optical fibre with the sensing film

A 2 × 2 multiple-mode optical fibre coupler (3dB, F-CPL-M22855, Newport, UK) was used to incorporate the sensing film on its two distal tips as illustrated in Fig 5.5. One tip is dip coated in the sol-gel solution with a withdraw speed of 6 mm/s for 4 times with 2 mins interval between each coating. The other tip is then dip coated with the ammonia coating solution with a withdrawing speed of 6 mm/s. The coated fibre was left in ambient to dry for 24 hours before use. As the coupler is an integrated component, the two tips with different coatings are treated and used as one integrated sensor. And the FOS in the experimental description refers to the coupler with two coating film.

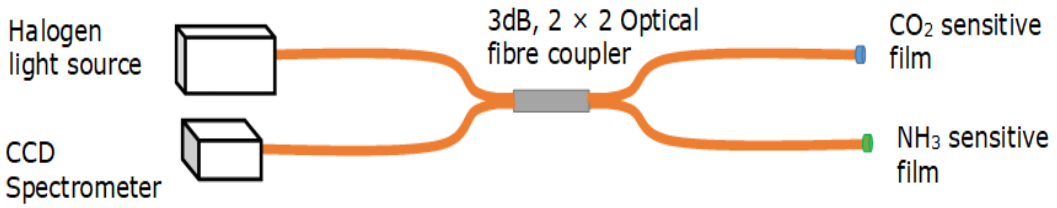


Fig 5.5 Schematic of the FOS using a 2 × 2 optical fibre coupler with two separate films coated on its two distal tips.

Moreover, the coating procedure was repeated on the tip of a 3dB 2 × 1 multiple-mode optical fibre coupler (F-CPL-M12855, Newport, UK) for characterising the individual absorption spectrum of each film.

5.6 LPG sensor incorporated with molecularly imprinted polymer (MIP) nanoparticles for the detection of carboxyl-fentanyl.

5.6.1 Fabrication of LPG array sensor

An LPG sensor with a grating period of 111.5 µm, a length of 1.5 cm is fabricated by using the amplitude mask described in Chapter 2. A second LPG with an equal length and a grating period of 110 µm is inscribed on the same fibre at 1 cm away from the first LPG by using the same fabrication method. A schematic of the LPG array is illustrated in Fig 5.6.

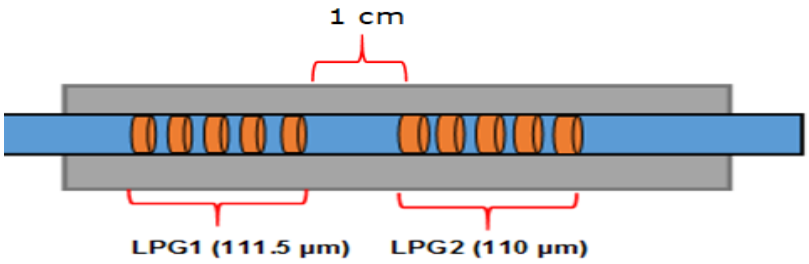


Fig 5.6 Schematic of the LPG array.

5.6.2 Functionalisation of an LPG sensor for the detection of carboxyl-fentanyl

The coating of MIP nanoparticles is illustrated in Fig 5.7 that can be divided into three steps: (i) silanisation of LPG with amine group $-NH_2$; (ii) modification of MIPs with EDC/NHS linkers; (iii) incubation of the LPG with modified MIPs.

(i) The bare LPG (111.5 μm) was immersed into a 1wt% ethanolic KOH (ethanol/water=3:2 v/v) solution for 30 mins to hydroxylate the LPG surface. After washing with distilled water and drying with N_2, the LPG was immersed into a 2 % v/v APTES solution in ethanol for 20 mins followed by washing with ethanol and distilled water for four times each. Then the LPG was put into a pre-heated oven at a temperature of 120 ℃ for 20 mins.

(ii) A 150 μL of the sonicated MIPs solution (0.13 mg/mL) was added into 400 μL of a 1 mg/mL EDC solution in MES buffer (0.1M, pH=5.6), continuously adding 1 mg NHS into the solution for a stir of 15 mins.

(iii) Subsequently adding 175 μL of carbonate buffer (pH=11) to the solution and incubating with the prepared LPG in (i) for overnight (~12 hours). After the incubation, the fibre was washed with distilled water for a couple of times to remove loosely bonded MIPs. It was then immersed into a carbonate-bicarbonate buffer (pH=9.2) for 2 hours before the measurement.

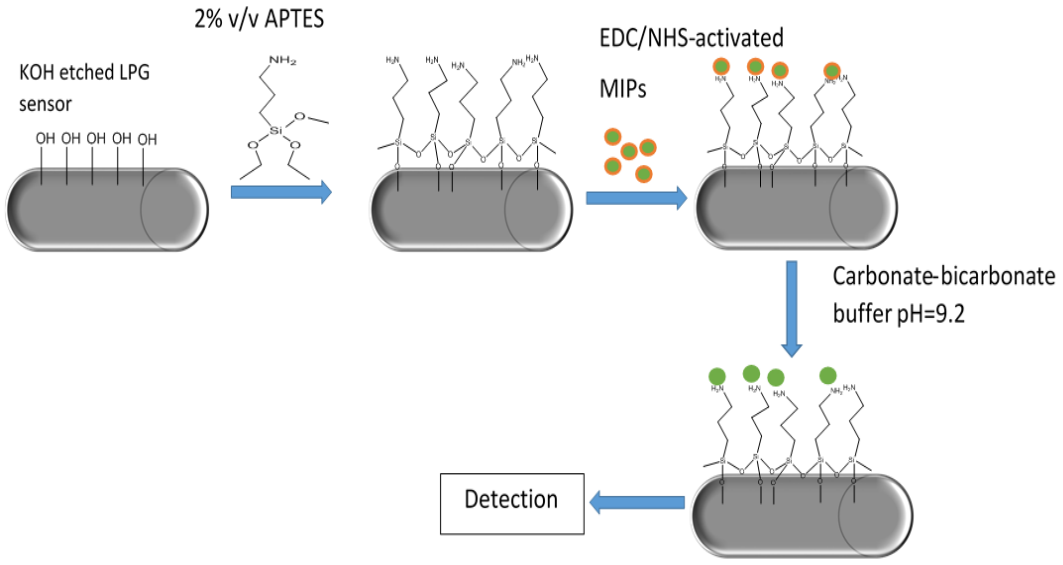


Fig 5.7 Schematic of modification process of an LPG with carboxyl-fentanyl MIPs.

5.7 Conclusion

This Chapter describes the materials, sensing film preparation as well as its coating method for incorporating to the optical fibre sensing platform.

The LPG based biosensor for the detection of proteins is fabricated by coating the LPG with three layers of bilayers containing PAH/SiNPs via a LBL deposition technique, and AuNPs (~3 nm) are covalently deposited on the surface of the coated silica nanoparticle forming shell structure. The LPG sensor is then further functionalised with biotin and anti-IgM for the detection of streptavidin and human IgM, respectively. The details of the sensor performance is demonstrated in Chapter 6.

A reflection mode colourimetric fibre optic CO_2 sensor is prepared by dip coating the tip of an 2×1 optical fibre coupler with a film that comprises of a silica/EC matrix doped with a pH dye, thymol blue and a phase transfer agent,TMAH. An FPI sensor is fabricated by controlling the thickness of the film (silica matrix doped with thymol blue and TMAH) coated on the tip via adjusting the withdrawing speed of dip coating process. Such a sensor combines the colourimetric and FPI technique and is used for sensing of CO_2 and RH simultaneously as shown in Chapter 7.

An FOS that integrates two sensitive dyes (thymol blue and TSPP) into one fibre detection system is proposed for the detection of CO_2 and NH_3 simultaneously. The two dyes are doped into two independent matrix films, i.e. silica and EC and dip

coated on the tip of a 2×2 fibre coupler. The sensor performance is explicited in Chapter 8.

An FOS for the detection of carboxyl-fentanyl is proposed. The sensor uses an LPG as the sensing platform and the MIP nanoparticles as the sensing element. An LPG array sensor contains two LPGs with a different grating period and is fabricated with one LPG coated with MIP nanoparticles as the detection sensor and the other unmodified LPG as a reference sensor for compensating the temperature effect. The sensor is then used for detecting of carboxyl-fentanyl from aqueous solution in Chapter 9.

Chapter 6 Development of LPG based biosensors

6.1 Introduction

As discussed in chapters 2 and 3 LPGs are sensitive to the RI surrounding the cladding region, and therefore bio-sensing can be achieved by modifying the outside of the cladding with a functional material whose RI changes in the presence of an analyte of interest. This removes the need for enzyme labelling and provides a prospect for a label-free, low-cost, rapid, POC detection of bio-molecules. The optimum functional coating combines high sensitivity and high specificity. In Chapter 4, the methods of synthesising SiNPs and AuNPs, and their advantages in constructing biosensors were described and discussed. Previous work by our research group [269] developed an LPG bio-sensor modified with poly(allylamine hydrochloride)/silica core-gold shell nanoparticles for detection of the streptavidin with a high sensitivity (6.9 nm/(ng/mm^2)) and the minimum detectable concentration of 19 nM. However, the sensor performance was not optimal due to the poor surface coverage and uniformity of the coating. In addition, a selected grating period of the LPG sensor was near, rather than at, the PMTP which also did not lead to the optimal performance.

In this chapter, these points are addressed to fully realise the optimum performance of this sensor. In particular, a new approach of functionally coating the LPG is reported here in order to provide significantly improved sensitivity (minimum detectable concentration of 1.25 nM for streptavidin compared to 19 nM previously demonstrated [269]). SiNPs are first deposited onto the LPG using the LBL method in order to address the surface coverage problem providing a more uniform surface coverage. The surface of the silica particles is then further modified with 3-aminopropyltriethoxhysilane (APTES) via a silanisation process to covalently attach AuNPs (diameter of 3.4 ± 1.08 nm) to the SiNPs, forming a shell structure via a chemisorption process. In addition, chemical linkers are applied to covalently link the AuNPs and the bio-receptor in order to minimise unspecific binding to the gold surface. Crucially the LPG sensor is fabricated close to the phase matching condition

and, at the deposition of sensing film, the coupling conditions are modified such that sensors operate at the highly sensitive PMTP. The transmission changes at a specific wavelength, corresponding to the resonance band at the PMTP, are detected which has been reported to be more sensitive than the wavelength shift [270]. After optimising the LPG sensor performance using streptavidin, it was then used for the first time to the best of my knowledge to detect human IgM by functionalizing the coated LPG with anti-human IgM antibody as a proof of concept towards application in clinical POC. The result reported in this chapter have been published in [183].

6.2 Definition of LPG biosensor parameters

The adsorption of protein on the LPG is simulated by using of the Langmuir-Freundlich (LF) isotherm approaches [271]:

$$a = \frac{(kC)^{\beta} M}{[1+(kC)^{\beta}]} \tag{6.1}$$

Where a is the amount of protein adsorbed, k is equilibrium constant, C is the concentration of protein in solution, M is the maximum adsorption and β is the heterogeneity parameter. When β = 1, the LF Eq 6.2 will become the Langmuir isotherm equation as described in [269].

It is assumed that the adsorption of protein is proportional to the change of transmission (or wavelength shift，$\Delta\lambda$) of the LPG at the PMTP. The Eq 6.2 can be written as:

$$\Delta P = \Delta P_{max} \frac{(kC)^{\beta}}{[1+(kC)^{\beta}]} \tag{6.2}$$

Where ΔP is the transmission change (or wavelength shift) of the LP_{019} mode at the phase matching condition as a result of RI change induced by the adsorption of protein on the LPG surface and ΔP_{max} is the maximum change of transmission (or wavelength shift) when the sensor surface reaches saturation and cannot bind any further protein.

The sensitivity (S) of the LPG sensor is defined as the maximum transmission change (or wavelength shift) for the unit surface density of bonded protein.

$$s = \frac{\Delta P_{max}}{\delta_{max}} \quad (6.3)$$

Where δ_{max} is the surface density of target protein immobilised on the sensor when all the capture sites are occupied.

The theoretical of LOD is given by the resolution of sensor divided by the sensitivity [272].

6.3 Method

6.3.1 Thin film characterisation

A disposable cuvette containing 1 mL of sonicated SiNPs suspension (0.5 wt%) was mounted into Malvern Zetasizer Nano-ZS (Malvern Instruments, UK) with a temperature of 25 ℃ and RI setting of 1.458 for measuring the size distribution of SiNPs. The coated silicon substrates with PAH/SiNPs bilayers were examined under ellipsometry (alpha-SE, J.A.Woollam, USA) for achieving thickness and RI information. The coated SiNPs with gold shell structure on optical fibre was imaged using transmission electron microscopy (TEM) (JEM-3010, JEOL, Japan). The morphology of the PAH/SiNPs film was studied using scanning electron microscopy (JSM-7100F, JEOL, UK).

6.3.2 Streptavidin detection

The prepared streptavidin solutions were left at the laboratory room temperature for 1 hour in order to obtain a uniform temperature across each testing solutions (controlled at 22 ℃). The functionalised LPG was immersed for different time intervals depending on the concentration range of streptavidin in water ranging from 1.25 nM to 2.7 µM for 20 mins (1.25 nM to 5 nM), 30 mins (10 nM to 0.3 µM) and 1 hour (2.7 µM). Different time intervals were used to ensure the saturation of the sensor response. Between each concentration test, washing and drying took place to remove streptavidin with non-covalent binding and to avoid bulk RI of the solution. The transmission spectra were subsequently recorded at a frequency of 0.5 Hz. The RI of the streptavidin solution with a concentration of 2.7 µM and deionised water were measured using a digital refractometer (Reichert 13940000).

6.3.3 IgM detection in solution

The human IgM antibodies were suspended into Tris buffer (50 mM Tris.Cl, 200 mM NaCl and 0.025 % NaN_3, pH=8) at concentration range from 15.6 µg/mL to 1 mg/mL. The modified LPG sensor was subsequently immersed at room temperature (temperature regulated at 26.1 ± 0.26 ℃, Fig 6.11) for 30 mins in the IgM solution from the lower to higher concentration and washed between each test with buffer solution to remove unspecific bonded IgM and avoid accumulation of IgM at the surface that increases bulky RI. The RI of the buffer solution and the IgM solution with the highest concentration (1 mg/mL) were measured using a digital refractometer. The specificity test of the developed sensor was conducted by immersing the prepared sensor into 1 mg/mL of BSA in Tris buffer for 30 mins.

6.3.4 Detecting IgM from blood serum

Four blood serum samples with different IgM concentrations were prepared by mixing blood serum samples with 1 mg/mL of IgM solution with a volume ratio of 1:0, 5:1, 2:1 and 1:1, respectively. The anti-IgM functionalised LPG is subsequently immersed into the four prepared samples for 30 mins each and thoroughly washed with PBS buffer (0.1M) to remove unbound biomolecules between each sample.

6.3.5 Experiment set-up

The coated LPG of length 3 cm, period 110 μm and duty cycle of 50:50 was prepared by using an amplitude mask and UV inscription (as described in Chapter 3, section 3.2).

The LPG sensor region was placed into a Teflon fibre bath (inner well diameter: 55(L) ×5(W) ×4(D) mm) containing the solution under test (Fig 6.1) for streptavidin detection and IgM detection. The proximal and distal end of the optical fibre was connected to a Halogen light source (Ocean Optics, HL-2000, UK) and CCD spectrometer (Ocean Optics, HR4000, UK) respectively with data transferred to a computer for post-processing.

Temperature variation of the lab was monitored by using a thermocouple logger (TC-O8, Pico Technology, UK), the thermocouple is placed close to the Teflon fibre bath and temperature data was recorded with a sampling frequency of 0.1 Hz for 24 hours.

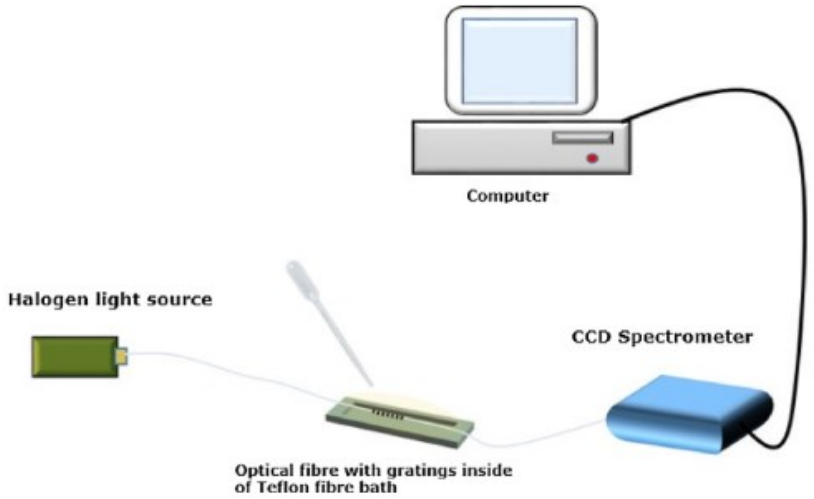


Fig 6.1 The LPG sensor set-up.

6.4 Results and Discussion

6.4.1 LBL film deposition

The hydrodynamic size (Z-average size) of SiNPs is 137 nm with a PDI value of 0.08 based on the analysis of DLS (Fig 6.2).

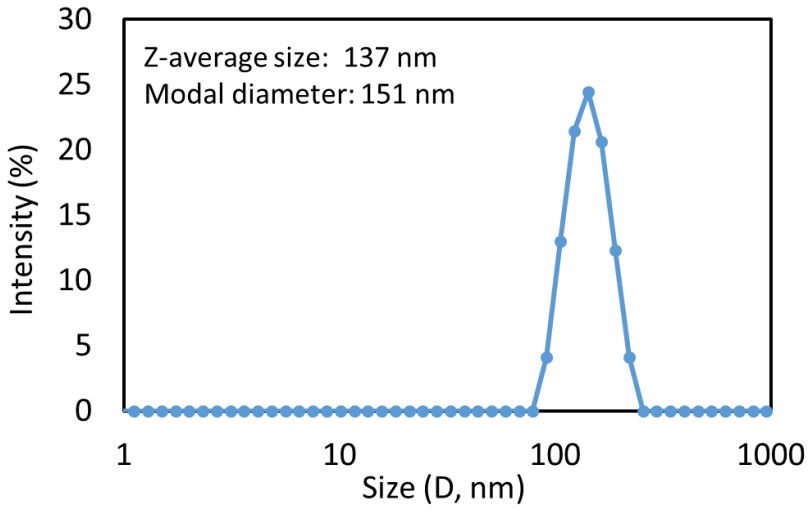
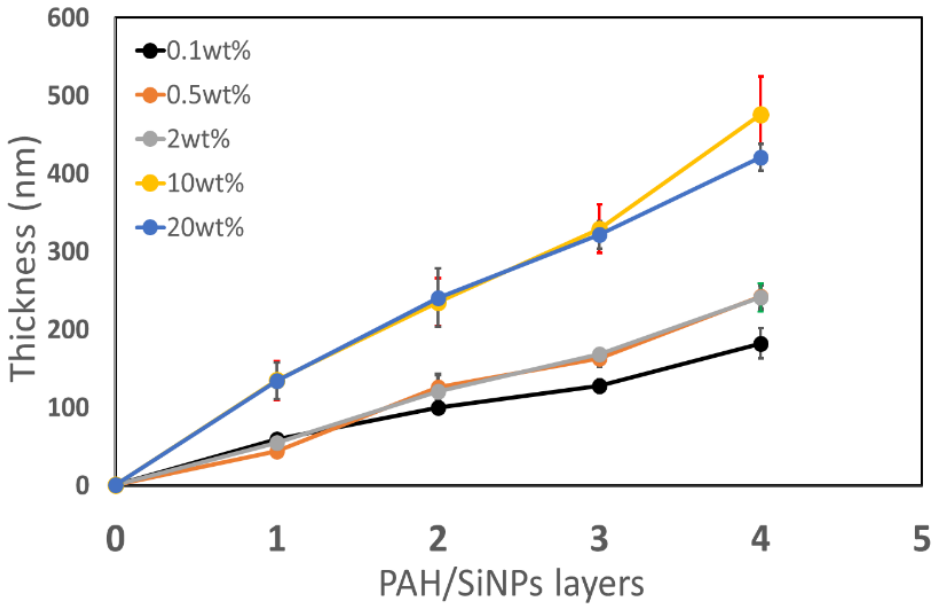


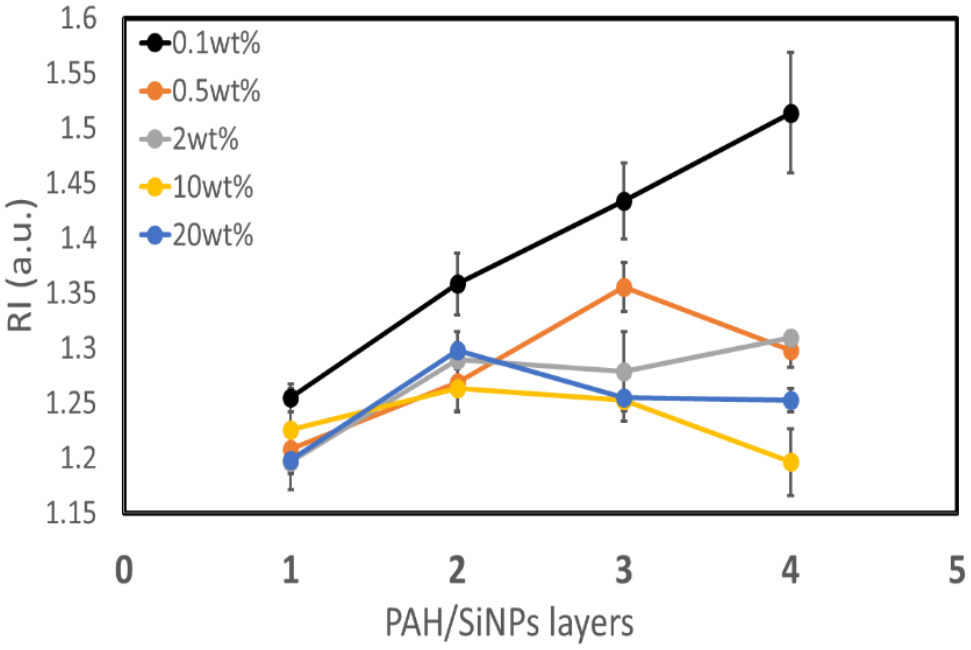
Fig 6.2 Size distribution of commercial SiNPs. The mean size of SiNPs based on the size distribution is calculated as: 137 ± 46 nm.

The electrostatic force based self-assembly LBL technique relies on the surface charge of particles or polymers. Higher magnitude and density of surface charge produce strong attractive force resulting in the formation of layers. SiNPs can obtain a negatively charged surface when dispersed in water due to the deprotonation of silanol group (Si-OH). The charge density of SiNPs surface is dependent on the pH, particles size as well as salt concentration dissolved in water [273]. Generally speaking, the magnitude of the surface charge density increases as pH increases. As the concentration of H^+ ions decreases with increasing of pH, more negatively charged SiO^- are dissociated from the functional groups SiOH resulting in higher negative surface charge density. The size of SiNPs also affects the surface charge of nanoparticles due to curvature effects, and surface charge density decreases with increased particle size and asymptotically reaches that of a flat plate [273-275]. The concentration of salt in solution determines the charge distribution inside of the electrical double layer (EDL) around particles, and the particle's surface charge density increase with an increase in background salt concentration [273].

The self-assembly film comprises alternate PAH and SiNPs layers. Since the thickness of a monolayer of PAH film is less than 2nm [276], it can be neglected (considering the diameter of SiNPs is above 100 nm) and the thickness of such bilayers is approximately the thickness of SiNPs. Assuming they form uniform monolayers on the silicon substrates, the overall thickness of the film should equal the number of bilayers multiply by the size. The coating thickness and RI after each bilayer are illustrated in Fig 6.3. It is clear that the self-assembly film thickness linearly increases as the number of bilayers increase and the thickness varies with the concentration of SiNPs in the coating solution. When the concentration is above 10 wt%, the thickness of each layer of the coated film match to their theoretical thickness (theoretical thickness of one layer of the film is considered as the average size of SiNPs (137 nm)). The film thickness decreases for each layer with the decrease of the concentration (< 10 wt%), which is attributed to lower surface coverage of SiNPs film (illustrated in Fig 6.4a) resulting in a lower average thickness value. The RI value of the film also varied based on surface coverage. The RI value of PAH/SiNPs bilayers is ~ 1.25 when SiNPs are uniformly covered.



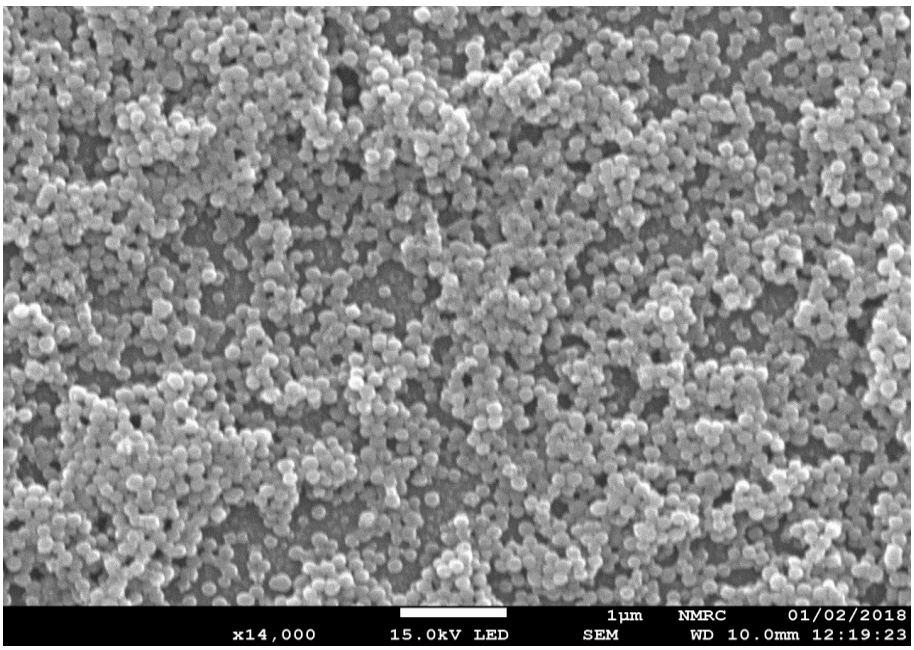
(a)



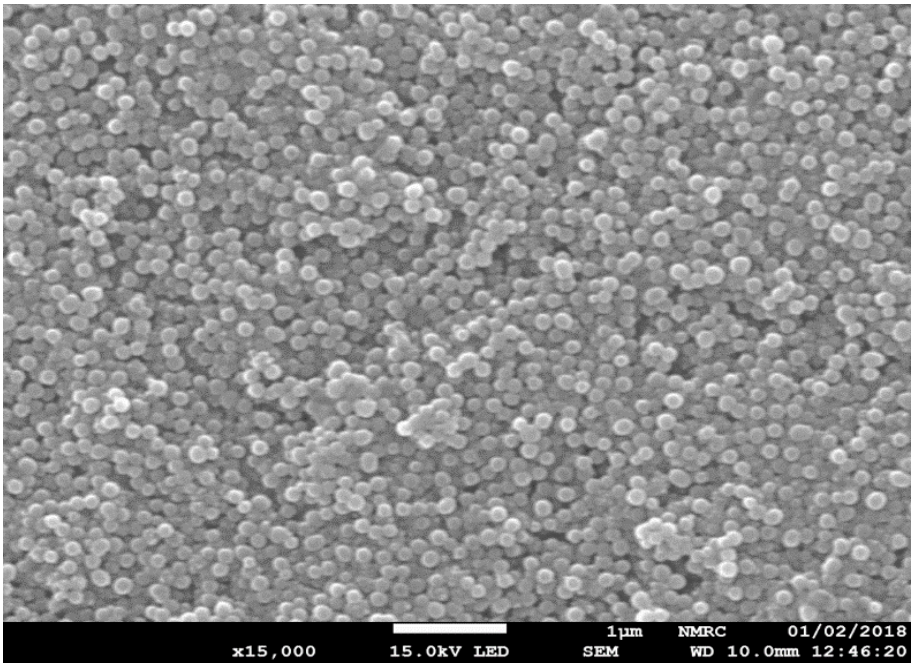
(b)

Fig 6.3 The measurement of the coated silicon substrates using Ellipsometry. Each point in the graph is the average value of five independent measurements at different positions of the substrate and error bars represent the standard deviation of the five independent measurements: (a) the thickness of self-assembly PAH/SiNPs film as a function of the number

of layers. The 0 layer is the measurement of KOH treated silicon substrate only; (b) RI of the film after each bilayer.



(a)



(b)

Fig 6.4 SEM image of 4 layers PAH/SiNPs on silicon substrates prepared by using SiNPs concentration of : (a) 0.1wt% , scale bar= 1µm; (b) 20 wt%, scale bar= 1µm.

6.4.2 LPG characterisation

Fig 6.5 illustrates the surface coverage of the three bilayers on an optical fibre that is prepared by using home-made SiNPs with the size of 300 nm. The SEM image shows a poor surface coverage which is probably due to the lower density of surface charge of large size of SiNPs [273-275] or lower concentration of SiNPs.

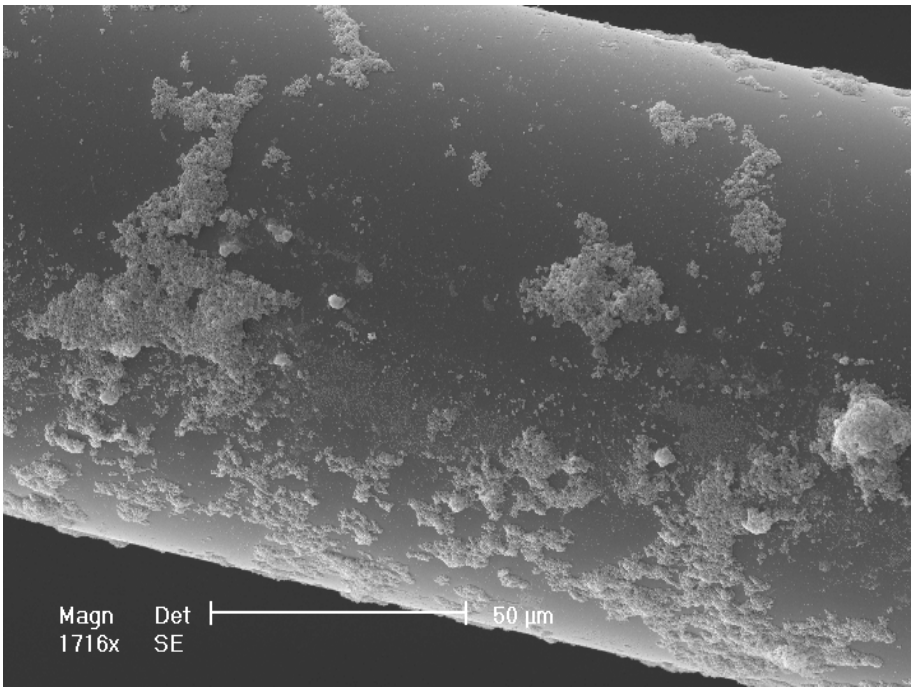
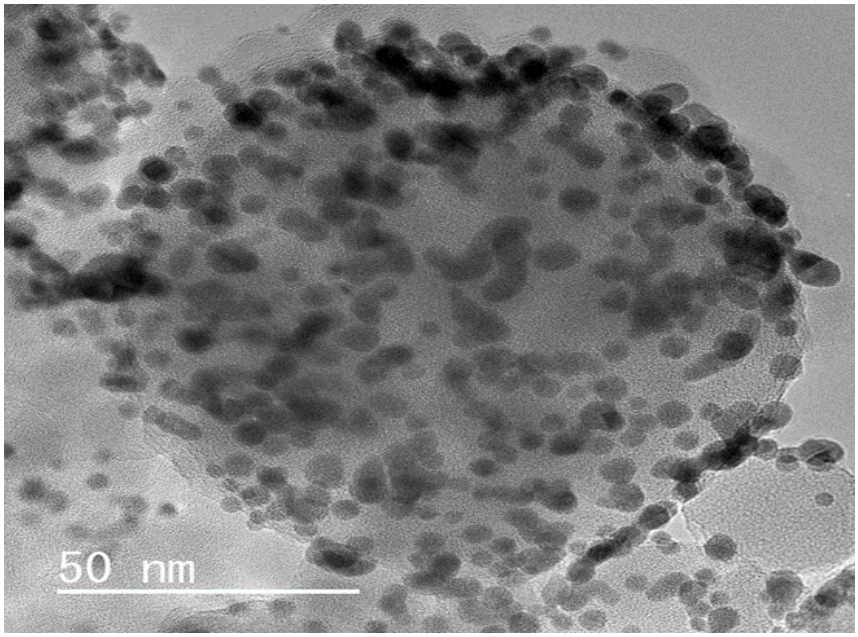
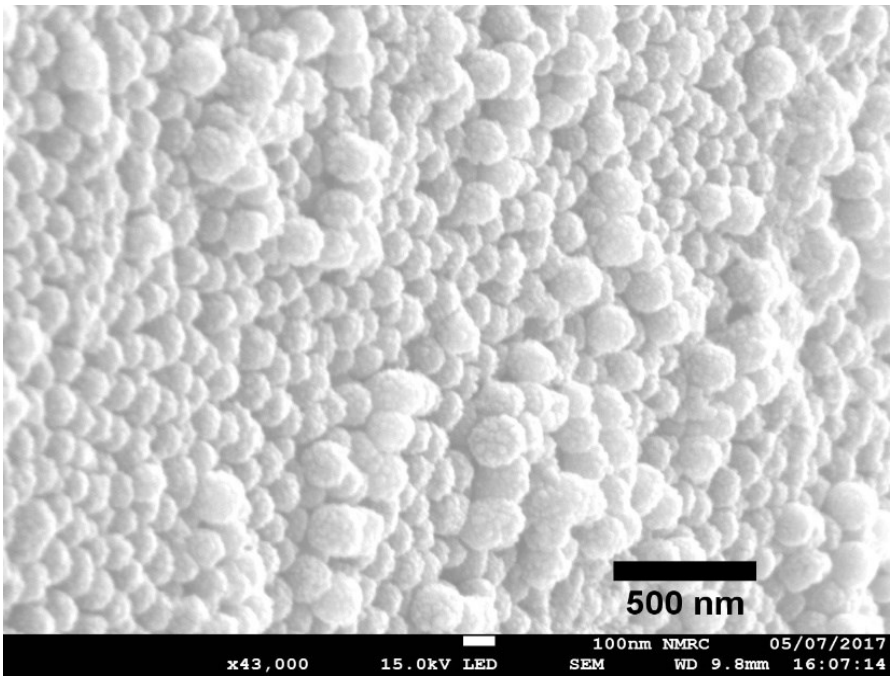


Fig 6.5 SEM image of 3 layers PAH/SiNPs bilayers, SiNPs were prepared with an average size of 300 nm. Scale bar = 50µm

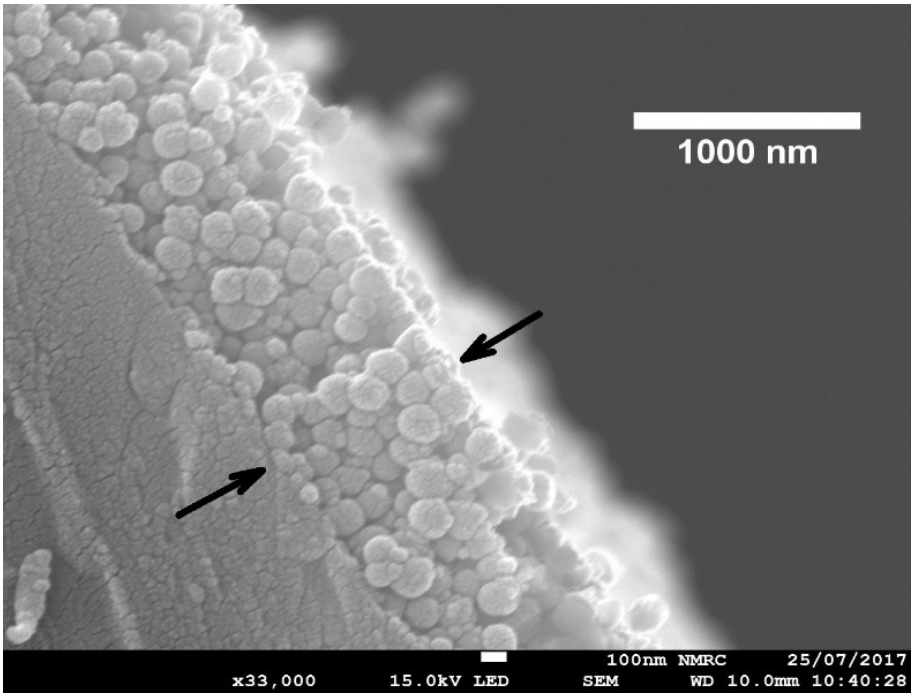
The sensor optimisation in terms of the size of SiNPs was investigated in our previous work [269] where the large particles (300 nm) exhibit a higher sensitivity than the small one (80 nm). Due to the limitation of surface coverage encountered using large size of nanoparticles, particles with average size 137 nm (Fig 6.2) were used in this work. The concentration of AuNPs was chosen such that the shell structure illustrated in Fig 6.6a can be produced.


50 nm

(a)


500 nm
x43,000 15.0kV LED 100nm NMRC SEM WD 9.8mm 05/07/2017 16:07:14

(b)



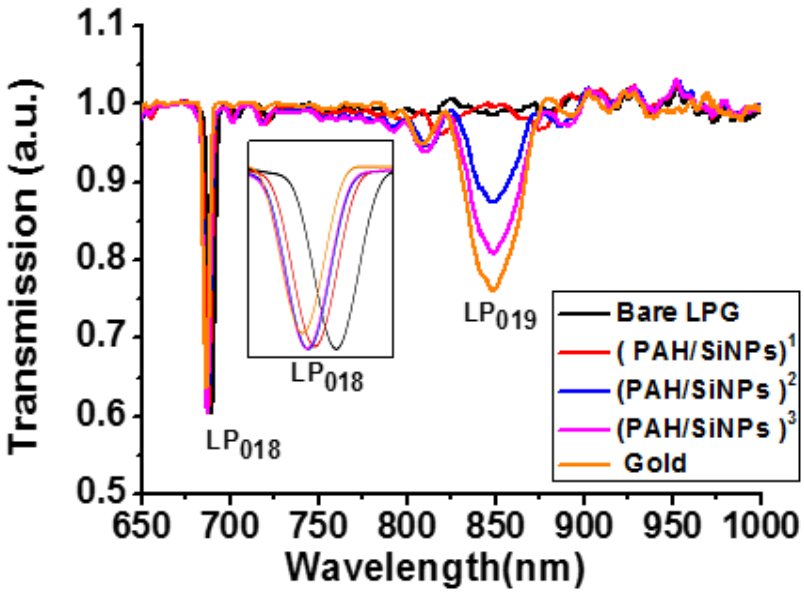
(c)

Fig 6.6 (a) TEM image of SiNPs with gold shell, the particles were scratched from the coated glass substrates confirming the attachment of AuNPs with the shell structure (scale bar = 50 nm). (b) SEM image of three layers of PAH/SiNPs with gold shell (scale bar = 500 nm). (c) Cross-section of optical fibre with three layers of PAH/SiNPs with gold shell (scale bar = 1 µm). The arrows illustrate the thickness of the film, measured as 863 nm.

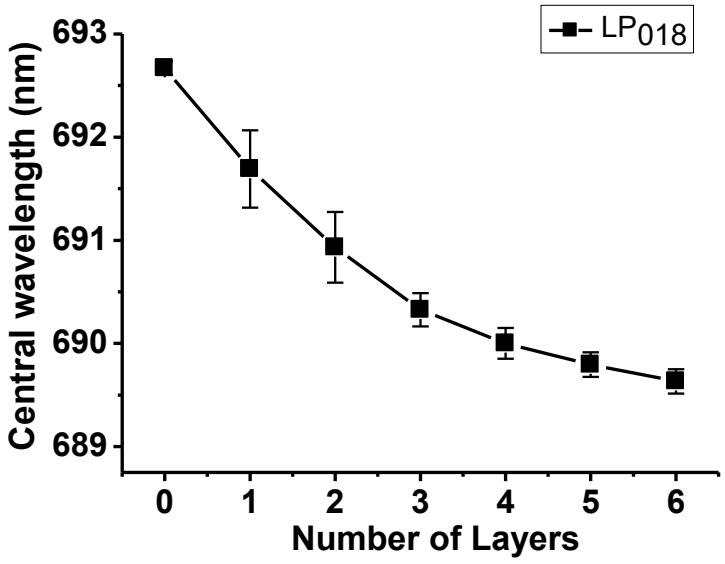
The TEM image of SiNPs coated with a gold shell is shown in Fig 6.6a. The image confirmed the successful deposition of AuNPs onto the coated SiNPs. A film containing three layers of PAH/SiNPs with gold coated on the surface was deposited onto the optical fibre, and its SEM results are shown in Fig 6.6b indicating a uniform surface coverage. The thickness of three layers on the optical fibre is measured as 863 nm from the SEM image in Fig 6.6c. The film thickness of the three layers of film is more than twice the expected thickness based on the nanoparticles diameter (414nm, neglecting the contribution of PAH). It is also twice of thickness than on silicon substrates, which can be attributed to high magnitude of surface charge induced by curvature structure of silica fibre that leads to the strong ionic interaction or the aggregation of SiNPs on PAH film [277].

The deposited film increases the RI probed by the LPG. This causes a wavelength shift in the attenuation bands and triggers the phase matching condition. As illustrated in

Fig 6.7a, the attenuation band corresponding to the coupling of the 18th linearly polarised mode (LP_{018}) undergoes a blue-shift in response to each layer deposited, and LP_{019} with a central wavelength of 850 nm starts to appear as a wide attenuation band that further grows as each layer is deposited. The attachment of AuNPs can also be observed in the transmission spectrum which causes a further increase in attenuation. Since the sensitivity of the LPG sensor to ambient RI change is thickness-dependent [278], the sensor was coated with 6 layers of PAH/SiNPs thin film (Fig 6.7b). As can be observed from Fig 6.7b, the slope of wavelength decreases after 3 layers confirming that the optimal thickness of the PAH/SiNPs thin film is reached after 3 deposited layers, corresponding to ca 900 nm (Fig 6.6c).



(a)



(b)

Fig 6.7 (a) Transmission spectra of LPG in water after deposition of $(PAH/SiNPs)^n$ film (n=1,2,3 layers) and gold. Central wavelength of LP_{018} shifts to the left with each layer deposition process and the transmission of attenuation band at LP_{019} decreases with increasing of layers. (b) The central wavelength of LPG at LP_{018} in water as a function of layers. The error bars represent the standard deviation between two times repeated deposition process.

To avoid the effect of the bulk RI change in different solutions during the deposition process, spectra were always measured and then compared to those measured in water. This allows taking into account the single change caused only by the specific binding. For binding measurement, the RI of the blank sample and target samples were measured using a refractometer, and no detectable change was measured.

6.4.3 Streptavidin detection

The modified LPG was first immersed into a biotin solution with concentration of 1 mg/mL (2.9 mM). The biotin molecules start to react with –NH2 group of the AuNPs. The bound biotin molecules on LPG surface increase the RI of the film coated on the LPG, which leads to a wavelength shift of 0.5 nm for LP_{018} mode and a transmission change of an approximate 7% (0.06988) for LP_{019} mode (Fig 6.8a). The wavelength shift induced by the bonded biotin at the first attenuation band (LP_{018}) is bigger than determined previously (0.11nm) [269].

Streptavidin has a very high affinity of binding to biotin [279] and is known as the strongest noncovalent interaction between proteins and ligand [280]. One STREPTAVIDIN molecule has the ability to bind with up to four biotin molecules. The bond formation between biotin and streptavidin is rapid (in a range of 3.0×10^6 - 4.5×10^7 M^{-1} s^{-1}) [281].

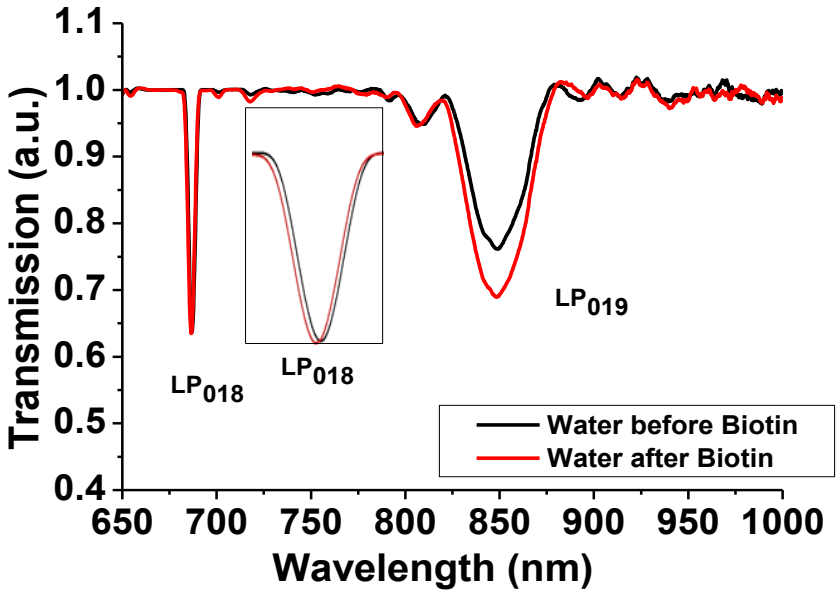
The transmission spectra as the LPG is immersed in different concentrations of streptavidin solutions are shown in Fig 6.8b. The attenuation band at 850 nm (LP_{019} central wavelength) becomes bigger and broader with increasing streptavidin concentration. The optical transmission measured at 850 nm shows a step change with increasing streptavidin concentration (illustrated in Fig 6.8c). The transmission value at this wavelength in air equals to 1 indicating that the sensor is not at the phase matching condition when operating in air due to lower RI (n_{air}=1) when compared with the aqueous solution. The RI of the tested streptavidin solution measured with a refractometer showed the same value as deionised water (1.3330). Therefore, the contribution of RI caused by different streptavidin concentrations is negligible. For the lower concentration of streptavidin (up to 19 nM), the response time of the sensor is less than 10 mins and binding events between biotin and streptavidin were finished after 20 mins. For the concentration above 19 nM, the sensor shows dynamic change of transmission indicating the binding of streptavidin. The slope of the transmission signal increases with increase of streptavidin concentration. This is attributed to the higher association ratio of the binding reaction caused by the higher concentration of reactant (streptavidin). The change of transmission signal at higher concentration (83 nM to 2.7 µM) did not stop within the observed 20mins and shows no saturation even when an additional 10mins is provided. During the one hour reaction at a concentration of 2.7 µM, the transmission signal shows gradual saturation of signal indicating the ending of binding events. The transmission intensity value starts to increase at a concentration of 1.4 µM due to the further development of attenuation band at LP_{019} and its split into two coupled bands moving in opposite directions as RI increases resulting in the increase of the transmission intensity value (illustrated in Fig 6.8b).

The theoretical value of transmission signal of the sensor is calculated using Eq 6.2. The value of parameters (k, M and β) are defined by the means of nonlinear least-squares data fitting [271, 282]. From the calculation based on Solver [282], the best fitting is achieved when the parameters are set as k=0.000001, M=24.8617 and β=0.660836, respectively. Thus, the maximum transmission change and binding constant are 24.8617 and 0.001 $(pM)^{-1}$. Fig 6.8e shows that the transmission change at the central wavelength (850 nm) after 20 mins reaction fits to the Langmuir-Freundlich isotherm. The coefficient of determination R^2=0.9899, $p<0.05$.

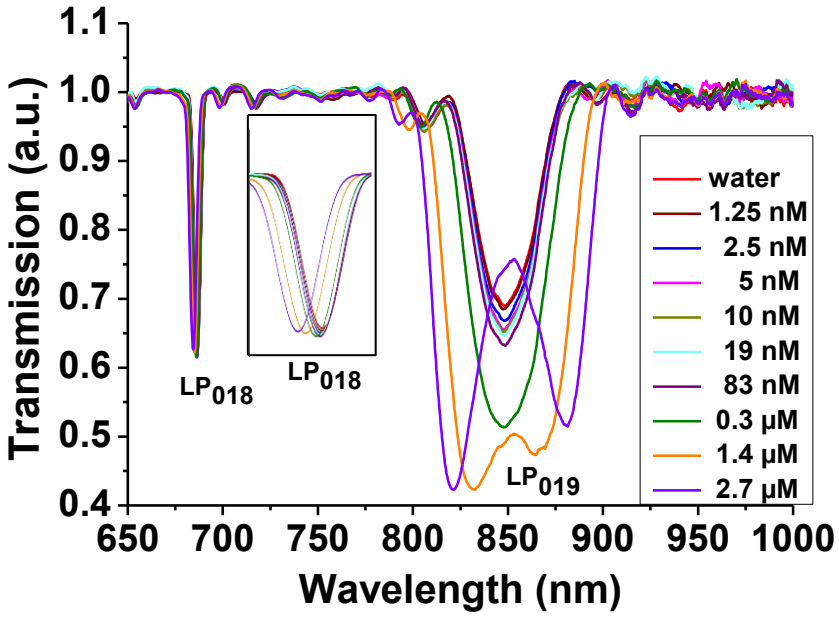
As described in [269], the theoretical surface density of a streptavidin monolayer is 6.4 ng/mm^2 making the sensitivity of the LPG sensor = 3.88 $(ng/mm^2)^{-1}$ based on the calculation from (4). The resolution of the system is defined by the noise level in the blank measurement which is the fluctuation of transmission at the central wavelength (850 nm) in water measurements (Fig 6.8c). The system resolution is two times the standard deviation of the stabilised transmission signal in water (2 × 0.00167=0.00334). The theoretical LOD of the sensor is then calculated as 0.86 pg/mm^2.

The central wavelength at LP_{018} continuously shifts to a lower wavelength as the concentration of streptavidin increase. The dynamic binding can be observed in the same concentration range as the transmission value at LP_{019} (Fig 6.8d). Fig 6.8f illustrates wavelength shift of LP_{018} attenuation band after 20 mins reaction at each concentration and its Langmuir-Freundlich isotherm. The analysis of LP_{018} revealed the same binding constant of 0.001 $(pM)^{-1}$ as compared with the LP_{019} and a maximum wavelength shift of 92.3 nm. The sensitivity and LOD are then calculated as 14.04 $nm/(ng/mm^2)$ and 12.1 pg/mm^2, respectively. The sensitivity is also higher than the highest sensitivity reported in [269] (6.9 $nm/(ng/mm^2)$).

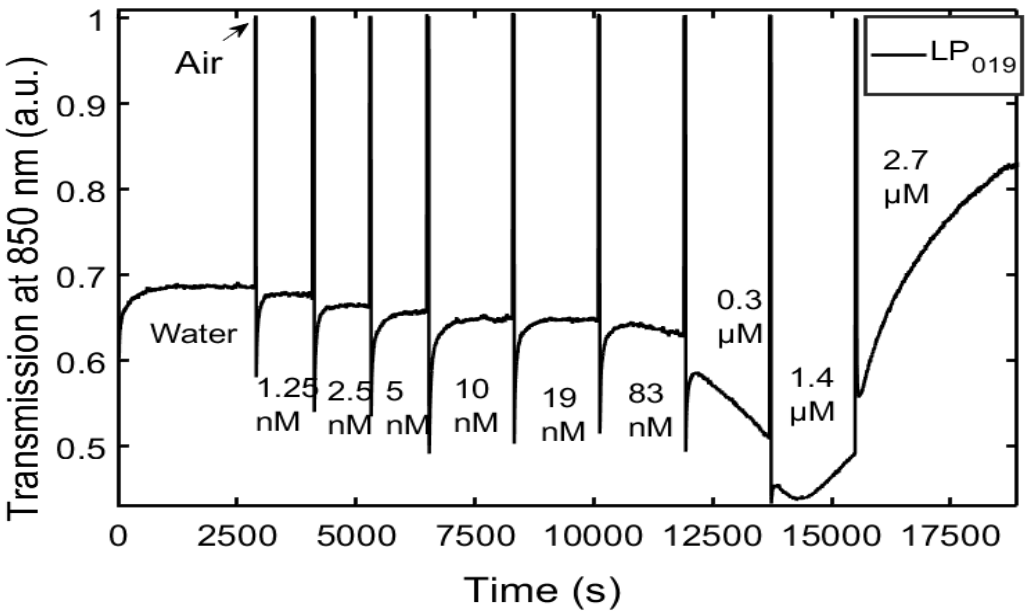
Table 6.1 lists the LOD values between this sensor and that reported in [269]. Compared with the previous sensor [269], the developed sensor has higher sensitivity (3.88 $(ng/mm^2)^{-1}$) and 22 times lower LOD. The main reason of higher sensitivity is attributed to the optimisation of the sensor parameters such as grating period and film coverage.


Transmission (a.u.)
Wavelength (nm)
LP018
LP018
LP019
Water before Biotin
Water after Biotin

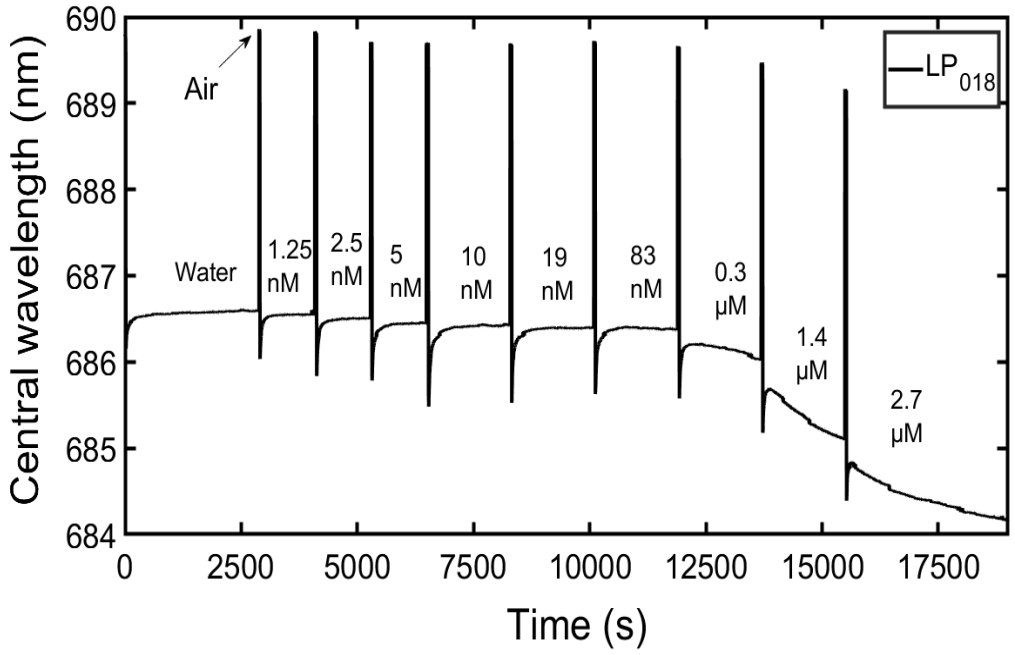
(a)


Transmission (a.u.)
Wavelength (nm)
LP018
LP018
LP019
water
1.25 nM
2.5 nM
5 nM
10 nM
19 nM
83 nM
0.3 µM
1.4 µM
2.7 µM

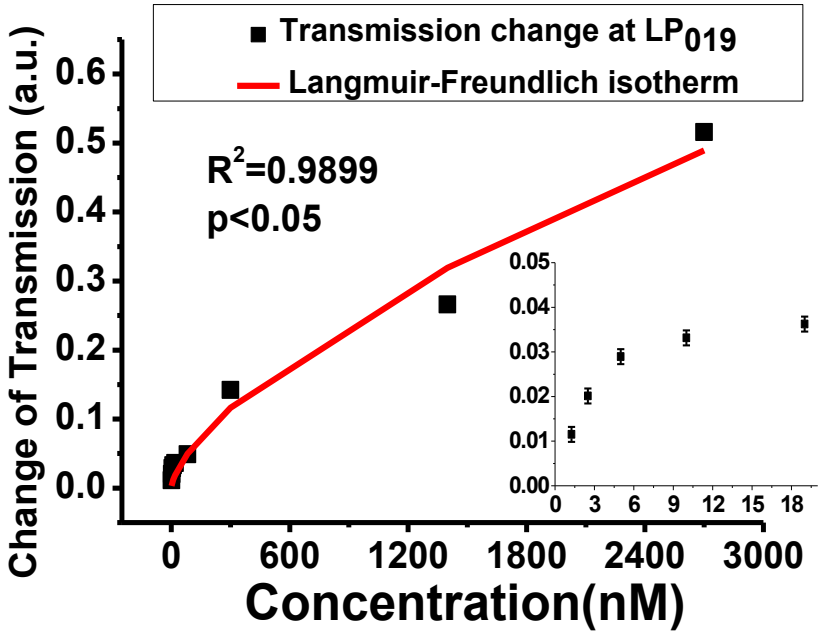
(b)


Transmission at 850 nm (a.u.)
Time (s)
Air
Water
1.25 nM
2.5 nM
5 nM
10 nM
19 nM
83 nM
0.3 µM
1.4 µM
2.7 µM
LP019

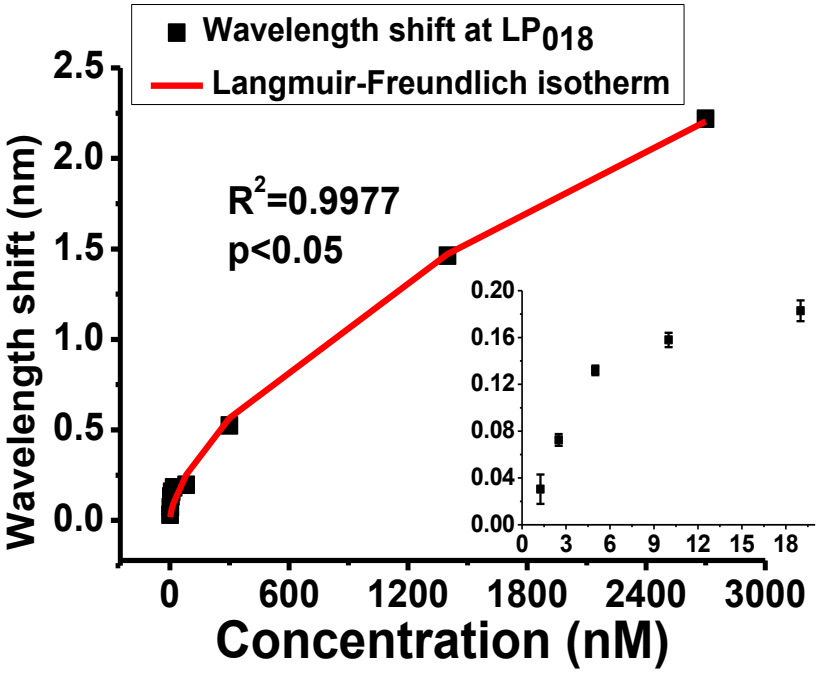
(c)


Central wavelength (nm)
Time (s)
Air
Water
1.25 nM
2.5 nM
5 nM
10 nM
19 nM
83 nM
0.3 µM
1.4 µM
2.7 µM
LP018

(d)



(e)



(f)

Fig 6.8 (a) Transmission spectrum of the LPG measured in water before and after biotin binding. (b) Transmission spectrum of the LPG in different concentration of streptavidin solution. (c) The transmission value at wavelength of 850nm of LP_{019} against time during measurement; the signal was recorded continuously for each measurement of concentration, excluding the wash steps. (d) The wavelength shift of LP_{018} against time during measurement;

(e) Langmuir-Freundlich fit of data. Each data point represents the change of transmission signal after 20min reaction time in different concentrations of streptavidin; the graph inset shows lower concentrations (up to 19 nM), the error bars represent the standard deviation of the signal in blank measurement. (f) Langmuir-Freundlich fit of the data at the wavelength shift of LP_{018}, inset: lower concentration range

The reproducibility of the LPG sensing platform performance relies on the precise fabrication of LPG sensor and functionalisation process that allows the sensor to operate at or close to the phase matching condition. This can be achieved by tightly controlling the laser fabrication process of the LPG sensor [283] and an automation based functionalisation process that helps to reduce the variation of each sensor from manual production of the functional coating by the strict control of immerse time, wash step and drying process [284].

6.4.4 IgM detection

The binding of anti-IgM was obtained via the reaction of the primary amine group of anti-IgM with the succinimidyl ester group presented on the surface of AuNPs. The suspended anti-IgM in solution started to attach on the surface of the LPG sensor, causing a change of RI surrounding the LPG leading to a total wavelength shift of 8.57 nm in the resonance band of LP_{019} (illustrated as Fig 6.9a). The wavelength shift at the resonance band of LP_{019} during the binding of anti-IgM in the solution was observed as a gradual saturation within the 1 hour immersion time (Fig 6.9b).

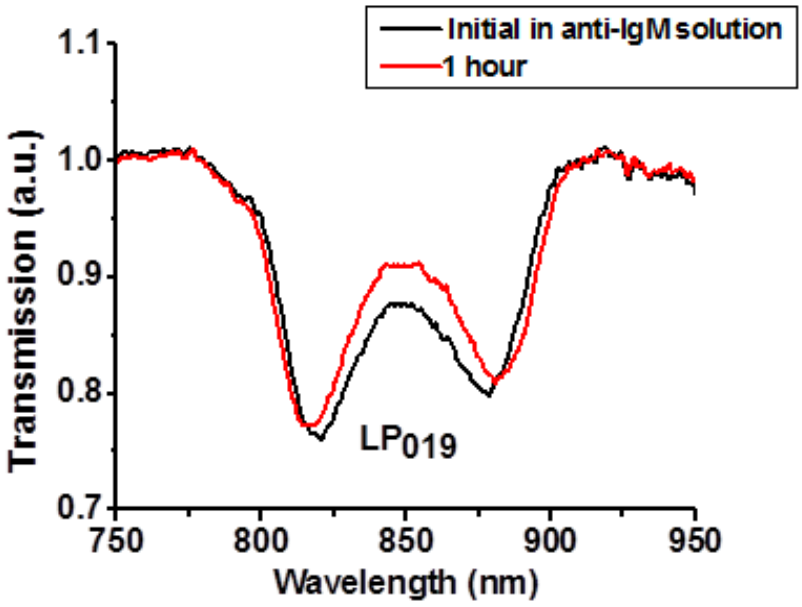
The anti-IgM functionalised LPG sensor exhibits a wavelength shift of 4 nm at LP_{019} during 1 hour of immersion as a result of attachment of BSA on the sensor surface (Fig 6.9c).

Different concentrations of IgM (from 15.6 µg/mL (16.42 nM) to 1mg/mL (1µM)) were detected. The central wavelength of LP_{019} (at 850nm) undergoes an increase in transmission value and the separation of dual bands at LP_{019} gets wider as increasing the concentration (Fig 6.9d). Fig 6.9e shows the separation of dual bands at LP_{019} with time during the measurement of different concentration of IgM. The data for washing steps and immersing process are excluded. The LPG sensor exhibits the immediate response at the presence of IgM in solution. The dynamic binding process

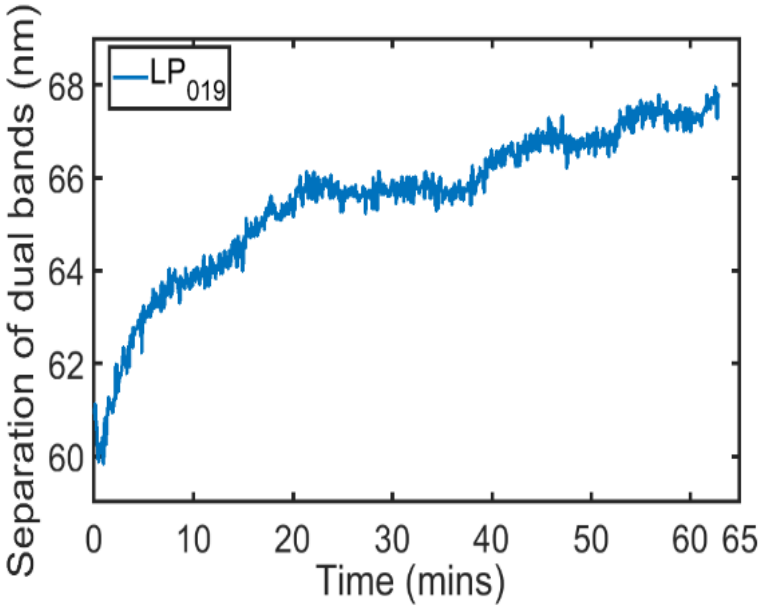
can be observed from each concentration as the wavelength separation of dual bands starts to increase during immersion time of each concentration. A fast binding and the gradual saturation of signal are observed in higher concentration (≧ 125 μg/mL) which indicates the gradual saturation of available binding sites on the sensor surface.

The shift of wavelength at LP_{019} mode introduced by each concentration of IgM fits well to the applied Langmuir-Freundlich isotherm by using the method demonstrated in Eq 6.2 with a coefficient of determination value $R^2 = 0.9965$ (Fig 6.9g) ($p<0.05$). The heterogeneity parameter $\beta = 1$ in Eq 6.2 and the fitting becomes the Langmuir isotherm. The binding constant and maximum wavelength shift are determined as 0.012 $(\mu g/mL)^{-1}$ and 13.72 nm, respectively. The theoretical surface density of an IgM monolayer is 1.26 ng/mm^2 based on the average size of IgM reported by [285] and [286]. Thus, the sensitivity of the LPG for IgM detection is calculated as 11 $nm/(ng/mm^2)$ based on Eq 6.4. The resolution of the spectrometer is 0.17 nm. Thus the LOD is calculated as 0.015 ng/mm^2.

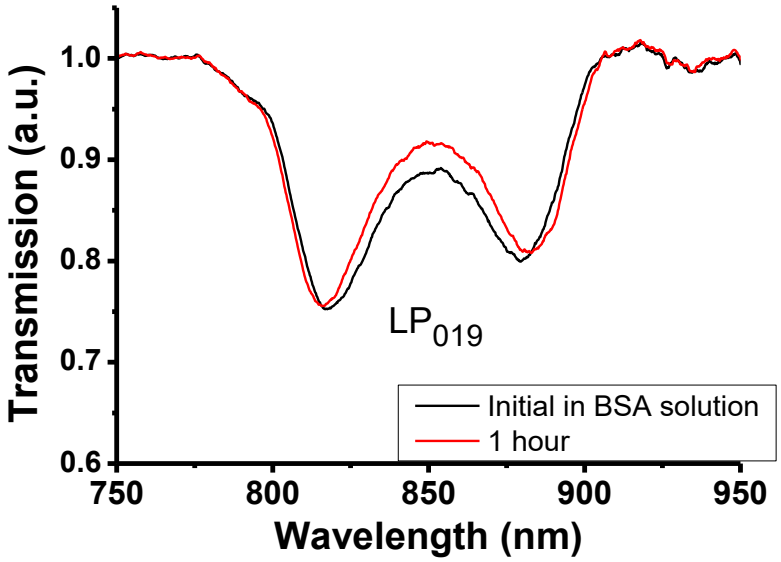
The RI of IgM solution (1mg/mL) is measured as 1.3365 which shows no detected RI difference compared with the blank sample (buffer solution). Therefore, the signal change contributed by the different RI of each tested solution is negligible. The specific binding of anti-IgM with IgM ensures the high specificity of the developed sensor for detection of IgM. BSA was used as a blocking agent to block the potential unspecific binding of biomolecules on AuNPs surface. The prepared IgM sensor was tested in the 1 mg/mL BSA solution that revealed a total shift of 1.14 nm (most likely due to bulk RI change due to very high concentration) in wavelength (Fig 6.9e) which is smaller than the contribution of any tested IgM concentration confirming the specific response of developed sensor to the human IgM (Fig 6.9f).


Initial in anti-IgM solution
1 hour
Transmission (a.u.)
1.1
1.0
0.9
0.8
0.7
LP019
750
800
850
900
950
Wavelength (nm)

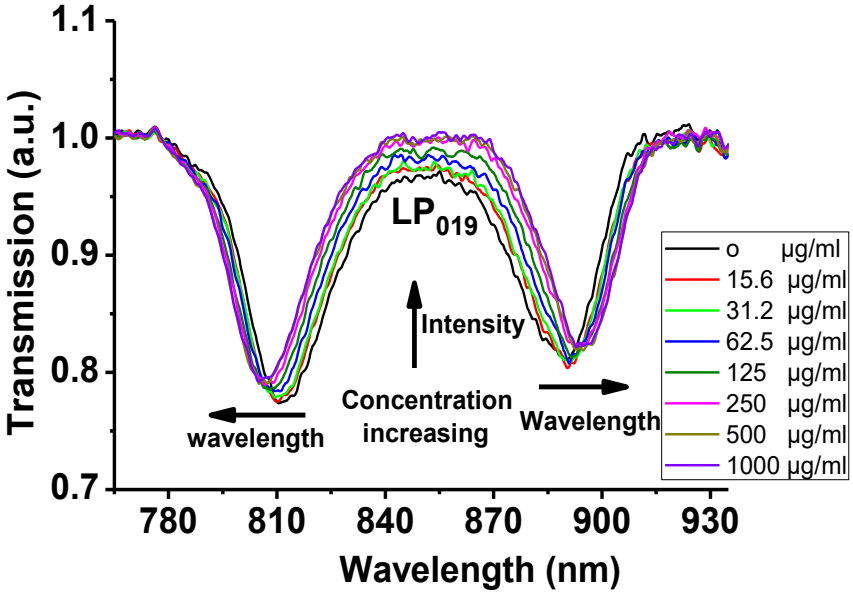
(a)


LP019
Separation of dual bands (nm)
68
66
64
62
60
0
10
20
30
40
50
60
65
Time (mins)

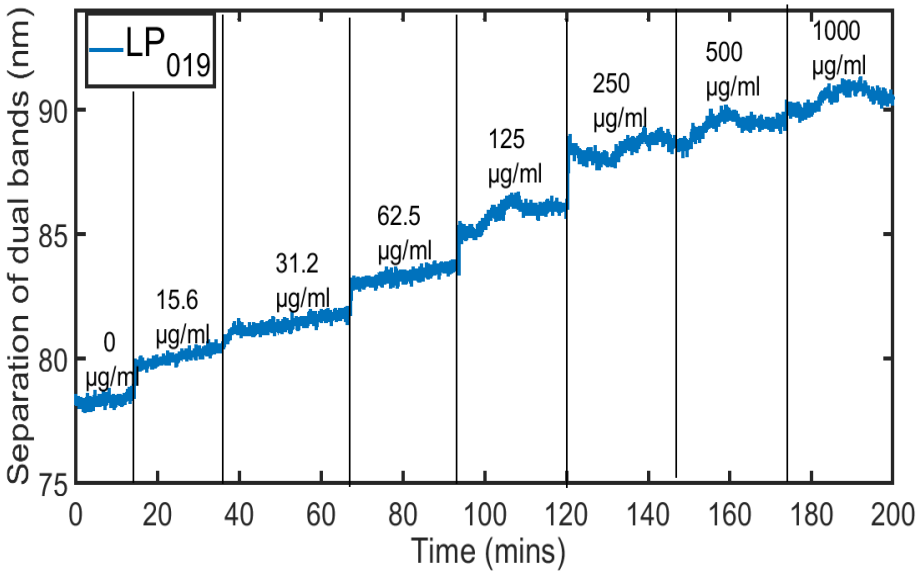
(b)


Transmission (a.u.)
1.0
0.9
0.8
0.7
0.6
750
800
850
900
950
Wavelength (nm)
LP019
Initial in BSA solution
1 hour

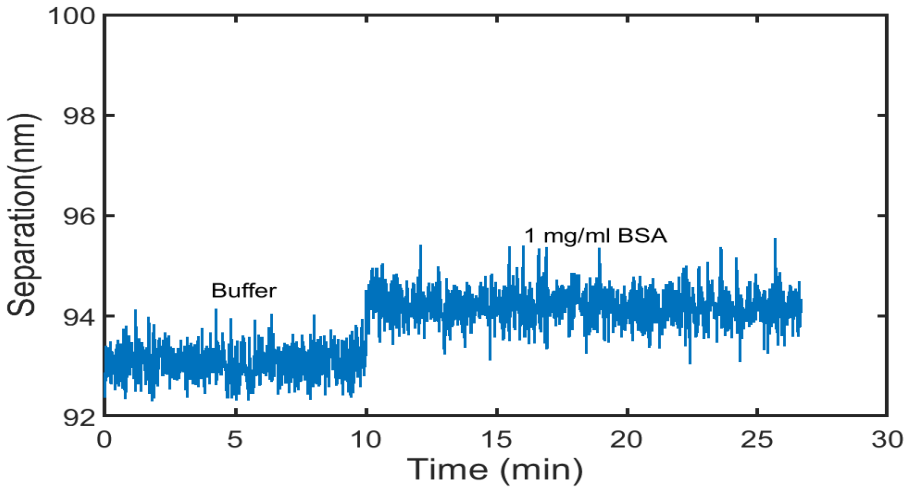
(c)


Transmission (a.u.)
1.1
1.0
0.9
0.8
0.7
780
810
840
870
900
930
Wavelength (nm)
LP019
Intensity
Concentration
increasing
wavelength
Wavelength
o µg/ml
15.6 µg/ml
31.2 µg/ml
62.5 µg/ml
125 µg/ml
250 µg/ml
500 µg/ml
1000 µg/ml

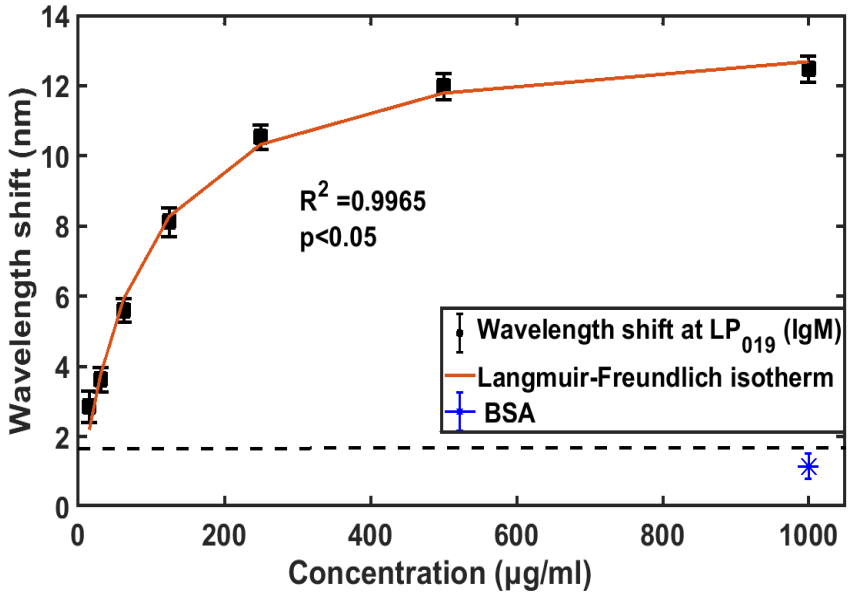
(d)


LP 019
Separation of dual bands (nm)
Time (mins)
0 µg/ml
15.6 µg/ml
31.2 µg/ml
62.5 µg/ml
125 µg/ml
250 µg/ml
500 µg/ml
1000 µg/ml

(e)


Separation(nm)
Time (min)
Buffer
1 mg/ml BSA

(f)



(g)

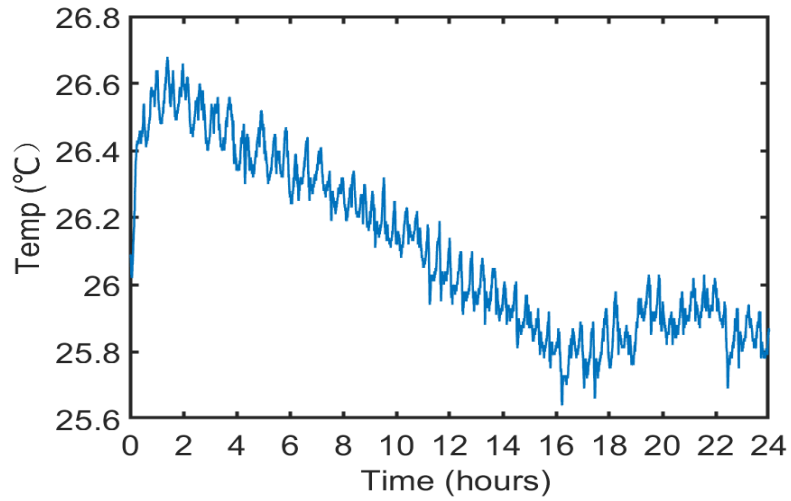
Fig 6.9 (a) Transmission spectrum of the LPG in anti-IgM solution before and after binding. (b)Wavelength separation of LP_{019} as a function of time during functionalisation of anti-IgM. (c) Transmission spectrum of the LPG in BSA solution. (d) Transmission spectrum of the LPG in different concentrations of IgM. (e) The separation of dual bands at LP_{019} in response to the different concentration of IgM suspension solution. (f) Wavelength separation of the LPG at blank (buffer) and 1 mg/mL BSA solution. (g) Langmuir isotherm fit of data. Each point is the average wavelength shift of the last 5 mins reaction in each concentration. The error bars represent the standard deviation for the stabilised signal in each testing solution. The sensor response for 1 mg/mL BSA is labelled as a comparison for evaluation of sensor specificity.

Table 6.2 shows the comparison of the developed LPG IgM sensor with other reported IgM biosensors. The developed LPG sensor has comparable performance in terms of LOD to SPR [287]. Among these types of sensors, the LPG sensor is the only one that is low cost, high sensitivity and has label-free operation. The IgM levels reported in adults and children with SIgMD are 29.7 ± 8.7 mg/dL (mean ± SD) and 16.5 ± 13.8 mg/dL (mean ± SD) [288, 289]. In the developed sensor, the concentration range detected is from 1.56 mg/dL to 100 mg/dL. The developed sensor exhibited the capability of detecting IgM levels in a wide range concentration and is useful in screening SIgMD (<20 mg/dL) and diagnosis of neonatal infection (> 20 mg/dL).

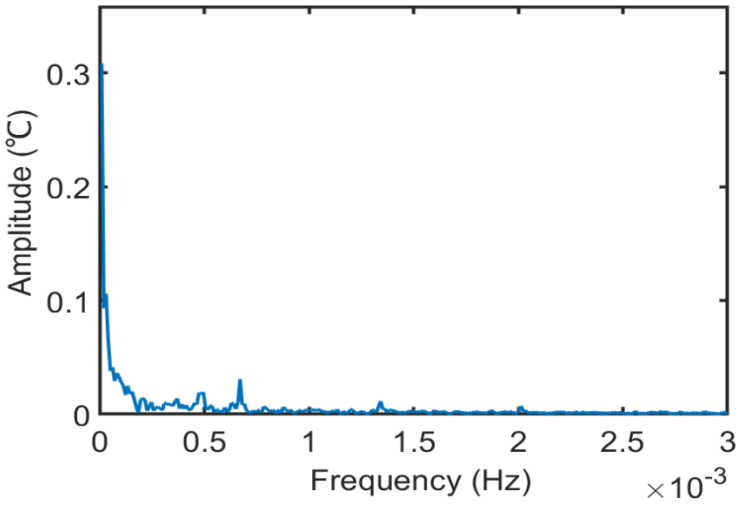
Besides, the ability of dynamic monitoring the binding process supports the application of the sensor in POC diagnostics.

For IgM detection, the LPG with the same grating period and coating thickness as for streptavidin detection is used. However, the IgM experiment is conducted in buffer solution with a slightly higher RI (1.3365) than the water (1.3330) used in the streptavidin experiment causing the change in the transmission spectrum. The LOD when using the transmission of central wavelength as signal is 97 pg/mm^2 which is higher than the value of wavelength shift (15 pg/mm^2).

In order to achieve the optimal phase matching condition, the grating period of LPG sensor, sensor functionalisation process as well as the working environment such as solvent of target molecules and temperature of sample need to be taken into account when designing such biosensor. Among those parameters, the LBL coating process described in this chapter is a reliable and repeatable coating process. If the working environment parameters (e.g. RI and temperature) are known, the optimal sensor performance can be achieved by properly design the right grating period of LPG sensor based on the provided working environment parameters. The results presented in the Chapter were achieved in a temperature regulated lab condition in which the temperature cross-sensitivity is neglected (according to the measured data Fig 6.10). Fig 6.10b illustrates the result of the temperature data in Fig 6.10a after taking fast Fourier transform (FFT) algorithm. The DC signal has been removed from the figure. The amplitude in the graph represents the temperature variation which may contribute to the noise level of the LPGs. The biggest spike is about 0.3 ℃ but with a frequency of 10^{-5} Hz which is believed not affecting the LPG response due to either small amplitude or low frequency. The temperature is therefore considered as constant for LPG sensor. However, in the practical application, temperature will always need to be taken into account. A reference LPG sensor can be added to compensate the temperature effect as well as the bulk RI induced signal change [290].



(a)



(b)

Fig 6.10 (a) Temperature fluctuation of 24 hours in the temperature regulated lab; (b) Frequency distribution of the temperature signal in (a) after removing the DC.

6.4.5 IgM detection in blood serum

Blood serum of a healthy adult human contains IgM concentration range from 0.4 to 2.3 mg/mL (0.4 -2.42 µM). Fig 6.11 shows the wavelength separation of dual bands at LP_{019} at different samples. The wavelength signal shows a step change and dynamic increasing of separation in blood serum indicating a gradual binding of IgM in serum. As increase of IgM concentration, there is a saturation of signal due to the saturation of available binding sites (anti-IgM). However, the level of IgM in blood serum is

unknown so that the exact concentration of IgM in the four tested samples are not clear.

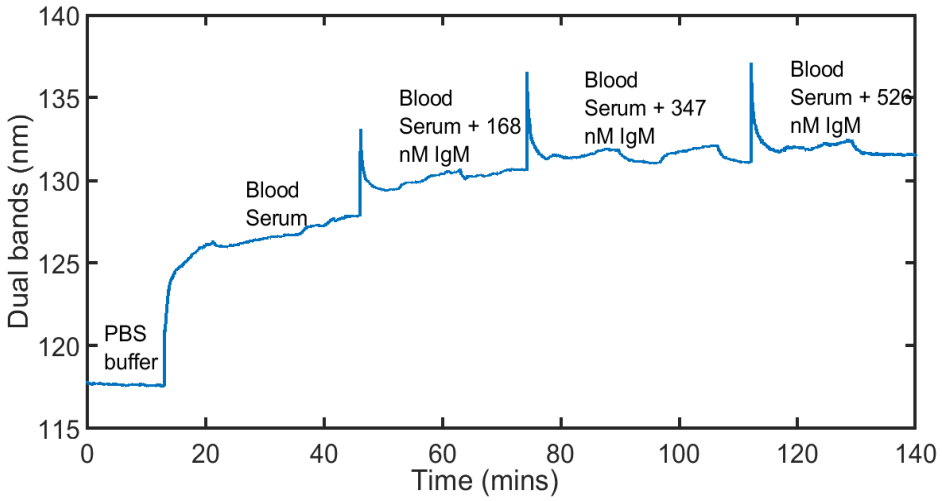


Fig 6.11 The wavelength separation of LPG at LP_{019} for the response of 4 blood serum samples.

6.5 Conclusion

An LPG optical fibre-based sensor coated with a film comprising three layers of PAH/SiNPs with gold shell for detection of streptavidin and IgM was constructed. The data for binding events fit the Langmuir isotherm. The LPG sensor operating close to phase matching condition shows a high sensitivity of 3.88 $(ng/mm^2)^{-1}$ with a detection limit of 0.86 pg/mm^2 for the detection of streptavidin. The minimum detectable concentration of streptavidin is 1.25 nM. The sensor performance has been improved compared to the previous best performance for this type of sensor reported by [269] (LOD: 19 pg/mm^2, minimum detected concentration: 19nM) due to the selection of the LPG sensitive working region and improvement of the uniformity of the coating surface.

The LPG sensor also demonstrates the capability of detecting human IgM with a sensitivity of 11 nm / (ng/mm^2) and an LOD of 15 pg/mm^2 in buffer solution. The low cost, real-time detection, high specificity would enable the sensor to be applied in clinical POC for the diagnosis of IgM related diseases. The LPG sensor was tested in the blood serum sample and exhibits a response to the increase of IgM concentration. Due to the lack of a gold standard method to verify the concentration of IgM in the blood serum sample, the exact concentration of four tested sample remains unclear.

Table 6.1. Comparison of developed sensor with sensor in [269].

References	Type of sensor	Type of film	Uniformity of film	Type of protein detection	LOD
[269]	LPG sensor at PMTP (Wavelength shift)	Silica core gold shell NPs	Poor	Biotin-streptavidin	19 pg/mm^2
Developed sensor	LPG sensor close to PMTP (Change of transmission)	Silica core gold shell NPs	Good	Biotin-streptavidin	0.86 pg/ mm^2

Table 6.2. List of biosensors for the detection of IgM.

Reference	Type of sensor	Analyte (target)	Sensitivity	LOD
[287]	Surface Plasmon waveguide	IgM antibody	N/A	12 pg/mm^2
[291]	chemiluminescent optical fibre immunosensor (OFIS)	IgM antibody	98.1%	1:10^6 dilution
[292]	Giant Magnetoresistance (GMR)	IgM antibody	50 ng/mL	N/A
Developed sensor	LPG sensor	IgM antibody	11 nm/ (ng/mm^2).	15 pg/mm^2

Chapter 7 Development of FOS for the measurement of CO_2 & RH from breath

7.1 Introduction

Chapter 2 introduced the typical configuration of an FOS, film deposition techniques and the working principle of pH indicators for the measurement of CO_2. In this Chapter, optical fibre-based CO_2 sensors are fabricated by the combination of an optical fibre coupler with a CO_2 sensitive film which contains a matrix film doped with pH indicator (thymol blue) and phase transfer agent (TMAH). Ethyl cellulose (EC) and organically modified silica (Ormosil) were used as the matrices for the thymol blue. Ormosil is a product formed by the sol-gel process (described in Chapter 2). It generally has better properties than polymers regarding resistance of mechanical force and heat [293]. The response time of such sensors depends on the permeability and the thickness of the film. The EC film is prepared by coalescing the chain polymer into a network structure with a plasticiser. A Fabry–Pérot interferometer (FPI) sensor is fabricated by controlling the thickness of the Ormosil film via the dip coating process. The film doped with thymol blue and TMAH is used for the sensing of CO_2 through the change of reflection value at a specific wavelength, and the wavelength of the FPI peak is found to be sensitive to the atmospheric RH.

This Chapter investigates key steps required to turn these sensors into useful measurement tools in end-tidal CO_2 ($ETCO_2$) monitoring specifically regarding sensor longevity, dye concentration, response time and cross-sensitivity to temperature and humidity. The tip-based CO_2 sensor significantly reduces the size of the sensing area (125 µm diameter) and has more flexibility in real-world application compared with evanescent field sensors previously proposed [68] (10 cm length of the sensitive region). It has been reported that sensors based on pH-sensitive dyes completely lose sensing capability after ~1 week, which may be attributed to the thermal degradation of the quaternary ammonium hydroxide catalyst or photobleaching of the dye compound [69, 70]. It is demonstrated in the Chapter that appropriate storage methods can be used to extend longevity significantly. The prepare FPI sensor is

exclusively sensitive to two parameters (CO_2 and RH) with a neglectable cross-talk demonstrating the capability in simultaneously measuring CO_2 and relative humidity (RH) from human breath. The results reported in this chapter, section 7.3 have been published in [294].

7.2 Method

7.2.1 Sensing mechanism for CO_2

Thymol blue, as a pH indicator, has two detectable ranges [295] . Its colour transitions from red to yellow when the pH rises from 1.2 to 2.8 and from yellow to blue at pH 8.0-9.2. The colour transition during the reaction of CO_2 can be explained by:

$$QOH + HT\ (red) \rightleftharpoons Q^+T^-\ \cdot xH_2o(blue) \quad (7.1)$$

$$CO_2(g) \rightleftharpoons CO_2(aq) \quad (7.2)$$

$$\{Q^+T^-\ \cdot xH_2o\}(blue) + CO_2(aq) \rightleftharpoons Q^+HCO_3^-\ \cdot (x-1)H_2o + HT(yellow) \quad (7.3)$$

Where HT is the acidic form of thymol blue, QOH is TMAH, Q^+ is a tetramethylammonium ion and T^- is the deprotonated thymol blue. $Q^+T^-\ \cdot xH_2o$ is the ion pair formed between acidic thymol blue and TMAH in the matrix film that causes the colour change due to change of protonation status (Eq 7.1). The formation of the ion pair and the above sensing mechanism have been confirmed and proposed by Mills et al. [296]. Gas phase CO_2 (g) transitions into aqueous CO_2 (aq) when it permeates from outside into the matrix film. CO_2 (aq) reacts with the hydrated water molecule (H_2O) to form carbonic acid (H_2CO_3) which further dissociates into a bicarbonate ion (HCO_3^-) and a hydrogen ion (H^+). The latter converts the T^- into protonated status HT as illustrated in Eq 7.3 and the colour turns from blue to yellow correspondingly.

7.2.2 Sensing mechanism for RH

As illustrated in Fig 7.1, the sensitive layer that is dip coated on the tip of the optical fibre forms an FP cavity with a length of few micrometres (~6µm, measured from Fig 7.3a). The light transmits from the fibre into the film and from the film into air and reflection occurs at each interface (differential RI medium) on its pathway.

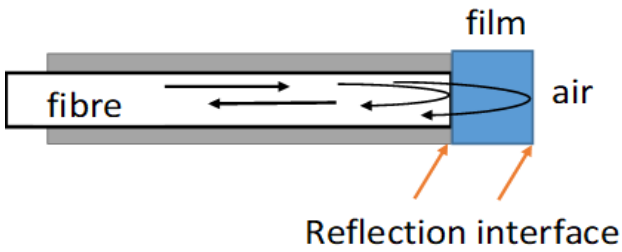


Fig 7.1 Schematic of the FPI sensor.

Due to the differential phase of the reflected light between the two interfaces, interference fringes can be observed when the thickness of the coated film is less than the coherence length of the light source. The phase difference of the FPI can be simplified as Eq 7.4:

$$\partial_{FPI} = \frac{2\pi}{\lambda} n2L \tag{7.4}$$

Where λ is the wavelength of incident light, L is the thickness of the film and n is the RI of the cavity material. The reflection spectrum can be described as wavelength dependent intensity output, the intensity of FPI at a particular wavelength are in-phase and out-of-phase resulting in a maximum and minimum peaks in the reflection spectrum. When a perturbation is introduced to the FPI such as a change of RI, the phase difference is changed with the variation in optical path length of the interferometer. The change of phase difference is observed as a shift of the wavelength of the interference fringes in the reflection spectrum, and the degree of the perturbation can be quantitatively correlated to the shift in wavelength. When increasing the atmospheric RH level, the water molecules are adsorbed by the unreacted hydrophilic silanol group (Si-OH) of the sol-gel film leading to a change of RI of the sol-gel film. As a result, the phase difference of the two interference beams of the FPI is changed and the interference fringes undergo a shift.

7.2.3 Determination of the sensor parameters

The geometry of the coated film on the fibre tip was imaged and measured using scanning electron microscopy (SEM) (JEOL 7100F, UK). The fibre with the coated film was cut into a 4 cm length from the tip and mounted horizontally in SEM stubs. The

sample was then coated with an 8 nm thick layer of Iridium using a sputter coater (Quorum and Polaron, UK) to increase the conductivity for electrostatic discharge.

The RI of the prepared CO_2 sensitive film was measured by a Spectroscopic Ellipsometer (alpha-SE, J.A.Woollam, US). A silicon wafer was cut into 1 cm wide pieces and dip coated with the film and dried in air after 24 hours before the measurement. The measurement is taken at three different positions of the coated substrate for obtaining the RI value. And the final value presented is the average value of the three times measurement.

The thickness of sensing film of the FPI sensor can be calculated using Eq 7.5:

$$L = \frac{\lambda_1 \lambda_2}{2n(\lambda_2 - \lambda_1)} \tag{7.5}$$

where *L* is the thickness of the film (cavity length), *n* is the RI of the film, λ_1 and λ_2 are the central wavelength of two adjacent inteference peaks.

The reflection value that described in this Chapter is defined as:

$$R = \frac{I_0}{I_1} \times 100\% \tag{7.6}$$

Where I_1 is the intensity of light that is reflected from the fibre tip when there is no film present and I_0 is the intensity of the light after interaction with the coated film. The absorbance is calculated from R using:

$$\text{Absorbance} = 2 - \log_{10} R \tag{7.7}$$

The sensitivity of the FOS is defined as the magnitude of the reflection change per unit of a given target analyte, in this case, CO_2 concentration.

The response time and recovery time of the FOS is calculated as the time between the 10% of the signal change to the 90% of the signal change.

7.2.4 Experimental set-up

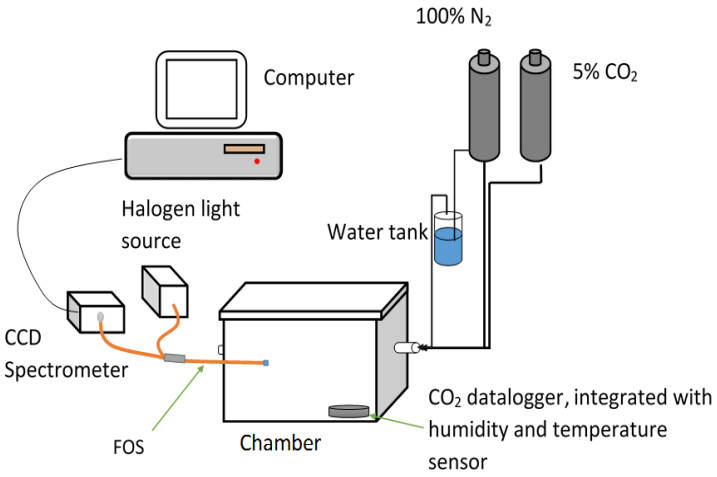
The reflection absorption spectrum of the FOS was measured using the set-up illustrated in Fig 7.2a utilising a multimode 1x2 optical fibre coupler (F-CPL-M12855, Newport, UK). A halogen light source (HL-2000, Ocean Optics, UK) illuminates the tip

and the reflected light is detected using a CCD spectrometer (USB 2000, Ocean Optics, UK) which is connected to a computer for post-processing.

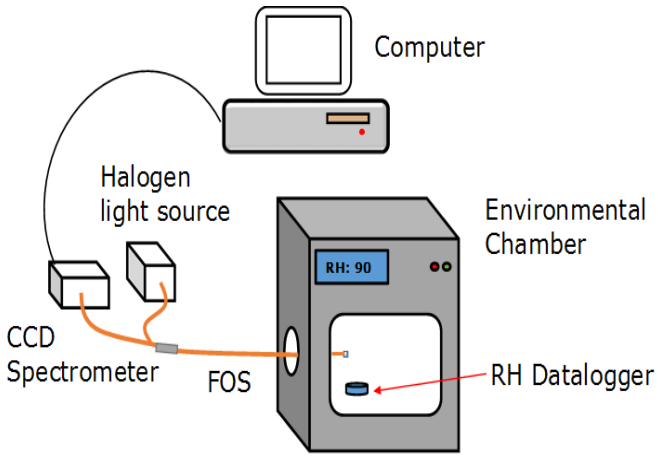
The FOS is placed inside a gas chamber (15 cm (L) ×13 cm (W) ×8 cm (H)) which has an input channel and output channel for gas infusion and expulsion respectively. A commercial CO_2 datalogger integrated with a humidity and temperature sensor (K-33 BLG, CO_2 Meter, USA) was positioned inside the chamber for calibration purposes. The concentration of CO_2 inside the chamber is regulated by mixing N_2 and CO_2 gas. For the humidity cross-sensitivity test, humidity is regulated by flowing humidified N_2 /CO_2 created by bubbling the gas in distilled water into the chamber (Fig 7.2a).

Due to the limitation of the set-up for generating very high RH level, the FOS was also tested in an environmental chamber (Bench Top, C-TH40-20/1, Climatic Ltd, UK) for the RH calibration at a high level (up to 100 %) (illustrated in Fig 7.2b). A humidity datalogger (iButton Hygrochron Temperature/Humidity datalogger, DS1923, Maxim Integrated Ltd) was placed inside the chamber along with the FOS to provide the real-time RH and temperature reading. The light source and spectrometer were used the same as introduced previously in Fig 7.2a.

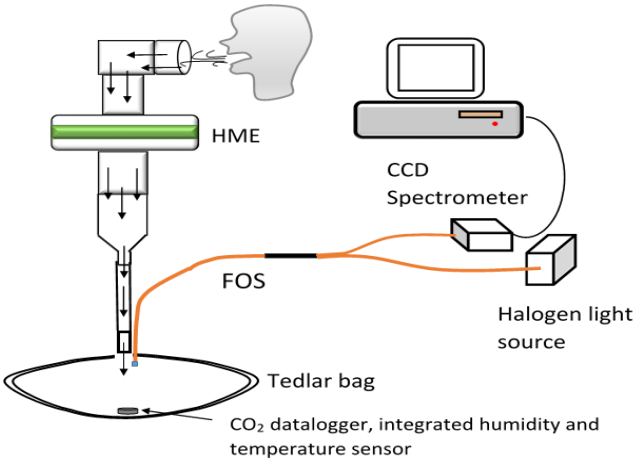
Fig 7.2c shows the set-up for measuring the CO_2/RH level from the breath by using the developed FOS. The tip of the fibre sensor is inserted in a Tedlar bag (2 litres, Sigma-Aldrich, UK) through a syringe needle (inner diameter: ~1 mm), and the CO_2 datalogger (K-33 BLG, CO_2 Meter, USA) is sealed into the Tedlar bag to provide a reference for the CO_2 and RH value before and after breathing. A heat moisture exchanger (HME) (Clear-ThermTM 3, Intersurgical Ltd, UK), typically used in mechanical ventilators [297], was applied behind the mouthpiece to prevent the condensation of humidity after the breath gas leaving from the human body (37 ℃) to ambient temperature (22 ℃). The light source and spectrometer were used, the same as introduced previously in Fig 7.2a.



(a)



(b)



(c)

Fig 7.2 (a) Schematic illustration of the experimental setup for FOS CO_2 calibration. Orange line - optical fibre. A commercial CO_2 datalogger was placed inside the chamber for recording

the CO_2 and humidity inside the chamber. (b) The set-up for the RH calibration (RH>50%) of FOS by using environmental chamber. (c) The set-up for the measurement of breath CO_2 and RH by using FOS.

An alternative set-up used to measure response time replaces the gas chamber with a Tedlar bag (2 litres, Sigma-Aldrich, UK) which was filled with the CO_2 gas with concentration ~6% into which the FOS was inserted and removed.

7.3 Fibre-optic sensor (FOS) for the CO_2 measurement

7.3.1 Experimental procedure

The prepared sensor is calibrated using the set-up shown in Fig 7.2a. The chamber is initially filled up with 100 % N_2, and then the concentration of CO_2 is gradually built up in the chamber from 0 up to 6% by controlling the CO_2 gas flow. The reflection spectrum of FOS and the reading from CO_2 datalogger are recorded simultaneously for all the tests.

For the RH cross-sensitivity test, the CO_2 and RH level inside the chamber (Fig 7.2) was initially brought down close to zero by filling up the chamber with dry N_2, and then flowing distilled water bubbled N_2 into the chamber to gradually increase the RH level step by step and maintain the CO_2 at an undetectable level (<20 ppm). For investigating the effect of RH to the interaction of CO_2 with sensitive film, the humidity level in the chamber is brought down to zero again with dry N_2, and then the chamber is filled up with about 6% of CO_2, and continuously flowing distilled water. CO_2 is bubbled into the chamber to increase the RH level and maintain the concentration of CO_2 at a stable value (~6%).

For evaluating temperature effect on the FOS in response to CO_2, the FOS and the CO_2 data logger are placed inside the gas chamber that is initially filled with~6% CO_2. The chamber is then put into an oven with temperature programmed to increase from 25 to 40 ℃ (this range of temperature covers both ambient and physiological temperature of the human body).

The response/recovery time test of the FOS to CO_2 is conducted by inserting the tip of the sensor into a Tedlar bag which is filled with 6% of CO_2, waiting until the signal

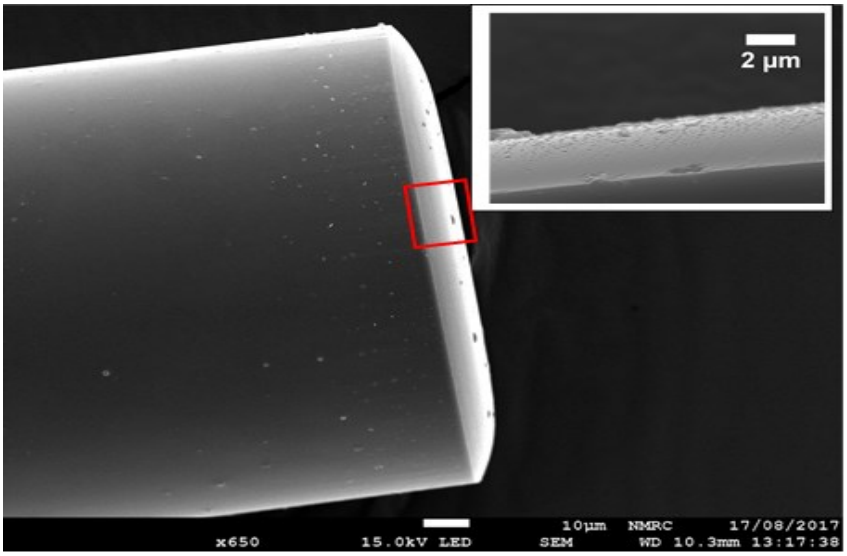
saturates and then removing the sensor back to ambient. The process is repeated for three times for achieving the average value.

7.3.2 Results and discussion

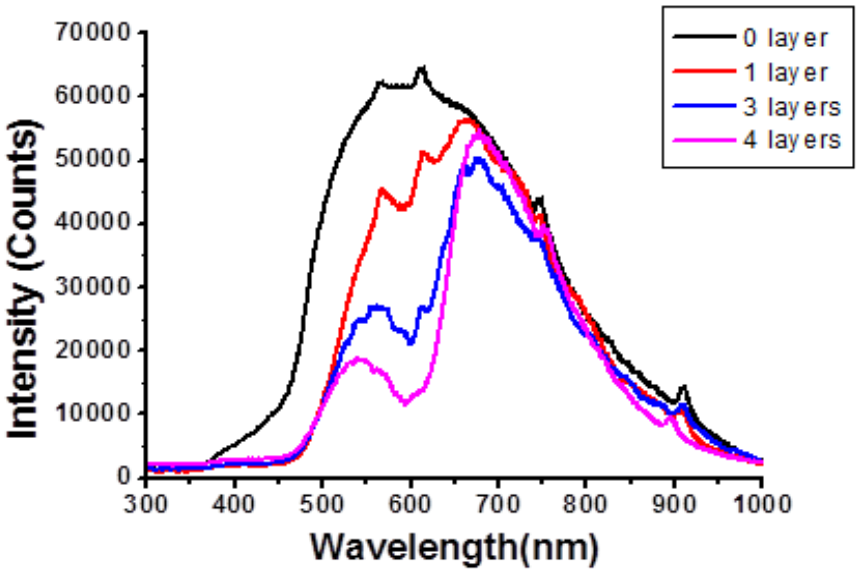
7.3.2.1 FOS fabricated with sol-gel film

7.3.2.1.1 Characterisation of FOS

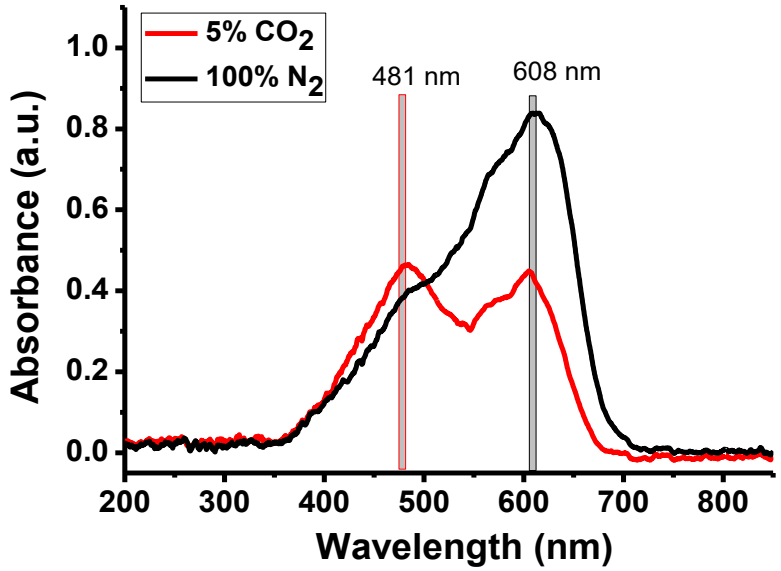
Fig 7.3a shows an SEM image of the optical fibre tip with four layers of dip-coated film. It confirms that the film is successfully deposited on the tip of the optical fibre with a film thickness of approximately 2.7 ± 0.1µm. The reflected intensity at 608 nm decreases as each layer is deposited (Fig 7.3b) due to the higher absorption value caused by the thick film based on Lambert's law. A single dip coating is observed to have lower absorption value due to the thinner film. This is not suitable for the application as insufficient colour change is produced after interacting with CO_2. The absorption spectra of the FOS under CO_2 free (100% N_2) and 5% CO_2 are illustrated in Fig 7.3c. Two absorption peaks appear at wavelengths of 450 nm and 608 nm and the two peaks respond oppositely to the change of CO_2 concentration; the peak at 608 nm undergoes a decrease in the absorbance value at 5% CO_2 and the peak at 481 nm increases its absorbance value at 5% CO_2 atmosphere. Because the change of absorbance at wavelength of 608 nm is bigger than the wavelength of 481 nm, the wavelength of 608nm is therefore used for the measurement of CO_2. As the reflection is correlated to the absorbance in Eq 7.7, the reflection value of 608 nm is then used as the optical signal for the CO_2 measurement. The reflection value of 481 nm can be used for self-reference. The signal using the difference in the reflection value of the two wavelengths or the ratio of the reflection value would be beneficial for the measurement as they would provide a higher sensitivity to CO_2 than signal wavelength due to the opposite change between the two wavelengths.


2 µm
x650
15.0kV LED
10µm NMRC
SEM
17/08/2017
WD 10.3mm 13:17:38

(a)


0 layer
1 layer
3 layers
4 layers
Intensity (Counts)
Wavelength(nm)
70000
60000
50000
40000
30000
20000
10000
0
300
400
500
600
700
800
900
1000

(b)



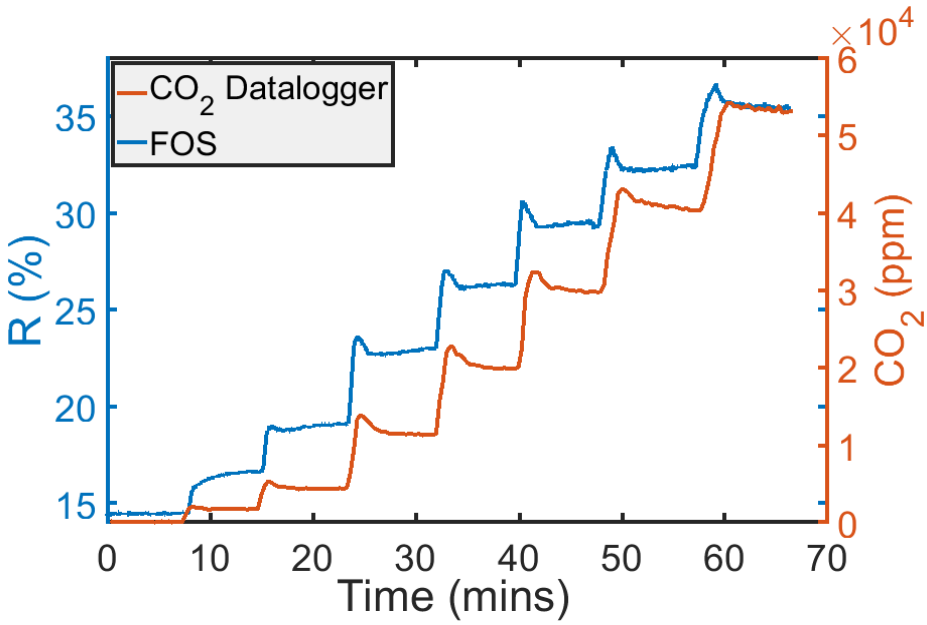
(c)

Fig 7.3 (a) SEM of the 4-layer dried film on the tip of optical fibre; the average film thickness measured at 10 different positions on the film in the inset is 2.78 ± 0.1µm. (b) Reflection spectrum of FOS for 0 layer, 1 layer, 3 layers and 4 layers coating after drying. (c) Absorption spectra of FOS under N_2 and CO_2 atmosphere; FOS was coated with 4 layers and dried in air for 24 hours. The absorbance value is calculated as Eq 7.7.

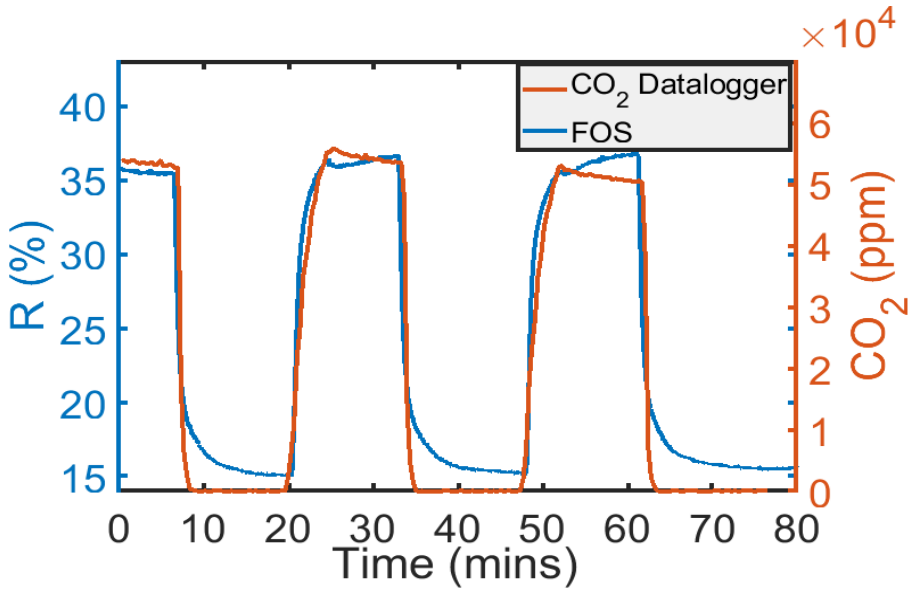
7.3.2.1.2 CO_2 sensor response and repeatability

Fig 7.4a shows a typical step response of the FOS (prepared using a thymol blue concentration of 4.2 mg/mL) to the concentration of CO_2 that was measured using the set-up shown in Fig 7.2a. The reflection intensity (at 608 nm) changes in accordance with the change of CO_2 concentration from the commercial CO_2 datalogger. The reflection of the FOS increases (absorbance decrease) with increasing CO_2 concentration from 0-60000 ppm (6%). RH in the measurement chamber remains stable at a level of 13 ± 1 % during the measurement of CO_2. The reflection value decreases as the CO_2 concentration decreases and the FOS exhibits a repeatable and reversible response as illustrated in Fig 7.4b. The reversibility of the sensor is determined by the equilibrium in Eq 7.3, in which a decrease of CO_2 concentration around the FOS causes a left-side shift of the equilibrium. And as a result, the number of protonated thymol blue is reduced. Fig 7.4c shows the reflection value of 481 nm response to the concentration of CO_2. It shows a step

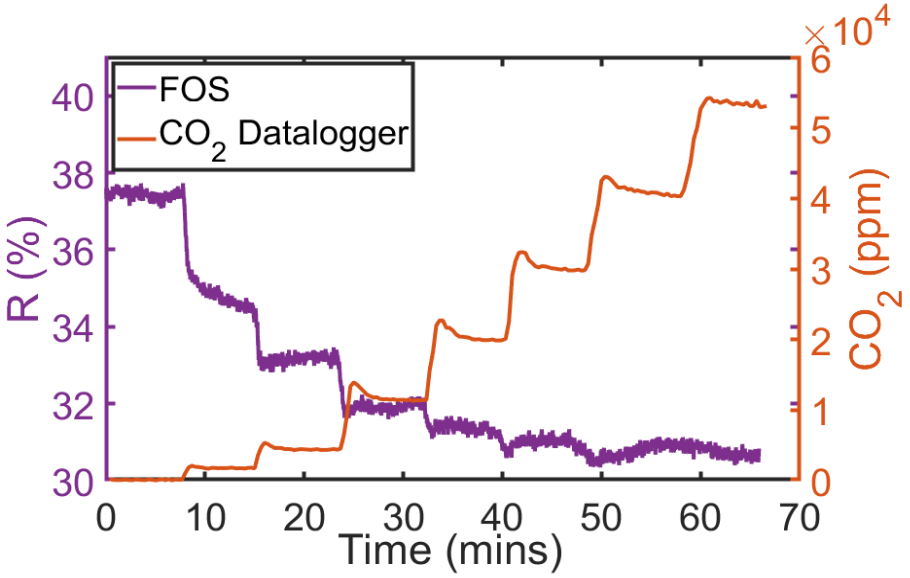
decrease in the reflection value as the concentration of CO_2 increases step-by-step, which is an opposite change to the wavelength of 608nm. The reflection value of the two wavelengths is related to the CO_2 concentration via a polynomial as shown in Fig 7.4d. The wavelength of 608 nm demonstrates a higher sensitivity to CO_2 than that of 481 nm. The FOS has a response time of 19 s when the FOS was exposed to a 6% of CO_2 atmosphere from ambient air (~400 ppm) and a recovery time of 170 s when the sensor is exposed to ambient air (Fig 7.4e). This indicates that the affinity for the backward reaction of the equilibrium in Eq 7.3 is lower than it is for the forward reaction. Fig 7.4f shows the sensor response to CO_2 by using the ratio of the reflection value of the two wavelengths (608 nm against 481 nm). The use of the ratio may potentially overcome the drifting of the optical signal caused by the light source or the change of the baseline signal caused by the massive bending of the optical fibre in the real world application.



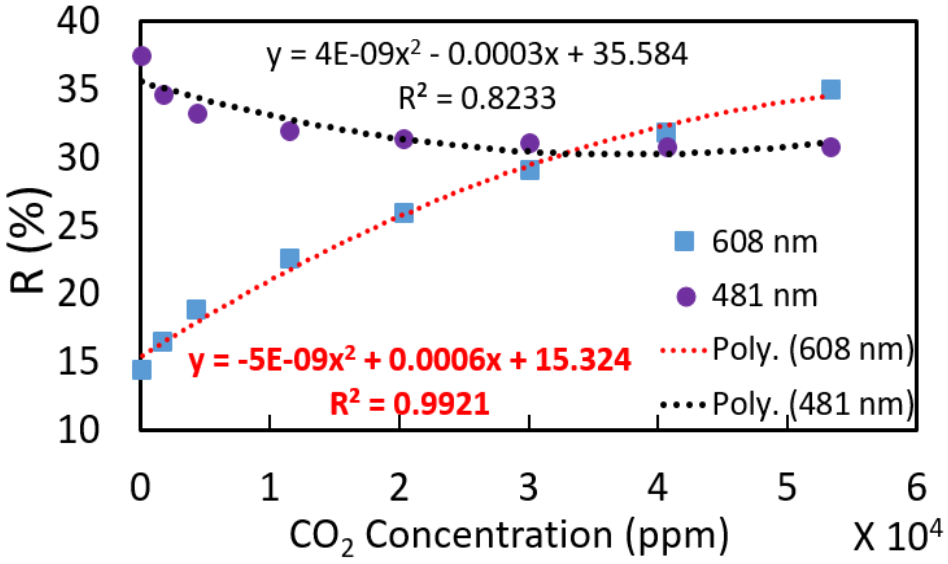
(a)


×10^4
CO2 Datalogger
FOS
R (%)
CO2 (ppm)
Time (mins)

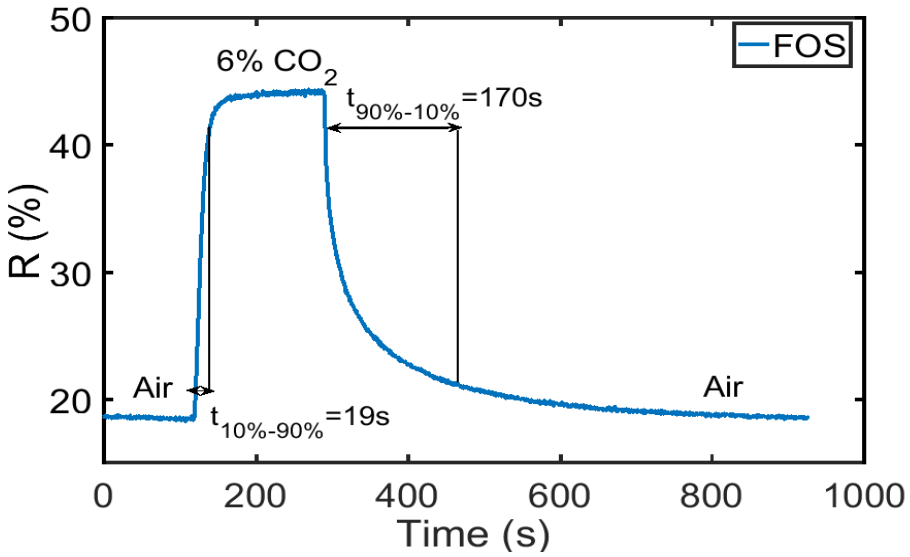
(b)


×10^4
FOS
CO2 Datalogger
R (%)
CO2 (ppm)
Time (mins)

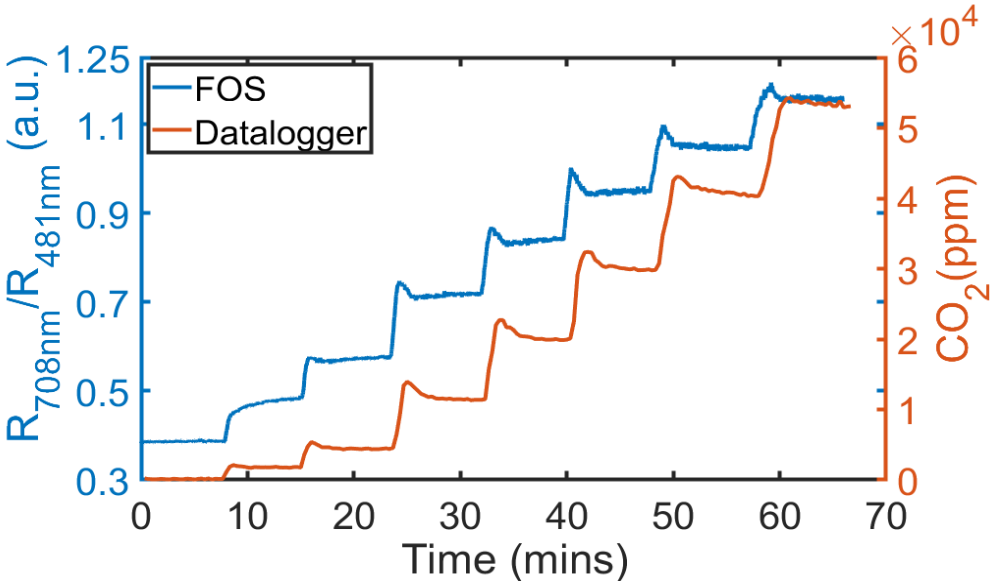
(c)


y = 4E-09x² - 0.0003x + 35.584
R² = 0.8233
y = -5E-09x² + 0.0006x + 15.324
R² = 0.9921
608 nm
481 nm
Poly. (608 nm)
Poly. (481 nm)
R (%)
CO2 Concentration (ppm)
X 10⁴

(d)


FOS
6% CO2
t90%-10%=170s
t10%-90%=19s
Air
Air
R (%)
Time (s)

(e)



(f)

Fig 7.4 (a) Response of FOS (608nm) to different concentrations of CO_2. CO_2 reading was achieved from a commercial CO_2 datalogger. (b) Reversibility of FOS (608nm) to the concentration of CO_2. (c) The reflection value of 481 nm response to the concentration of CO_2. (d) Polynomial fitting of reflection value of FOS to the concentration of CO_2. Each point of the reflection value represents the average value of each stabilised step in (a)(c), the error bar is smaller than the marker size. (e) The response time measurement of FOS (608nm) for 6% CO_2. The response time and recovery time are calculated as the time between the signal change between 10% and 90%. (f) The ratio of the reflection value of the two wavelengths response to the concentration of CO_2.

7.3.2.1.3 Effect of dye concentration on sensitivity

Different concentrations of deprotonated dyes that are present in the Ormosil film provide different absorption values of the FOS. Fig 7.5 shows the response of FOS prepared from 5 different concentrations of thymol blue coating solution in response to different concentrations of CO_2. The result demonstrates that different concentrations of dye in the film will render different sensitivity that correlates well with the previously published reports on a different dye compound [20]. The sensitivity initially undergoes an increase and then a decrease with increasing dye concentration. The highest sensitivity is achieved with the concentration of 2.9 mg/mL. It reduces to almost half after the concentration further increases. The concentration-dependent sensitivity may be explained by the limited solubility of the

CO_2 in the silica film. When the concentration of the thymol blue is above the optimal point, the excess of dye forms more hydrate molecules that reduces the permeability of CO_2 inside of the film. In this case, the CO_2 likely reacts only to outer layer of the film and reduces the sensitivity. The sensitivity in 4.2 mg/mL exhibits a slightly higher than that of 3.6 mg/mL, the reason of that remains unclear and one hypothesis is that the higher concentration of the thymol blue causes cracking in the silica film due to the limited dye solubility leading to higher gas permeability.

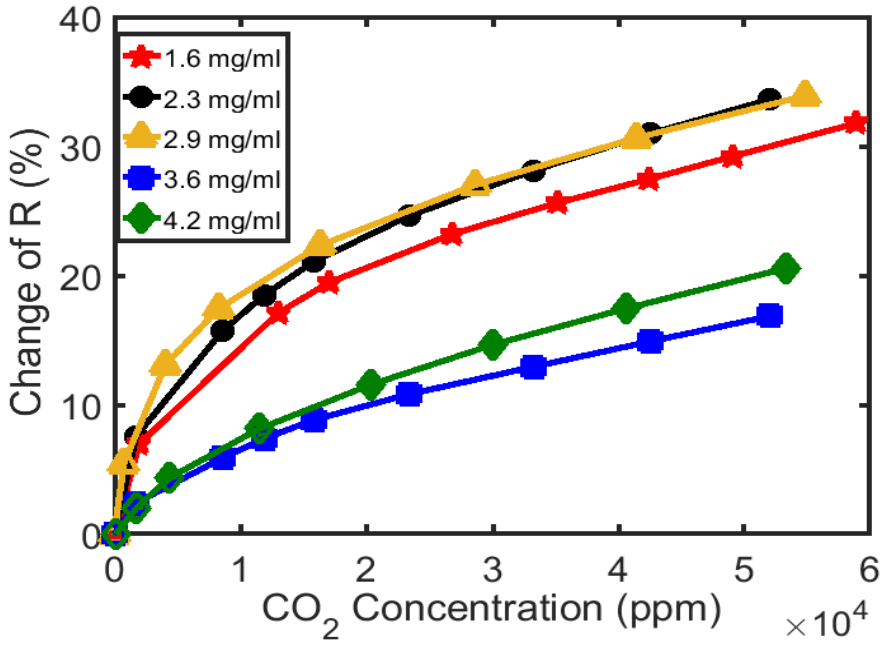


Fig 7.5 Reflection change at a wavelength of 608 nm against the concentration of CO_2 for different concentrations of thymol blue. Error bars are smaller than the marker size.

The selected dye, thymol blue has a pK_a =8.9 which changes its colour for sensing of CO_2 as a result of pH change. The previous study has demonstrated that pH dyes whose pK_a is 7-9 are suitable for the CO_2 fibre-optic sensor [68]. It also demonstrated that the sensitivity of the dyes does not depend on the type of the dye if their pK_a value is within 7-9.

7.3.2.1.4 Effect of temperature on sensor response

The dissolution of CO_2 in the coated film (Eq 7.2) obeys Henry's gas law, which defines the solubility of CO_2 in water according to the partial pressure of gaseous CO_2. As Henry's law constant is a temperature and pressure dependent parameter, it renders different CO_2 solubility at different temperature [298]. Besides, the dissociation

constant of carbonic acid in Eq 7.3 is also temperature dependent [299], it increases with the increase of temperature below 100 ℃ [300]. Consequently, it may also affect the pH value (high temperature leads to low pH) and the measurement of CO_2. The temperature effect of the FOS to the measurement of CO_2 is therefore investigated. Fig 7.6 illustrates the reflection signal of FOS at ~6% of CO_2 with increasing of temperature from 25 ℃ up to 40 ℃ that is within the operating temperature range of the CO_2 datalogger(0-50 ℃). During the measurement, the temperature that is read out from the datalogger linearly increases and reflection signal of FOS exhibits a gradual decrease. The small reduction in the reflection attributes to the decline of the CO_2 concentration that is caused by the imperfect sealing of the chamber. This change in CO_2 is also seen in the datalogger. Therefore, the CO_2 reading can be considered immune from temperature effect at 25 -40 ℃.

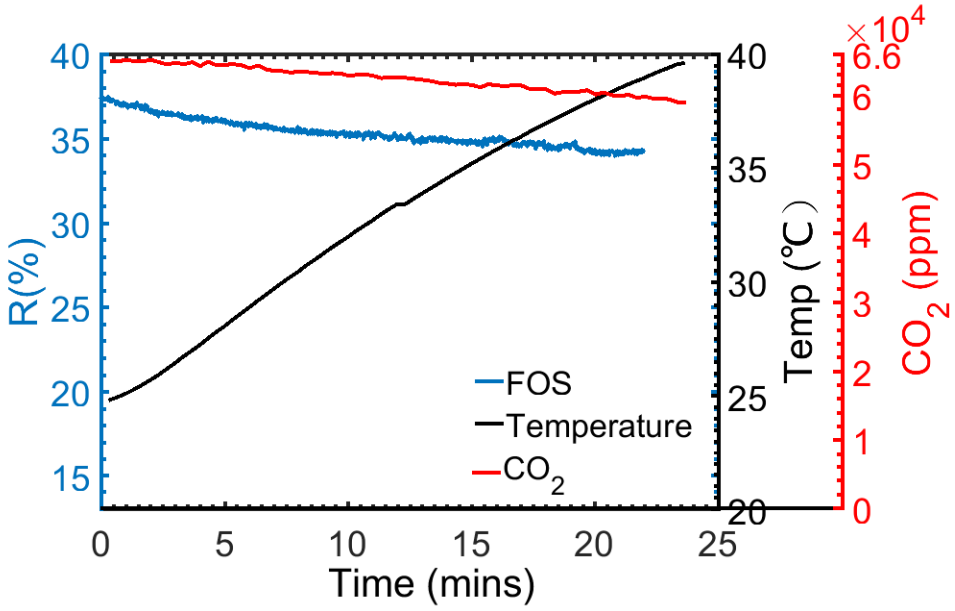


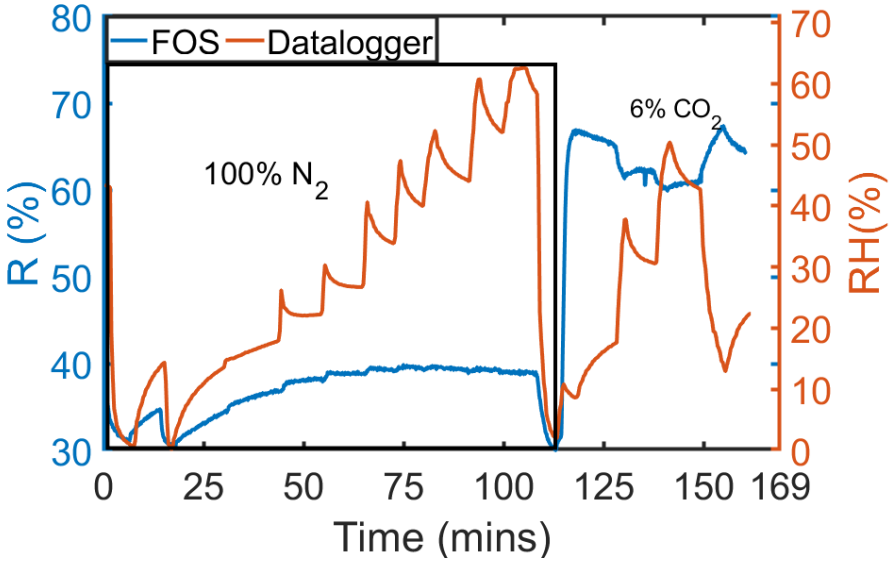
Fig 7.6 Reflection value of FOS in 6% CO_2 as temperature increases.

7.3.2.1.5 Effect of humidity on sensor response

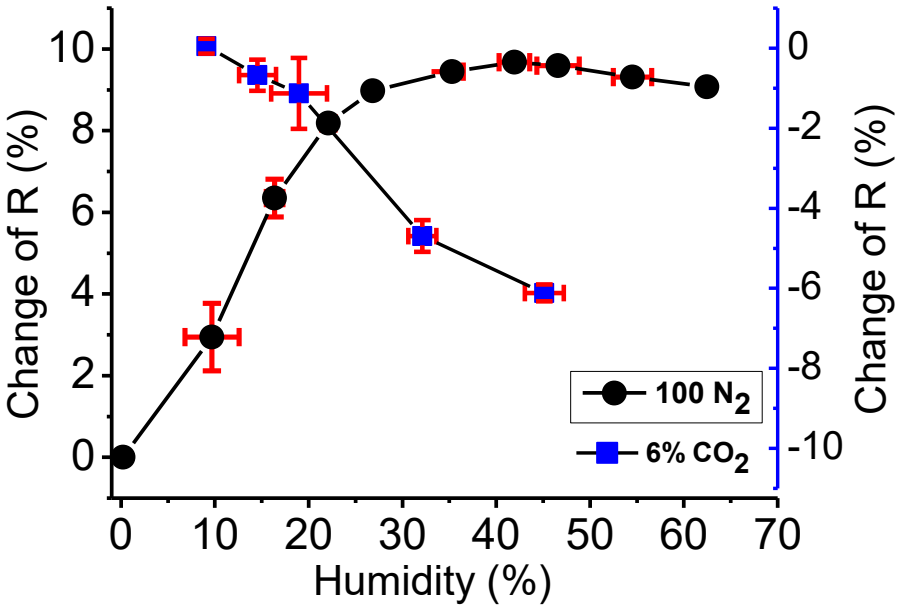
The reflection value increases because of the protonation of thymol blue during the measurement of CO_2. Humidity or water molecules containing protons may have the same protonation effect on the sensor. Moreover, the humidity existing in the CO_2 atmosphere may have either a positive or adverse effect during the sensing of CO_2 depending on the pore size of the matrix film. The external water molecules existing in the pores of the Ormosil film may help to dissolve more CO_2 (promoting the

reaction in Eq 7.3) due to the interaction of CO_2 with water molecules if the pore sizes are large enough to allow both humidity and CO_2 to travel freely without constraint. On the other hand, the water molecules could adsorb on the silica layer and block the transition of gas-phase CO_2 (aq) from outside of film into CO_2 (aq) inside of the film (Eq 7.2). The effect of RH on the sensor response was therefore investigated. Fig 7.7 illustrates the reflection signal change with increasing RH level in the chamber (set-up in Fig 7.2a) without and with CO_2 present. It shows that the reflection increases while increasing the RH level from 0 to 30 % as the water molecules protonate the thymol blue. The reflection value remains stable while the RH concentration rises to 62 %. The magnitude of the change of reflection signal is 9.5 % which is equivalent to the CO_2 concentration of 1855 ppm based on its correlation in Fig 7.7c. This is probably due to the saturation of humidity inside of the pore of the film above 30% RH. This protonation caused by water molecule is reversible, the reflection intensity drops as the RH decreases as illustrated in Fig 7.7a (~110 mins). The following sudden increase of reflection value is due to the infusion of CO_2.

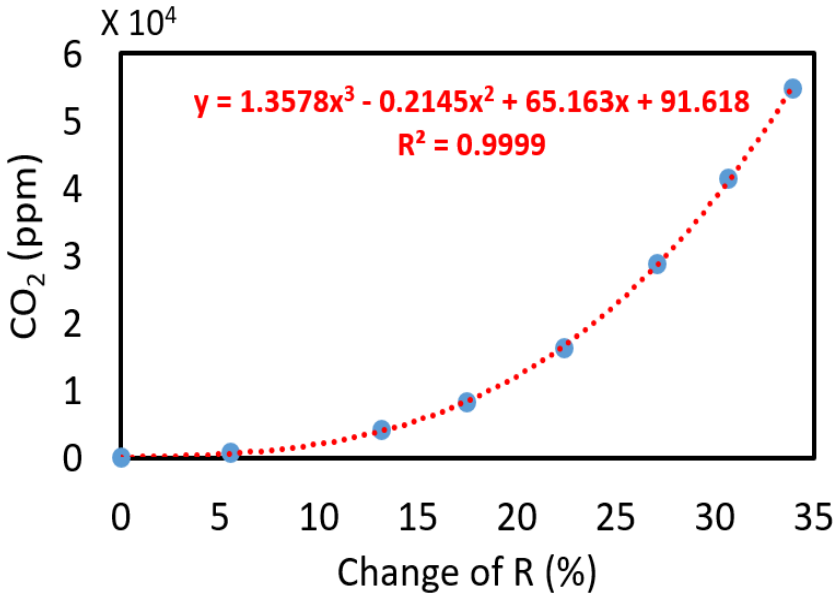
The CO_2 permeates into the Ormosil film and interacts with the dye-ion pair producing the reflection signal change. The sensitivity of such a sensor depends on the permeability of CO_2 to the Ormosil film. Water molecules have higher permeability and diffusion rate in the Ormosil film [301] that may reduce the permeability of CO_2 due to selective absorption by the silanol group (Si-OH) of the Ormosil film and a blocking effect to the pore gas channel. This effect highly depends on the pore size of film, the drying condition of the film and gas pressure [302]. A high temperature (200 ℃) annealing process can significantly reduce the number of silanol groups, but such high temperature will degrade the base catalyst (TMAH) resulting in insensitivity to CO_2 [68]. A decrease of reflection value at 6 % of CO_2 while increasing the RH concentration (up to 50 %) is observed confirming the blocking of humidity to the permeability of CO_2 (Fig 7.7a and Fig 7.7b). The magnitude of the signal change would cause a percent error of ~30% according to the graph in Fig 7.7c.


FOS
Datalogger
100% N2
6% CO2
R (%)
RH(%)
Time (mins)

(a)


Change of R (%)
Change of R (%)
Humidity (%)
100 N2
6% CO2

(b)



(c)

Fig 7.7 (a) The influence of relative humidity to the reflection value of FOS (at 806 nm) at 100% N_2 (up to ~110 mins) and 6% CO_2 atmosphere (after 110 mins). (b) Change of reflection signal against the relative humidity at the two atmospheres; this graph is derived from (a). (c) The correlation of the change of R to the concentration of CO_2.

7.3.2.1.6 FOS stability

7.3.2.1.6.1 Sensor Longevity

The sensing film will gradually become less sensitive because of the degradation of base catalyst (TMAH) due to thermal degradation or the chemical attack of air to the film. Previous research has demonstrated that this occurs after approximately one week [69, 70]. It is therefore important to investigate methods of extending the lifetime of such films so that they can find practical application. Fig 7.8 shows the reflection value of two FOS during storage in N_2 (CO_2 and humidity free) and ambient air atmosphere, respectively. The reflected intensity of the sensor stored in ambient air gradually increases and most absorption is lost after 10 days after which sensitivity to CO_2 is lost. The FOS stored in N_2 exhibits a relatively stable reflection value compared to air storage and provides an extended lifetime.

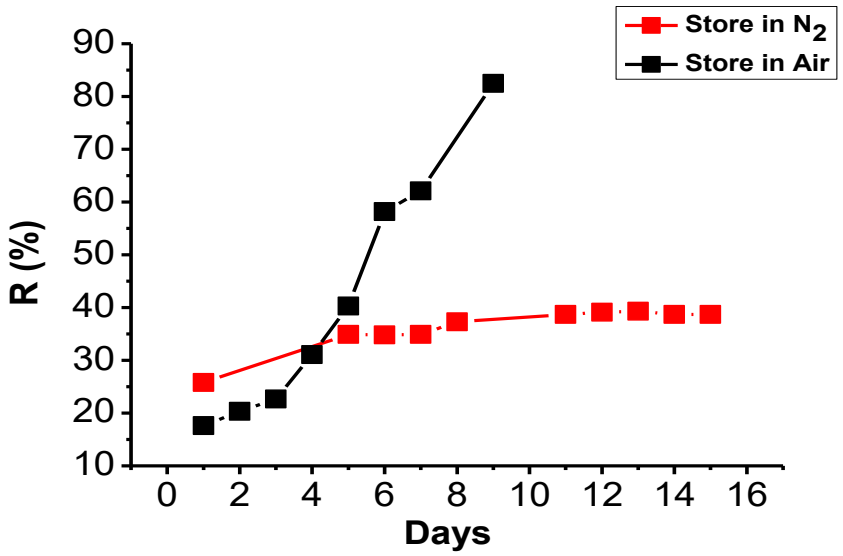


Fig 7.8 Reflection value of FOS for consecutive days under N_2 and air storage condition.

7.3.2.1.6.2 Sensor Photobleaching

The photostability of the dyes is of crucial importance for the accurate measurement of CO_2, especially for long-term monitoring. It is an important property in determination of a dye for sensor application as photobleaching leads to an irreversible loss of absorbance, which limits the statistical accuracy of the detection [131]. On the other hand, the input power needs to be carefully selected which should have a satisfactory signal-to-noise ratio and an optical power that does not produce bleaching effect. Fig 7.9 illustrates the normalised reflection value of the FOS under different illumination power. The optical power is directly measured from the tip of optical fibre without the film present by using an optical power meter (PM100, Thorlabs). It is clear that the stability of the intensity signal is affected by the input optical power. Higher power induces a higher bleaching rate and as a result a higher slope of drifting of the signal. However, it remains stable at a power of about 400 nW during the 1-hour measurement.

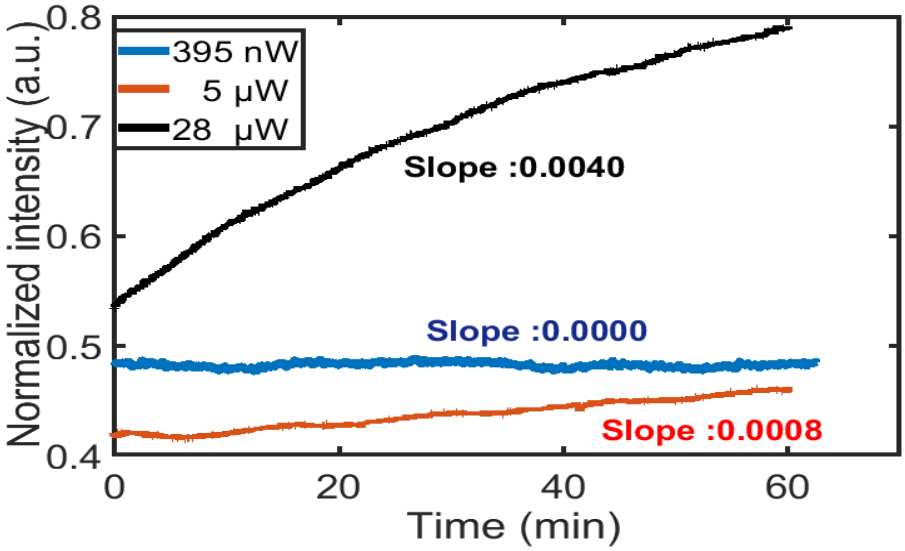


Fig 7.9 Reflection intensity of FOS against time during 1-hour measurement with different input optical power; the power represents optical power at wavelength of 608 nm.

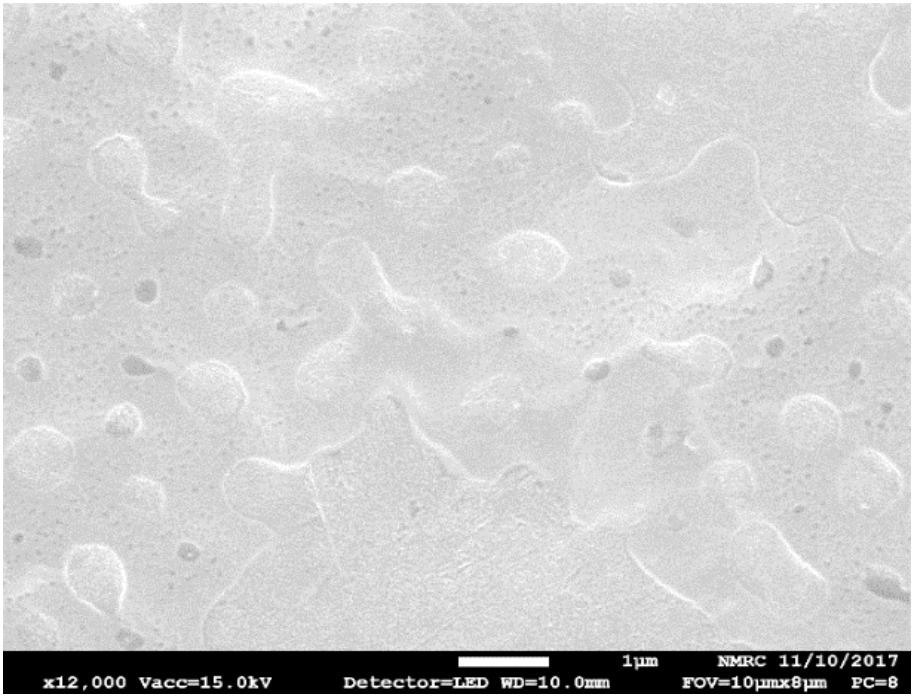
Regarding sensor applications, low-power illumination should be chosen to ensure the stability of optical signals. In addition, the absence of photobleaching avoids the decay of lifespan caused by irreversible bleaching of the sensitive dyes. Besides, the illumination can also only be switched on when required as a point measurement instead of continuous illumination. As the sensor measures at a single wavelength, the broadband wavelength light source in the experiment can be replaced by a small single wavelength of LED, which reduces the overall optical power without reduction of signal strength.

The reported sensor suffers cross-sensitivity to the RH, and the presence of RH disturbs the measurement of CO_2 as a result of the blocking effect to CO_2 diffusion. Such a sensor can be applied for the measurement of CO_2 in a scenario where the RH level is relatively stable. For the breathing CO_2 measurements, due to the presence of high RH, the sensor cannot be applied without the pre-treatment of breathing gas to reduce the RH to ambient condition. Alternative ways have been attempted to address the issue of RH by replacing the silica matrix film with hydrophobic ethyl cellulose (EC) film and by the combination this sensor with the FPI technique.

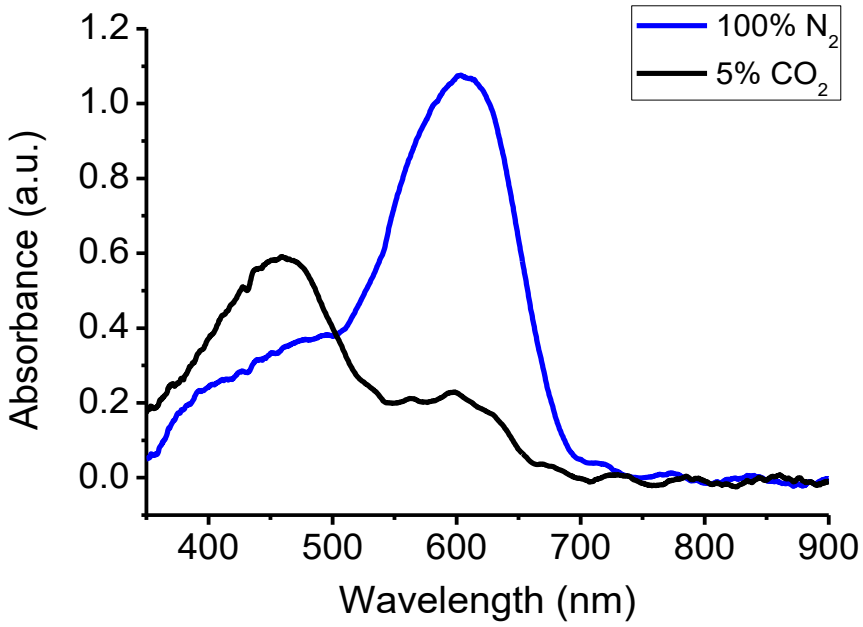
7.3.2.2 FOS fabricated with ethyl cellulose film

7.3.2.2.1 Characterization of FOS

Ethyl cellulose (EC) is a water-immiscible polymer that has been previously reported to be used for the preparation of a colourimetric plastic film on a glass substrate for the sensing of CO_2 [296]. The matrix film is formed in combination of tributyl phosphate which is a plasticising agent that coalesces the chain polymers into a network structure [303]. The SEM image of the film is illustrated in Fig 7.10a which shows visible pores on the surface of film (that is not seen in a silica sol-gel film). Fig 7.10b shows the absorption spectrum during exposure of the FOS to 100 % N_2 and 5 % CO_2. It exhibits a decrease in absorbance value of 608 nm and an increase in absorbance of 480 nm in response to CO_2, which is same trend as that of sol-gel film (Fig 7.3c) due to the same dye. Again, the same reflection value of the wavelength (608 nm) as in the previous section (7.3.2.1) is used to monitor CO_2.



(a)

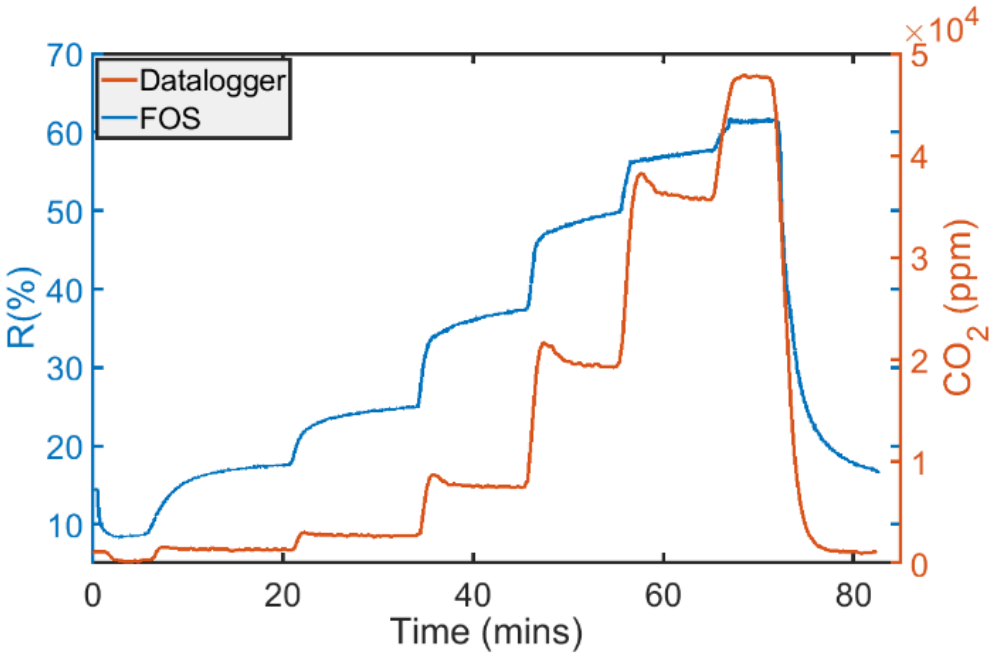


(b)

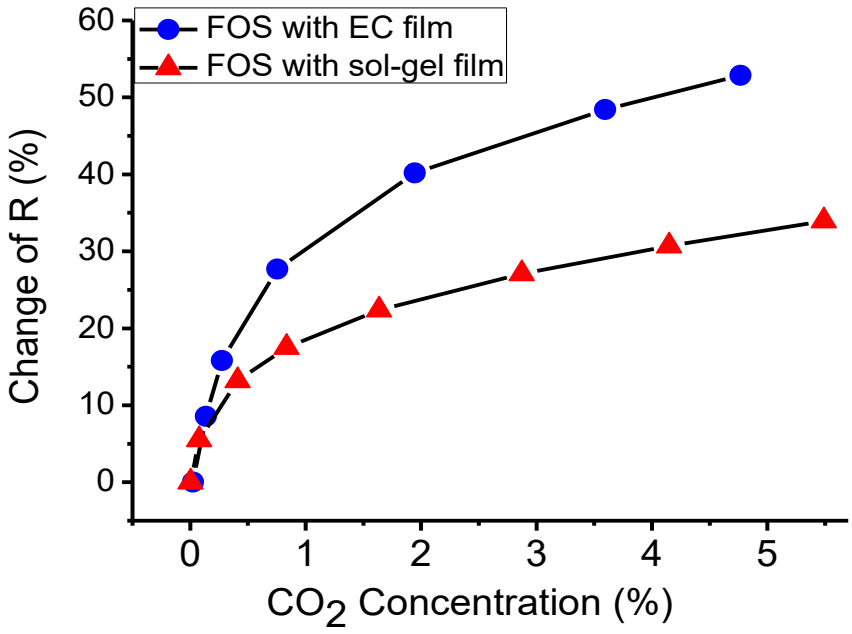
Fig 7.10 (a) SEM of the EC film; Scale bar= 1 µm. (b) Absorption spectrum of FOS in 100% N_2 and 5% CO_2.

7.3.2.2.2 CO_2 sensor response

The reflection value of the sensor related to the concentration of CO_2 is illustrated in Fig 7.11a, and the response correlation curve is plotted as Fig 7.11b in comparison of the FOS that was prepared with the sol-gel film. It appears that the sensor with EC film obtains a higher sensitivity than that of sol-gel silica film, which can be attributed to the higher gas permeability of EC film due to the large pore size. The higher sensitivity, on the other hand, limits the detection range of CO_2 and it shows saturation at ~6 % of CO_2 (reflection value close to 100 %). Fig 7.12 shows the reflection signal of FOS when it is repeatedly exposed to 6 % of CO_2 from ambient air (CO_2 concentration of ~400 ppm). The response time ($T_{10\text{-}90\%}$) is then calculated as 10.6 ± 0.6 s, and recovery time ($T_{90\text{-}10\%}$) is 328.8 ± 2.5 s based on the three times measurement.



(a)



(b)

Fig 7.11 (a) Dynamic change of reflection value as the change of CO_2 concentration. (b) CO_2 response of FOS prepared with two different matrix film. Error bars are smaller than the marker size.

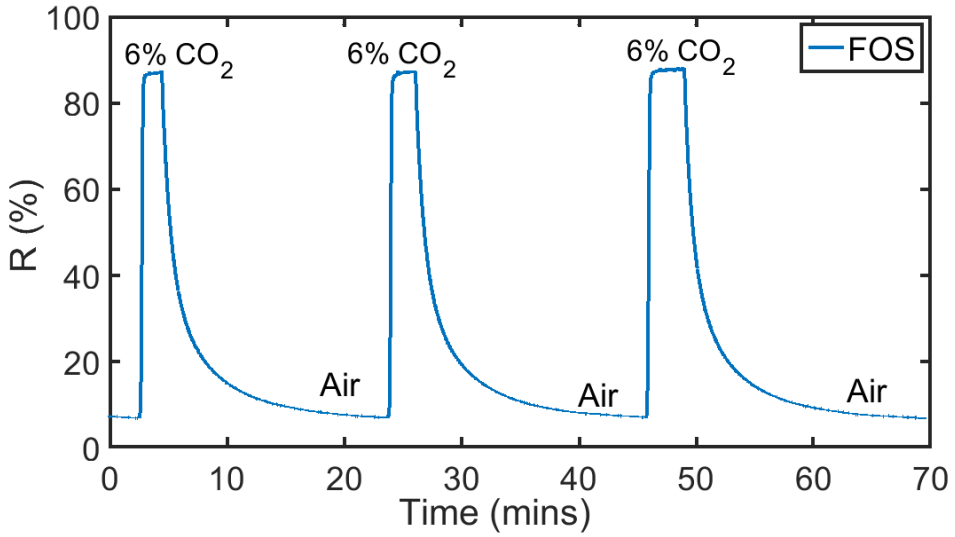
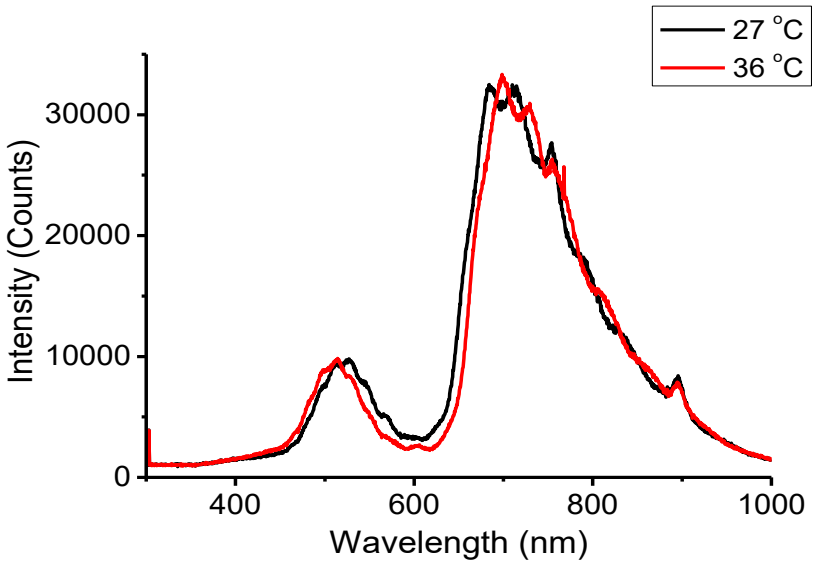


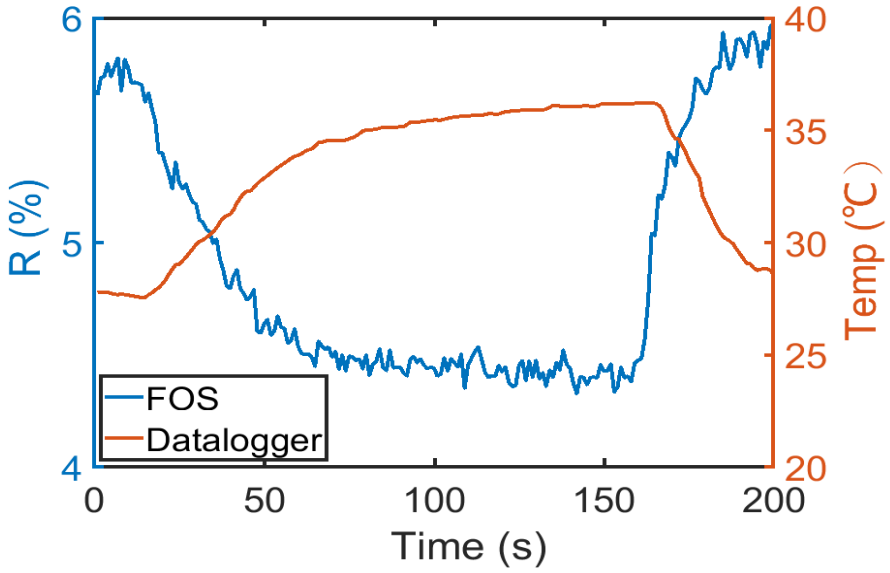
Fig 7.12 Repeatability test of the FOS for 6% of CO_2; the sensor was alternately exposed to 6% of CO_2 and air. Response time and recovery time are defined as time between 10% and 90% of signal change.

7.3.2.2.3 Effect of temperature and relative humidity

Interestingly, the FOS made with EC film is very susceptible to temperature. As illustrated in Fig 7.13b, the reflection value reversibly responds to the change of temperature; it decreases as temperature increases. This can probably be attributed to the thermal expansion of the plastic polymer film. The reflection spectrum is shown in Fig 7.13a at two different temperatures. The weak fringes that appear in the reflection spectrum is caused by interference of light between the reflected light from the two interfaces of the film. The thickness of the film can be calculated as Eq 7.5 provided the refractive index of the film is known. The shift of the wavelength at the two temperatures can be attributed to the slight change of the property of the film, either the change of RI or change of cavity length, or both.



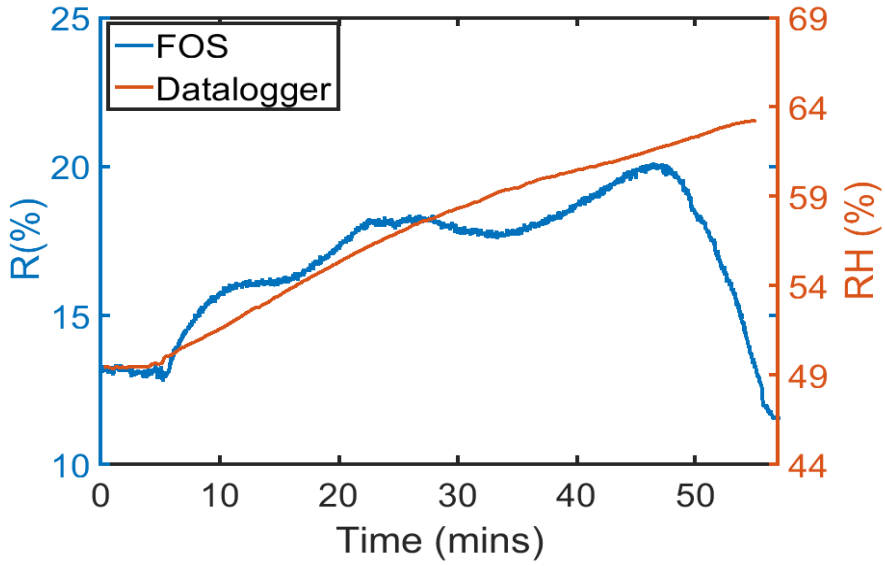
(a)



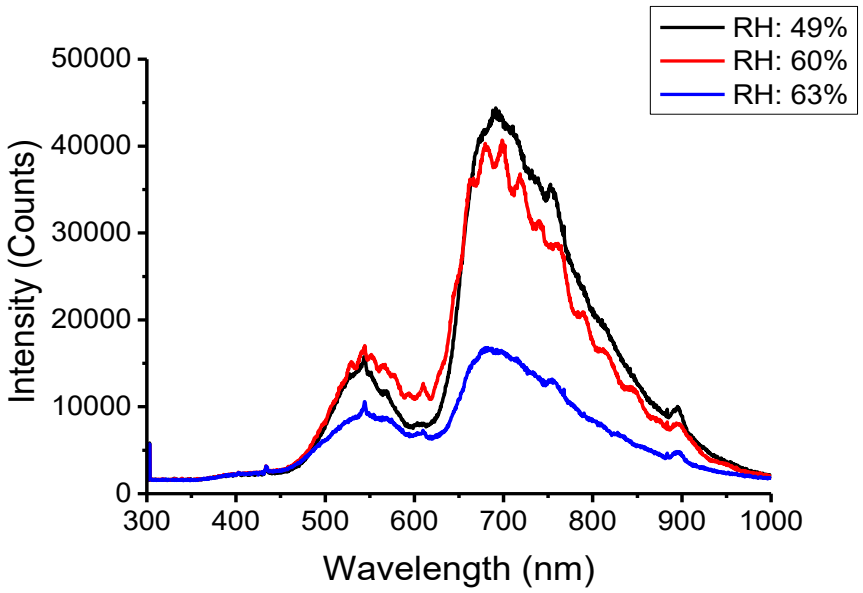
(b)

Fig 7.13 (a) Reflection spectrum of FOS at temperature of 27 ℃ and 36 ℃, respectively. (b) Reflection value of FOS changes with temperature.

As explained previously, a water molecule works as a proton donor that alters the protonation status of the dye. Consequently, the reflection value of FOS increases as RH increases. The FOS exhibits the similar behaviour in response to RH but is less tolerant to humidity above 60%, in which reflection intensity drops due to lower reflectivity induced by accumulation of humidity inside of the film. (illustrated in Fig 7.14)



(a)



(b)

Fig 7.14 (a) The response of FOS to RH. (b) Reflection spectrum of FOS at different RH atmosphere

7.3.2.2.4 FOS stability

The longevity of such a sensor is approximately 4-7 days (illustrated in Fig 7.15), after which the absorbance value of around 600 nm is weak resulting in a very small signal change to CO_2.

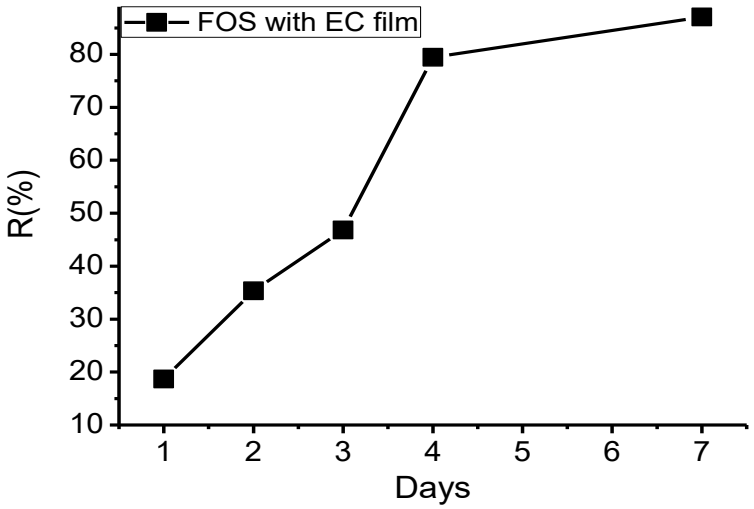


Fig 7.15 Reflection value of FOS of each day while stored in ambient air.

7.3.2.3 Comparison of two sensors

Table 7.1 lists the characteristics of the FOSs that are prepared with two different matrix films. The sensor with EC film exhibits a higher sensitivity (~50% of reflection change for 5% of CO_2) and shorter response time (10s) than that of the sol-gel film (~30% and 19s, respectively). The short response time can be attributed to the lower diffusion time of gas induced by large pore size of the polymer film. Nevertheless, it exhibits an even longer recovery time. Both sensors suffer from a short lifetime and the one with silica film has a relatively longer lifetime (~10 days) than that of polymer film (~4-7 days) when stored in ambient air. Due to the elastic property of the EC film, it is susceptible to temperature change, which is not observed in the rigid sol-gel film. Besides, it is less tolerant to RH, especially in the high level (>60 %) as the accumulation of humidity causes an increase of RI and reduces the reflectivity of light from the film-air interface. Most biomedical applications target CO_2 at a concentration of ~40 mmHg (5%) [51] [57], both sensors cover the detection range. However, the sensor with the polymer film suffers from thermal effect and poor humidity resistance. The sensor with the sol-gel film has a good thermal resistance and a better humidity tolerance but will require a stable RH operation atmosphere for the accurate measurement of CO_2 due to the blocking effect.

Table 7.1 Comparison of two FOS prepared with different matrix film.

FOS prepared with matrix of	Change of R/ 5% CO_2	Response time (s)	Recovery time (s)	Longevity when store in air
Polymer film (EC)	50 %	10.6 ± 0.6	328.8 ± 2.5	~ 4-7 days
Sol-gel film	30 %	19 ± 1.6	170 ± 8.4	~ 10 days

7.4 Fibre optic Fabry–Pérot interferometer (FPI) sensor for the simultaneous measurement of CO_2 and RH

The biggest issue so far for the fabricated FOS to be applied for measuring of CO_2 from breath is the effect of RH. The measurement of RH would allow the subtraction of such an effect mathematically via the processing of the data with the correlation of RH. The tip based colourimetric sensor reported above can be made as an FPI sensor by carefully control the thickness of the film. The FPI sensor is very sensitive to RI change of the film and this means that it has the potential to be used for sensing of RH. The unreacted silanol group inside the silica film prepared via the sol-gel method would naturally act as functional groups for sensing of RH.

7.4.1 Experiment procedure

The calibration of the FPI sensor is done with the same protocol as described above in section 7.3.1. For the signal processing, the average reflection value of the wavelength between 596 nm to 617 nm (peak-to-peak), corresponding to the absorption band of the thymol blue, was utilised as the optical signal for calibration with the commercial datalogger. The CO_2 calibration curve was achieved by averaging the optical signal during the stabilised period (the last 5 mins of each step) against the average concentration of CO_2 achieved from the CO_2 datalogger in the same period.

The RH calibration is done separately with two set-ups for the different range of RH. For the RH concentration below 80%, the RH level is set by flowing the distilled water

bubbled with N_2 into the test chamber as described in 7.3.1. For the RH above 80%, an environmental chamber was used by programming the environmental chamber with the RH setting up from 50% to 100%. The wavelength of the interference peak was used to calibrate the RH level by comparing the central wavelength with the RH reading from the commercial RH datalogger.

For investigating the effect of RH on the CO_2 reading of the FPI sensor, a calibrated FPI sensor is sequentially exposed to ~6% of CO_2 (the maximum concentration of the CO_2 gas from the cylinder) at different RH level from ambient condition (0.08 % CO_2, 40% RH). The gas chamber is initially filled up with ~6% of CO_2 and the different RH level inside of the chamber is generated by simply flowing water bubbled with CO_2 into the chamber (set-up illustrated in Fig 7.2a). The CO_2 concentration inside the chamber is maintained at about ~6% by controlling the flow of CO_2 into the chamber.

The effects of temperature upon the FPI sensor was investigated by setting the RH of environment chamber (Fig 7.2b) to a constant RH value of 50% and continuously varying the temperature from 25 ℃ to 40 ℃ which covers the ambient room temperature (25%) to the physiological temperature (37 ℃).

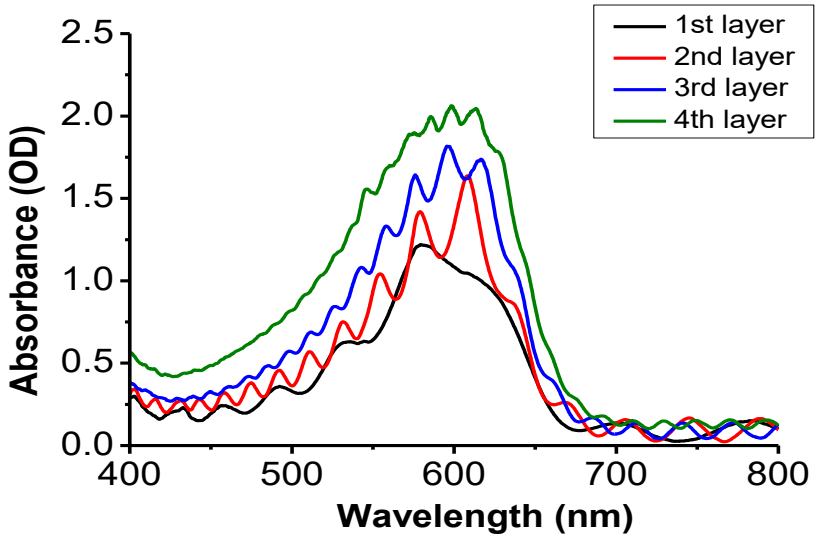
CO_2 response time measurement was conducted by filling up the gas chamber in Fig 7.2a with~6% CO_2, inserting the prepared sensor into the chamber and waiting until the optical signal is stabilised (approximately 10 mins). The cap of the chamber is then opened to release the CO_2 concentration back to ambient condition. For creating a high level of humidified environment, 50 mL of distilled water was poured into a petri dish and placed inside of chamber until the RH level inside of the chamber is stabilised (approximately 1 hour). The same insertion and open cap process are repeated to obtain the RH response time.

7.4.2 Results and discussion

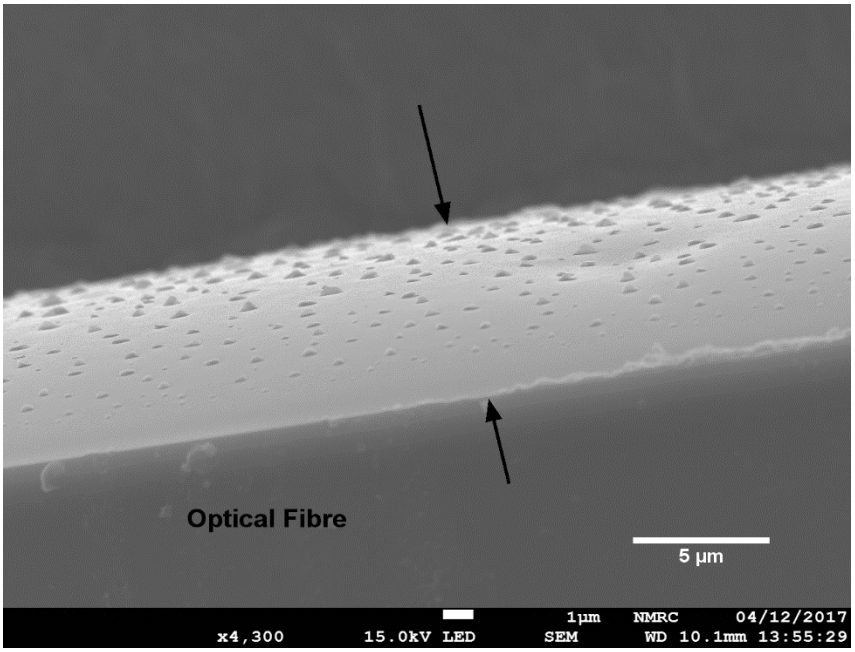
7.4.2.1 Characteristic of sensor

Fig 7.16a shows the absorption spectrum after each coating cycle on the tip of the optical fibre. The absorption window, corresponding to the absorption band of thymol blue, appears between 450 to 700 nm caused by the deprotonated form of dye (thymol blue) and interference fringes appear in each spectrum. The absorption

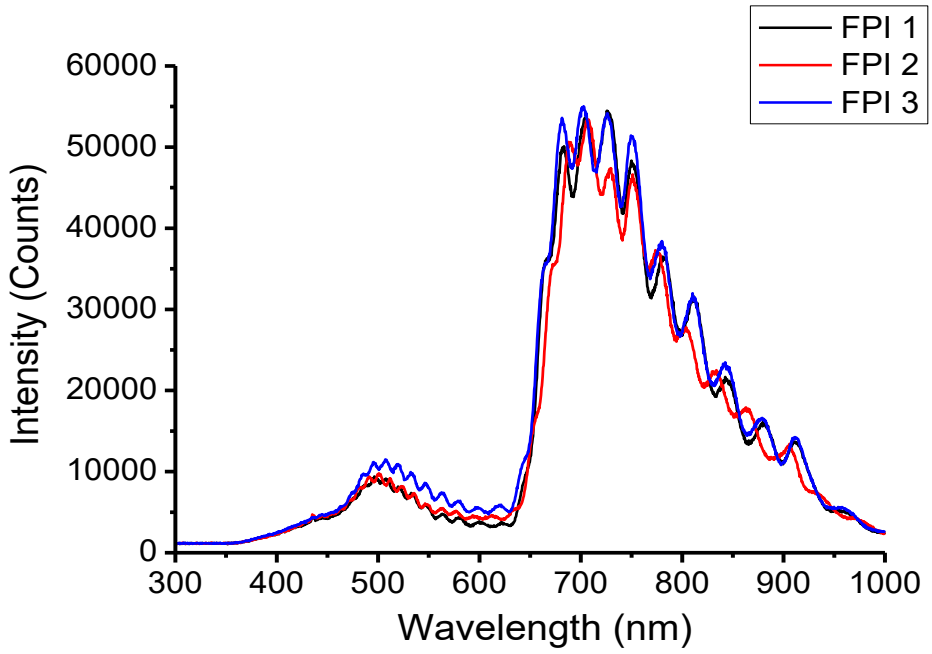
value increases after each coating cycle due to the increased thickness based on the Lambert-Beer law. The number of fringes increases after each layer coating as a result of the increase of cavity length (thickness of the film). The visibility of fringes decreases at the fourth layer and the fringes disappear after a further increase of the coating cycle as the thickness increases beyond the coherence length of the light source. Multiple coating cycles provide thicker films with more dyes encapsulated resulting in a higher absorbance value and measurable colour change after exposure to CO_2. Most importantly, the thicker film provides better lifespan than that of the thin film as demonstrated in later content (Fig 7.22). Three layers are used in this work as the film has sufficient absorption value as well as good visibility of fringes. The RI of sensing film after drying is measured as 1.501 ± 0.02 via ellipsometer and the thickness is calculated as 5.83 ± 0.09 µm from the Eq 7.4 compared to 5.95 µm which is the thickness measured with SEM in Fig 7.16b. The calculated thickness agrees well with the value measured using SEM.



(a)



(b)



(c)

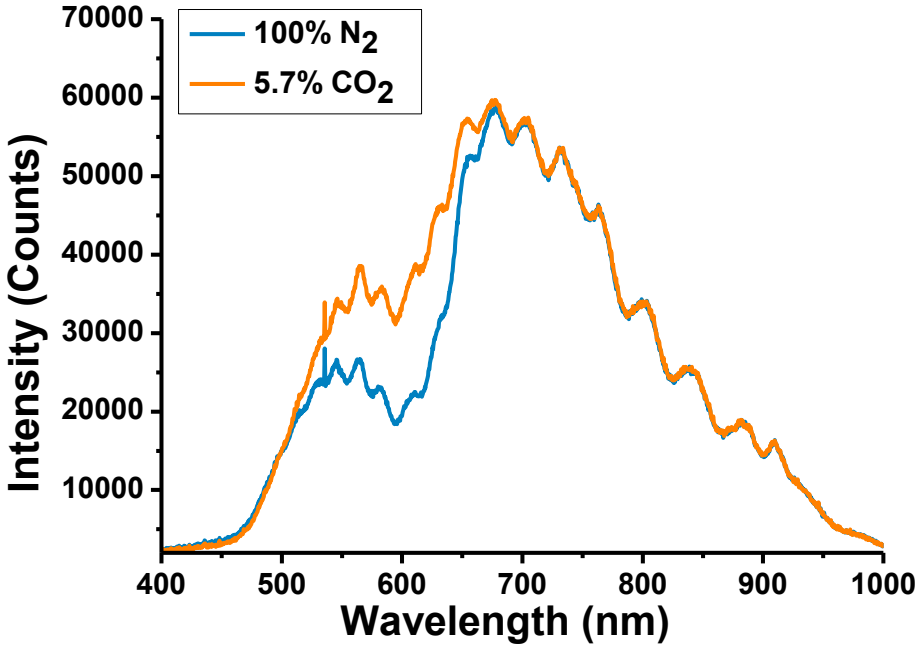
Fig 7.16 (a) Absorption spectrum of FPI after the n^{th} layer coating (n=1, 2, 3, 4); each spectrum is taken after 2 mins of each coating. (b) SEM image of three layers sensing film after dry in N_2 for 1 day on the tip of the optical fibre; the coated film is pointed between two black arrows and the thickness is measured about 5.95 µm (scale bar =5µm). (c) Reflection spectra of 3 different FPI sensors coated with three layers; the spectrum is recorded after 2 mins of the coating. The spectra of three sensors fabricated independently are illustrated.

The coating thickness of such film depends on the withdrawing speed of the dip coating process and the viscosity of coating solution [304]. By carefully controlling the reaction condition of the sol-gel process and dip coating process, the sensor can be fabricated in a repeatable manner. Fig 7.16c shows the reflection spectrum of three fabricated FPI sensors demonstrating the repeatability of the manufacturing process.

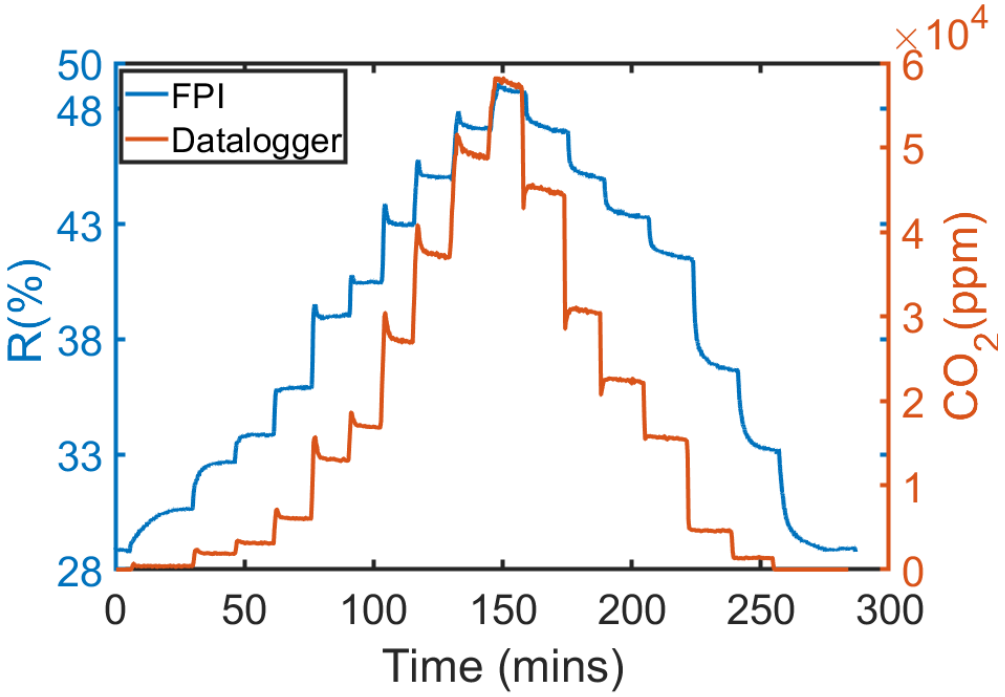
7.4.2.2 CO_2 measurement by using FPI sensor

The absorption value caused by the deprotonated dye exhibits a decrease after the wet film is stabilised and dried in N_2 as a result of degradation of the base catalyst during drying. The RH level during the CO_2 test was kept stable at 19 ±1.9%. Fig 7.17a illustrates that the intensity of the wavelength located at absorption window increase after exposure to CO_2 as a result of protonation of the dye in Eq 7.3. In this case, the colour of the film turns from blue (deprotonated status) towards yellow (protonated status). The position of the interference fringes remains unchanged during the test indicating no cross-talk between the fringe position and the concentration of CO_2. The average reflection value of the selected wavelengths (596 - 617 nm) is extracted to compare with the CO_2 reading from commercial datalogger as shown in Fig 7.17b. The change of the reflection value follows the change of CO_2 concentration as the concentration goes up and down demonstrating the reversibility of the FPI sensor in response to the decrease of CO_2 concentration. The reflection value exhibits a polynomial relationship to the concentration of CO_2 (shown in Fig 7.17c). Hysteresis is observed for the reverse trace, which is likely caused by incomplete releasing of CO_2 during the recording time as it is a slow process. Fig 7.17d shows the sensor response after exposing the FPI sensor from ambient (0.06 %) into a 5.4 % of CO_2 atmosphere. The response time ($t_{10\%-90\%}$) and recovery time ($t_{90\%-10\%}$) is calculated as 98 s and 418 s, respectively. The sensor exhibits a longer recovery time than the commercial datalogger due to the low equilibrate time of the chemical reaction. The FPI sensor was inserted into the CO_2 chamber and it is immediately exposed to CO_2 atmosphere so that the calculated response time is considered as the sensor response time. The sensor recovery time was achieved by opening the chamber cap and allowing the CO_2 to diffuse into air

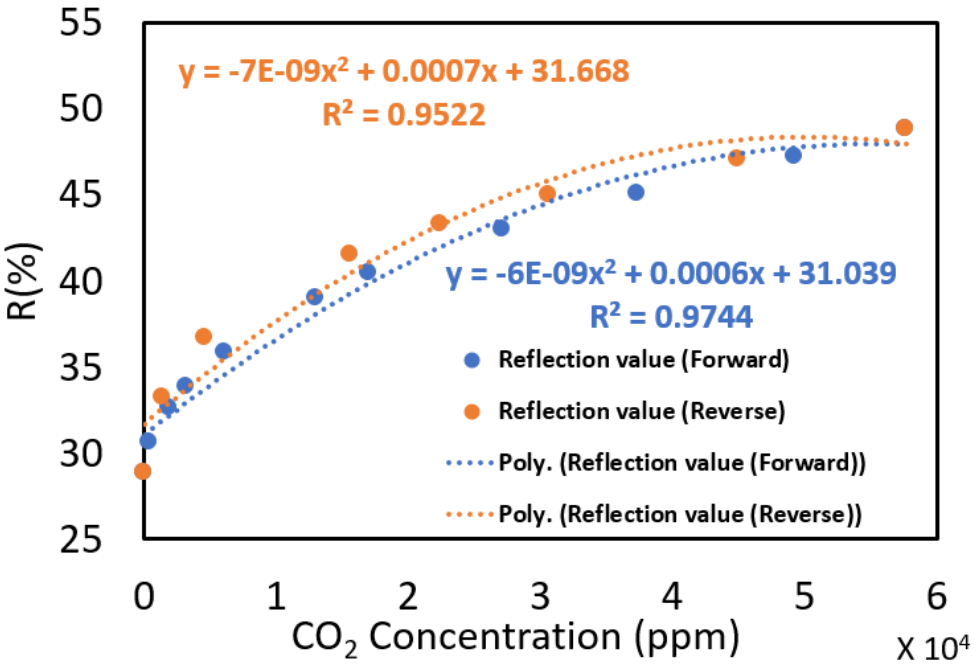
and be diluted. As the CO_2 has higher gravity than the other gases in air, it tends to diffuse slowly and therefore the recovery time of FPI sensor is considered including the CO_2 diffusion time.



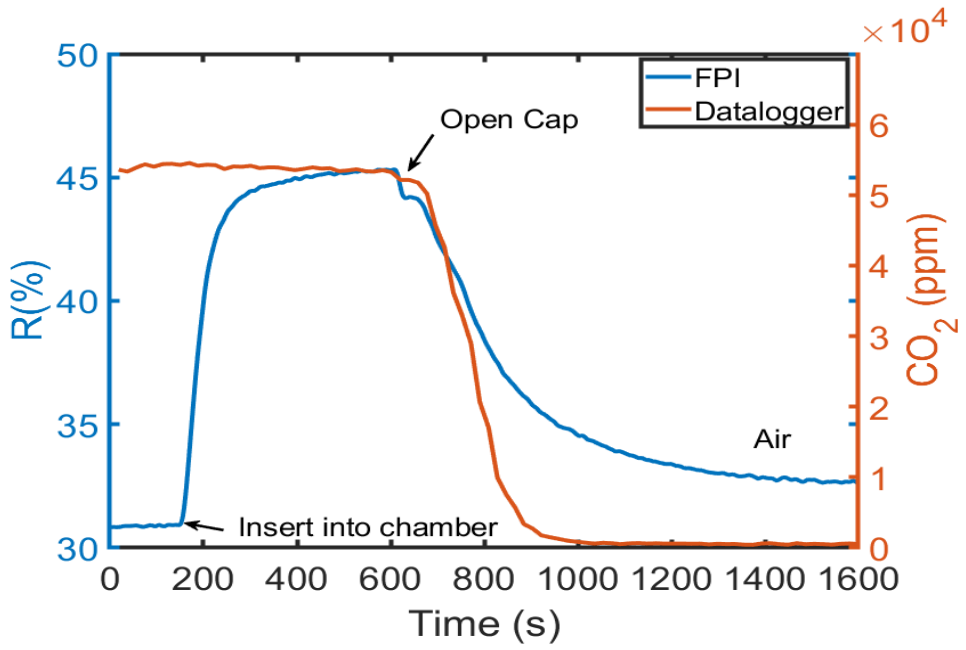
(a)



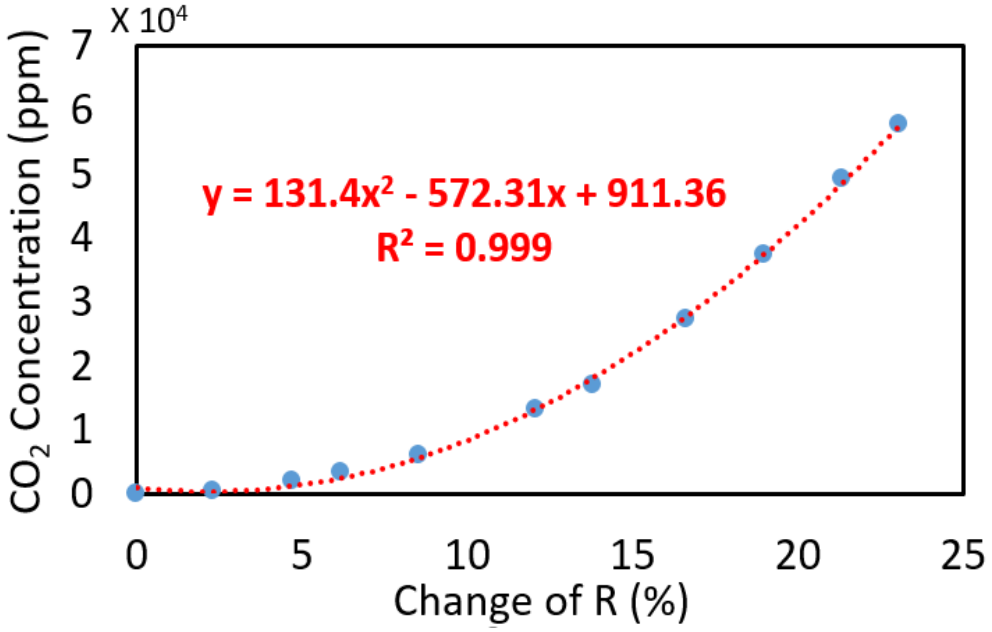
(b)


y = -7E-09x² + 0.0007x + 31.668
R² = 0.9522
y = -6E-09x² + 0.0006x + 31.039
R² = 0.9744
Reflection value (Forward)
Reflection value (Reverse)
Poly. (Reflection value (Forward))
Poly. (Reflection value (Reverse))
R(%)
55
50
45
40
35
30
25
0
1
2
3
4
5
6
CO2 Concentration (ppm)
X 10⁴

(c)


FPI
Datalogger
Open Cap
Air
Insert into chamber
R(%)
CO2 (ppm)
×10⁴
50
45
40
35
30
6
5
4
3
2
1
0
0
200
400
600
800
1000
1200
1400
1600
Time (s)

(d)



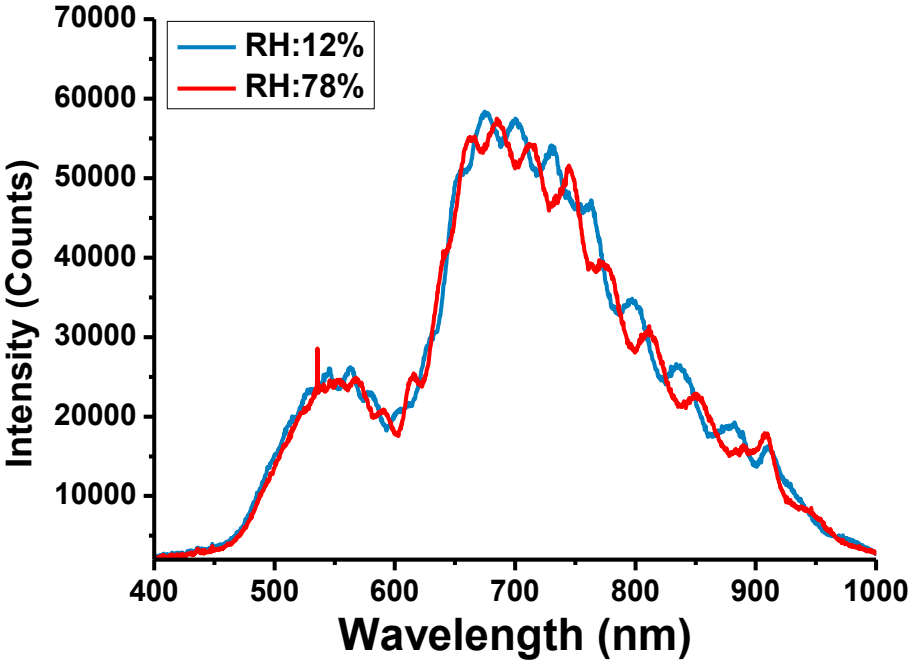
(e)

Fig 7.17 (a) Reflection spectrum of FPI in 100 % N_2 and 5.7 % CO_2. (b) The signal response of FPI in comparison of the CO_2 reading from commercial datalogger against time. The intensity value is taken as average reflection value between wavelengths of 596 – 617nm. (c) The polynomial fitting of the data; each point is achieved by taking the average value of each stabilised step in (b) and error bar is smaller than the marker size; the forward trace is the optical signal when gradually raising the CO_2 concentration and reverse trace is the signal when the CO_2 concentration gradually decrease. (d) Response time test of FPI; the FPI was inserted into the chamber where the CO_2 is 5.4% at about 152s and open the cap to release CO_2 at about 612s. (e) The correlation of the change of the reflection value to the concentration of CO_2. Error bar is less than marker size.

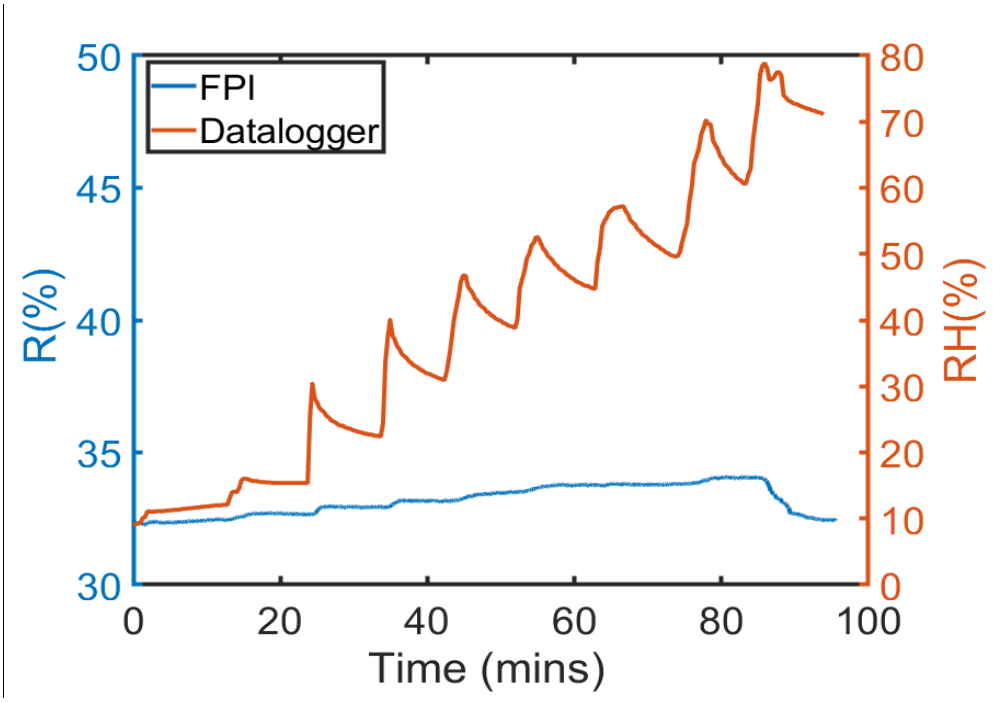
7.4.2.3 RH measurement by using FPI sensor

The concentration of CO_2 was kept under the LOD of the commercial datalogger (< 20 ppm) during the RH test, thus the test environment can be treated as CO_2 free. The interference fringes undergo a redshift after exposure to a higher level of RH (from about 10 % to 80 %), and the reflection value of the absorption window does not show an obvious change in its amplitude as illustrated in the reflection spectrum in Fig 7.18a. The average reflection value of the selected wavelengths (596-617 nm) is tracked to evaluate the humidity cross-sensitivity for the CO_2 sensing. The selected wavelengths are defined as one interference waveform (peak-to-peak) and the

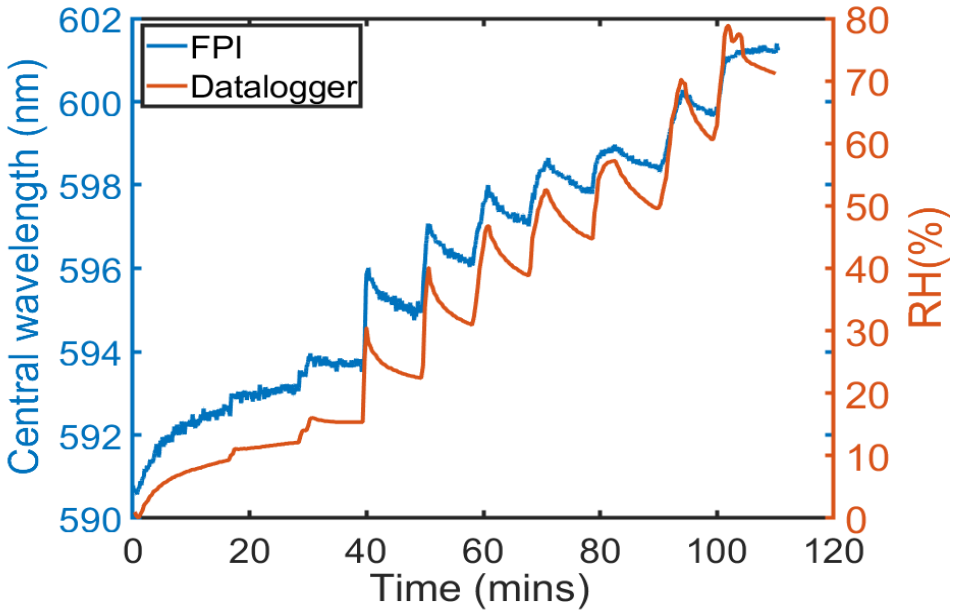
average reflection value is considered insusceptible to the shift of the wavelength. Fig 7.18b shows the reflection value under different humidity levels between 10 % to 80 %. The reflection value maintains relatively stable during the test. The reflection slightly increases as the concentration goes from 10 % to 65 %, this is due to the protonation of water molecules to alkalic thymol blue. The maximum increased reflection value with a magnitude change of ~1.8 % caused by 65 % of RH is equivalent to a CO_2 concentration of 232 ppm according to the CO_2 response in Fig 7.17e. The small drop of the intensity when RH is above 70 % (at about 85 mins) is caused by the decrease of reflectivity of light due to the higher RI value induced by higher RH. Thus, this relatively stable reflection value ensures the sensor has a negligible cross sensitivity to RH. Each peak of interference fringes can be treated to bear the same magnitude of the shift of wavelength. The wavelength of the highest peak in the absorption spectrum (initial position: 596 nm) is tracked to indicate the RH change in comparison of the reading from the commercial datalogger. As illustrated in Fig 7.18c, the position of the peak change corresponds to the change of RH. The peak position shifts to a higher wavelength as RH increases. The wavelength of the peak shows a linear regression to the level of RH with a sensitivity of 0.14 nm/%RH (Fig 7.18d). Fig 7.18e demonstrates the RH measurement in the range of 50-90 % in the environmental chamber (illustrated in Fig 7.2b). The wavelength shift of FPI sensor shows good agreement with the RH change inside of the environmental chamber. The RH calibration curve is displayed in Fig 7.18f and the sensitivity for the range of 50-90% matches to the sensitivity in the range of 0-80 %. The response and reverse time of the sensor for the relative humidity from about 30% to 76 % are calculated as 32 s and 56 s, respectively (Fig 7.18g). The faster response time of RH than that of CO_2 attributes to the faster diffusion speed of water molecule inside of porous silica film. As water molecule has small molecular weight than CO_2, the diffusion is then faster according to the Fick's first law of diffusion and Knudsen diffusion as explained in Eq 2.30, Chapter 2.


RH:12%
RH:78%
Intensity (Counts)
Wavelength (nm)
70000
60000
50000
40000
30000
20000
10000
400
500
600
700
800
900
1000

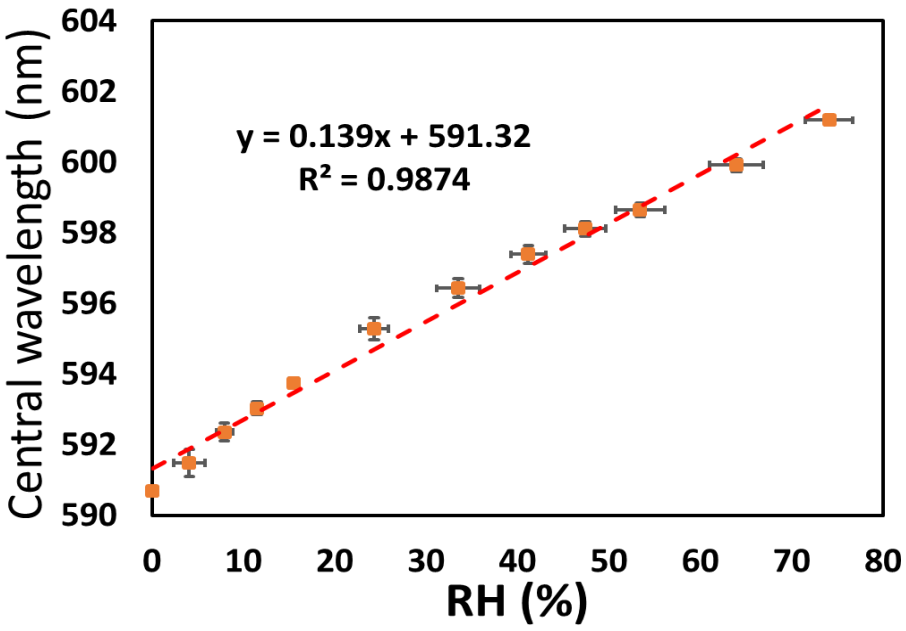
(a)


FPI
Datalogger
R(%)
RH(%)
Time (mins)
50
45
40
35
30
80
70
60
50
40
30
20
10
0
0
20
40
60
80
100

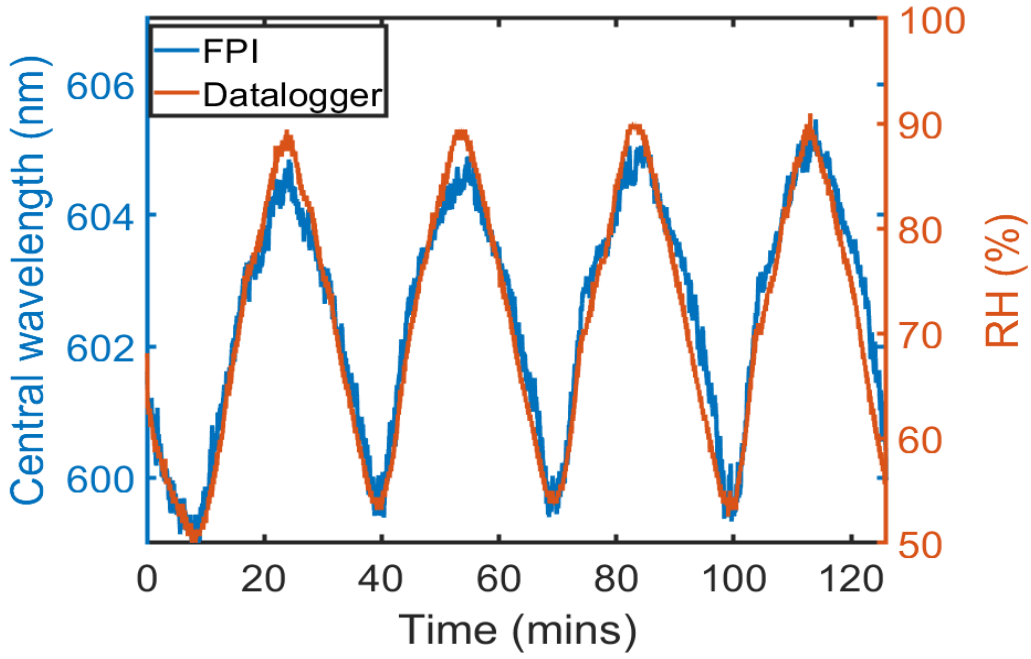
(b)


FPI
Datalogger
Central wavelength (nm)
RH(%)
Time (mins)
602
600
598
596
594
592
590
80
70
60
50
40
30
20
10
0
0
20
40
60
80
100
120

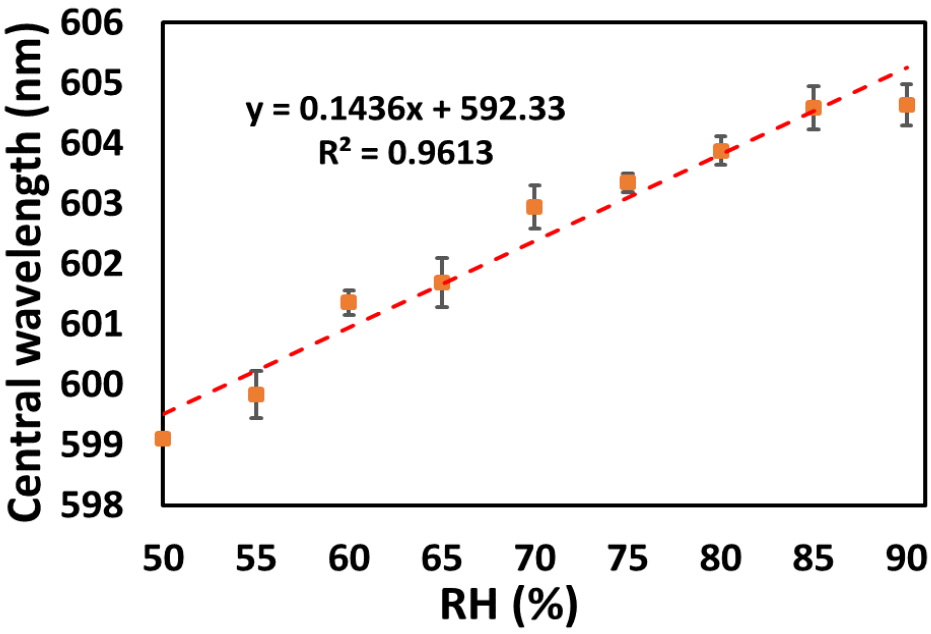
(c)


y = 0.139x + 591.32
R² = 0.9874
Central wavelength (nm)
RH (%)
604
602
600
598
596
594
592
590
0
10
20
30
40
50
60
70
80

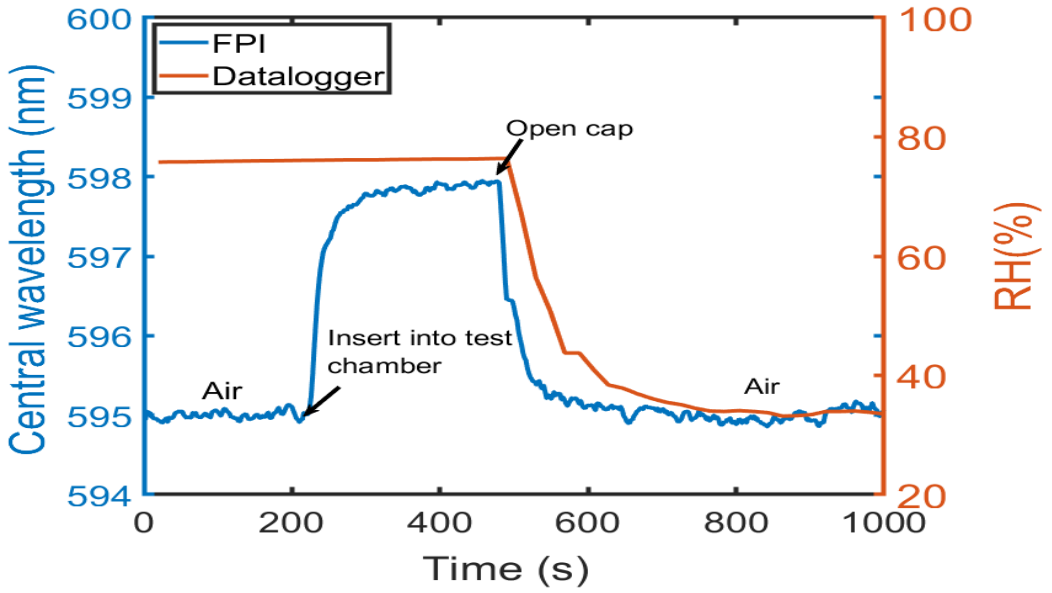
(d)


FPI
Datalogger
Central wavelength (nm)
606
604
602
600
100
90
80
70
60
50
RH (%)
0
20
40
60
80
100
120
Time (mins)

(e)


y = 0.1436x + 592.33
R² = 0.9613
Central wavelength (nm)
606
605
604
603
602
601
600
599
598
50
55
60
65
70
75
80
85
90
RH (%)

(f)

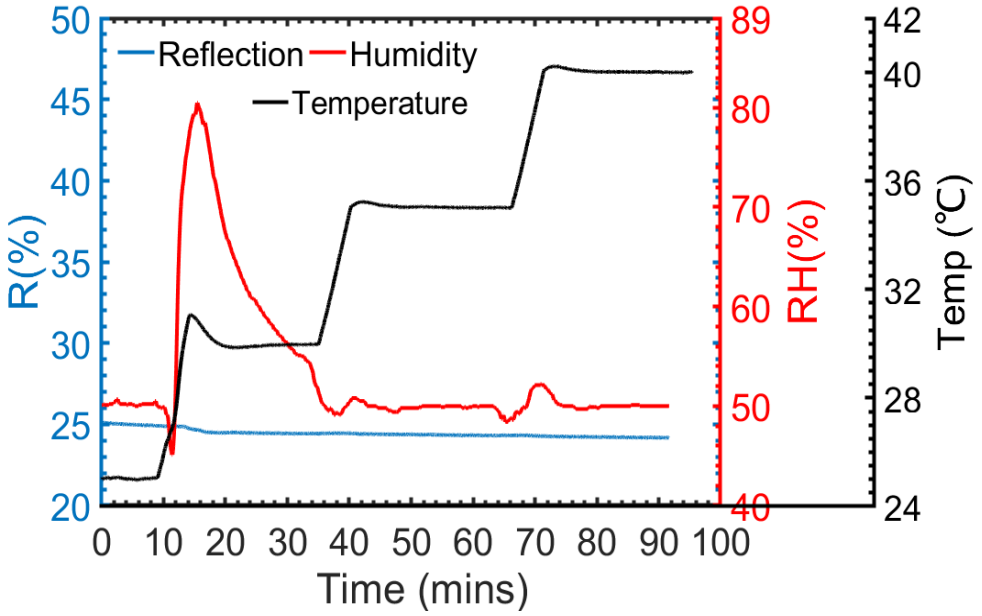


(g)

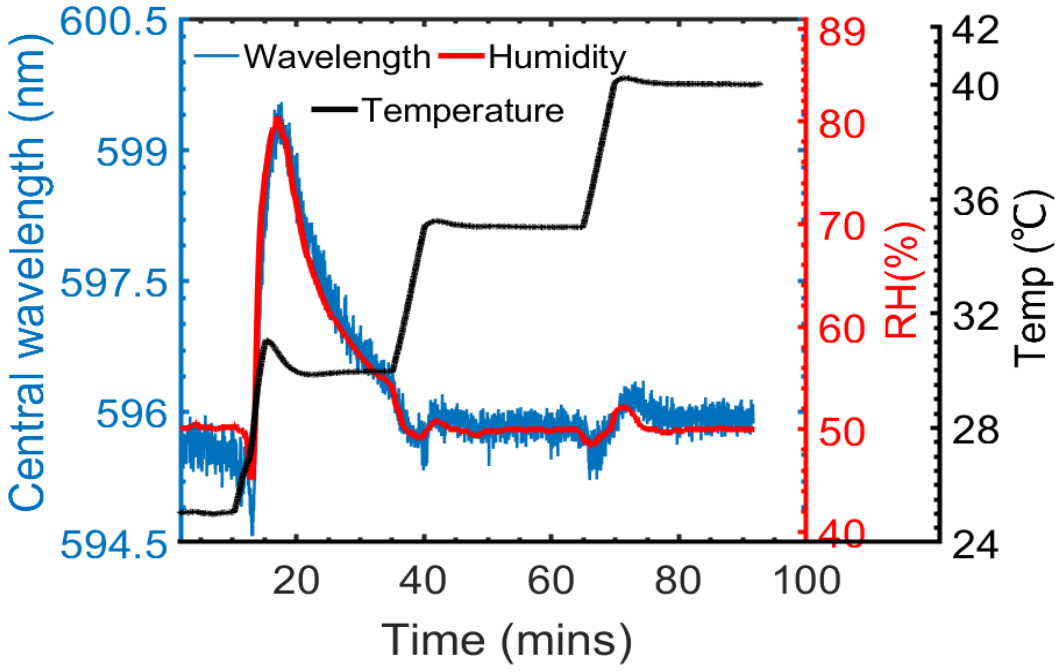
Fig 7.18 (a) Reflection spectrum of FPI in different humidity level. (b) The average reflection value of selected wavelengths (between 596 nm to 617 nm) under different humidity level. (c) The central wavelength of the peak in comparison of the relative humidity reading from commercial datalogger during the test. The data was achieved by using the set-up in Fig 7.2a. (d) The fitting of central wavelength as a function of RH for the range from 0 to 80%. (e) The central wavelength of FPI in comparison of RH inside of environmental chamber (Fig 7.2b). (f) The linear fitting of central wavelength against the RH for the range from 50 % to 90%. (g) Response time of FPI to RH; the sensor was inserted into the chamber with RH level of 76% at the time of 220 s and the cap was opened at 478s to reduce the RH back to ambient level (33%).

7.4.2.4 Temperature effect on the FPI sensor

The effect of temperature upon the FPI sensor was investigated following the method described in 7.4.1.1. When temperature increases step-by-step from 25 ℃ to 40 ℃, the average reflection value in the selected wavelengths (596 – 617nm) of the FPI sensor does not show a measurable change as illustrated in Fig 7.19a. The wavelength of the interference fringes of the FPI in Fig 7.19b shifts in accordance with the RH change; when the RH remains constant at different temperatures of 25 ℃, 35 ℃, 40 ℃, the wavelength remains constant too. Therefore, the temperature effect in the range of 25-40 ℃ on the CO_2 and RH FPI is considered negligible.



(a)

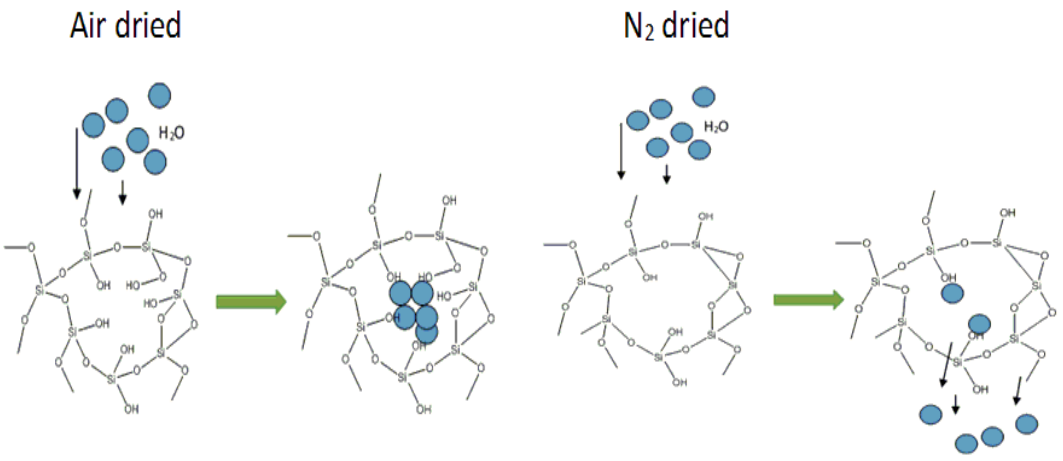


(b)

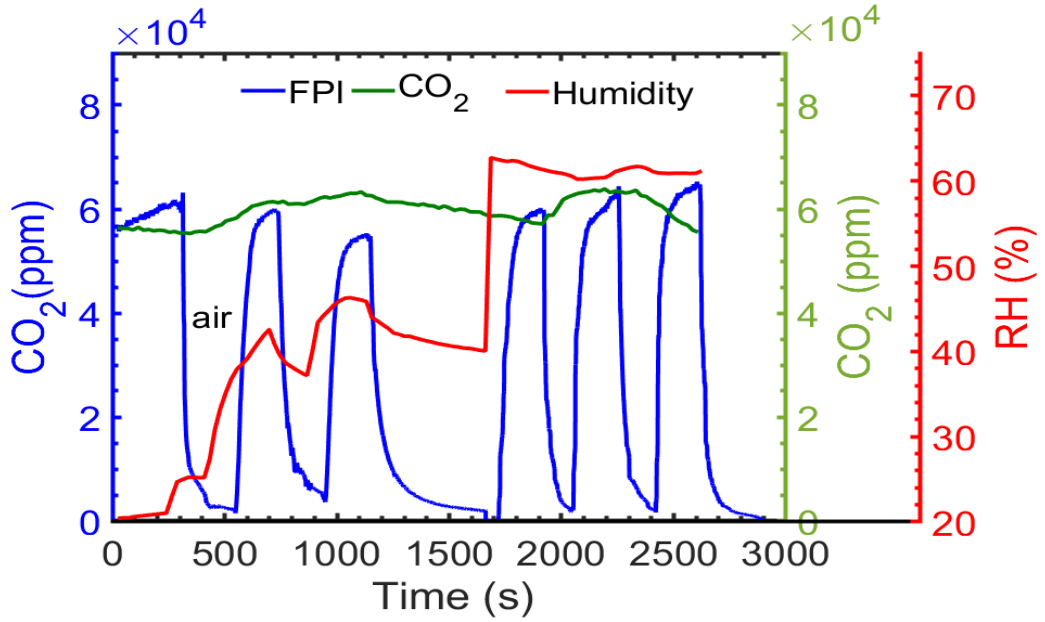
Fig 7.19 (a) Plot of the average reflection of the selected wavelength (between 596 nm to 617 nm) in comparison to RH and temperature change; (b) The wavelength of interference fringes for the response of RH and temperature.

7.4.2.5 *The effect of RH on the CO_2 reading of FPI sensor*

The previous section (7.3) has revealed an inhibition effect of RH on the CO_2 measurement of FPI sensor due to the blocking effect of RH to CO_2. The calibrated FPI sensor prepared above was tested in a CO_2 atmosphere (~6 %) at different RH levels. Fig 7.20b illustrates the consecutive CO_2 measurement of FPI sensor at different RH values. The CO_2 measurement from the FPI sensor is interpreted from the reflection value based on the calibration curve described in Fig 7.17e. It shows that the CO_2 measurement of the FPI sensor in the different RH levels ranging from 20 % to 60 % remains almost the same (~6 %) which is the concentration of CO_2 filled in the chamber according to the reading from the CO_2 datalogger. The maximum percent error compared to the reading of datalogger in Fig 7.20b is about 9 %. This indicates that the CO_2 measurement of FPI sensor is less interfered by RH, which is a significant improvement compared to that of the result in Fig 7.7 (~30 %). The improved immunity of RH for sensing of CO_2 is most likely attributed to the drying process. The lack of water molecules in the pure N_2 atmosphere may have reduced the number of unreacted silanol groups (Si-OH) inside of the silica matrix film and as a result, the film becomes more hydrophobic (as explained in Fig 7.20a). The interaction of the water molecule with the film becomes weak, and no clustered water molecules formed on the mesoporous of the silica film so that the blocking effect is eliminated. As the limitation of the set-up in the generation of very high RH, the CO_2 measurement at very high RH, i.e. >90 %, is not done.



(a)



(b)

Fig 7.20 (a) Schematic explanation of two films that are dried in two conditions, air and dry N_2;(b)The measurement of CO_2 by using FOS in different RH atmosphere; the concentration of CO_2 inside of the chamber is maintained at its maximum of ~6 %. The FPI sensor was alternately exposed to the CO_2 atmosphere and air by inserting in and pulling out the FPI sensor from the chamber.

7.4.2.6 Stability of the CO_2 sensor

The Fig 7.21 illustrates the peak wavelength and the reflection value during the 1-hour continuous recording in an N_2 atmosphere CO_2 at room temperature. The reflection and central wavelength show stable signals under 1-hour continuous illumination. Due to the decomposition of base catalyst (TMAH) inside of film and the toxicity of air to the sensing film, the pH of the sensing film decreases gradually. As a result, the sensor loses its capability for sensing of CO_2 within 15 days when exposing the sensor to ambient air as illustrated in Fig 7.22. The absorbance value at a wavelength around 608 nm gradually decreases to zero leading to the insensitivity of CO_2. It is clear that the longevity of the FPI sensor is thickness dependent, the thicker of the film, the longer lifespan. One layer of coating exhibits a very short lifespan of 1 day after drying, two layers of coating are on the other hand has a longer lifespan of about 10 days. Three layers coating shows an even longer lifespan of 15 days. As

discussed in the previous, storing the sensor in an N_2 atmosphere can significantly extend the lifespan of such sensors.

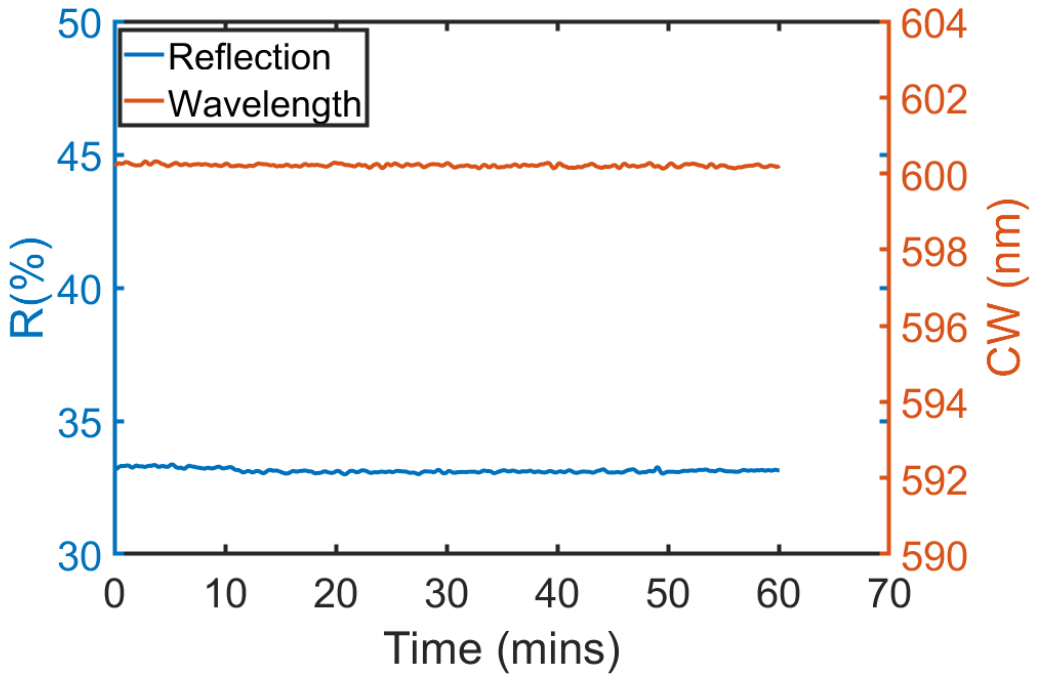


Fig 7.21 The signal of FOS when exposed in a 100% N_2 atmosphere during 1-hour recording.

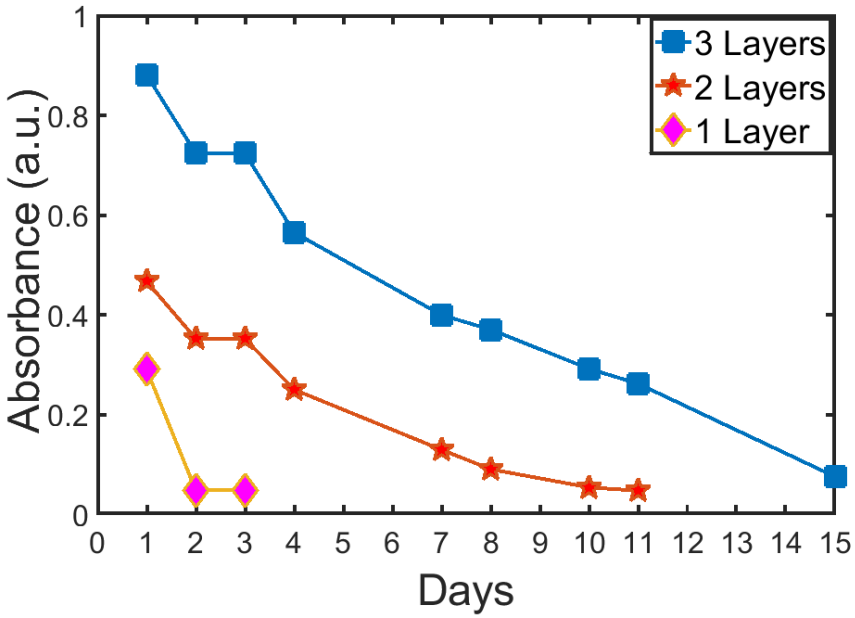


Fig 7.22 Absorbance value as a function of time while storing in ambient air.

7.4.2.7 Comparison of the FPI sensor to FOS

Table 7.2 lists the critical parameters of the FPI sensor in comparison to the FOS described in section 7.3.3.1. Despite the same composition in the coating material, the FPI sensor exhibits a lower sensitivity (a reflection change of 18 % for 5 % of CO_2) compared to the FOS (30 % of reflection change for 5 % of CO_2). The response time of the FPI sensor (98 s) is also much larger than the response time of the FOS (19 s). This is probably attributed to the thicker film (~6 µm compared to ~3 µm) and less porosity of the film after drying in N_2, in which the absence of water molecule in N_2 may induce a higher condensation ratio compared to when it is in air leading to a denser film. The effect of water on the CO_2 sensing of the sensor is reduced. The false signal generated by RH at a zero CO_2 atmosphere is 1.8 % that equals to 232 ppm of CO_2, which is less than that of the FOS (9.5 %, 1855 ppm equivalent) .The blocking effect of RH to the interaction of CO_2 is much improved as the percent error for 6 % of CO_2 down from about 30 % to less than 9 %. The most significant advantage of the FPI sensor compare to the FOS is the capability of directly measuring RH.

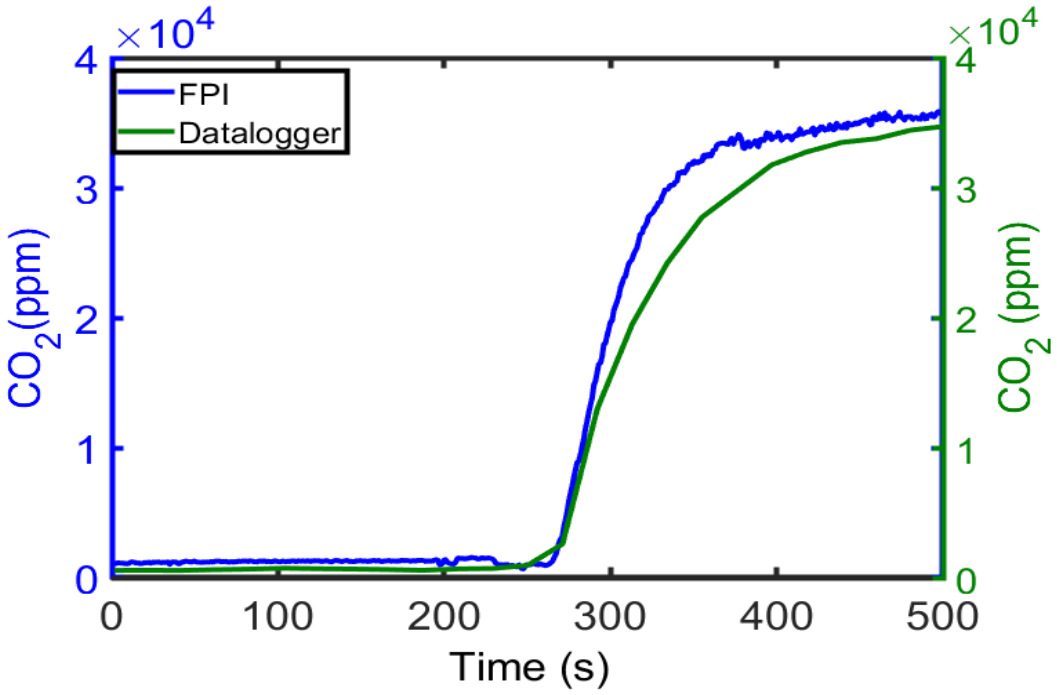
Table 7.2 Comparison of the FPI sensor to the FOS presented in 7.3.3.1

Fibre Sensor	Film thickness	Change of R for 5% CO_2	CO_2 response time	CO_2 equivalent from RH (Max)	Direct measuring of RH	Percent error for 6 % of CO_2 at 50-60% RH
FOS	2.7 ± 0.1 µm	30 %	19 ± 1.6 s	1855 ppm	N/A	~30 %
FPI	5.95 µm	18 %	98 s	232 ppm	0.14 nm/%RH	< 9 %

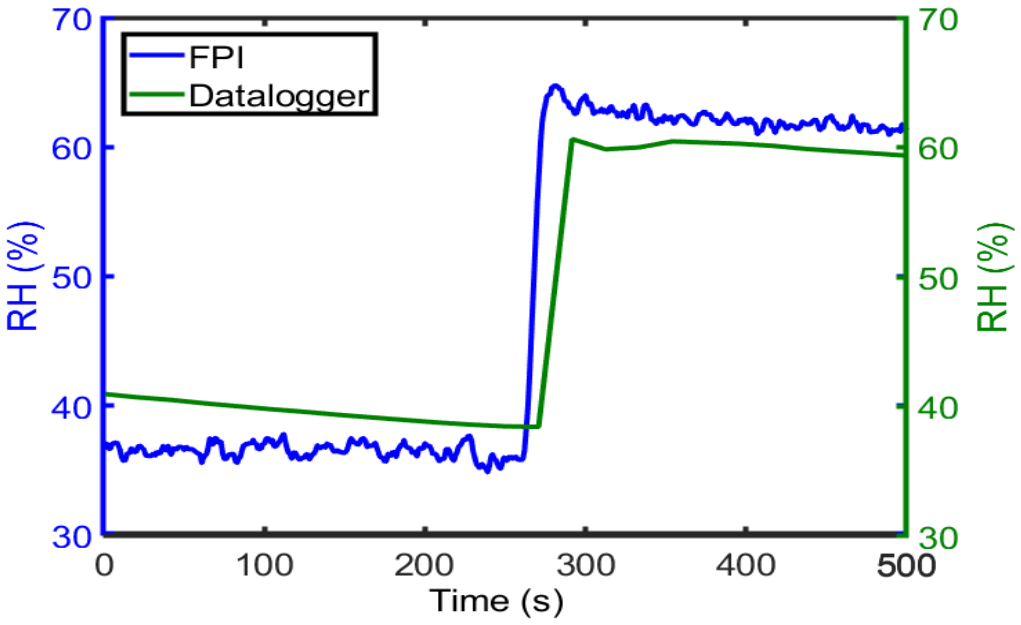
7.5 The measurement of CO_2 and RH from human breath

The above contents have introduced three FOSs for the CO_2 measurement. The one with EC matrix film has poor tolerance to temperature and RH change and cannot be used for breath measurement. The second FOS suffers the blocking effect of RH to CO_2 measurement, the percent error is too big (30 %) for measuring the CO_2 from breath considering the fact that breath gas contains large amount of humidity (>90 %). Therefore, the developed FPI sensor which measures the CO_2 with a percent error of less than 9 % was applied for the breath gas measurement.

Fig 7.23 illustrates the simultaneous measurement of CO_2 and RH from human breath by using the developed FPI based on the set-up in Fig 7.2c. Fig 7.23a and Fig 7.23b demonstrate the measurement CO_2 and RH using the FPI during breathing in comparison to the commercial datalogger, respectively. The datalogger shows that the concentration of CO_2 inside of the Tedlar bag raises from about 0.08 % to 3.5 % after breath and RH level increase from about 40 % to 60 %. The concentration for both parameters is actually less than the normal breath level (5 % CO_2, 90 % RH), this is most likely caused by the dilution of breath gas into the Tedlar bag as it was sealed approximately 100 to 400 mL of air for supporting the commercial sensor and FOS. The measurement reading of CO_2 and RH of the FOS is interpreted from the reflection and wavelength of the fringe by using the calibration curve as described above in Fig 7.17e and Fig 7.18d. It makes a good agreement with the datalogger with a percent error of 3.1 % for CO_2 and 2.2 % for RH. The signal of raising part for both commercial datalogger and FOS includes the breathing process and the gas diffuse time into the Tedlar bag.



(a)



(b)

Fig 7.23 (a) The response of FOS for the CO_2 from human breath gas. (b) The response of FOS for the RH from human breath gas.

The developed FPI exhibits a comparable performance with the commercial CO_2 datalogger in determining the concentration of CO_2 and RH level from the breath

sample. This is achieved with much smaller sensor size and it is probably the smallest sensor that is capable of measuring both CO_2 and RH compared with the other type of sensors that have been reported. This possesses a significant advantage of the FPI for the application in a confined space. For example, a measurement in a sealed environment where the FPI can be incorporated into a needle device without breaking the seal. The FPI can be easily incorporated within a ventilation system for supporting endotracheal intubation by detecting CO_2 expelled from the lungs and monitoring the RH delivered to patient from the ventilation system in the clinical intensive care unit. Due to the long response time of FPI to CO_2 (98 s) compared with the requirement for capnography (< 200 ms), it is difficult for the FPI to detect the CO_2 from breath-to-breath fully. Therefore, the FPI sensor is ideally applied in an application where the response time is less crucial, for example for monitoring the transcutaneous CO_2.

7.6 Conclusion

Two reflection-mode optical fibre CO_2 sensors are fabricated by dip coating a film that contains thymol blue and tetramethylammonia hydroxide doped inside (i) an Ormosil and (ii) an EC film. The colourimetric sensor showed a decrease of absorption value at wavelength of 608 nm when CO_2 concentration increases. The sensitivity of the FOS depends on the concentration of deprotonated dye inside the film. An optimal concentration of dye in the coating solution was found to be 2.9 mg/mL that renders the FOS a sensitivity of about 30 % of reflection change per 5 % CO_2. The sensor shows a gradual reduction in reflection value with each day after they were fabricated. The sensor fabricated with Ormosil film has less sensitivity than that of EC film but with a better tolerance to humidity and temperature and a faster sensor recovery time. Its longevity is completely lost after 10 days when stored in ambient air. This can be significantly improved by storing the sensor in pure N_2 in which the sensor showed a relatively stable reflectivity and an extended shelf life (more than 15 days). The sensor is immune to temperature change (25 ℃ to 40 ℃.) but cross-sensitive to RH with a maximum signal change that is equivalent to a CO_2 reading of 1855 ppm for RH ≤ 65 %. The interaction of CO_2 with the sensor is also subject to the

blocking effect from RH which produces a percent error of ~30 % while measuring 6 % of CO_2 in an atmosphere with RH about 50 %.

A novel FPI sensor for simultaneously measuring CO_2 and RH is presented. It is fabricated by controlling the thickness of the film via the dip coating process (controlling the withdrawing speed). The reflection value located in the absorption window of the deprotonated dye exhibits a reversible response to the concentration of CO_2 in the detection range of 0-6 %. The interference fringes of the FPI showed a linear response to RH with a sensitivity of 0.14 nm/%RH for the range between 0 to 90 %. The sensor demonstrates no cross-sensitivity to temperature between 25 ℃ to 40 ℃. Due to the improved drying process from ambient atmosphere to dry N_2 atmosphere, the CO_2 measurement of the FPI sensor exhibits a neglectable cross-talk to RH (232 ppm equivalent) and a lower sensitivity to CO_2 (18 % of reflection change per 5 % CO_2) compared to the FOS described above. The blocking effect of RH to CO_2 is also found to be minimised with a percent error less than 9 % for 6 % of CO_2.

The FPI sensor is successfully applied for measuring the CO_2 and RH from the exhaled breath sample with a comparable performance compared to the commercial datalogger (a percent error to the reading of commercial datalogger is about 3 % for CO_2, 2.2 % for RH). Due to the long response time (98 s for CO_2, 32 s for RH) and recovery time (418 s for CO_2, 56 s for RH), the FPI sensor is therefore not yet able to replace IR methods for routine breath to breath monitoring in the operating theatre or intensive care settings. However, the reported FPI is suitable for measuring the CO_2 and RH in applications where the response time is less critical. This has the potential of making a low-cost, portable and quantitative CO_2 sensor for the supporting endotracheal intubation in the emergency medicine.

Chapter 8 The simultaneous measurement of CO_2 and NH_3 using FOS

5.8 Introduction

This Chapter introduces the approach of using two colour dyes (thymol blue and tetrakis-(-4-sulfophenyl) porphine (TSPP)) for simultaneous sensing of CO_2 and ammonia (NH_3). The research originally intended to combine the two dyes on the same tip of an optical fibre, however, as they both operate at different pH range for sensing of target gases they are not compatible in one matrix film. In this case, the two dyes are doped inside of two separate films and coated individually on the two tips of a 2×2 optical fibre coupler. The approach demonstrates the novelty of using two dyes with different spectral properties for sensing of two analytes of interest from one detector. The integrated spectrum contains the absorption peaks of the two dyes which have no interference with each other at the selected wavelength. The cross-sensitivity of each dye to the other analyte is evaluated and demonstrates the ability to use this approach for the simultaneous measurement of the two analytes (NH_3 and CO_2) in one atmosphere.

5.9 Method

5.9.1 Sensing mechanism

CO_2 sensing by using the dye, thymol blue, is explained in Chapter 7. Briefly, the reaction is described as the following equation:

$$CO_2 + H_2O \rightleftharpoons H_2CO_3 \rightleftharpoons H^+ + HCO_3^- \quad (8.1)$$

The dissolved CO_2 reacts with the water molecule (H_20) to form carbonic acid (H_2CO_3) which partly dissociates to hydrogen ion (H^+) and bicarbonate ion (HCO_3^-). The hydrogen ion is the proton donor for the dye (thymol blue) that changes its colour.

The sensing of gaseous NH_3 is determined by the TSPP which has intense absorption bands (Soret bands) at around 420-480 nm and a weaker band (Q-band) in the region

of 500-700 nm [305]. The exact absorption peak depends on the aggregated status of molecules in the film [305]. The TSPP undergoes a molecular transform after interaction with NH_3 as illustrated in Fig 8.1. The interaction between NH_3 and TSPP leads to the deprotonation of the TSPP pyrrole ring and the formation of ammonium ions (NH_4^+). As a result, the deprotonation leads to the disruption of J-aggregation and the absorption spectra is changed correspondingly (mainly at 470 and 706 nm) [306, 307].

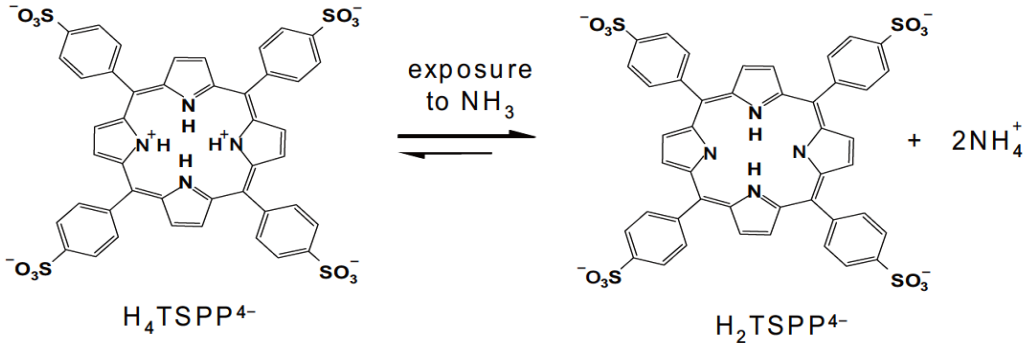


Fig 8.1 Schematic representation of the interaction between TSPP and NH_3 [104].

There are two distinct wavelengths (600 nm and 511 nm) located separately at the two absorption peaks of the two dyes (TSPP and alkalic thymol blue) in the integrated absorption spectrum, in which the colour change of one dye does not affect the intensity value of the other wavelength. The wavelength of 600 nm is from the absorption of alkalic thymol blue and 511 nm is from the TSPP. Such spectral property of the two dyes renders the multiple sensing for NH_3 and CO_2. The thymol blue and TSPP are doped separately into a silica sol-gel film and EC polymer film and dip coated on the two distal ends of optical fibre coupler, respectively. The thymol blue and the phase transfer that is used for sensing of CO_2 are co-doped into Ormosil via the sol-gel method as decribed in the previous Chapter (Chapter 7). The EC polymer film that is used to encapsulate TSPP is formed via the coalescence of an EC polymer chain with a plasticiser (tributyl phosphate) under heat treatment (the same matrix film as introduced in Chapter 7).

5.9.2 Sensor characterisation

The sensor response for CO_2 and NH_3 was conducted separately by using the same experimental set-up shown in Fig 8.2. For measuring of CO_2, the chamber is initially filled with N_2 gas (100 %) and then the concentration of CO_2 is gradually increased step-by-step from 0 to 60 000 ppm via regulating the flow of CO_2 gas. Each step is maintained for at least 5 mins to obtain a stabilised signal for each concentration. The decrease of the concentration of CO_2 is conducted by flowing N_2 into the chamber. The reflection spectrum of the FOS is recorded simultaneously along with the reading from the CO_2 datalogger.

The concentration of gaseous ammonia inside the chamber is regulated by adding subsequently 2 mL of different concentrations of ammonium hydroxide (NH_4OH) solutions (100-1000 ppm) into the beaker inside the chamber. Each solution is retained for 15 mins to reach equilibrium between the released NH_3 gas and the NH_3 reservoir. The generation of NH_3 from the ammonium hydroxide solution can be explained as:

$$NH_3(gas) \rightleftharpoons NH_3(aq) \tag{8.2}$$

$$NH_3(aq) + H_2O \rightleftharpoons NH_4OH \rightleftharpoons NH_4^+ + OH^- \tag{8.3}$$

The process involves two equilibriums, the first one in Eq 8.2 reflects the release of NH_3 from the solution into the air. And the second demonstrates the conversion of NH_3 to NH_4OH.

The NH_3 concentration inside the chamber after 15 mins is measured by using a commercial ammonia colourimetric gas detection tube (Honeywell, UK). The reversibility of the developed ammonia sensor is tested by adding 100 µL of HCl solution into the container.

The intensity value of the wavelength at 600 nm and 511 nm of the reflection spectrum are used for the response of CO_2 and NH_3, respectively. The LOD is defined as $LOD=3 \times \delta/S$, where δ is the standard deviation and S is the sensitivity of the sensor derived from the calibration curve.

5.9.3 Experiment set-up

The sensor characterisation was performed using the set-up in Fig 8.2. A halogen light source (HL-2000, Ocean Optics, UK) is used to launch light into the optical fibre from one arm of the coupler (2×2, 3dB, F-CPL-M22855, Newport, UK), and the reflected light is detected from the another arm by using a CCD spectrometer (USB 2000, Ocean Optics, UK) which is connected to a computer for post-processing.

The two tips were inserted into a test chamber (15cm (L) ×13cm (W) ×8cm (H)) which has an input channel and output channel for gas infusion and expulsion respectively. A commercial CO_2 data logger (K-33 BLG, CO_2 Meter, USA) was positioned inside the chamber for calibration purposes. The concentration of CO_2 inside the chamber is regulated by mixing N_2 and CO_2 gas.

A 20 mL glass beaker situates inside of the chamber as a reservoir for adding of the NH_4OH solution.

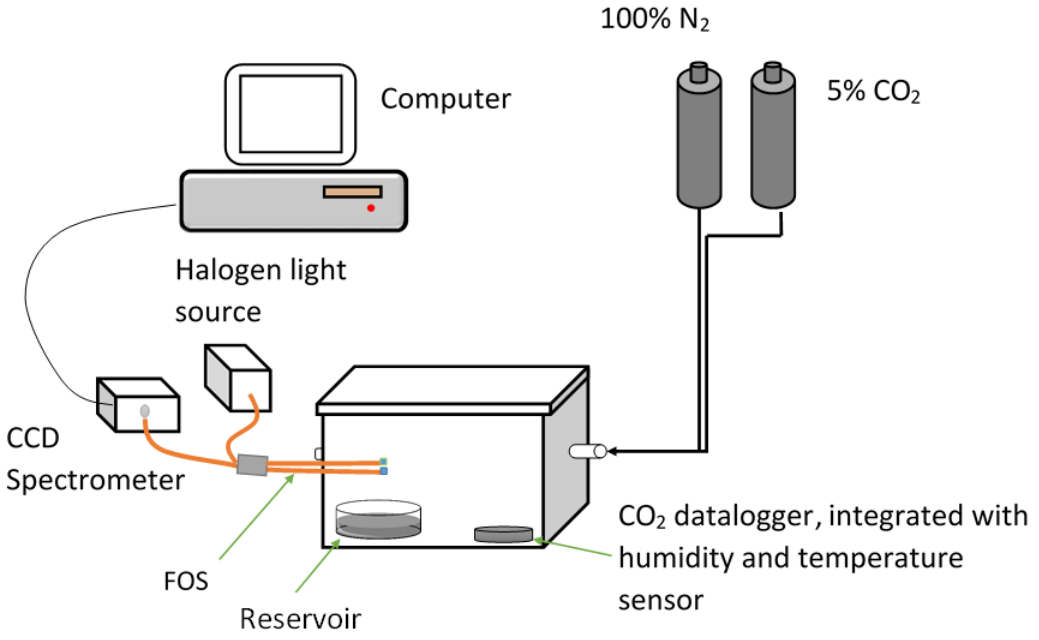
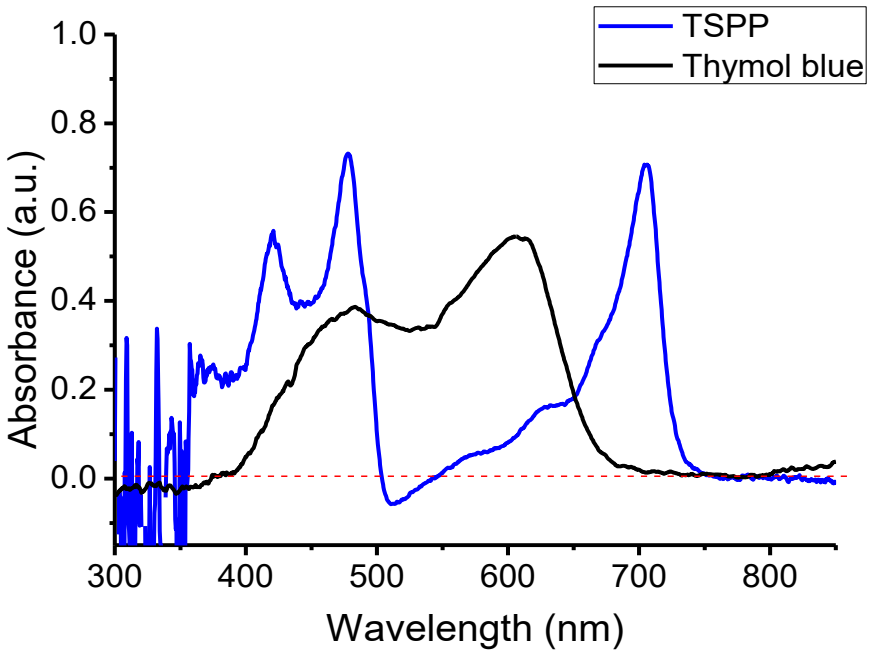


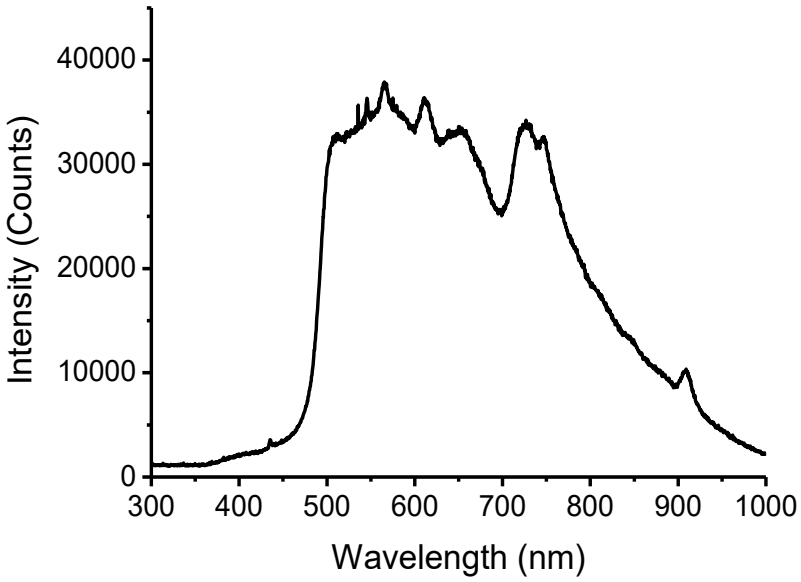
Fig 8.2 Schematic set-up of the sensor calibration; the two tips of the FOS were coated with two different films for sensing of CO2 and NH_3, respectively.

5.10 Result and discussion

Fig 8.3a illustrates the absorbance spectrum of the two coated films, which is measured from the tip of the optical fibre individually. The spectral property of thymol blue in the sol-gel film is the same as described in the previous Chapter (Chapter 7). The absorption spectrum of TSPP in the polymer film exhibits three distinction absorption peaks at the wavelength of 420nm, 478nm and 705nm respectively. The peaks are in accordance with the observation in previously published work [141]. Additionally, there is a weak negative absorption peak at the wavelength around 511nm that has not been reported previously by using the LBL deposition techniques in [141], and it exhibits a response to NH_3 concentration as illustrated in Fig 8.6d. Since the spectral property of TSPP can be manipulated by the interaction of the adjacent molecules [308], the negative absorption value is probably due to the fluorescent emission of the TSPP induced by the special arrangement of molecules in the polymer film. The reflection spectrum from two tips of the FOS is illustrated in Fig 8.3b.



(a)



(b)

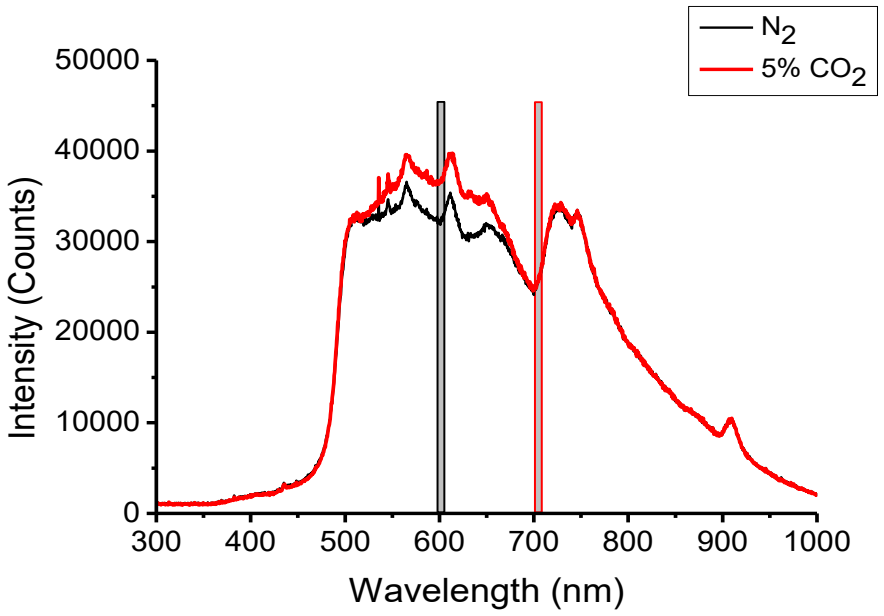
Fig 8.3 (a) The absorption spectrum of TSPP doped into the polymer film and the thymol blue doped into a sol-gel film; (b)The integrated reflection spectrum from the two tips of the FOS.

From Fig 8.3a, the TSPP has a distinct absorption peak of 705 nm from thymol blue so that the intensity change at this wavelength in the reflection spectrum (illustrated in Fig 8.3b) is attributed exclusively to the absorbance change of TSPP. The absorption peak of thymol blue at 600 nm partially overlaps with the absorption of the TSPP film. However, the intensity of this wavelength does not have a significant change in response to NH_3. Thus, the intensity change of this wavelength in the reflection spectrum is considered to be a result of the absorption change of thymol blue.

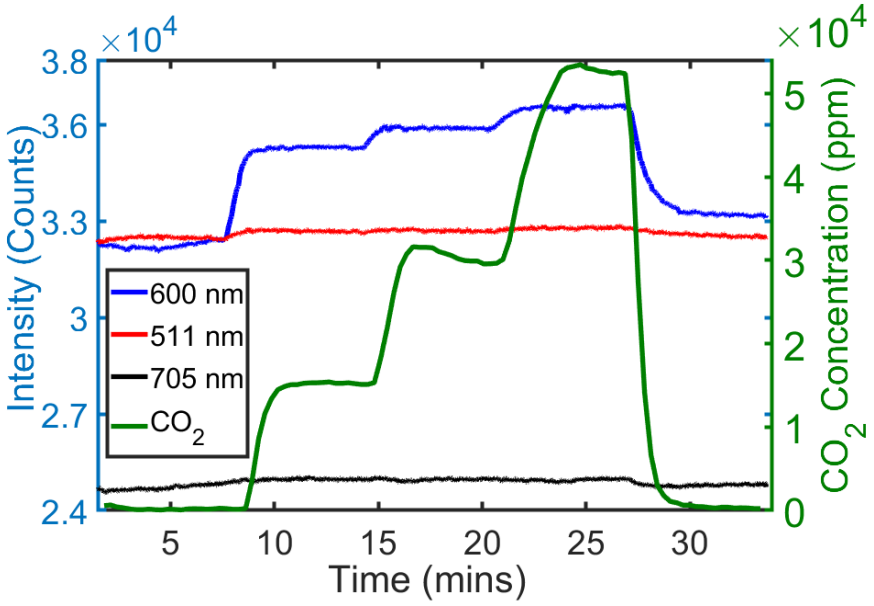
5.10.1 The measurement of CO_2

Fig 8.4a illustrates the reflection spectrum of the FOS at N_2 and CO_2 (~5 %) atmosphere. There is an increase in intensity in the region between 517 nm to 684 nm after the FOS is exposed into 5 % CO_2 compared with that of the N_2 atmosphere. Such an increase is due to the colour transmission of thymol blue after interaction with CO_2. The intensity value around 700 nm and 500 nm, on the other hand, remains unchanged indicating that there is no colour change of TSPP in the presence of CO_2. The response of the dynamic intensity of the three wavelengths (511 nm, 600 nm

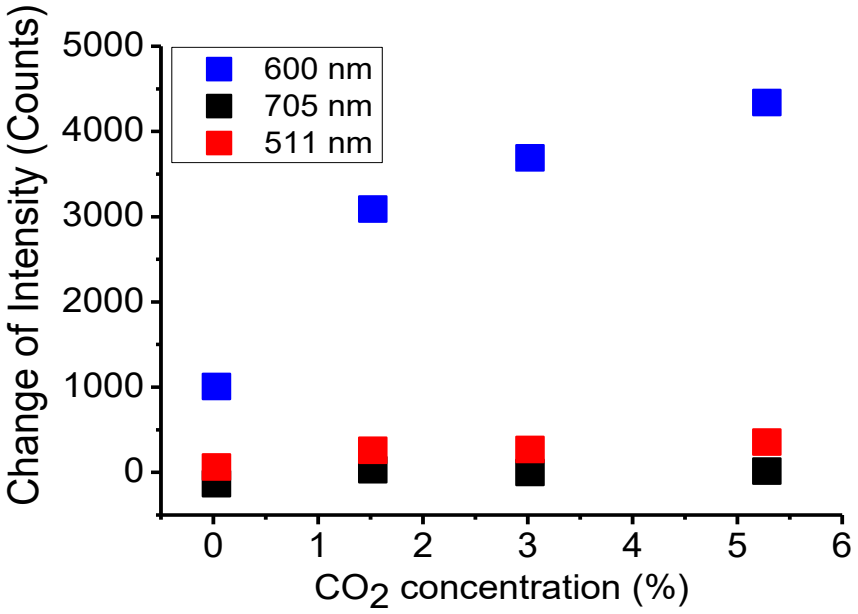
and 705 nm) to the concentration of CO_2 is illustrated in Fig 8.4b. The intensity of 600 nm increases as the increase of the concentration of CO_2 while the intensity of the 705 nm and 511 nm show stable values. The intensity changes to the concentration of CO_2 is illustrated in Fig 8.4c. The intensity of 600 nm has a higher magnitude change at higher concentration of CO_2 with an increase of 4339 Counts (equals to ~15 % of the intensity increase) in intensity for ~5 % of CO_2. The intensity value fits logarithmically to the concentration of CO_2 as illustrated in Fig 8.4d with R^2= 0.981.



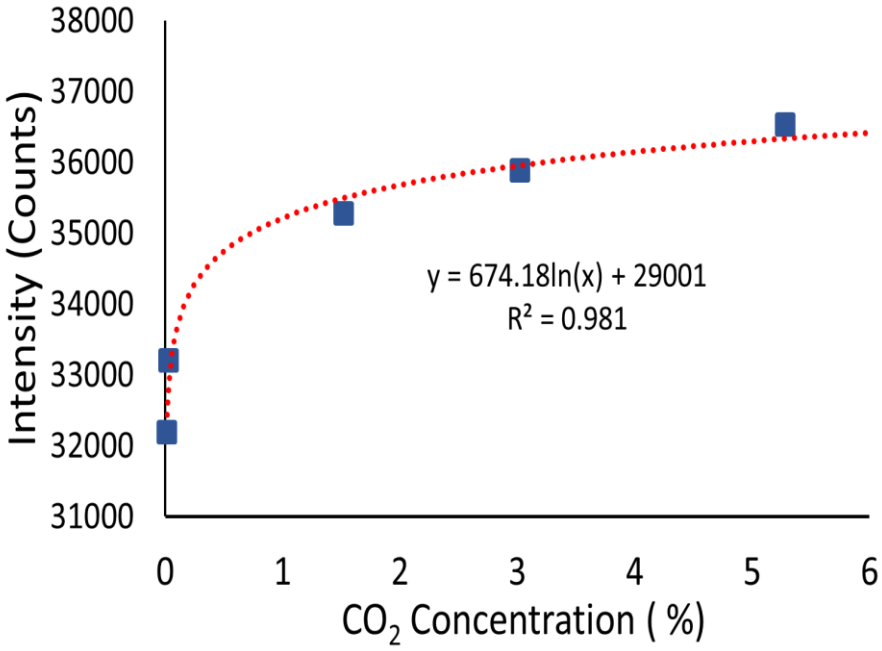
(a)



(b)



(c)



(d)

Fig 8.4 (a) Reflection spectrum of the FOS at N_2 and CO_2 atmosphere. The NH_3 is considered as atmospheric level (~0 ppm); (b)The intensity value of the wavelength of 600 nm and 705 nm responses to the concentration of CO_2; (c) The change of intensity of the two wavelengths as a function of CO_2 concentration; the error bars are smaller than the marker size; (d)The intensity of the wavelength at 600 nm as a function of CO_2 concentration; the error bars are smaller than the marker size.

5.10.2 The measurement of NH_3

As explained in Eq 8.1 and 8.2, the concentration of gaseous NH_3 inside of the chamber is proportional to the concentration of the NH_3 in the solution according to Henry's gas law [309], the latter is determined by the concentration of NH_4OH solution. Its actual value corresponding to the concentration of ammonium hydroxide is shown in Fig 8.5, which exhibits a linear correlation with a slope of ~0.2.

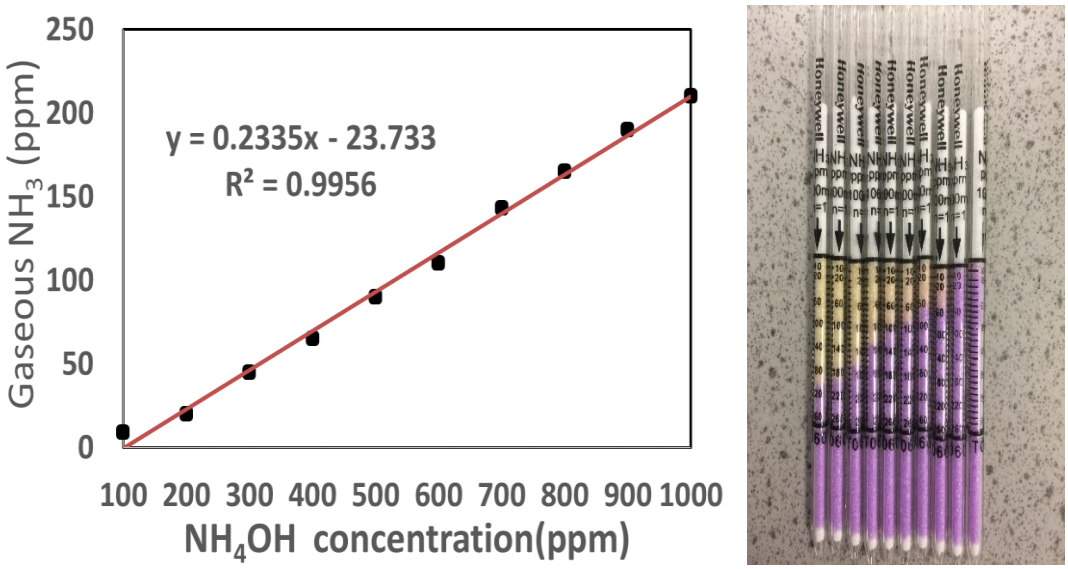
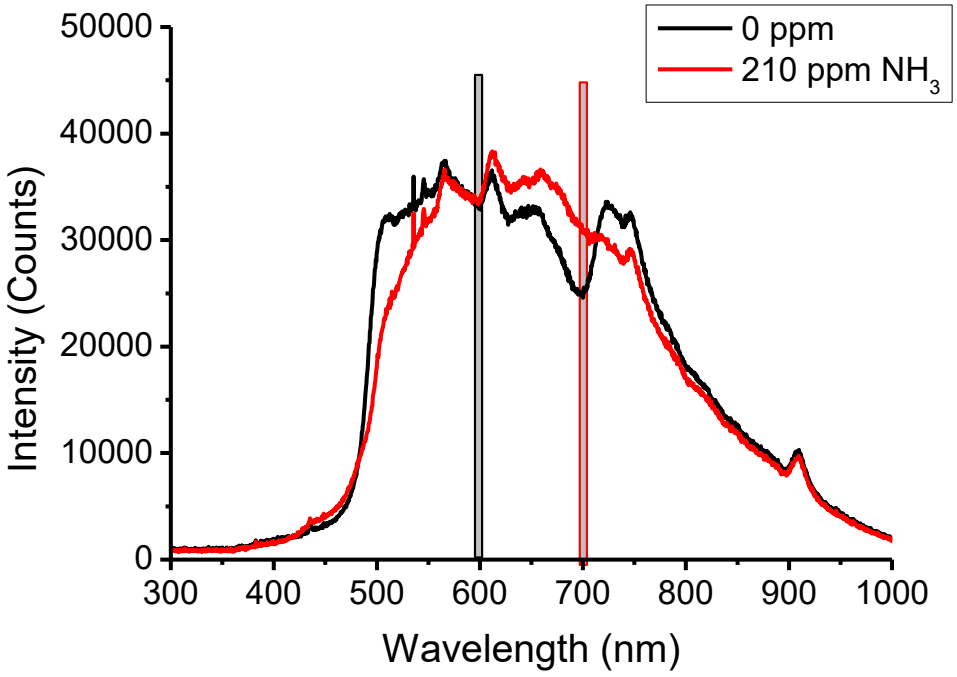


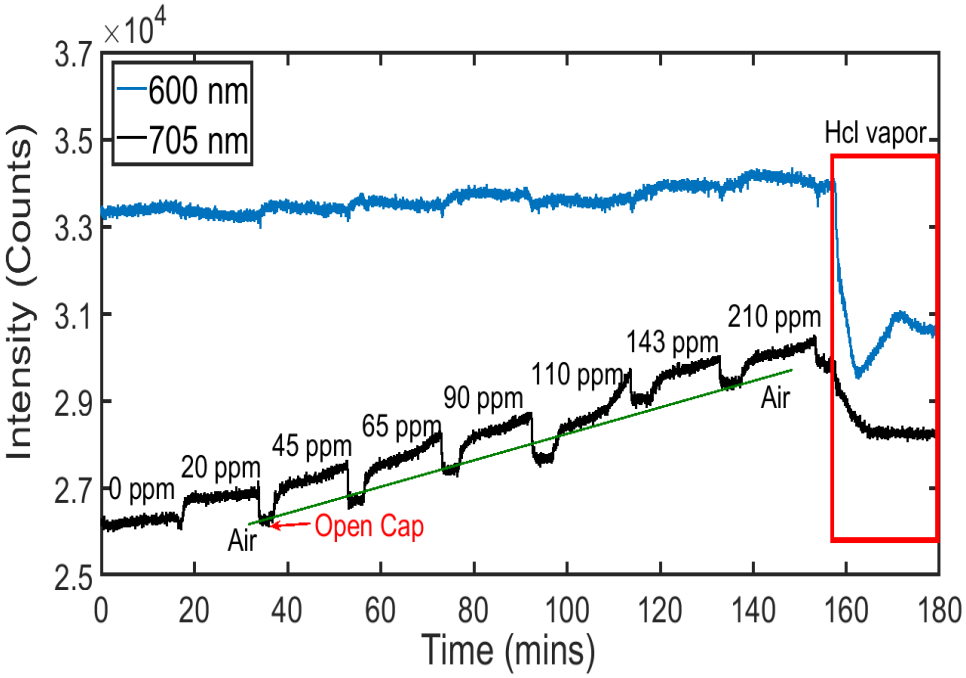
Fig 8.5 NH_3 gas in the chamber as a function of the concentration of NH_4OH in solution; each point in the graph is obtained from the reading of the colourimetric tube (right-hand side).

The response of the FOS to ammonia is illustrated in Fig 8.6. Its reflection spectrum changes after exposing the sensor to the ammonia atmosphere (210 ppm) as a result of the deprotonation effect caused by ammonia (Fig 8.6a). The wavelengths around 478 and 705 nm undergo an increase in their intensity while the wavelengths around 511 nm have a decrease. The different tendency of intensity change at the different wavelengths agrees with the report in [141]. The dynamic intensity of the two wavelengths (600 nm and 705 nm) for the response of NH_3 is illustrated in Fig 8.6b. The intensity value of 705 nm increases at each concentration of NH_3. It has a rapid increase in the initial part after the solution is added and then gradual increase within the observation time (15 mins). Such the pattern of intensity change is due to the equilibrium between gaseous NH_3 and NH_4OH solution. And the signal demonstrates incomplete reversibility with a decrease in intensity after removing the sensor back

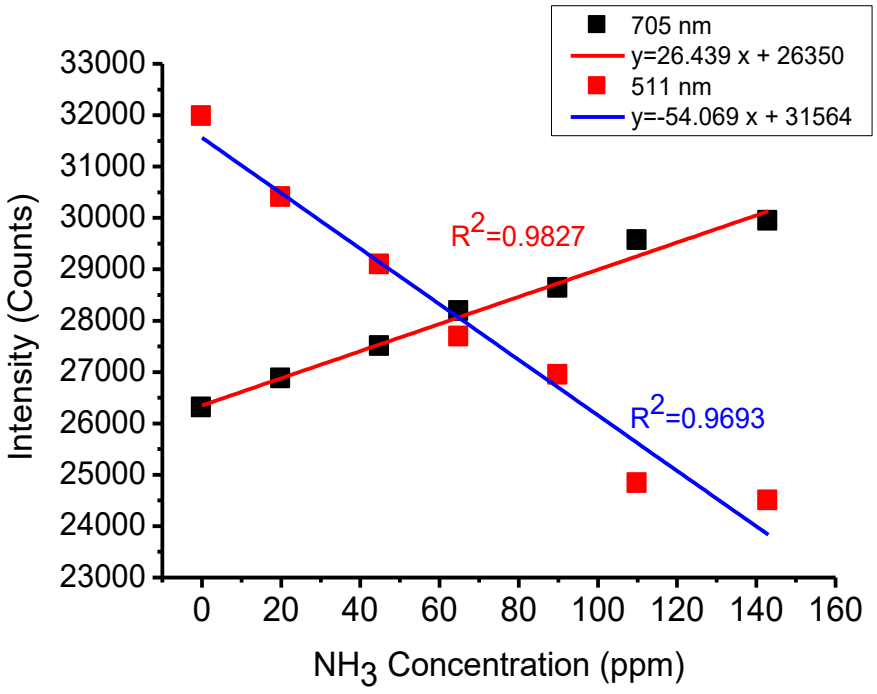
to atmospheric air. It is predictable that the sensor will lose the capability of sensing NH_3 after continuous exposure to a higher concentration of NH_3. The intensity of 705 nm shows a linear correlation to the concentration of NH_3 as illustrated in Fig 8.6c. On the other hand, the wavelength of 511 nm shows a decrease in intensity as increasing the concentration of NH_3. It shows a sensitivity of - 54 Counts/ppm which is double that of the wavelength of 705 nm (26 Counts/ppm) for the detection of NH_3. The LOD of the two wavelengths is calculated as 4.3 and 9 ppm, respectively. Due to the oppsoite change of the intensity of the two wavelengths in response to ammonia, a ratio of two wavelenths (705 nm over 511 nm) is taken as the siginal for sensing of ammonia that reveals a sensitivity of 0.003 /ppm and an LOD of 3.9 ppm. While exposing the FOS into the HCl atmosphere, the vapour protonates the TSPP compounds and reverses the signal for retrieving the ammonia sensing capability. However, the intensity at 600 nm has a significant drop in intensity in the HCl atmosphere. The reflection spectrum of the FOS before and after HCl exposure is illustrated in Fig 8.6f. It is seen that the absorption band around 705 nm becomes bigger due to the recovery by HCl. However, the wavelengths between 500 to 600 nm have a significant decrease. Such a decrease is caused by the blue shift of the absorption band of the thymol blue induced by the low pH (<2). In this case, the colour of thymol blue changes from blue to red. The individual reflection spectrum of the thymol blue sol-gel film is illustrated in Fig 8.7g, in which the absorption band shifts to a lower wavelength after exposure to HCl vapour indicating the intolerance of such film to the acidic vapour.


0 ppm
210 ppm NH3
Intensity (Counts)
Wavelength (nm)
50000
40000
30000
20000
10000
0
300
400
500
600
700
800
900
1000

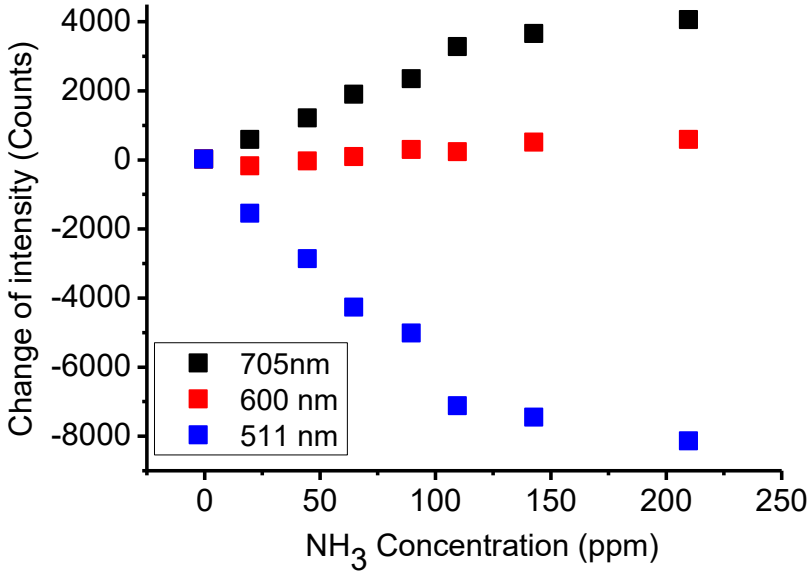
(a)


×10^4
600 nm
705 nm
Hcl vapor
0 ppm
20 ppm
45 ppm
65 ppm
90 ppm
110 ppm
143 ppm
210 ppm
Air
Open Cap
Air
Intensity (Counts)
Time (mins)
3.7
3.5
3.3
3.1
2.9
2.7
2.5
0
20
40
60
80
100
120
140
160
180

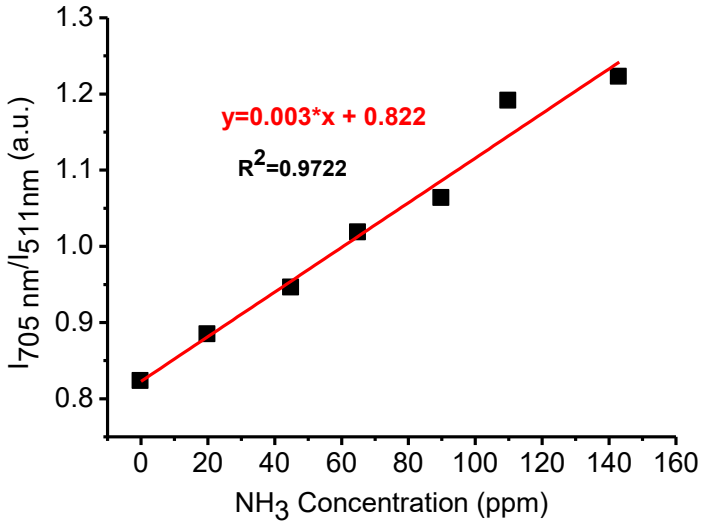
(b)


705 nm
y=26.439 x + 26350
511 nm
y=-54.069 x + 31564
R2=0.9827
R2=0.9693
Intensity (Counts)
NH3 Concentration (ppm)

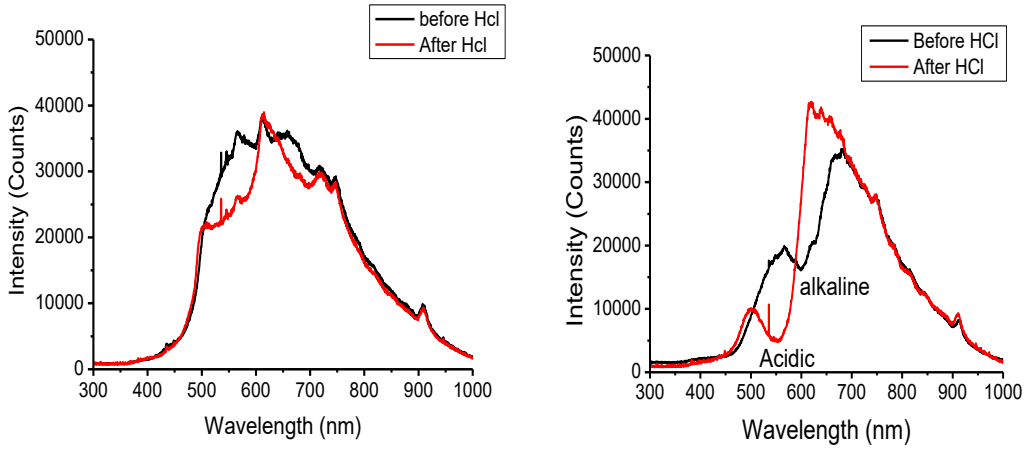
(c)


705nm
600 nm
511 nm
Change of intensity (Counts)
NH3 Concentration (ppm)

(d)



(e)



(f) (g)

Fig 8.6 (a) Reflection spectrum of the FOS at 0 and 210 ppm of NH_3; (b) The intensity of the two wavelengths at 600 and 705 nm in response to the concentration of ammonia; (c) The ammonia response of the intensity at two wavelengths: 705 nm and 511 nm; (d) The change of the intensity of different wavelengths to the concentration of ammonia; (e) The ammonia response of ratio of the two wavelengths; (f) Reflection spectrum of the FOS before and after exposure to HCl vapour; (g) Reflection spectrum of the thymol blue sol-gel film before and after exposure to HCl vapour.

Fig 8.6d illustrates the intensity change of three wavelengths in response to the concentration of NH_3 gas. There is a negligible increase of the intensity at the

wavelength of 600 nm, and the other two wavelengths show the opposite the direction of intensity change.

The two dye compounds that are used for sensing of CO_2 and NH_3 in the above experiment are pH dependent. The CO_2 sensitive dye (thymol blue) can only work in the presence of alkalic phase transfer as explained in Chapter 6. The NH_3 sensitive dye (TSPP), however, can only work when the pH is neutral or acidic. Therefore, the spectrum in Fig 8.3a which contains the absorption region for both NH_3 and CO_2 sensing cannot be obtained by doping the two dyes into one matrix film. In other words, the combination of the two dyes into one matrix film for the simultaneous measurement of CO_2 and NH_3 cannot be achieved. Efforts have been made to fabricate a hybrid film by depositing the two films with one on the top of the other to the tip of the optical fibre. However, it is found that the two sensitive films are not compatible to fabricate a hybrid film since one film does not survive in the other coating solution due to different pH value. Therefore, the sensor configuration with the two tips for each film is considered as the best design at this stage. Besides, such a configuration can leave the CO_2 sensing tip out of the HCl vapour while regenerating the ammonia sensor.

The sensing of CO_2 and NH_3 is a process of protonation and deprotonation of the relevant dye. The CO_2 is an acidic gas, and it reacts with water forming carbonic acid which is the proton donor. However, the majority of CO_2 (more than 99 %) in water exists as the dissolved gas and less than 1 % as carbonic acid [310]. In the CO_2 sensing film, the doping of alkaline phase transfer (TMAH) provides abundant hydrate molecule due to the formation of ion-pair with the dye and the equilibrium in Eq 8.1 shifts to the right side, and as a result, more dissolved CO_2 is converted into carbonic acid. Besides, the base doped in the film provides a higher pH that enhances the solubility of CO_2 (as a result of the shift in the equilibrium). When it comes to the NH_3 sensing film, the ambient water content is not enough to produce sufficient proton to change the spectral property of the TSPP.

On the other hand, the NH_3 is an alkalic gas and acts as a proton receptor that deprotonates the TSPP molecule. Its solubility is very low in a high pH value of water medium due to inhibition of the dissociation of ammonia hydroxide in Eq 8.3. As a

result, diffusion of NH_3 into the CO_2 sensitive film is very low leading to the non-cross-sensitivity of NH_3.

The FOS presented in this Chapter is to validate the idea of using two dyes (TSPP and thymol blue) for the simultaneous measurement of two gases. The results demonstrate the feasibility of the approach. The LOD of NH_3 is 4.3 ppm which is too low for the breath gas analysis (in ppb level). Optimisation of the FOS can be investigated in the future, i.e. the concentration of TSPP for the purpose to improve the sensitivity of NH_3. RH is also considered to be an issue as well and still needs to be investigated.

5.11 Conclusion

A novel approach of using two sensitive dyes (TSPP and thymol blue) with differential spectral property for simultaneously measuring of CO_2 and NH_3 is introduced. Due to the incompatibility in pH of the two dyes for the sensing of the gases, the two dyes are doped separately into a matrix film and dip coated on the two tips of the fibre coupler which integrates the signal from two tips to one detector. The reflection spectrum of the FOS contains the spectral information of the two dyes. The wavelength of 600 nm in the spectrum shows a distinctive response to CO_2 concentration as a result of the protonation of thymol blue. It exhibits a logarithmic increase in intensity to the concentration of CO_2 with an intensity increase ~15 % in response to ~5 % of CO_2 . Two wavelengths, 511 nm and 705 nm from the spectrum, are found to be sensitive to NH_3 due to the deprotonation of the TSPP. The intensity value of the two wavelengths exhibits an opposite change responding to the concentration of NH_3 . The ratio of the two wavelengths (705 nm over 511 nm) shows an linear response to the concentration of NH_3 with a sensitivity of 0.003 /ppm and LOD of 3.9 ppm. Despite low sensitivity to NH_3 for the application of breath gas analysis, the FOS offers the opportunity of exploring applications where both gases are required to be measured, for example, monitoring air quaility in industry.

Chapter 9 The detection of carboxyl-fentanyl using LPG functionalised with MIP nanoparticles

9.1 Introduction

As introduced in Chapter 1, monitoring of fentanyl has significant impact for the drug administration of patients in intensive care. A low-cost, portable and real-time monitoring device would be beneficial. Molecularly imprinted polymer (MIP) technology has bright future in the molecular diagnostic due to its ability to bind small molecules and is an alternative to antibodies [311]. The advantage of MIPs over traditional antibodies is their low cost and stability in ambient temperature [312]. Molecularly imprinting is defined as ''the construction of ligand-selective recognition sites in synthetic polymers where a template is employed in order to facilitate recognition site formation during the covalent assembly of the bulk phase by a polymerisation process, with removal of the template being necessary for recognition to occur in the spaces vacated by the templating species'' [313]. The process is schematically presented in Fig 9.1 where the template is mixed with the polymerisation mixture and cured either thermally or by UV light resulting in an insoluble matrix in which the template sites reside. The template is then removed from the imprinted polymer by washing with a solvent or through a combination of chemical treatments and washing steps, leaving behind binding sites that are both spatially and chemically complementary to the template molecules. Therefore, the template or its structural analogues may then be selectively rebound to the polymer in the sites vacated by the template. The formation of reversible interactions between the template and polymerizable functionality may involve one or more chemical interactions as illustrated in Fig 9.1: (A) reversible covalent bond, (B) covalently attached polymerizable binding groups that are activated for non-covalent interaction by template cleavage, (C) electrostatic interaction, (D) hydrophobic or van der Waals interaction and (E) coordination with a metal centre.

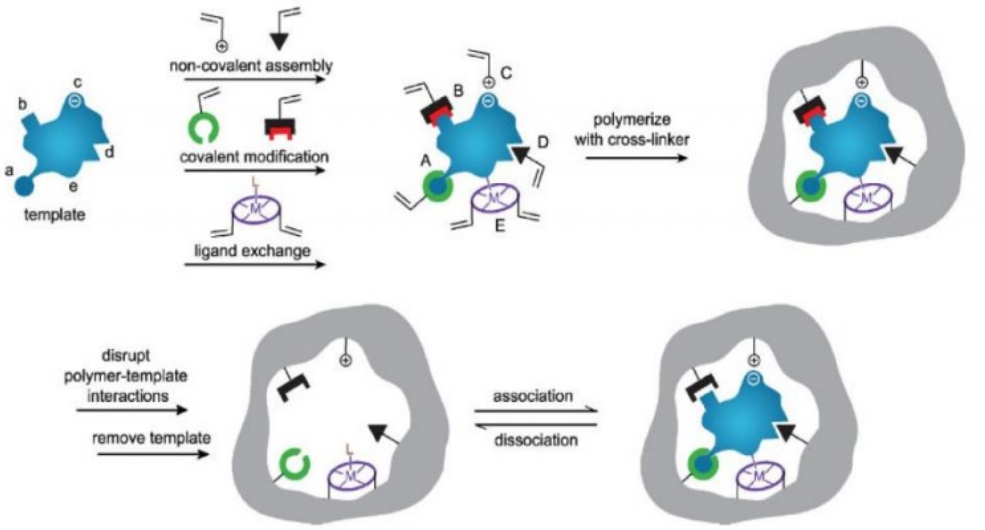


Fig 9.1 A schematic representation of the molecular imprinting process [313].

This chapter describes an LPG-based biosensor that is functionalised with MIP nanoparticles for the detection of carboxyl-fentanyl which is a modified fentanyl structurelly similar to fentanyl (shown in Fig 9.2). The MIPs that are synthesised by a group from the University of Leicester are successfully deposited on an LPG (grating period: 111.5 µm, grating length: 1.5cm) sensor surface via EDC/NHS linkers. A second LPG sensor with a grating period of 110 µm, length of 1.5 cm was inscribed on the same fibre (1 cm away from the coated LPG) as a reference sensor for compensating the temperature change during the carboxyl-fentanyl detection. The LPG sensor is used for the detection of carboxyl-fentanyl in solution with a concentration range from 0 ng/mL to 1000 ng/mL.

9.2 Method

9.2.1 Sensing based on molecularly imprinted techniques

Fentanyl, whose chemical structure is shown in Fig 9.2, is imprinted by using a solid-phase synthesis method described in [314]. Instead of having a polymer film, this method produces synthesised polymer nanoparticles. These MIP nanoparticles overcome the perceived drawbacks of the ground MIPs film, which includes binding site heterogeneity [315] and leaching of the residual template from the polymer [316]. In addition, nanoMIPs can be easily integrated with sensors. The fentanyl MIP

nanoparticles are synthesised and provided by Sergey Piletsky's group, University of Leicester, UK. The nanoparticles have recognition cavities that will selectively bind fentanyl or fentanyl analogues.

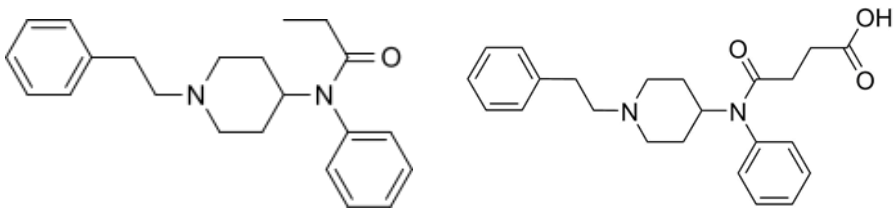


Fig 9.2 Chemical structure of fentanyl (left) and carboxyl-fentanyl (right).

An LPG sensor that is surface coated with the fentanyl MIP detects carboxyl-fentanyl molecules presented in the sample by detecting RI change induced by the binding of carboxyl-fentanyl to the LPG sensor.

9.2.2 Experimental procedure

Different concentrations of carboxyl-fentanyl solutions were prepared by dissolving the carboxyl-fentanyl powder into a solvent that contains a mixture of methanol and water in a ratio of 1:3 v/v with a concentration range from 0 to 1000 ng/mL. A bare LPG sensor with a grating period of 111.5 µm was used to evaluate the bulk RI caused by the concentration of carboxyl-fentanyl by subsequently immersing the LPG in the blank sample (0 ng/mL) and 1000 ng/mL carboxyl-fentanyl solution. For the measurement of carboxyl-fentanyl, the LPG array sensor was subsequently exposed to the different concentration of carboxyl-fentanyl for 20 mins each, followed by washing with distilled water three times and drying with N_2 between each immersion. The experiment set-up is illustrated in Fig 9.3 in which the two LPGs (coated and uncoated) are placed inside a Teflon fibre bath. Two ends of the LPG array are connected to a halogen light source (Ocean Optics, HL-2000) and a CCD spectrometer (Ocean Optics, HR4000) for launching light into the fibre and detecting the transmission spectrum of the LPGs.

The temperature calibration of the LPG array is conducted by using the set-up described in Fig 3.11, Chapter 3. The temperature of the water bath was programmed to increase the temperature step by step from 20 ℃ to 27 ℃ (this range of

temperature should have covered the fluctuation of room temperature) with an increment of 1 ℃ in each step. Each step is allowed to stabilise for at least 5 mins.

The sensor reversibility test was done by initially immersing the LPG array into gently boiling methanol (temperature around 65 ℃) for 10 mins with heating applied from a heating plate and then followed by subsequently immersion into a blank sample (the solvent only) and the 1 µg/mL of carboxyl-fentanyl solution for the rebinding tests.

Scanning electron microscopy (SEM) imaging of the MIP nanoparticles coated optical fibre is performed to validate surface coverage of the coating. The fibre was coated with approximately 8 nm of iridium to increase the conductivity of electrostatic discharge by using a sputter coater (Q150V, Quorum, UK), and then imaged by using Scanning electron microscopy (SEM) (JEOL 7100F, UK).

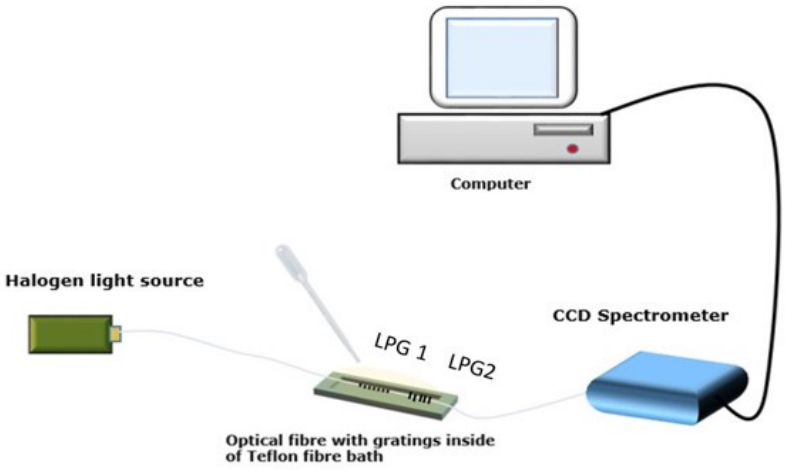


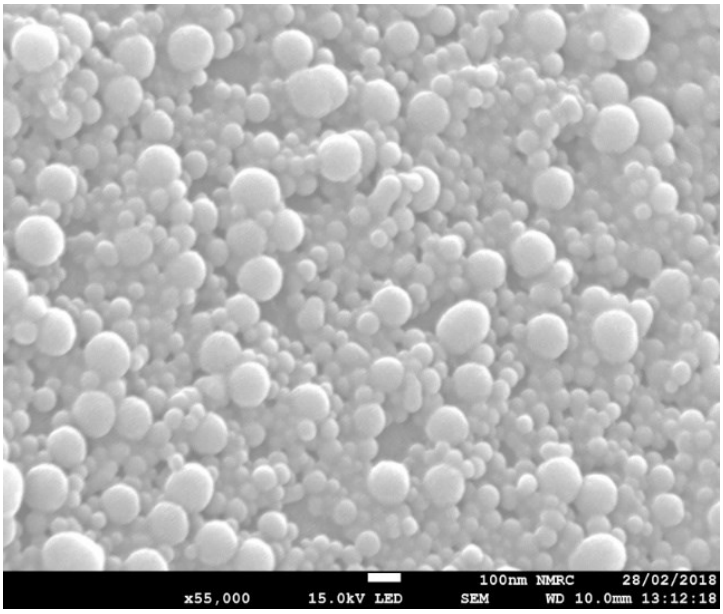
Fig 9.3 Experimental set-up of the LPG sensing system for the detection of carboxyl-fentanyl.

9.3 Results and Discussion

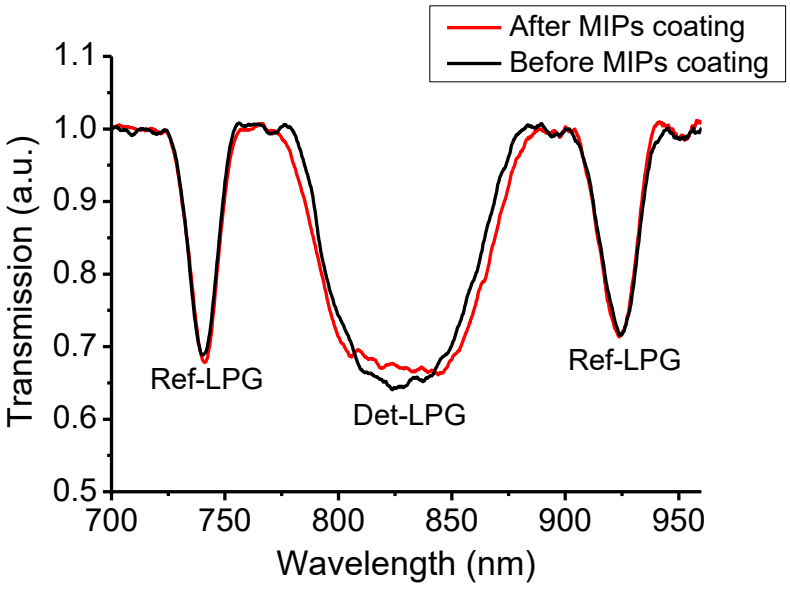
9.3.1 MIP nanoparticles on the optical fibre

The MIP nanoparticles are synthesised in the template of carboxyl-fentanyl by cross-linking monomers containing methacrylic acid. This renders the carboxyl group (-COOH) on the surface of nanoparticles, which are further activated by the coupling agent, EDC/NHS, to covalently attach to the amine group ($-NH_2$) functionalised

optical fibre surface. Fig 9.4a shows the SEM image of MIP nanoparticles after coating on the optical fibre. The attachment of MIP nanoparticles can be observed from the image. Fig 9.4b illustrates the transmission spectrum of the LPG array sensor before and after attaching MIP nanoparticles (surrounding medium is air). It is clear that the reference LPG (Ref-LPG) (the uncoated LPG, grating period: 110 µm) shows almost no change in its attenuation bands of LP_{019}. The attenuation band of the detection LPG (Det-LPG) (grating period: 111.5 µm) in the same cladding mode, on the other hand, shows a further development with the band at phase matching condition separating further indicating the attachment of MIP nanoparticles as a result of the increase of surrounding RI and effective thickness of fibre.



(a)



(b)

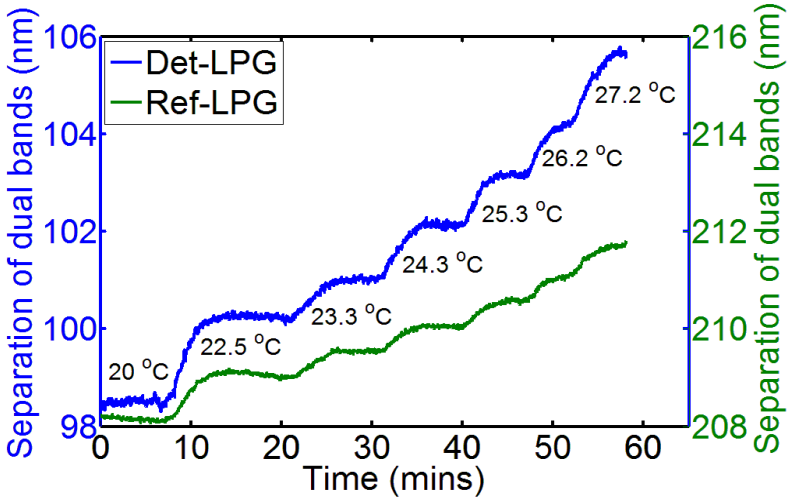
Fig 9.4 (a) SEM image of the MIP nanoparticles on the optical fibre; Scale bar= 100 nm. (b)The transmission spectrum of the LPG array before and after the attachment of MIP nanoparticles.

9.3.2 Temperature calibration of the LPG array

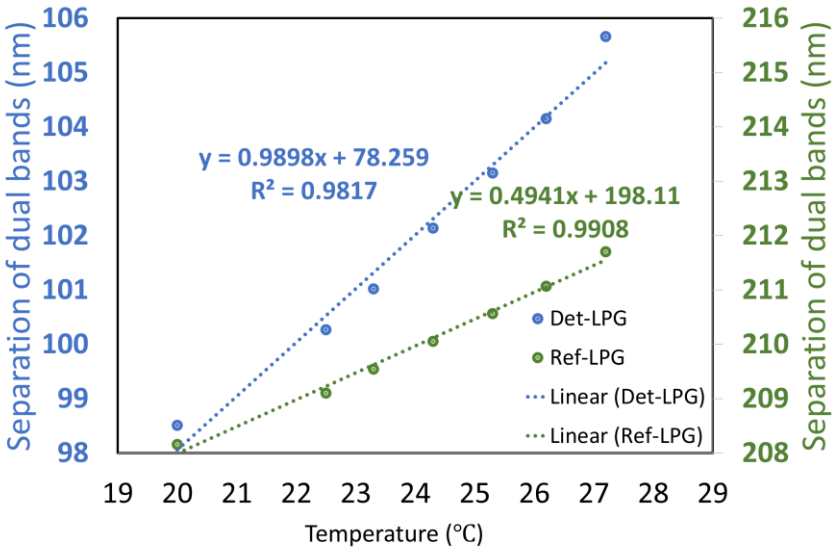
Fig 9.5a demonstrates the sensor response of the LPG array sensor to temperature. Both LPG sensors (detection and reference) exhibit a step increase as the temperature increases from 20 ℃ to 27 ℃. The temperature value labelled in the stabilised region of Fig 9.5a is taken from the average temperature value measured by the thermocouple during the same time period, and the temperature fluctuation (standard deviation) is less than 0.02 ℃. The calibration of two LPGs (coated and bare LPG) to temperature is shown in Fig 9.5b, in which both LPGs exhibit a linear response to the temperature. Each point in Fig 9.5b is the mean value of the step corresponding to Fig 9.5a. The sensitivity of those two LPGs is 0.49 nm/℃ and 0.99 nm/℃, respectively. And the detection LPG (coated LPG) shows a higher sensitivity to the reference LPG (bare LPG) by a factor of 2. The higher sensitivity of detection LPG is because its attenuation at LP_{019} is closer to the PMTP than that of reference LPG. Therefore, to subtract the temperature effect of the detection LPG sensor, the following equation can be applied:

$$\Delta\lambda = \Delta\lambda_{det} - 2 \times \Delta\lambda_{ref} \quad (9.1)$$

Where $\Delta\lambda$ is the wavelength shift induced by the binding, $\Delta\lambda_{det}$ and $\Delta\lambda_{ref}$ is the wavelength shift of the detection LPG and reference LPG, respectively.



(a)



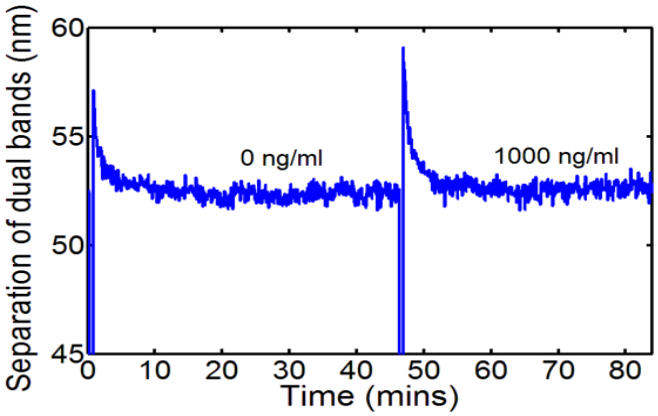
(b)

Fig 9.5 (a) The wavelength of the two LPGs in response to temperature. (b) Linear fitting of the wavelength to temperature. Error bars are smaller than the marker size.

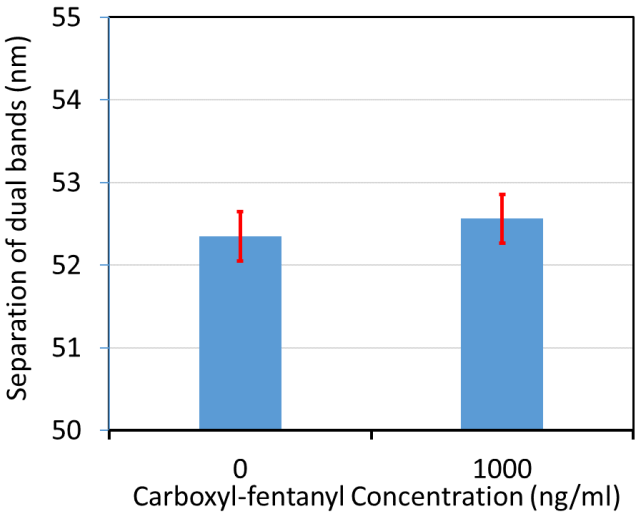
9.3.3 Detection of carboxyl-fentanyl

Fig 9.6 shows the wavelength response of the bare LPG sensor in a blank sample (solvent only, methanol/water=1:3 v/v) and a 1000 ng/mL of carboxyl-fentanyl

solution. Average wavelength separation of LP_{019} in the blank sample and 1000 ng/mL carboxyl-fentanyl solution is 52.3 ± 0.3 nm and 52.5 ± 0.3 nm respectively as shown in Fig 9.6b. The wavelength difference is about 0.2 nm which is less than the noise level (0.3 nm). Therefore, it is clear that the bare LPG sensor does not respond to carboxyl-fentanyl at all due to lack of receptors as no wavelength difference can be observed. Besides, it also demonstrates that there is no bulk RI change caused by the concentration of carboxyl-fentanyl between the range of detection (up to 1000 ng/mL).



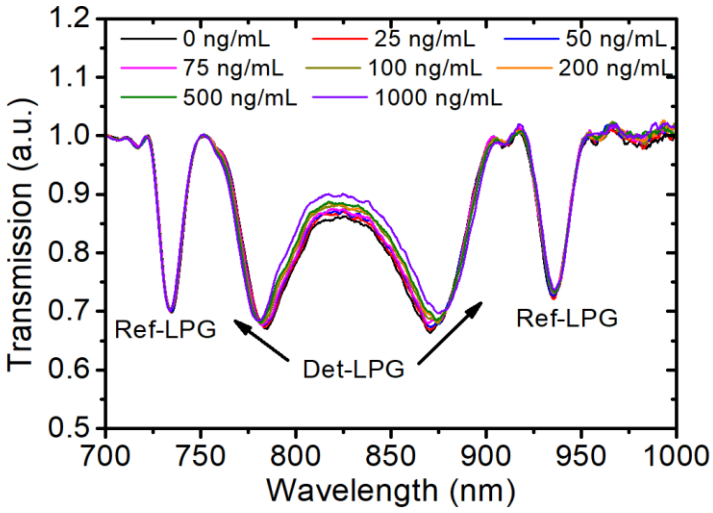
(a)



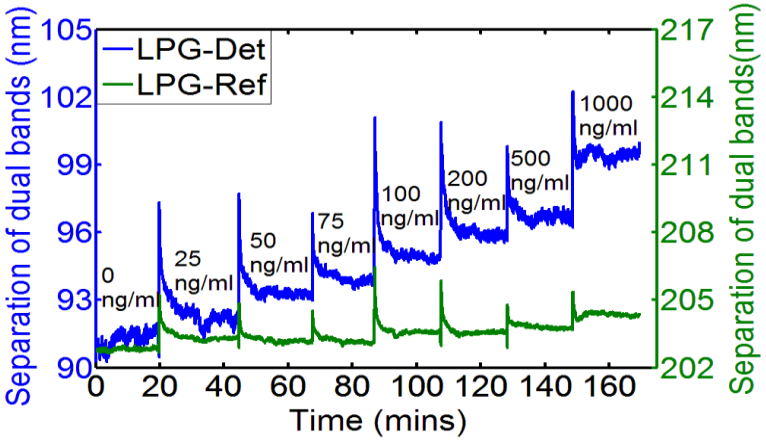
(b)

Fig 9.6 (a) Wavelength sepration of LP_{019} in 0 and 1000 ng/mL carboxyl-fentanyl solution as a function of time; (b) The average wavelength separation in 0 and 1000 ng/mL. Error bar represents the standard deviation of wavelength in each solution.

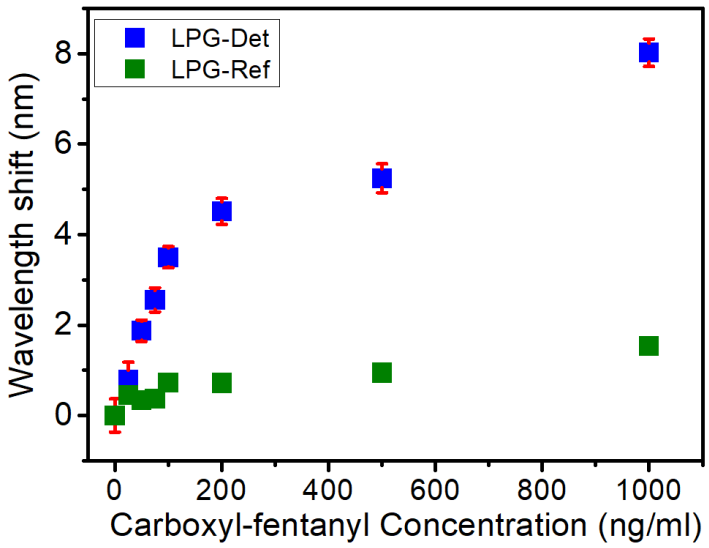
The response of the LPG array sensor to carboxyl-fentanyl is illustrated in Fig 9.7. Fig 9.7a demonstrates the transmission spectrum of the LPG array sensor in different concentrations of carboxyl-fentanyl. The attenuation bands of the detection LPG exhibits a shift in wavelengths, the dual bands at the LP_{019} shift to the opposite direction and the separation of the dual bands increase as a result of binding. The attenuation bands of the reference LPG, on the other hand, do not show an obvious change compared to the detection LPG. The wavelength separation of the dual bands of the two LPGs is illustrated in Fig 9.7b as a function of time during the measurement. There is a clear step change for the detection LPG that follows the step increase of the concentration of carboxyl-fentanyl in the solution from 0 to 1000 ng/mL. The wavelength shift of the LPGs caused by each concentration is shown in Fig 9.7c, in which the average wavelength shift increases as increasing the concentration from 0 to 1000 ng/mL. The error bar represents the fluctuation of the wavelength signal in each step. The wavelength shift in the reference LPG is caused by the temperature fluctuation during each measurement. Fig 9.7d shows the wavelength shift of the detection LPG after subtracting the temperature effect from the reference LPG by using Eq 9.1. The wavelength shift is thus the exclusive response to the binding of carboxyl-fentanyl. The wavelength exhibits a gradual saturation as the increase of the concentration indicating the gradual saturation of the capture sites. The data fits well to the Langmuir adsorption isotherm (described in Eq 6.2, Chapter 6) with a coefficient of determination value R^2=0.9629 ($p<0.05$). The Langmuir-Freundlich turns into Langmuir fitting as the best fitting appears when the heterogeneity parameter β=1. The binding constant and maximum wavelength shift are determined as 0.0053 $(ng/mL)^{-1}$ and 5.4 nm, respectively. The minimum detectable concentration is 50 ng/mL which corresponds to a wavelength shift of 1.20±0.2 nm. The biggest wavelength shift is observed as 4.95± 0.3 nm at the concentration of 1000 ng/mL.


0 ng/mL
25 ng/mL
50 ng/mL
75 ng/mL
100 ng/mL
200 ng/mL
500 ng/mL
1000 ng/mL
Transmission (a.u.)
Wavelength (nm)
Ref-LPG
Det-LPG
Ref-LPG

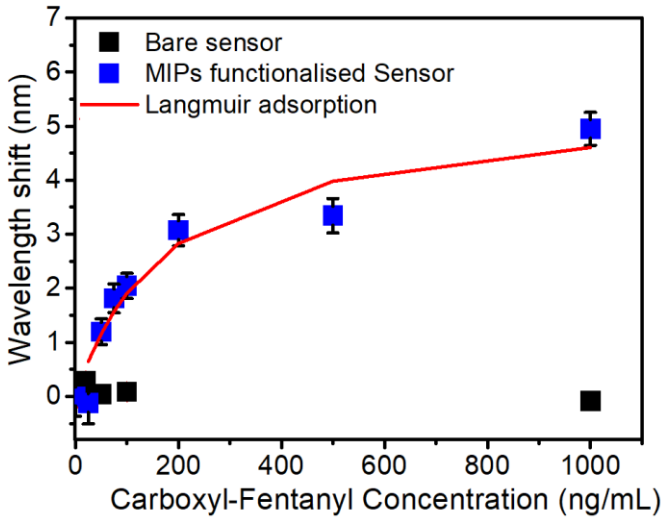
(a)


LPG-Det
LPG-Ref
Separation of dual bands (nm)
Separation of dual bands(nm)
Time (mins)
0 ng/ml
25 ng/ml
50 ng/ml
75 ng/m
100 ng/ml
200 ng/ml
500 ng/ml
1000 ng/ml

(b)


LPG-Det
LPG-Ref
Wavelength shift (nm)
Carboxyl-fentanyl Concentration (ng/ml)

(c)

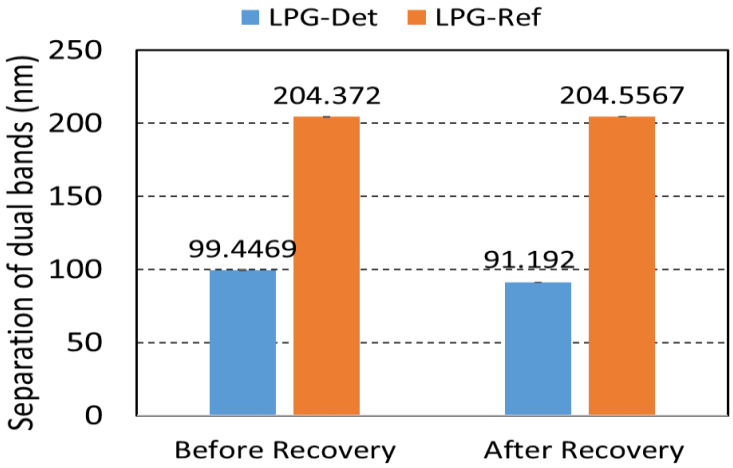


(d)

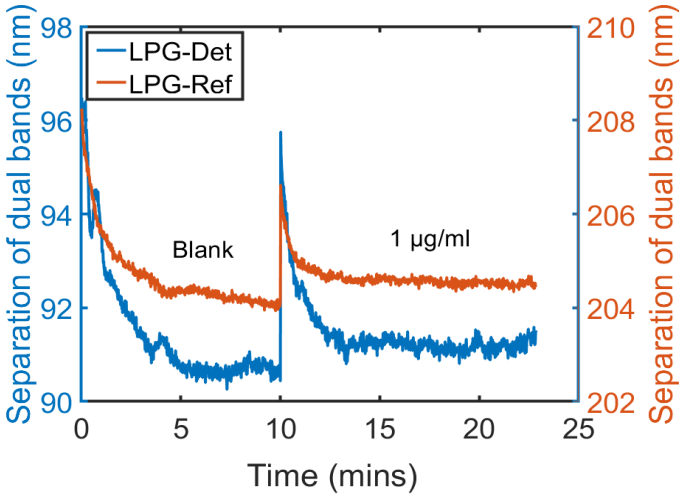
Fig 9.7 (a) The transmission spectrum of the LPG array in different concentration of carboxyl-fentanyl solution range from 1 to 1000 ng/mL. (b) The wavelength of the LPGs responses dynamically to the concentration of carboxyl-fentanyl. (c) The wavelength shift of the detection LPG in contrast to the reference LPG as a function of the concentration. (d) The detection LPG response to the carboxyl-fentanyl concentration after subtracting the temperature effect from the reference LPG; the red curve is the Langmuir adsorption isotherm.

The functionalised LPG sensor is then investigated for the reversibility test. According to the figure in Fig 9.8a, the saturated LPG array sensor after the immersion in boiling methanol exhibits a reverse signal change with the detection LPG shifts about -8.3 nm and reference LPG shift to about 0.2 nm. The negative shift of the wavelength in the detection LPG is attributed to the release of carboxyl-fentanyl from the MIP nanoparticles on the LPG surface as a result of reducing surrounding RI. The magnitude of the wavelength shift is bigger than shift induced by the binding (~5 nm), this most plausibly indicates that some of MIP nanoparticles are removed from the fibre during the immersion. The response of the recovered sensor to carboxyl-fentanyl is illustrated in Fig 9.8b, in which the wavelength separation of both LPGs undergoes a shift from blank sample to 1 µg/mL indicating there is a rise of temperature from the blank sample to the carboxyl-fentanyl solution. After subtracting the temperature effect by using the Eq 9.1, the wavelength shift induced by the carboxyl-fentanyl is -0.11 ± 0.17nm indicating there is no sensitivity to

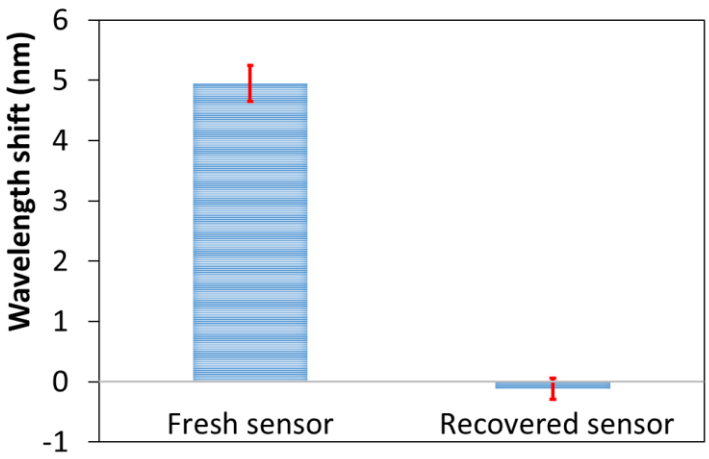
carboxyl-fentanyl after the sensor recovery. The sensitivity comparison of a fresh sensor and the recovery test is shown in Fig 9.8c as the recovered sensor shifts about 0 nm compared to ~5 nm in a fresh sensor. The loss of ability of the sensor in detecting carboxyl-fentanyl probably attributes to the loss of MIP nanoparticles coating after the recovery test.



(a)



(b)



(c)

Fig 9.8 (a) The comparison of the wavelength separation of the LPG array sensor before and after recovery with hot methanol. (b) The wavelength separation of the recovered detection LPG response to 1 µg/mL carboxyl-fentanyl in contrast to the reference LPG. (c) The sensitivity comparison of the recovery LPG to the fresh LPG sensor. Both results are subtracted from temperature effect from the reference LPG.

The mechanism of removal the MIP nanoparticles from the optical fibre sensor surface by using hot methanol is not clear. Further work is needed to test the cross-sensitivity of such sensor with molecules that are similar to fentanyl anlogues for the assessment of the specificity of the developed sensor, examples like other drugs such as cocaine and morphine. And most importantly to validate the developed sensor for detecting of fentanyl which is the ultimate aim of the project and is of significance for clinical application.

9.4 Conclusion

A sensor that detects carboxyl-fentanyl is fabricated based on an LPG array sensing system with one LPG (grating period: 111.5 µm) functionalised with MIP nanoparticles which acts as the receptors for carboxyl-fentanyl and the other LPG (grating period: 110 µm) as the reference sensor for compensation of the temperature effect. Both LPGs operate at phase matching condition of the cladding mode LP_{019} and exhibit different temperature sensitivities of 0. 49 nm/ °C and 0.99 nm/°C for the reference LPG and detection LPG, respectively. The LPG sensor that is coated with the MIP nanoparticles shows an increase of wavelength separation

as a result of carboxyl-fentanyl binding with the concentration from 0 to 1000 ng/mL. The minimum detectable concentration is 50 ng/mL with a wavelength shift of 1.20 ± 0.2 nm. The maximum wavelength shift is 4.95 ± 0.3 nm that corresponds to the concentration of carboxyl-fentanyl of 1000 ng/mL after subtracting the temperature effect from the reference LPG. An attempt to reverse the binding on the LPG is done by immersing the LPG into boiling methanol (~65 ℃). However, it appears that the particles are removed from the fibre surface as well, as the magnitude of the wavelength shift after the immersion is larger than the shift induced by the binding. Consequently, the sensor loses its ability to detect carboxyl-fentanyl.

Chapter 10 Conclusion and future work

5.12 Summary of current work

An FOS uses an optical fibre either as the sensing transducer that converts the external measurands into an optical signal or the medium to transmit the signal from a remote transducer. It generally has a small diameter of about a hundred microns and requires much small measurement volume. The optical method has numerous advantages over conventional electronic systems regarding the operation in harsh environments such as corrosive, high voltage, high EMI or RFI environment. Such advantages have boosted its application in healthcare sectors [5-7]. Fibre optic chemical sensor or biosensor is typically made in the combination of an optical fibre sensing system and a chemical transducer. This section summarises the study of the fibre optic bio-/chemical sensor for the detection of proteins (i.e. streptavidin and human IgM), the measurement of gases (i.e. CO_2, RH and NH_3) and the detection of drug (i.e. fentanyl) which are proposed in the previous Chapters. The detailed conclusion for each presented sensor is explicated below along with a discussion of the further work in Section 10.2.

Chapter 3 introduces the fabrication of an LPG sensor by using UV irradiation. Two methods depending on the order of grating point being inscribed on the photo-sensitive optical fibre are introduced: the point-by-point method and amplitude mask method. The point-by-point fabrication method provides more flexibility in fabricating a sensor with any designed period. In the latter method, one mask can only produce one fixed grating period. However, it takes longer time (~2 hours) for fabricating a typical 3 cm length of LPG than the latter (20 mins). The amplitude mask method is used if the required grating period matches one of the masks. The transmission spectrum of an LPG can be simulated by using the software *Optigrating* that helps to estimate the grating period of the desired LPG spectrum for the practical LPG fabrication, especially for the PMTP whose attenuation bands are very sensitive to the grating period. The depth of the attenuation band of an LPG sensor is determined by the grating length and RI modulation based on the experimental and simulation result. A longer length and a larger RI modulation produce a deeper band.

An LPG sensor operating at the PMTP of the cladding mode LP_{019} is experimentally characterised, and it exhibits a temperature sensitivity of 1 nm/℃, a strain sensitivity of -2.2 X 10^{-3} nm/με and an RI sensitivity of 407 nm/RIU. A reflection mode LPG is fabricated by coating one side of the LPG with a silver mirror through a redox reaction.

Nanoparticles, due to their unique physical, chemical and electronic properties, can be applied to configure and improve the measurement in biosensing. Chapter 4 described the chemical process for the synthesis of SiNPs and AuNPs for the application in sensor configuration and biosensing. SiNPs synthesised by using Stöber method exhibits a uniform spherical size and a narrow size distribution. The size is manipulated by adjusting the molar ratio of the reactant to the catalyst. The obtained SiNPs have a size range from 200 to 300 nm. AuNPs are synthesised through a redox reaction in which the Au^{3+} is reduced to Au^0 and further grows into a nanosphere; the concentration of the reducing agent determines the size of particles and also affects the stability of the colloid, insufficient reducing agent results in agglomeration and poor sample quality. Besides, the type of reducing agent also affects the size of the gold particle due to different reaction kinetics. AuNPs with a size range from 15 nm to 25 nm were prepared by using sodium citrate as a reducing agent by following the Turkevich method and failed to produce even smaller size due to the kinetic limit. The average size of ~3 nm of the gold solution was prepared by using sodium borohydride as a reducing agent following the Bonnard method.

Two LPG biosensors are presented in Chapter 6 for the detection of streptavidin and human IgM after being modified with relevant bio-receptor (i.e. biotin and anti-IgM) anchored Si-Au composite nanoparticles. SiNPs are initially deposited on the LPG surface via an LBL method, and then further packaged with ~3 nm of AuNPs forming a gold shell around the SiNPs. The streptavidin sensor shows a high sensitivity of 6.9 nm/(ng/mm^2) and a LOD of 0.86 pg/mm^2 for the tested range from 1.25 nM to 2.7 μM. The fabricated IgM sensor shows a sensitivity of 11 nm / (ng/mm^2) and an LOD of 15 pg/mm^2 for detecting the human IgM from the buffer solution. The sensor exhibits high specificity to detect IgM that would enable the sensor to be applied in clinical POC for the diagnosis of IgM related diseases.

CO_2 is the exhaust gas of the human body generated from the tissue breath. It is an important biomarker for evaluating the functionality of the respiration system [52] and the micro-circulation of the skin [57]. Chapter 7 described the development of a fibre optic CO_2 sensor that uses a pH dye (thymol blue) and a phase transfer (TMAH) co-doped inside of a silica film via a sol-gel method and coated on the tip of the optical fibre via a dip-coating method. The coated film on the tip of the optical fibre acts as a cavity (length of ~6 µm) for the FPI sensor. Such a sensor demonstrates the ability to measure gaseous CO_2 and RH simultaneously with the reflection change caused by the dye reflecting the change of CO_2 concentration and the central wavelength of the interference peak indicating the level of RH. The RH is another important biomarker in managing the micro-environment of the skin. The ability to measure dual parameters by using a single film makes the sensor superior to the general structure of the fibre optic chemical sensor (e.g. evanescent field sensor, general tip based reflection sensor without interference). The sensor was tested in the CO_2 atmosphere with concentration up to 6 % and the reflection value change about 18 % in response to 5 % of CO_2. The wavelength of the FPI exhibits a linear response to the RH for the tested range from 0 up to 90 % of RH with a sensitivity of 0.14 nm/%RH. The FPI sensor was successfully applied for measuring the CO_2 and RH from a breath sample with a percent error of 3.1 % and 2.2 % of the reading from commercial CO_2 datalogger, respectively. Suffering from the long response time of the FPI sensor for CO_2 (98 s) and RH (32 s), the FPI cannot be applied for measuring CO_2 and RH from breath-to-breath (required response time < 200ms). However, the reported FPI is suitable for measuring the CO_2 and RH in the application where the response time is less important, and the principle exhibits potential of making a low-cost, portable and quantitative CO_2 sensor for the supporting endotracheal intubation in emergency medicine.

The ability to measure multiple parameters is probably the advanced pursuit for an FOS as it will extend the potential applications of the FOS and obtain an advantage over the single measurement sensor. In Chapter 8, a novel approach is introduced by integrating two sensitive dyes (Thymol blue and TSPP) with differential spectral property into one fibre sensing detection system for the simultaneous measurement

of CO_2 and NH_3 in the gas phase. Due to the limitation in the pH of the two dyes for the sensing purpose, they are doped separately into a matrix film and dip coated on the two tips of an optical fibre coupler which integrates the optical signal from two tips to one optical detector. The spectrum obtained from the optical detector contains the spectral information for both dyes, and it revealed that three distinct wavelengths (705 nm, 511 nm and 600nm) in the spectrum corresponding to the absorbance of the two dyes respond to NH_3 and CO_2 respectively with negligible cross-talk. The sensor was tested in the CO_2 atmosphere with a concentration range from 0 to 6 % and NH_3 concentration range up to 210 ppm. The sensor shows an logarithmic increase in the intensity of 600 nm to response the concentration of CO_2 with ~15 % increase of intensity for response to ~5 % of CO_2. The intensity ratio of 705 nm over 511 nm shows a linear response to the concentration of gaseous NH_3 with a sensitivity of 0.003/ppm and a LOD of 3.9 ppm. For the breath gas analysis, the sensor should be able to measure NH_3 down to 50 ppb containing CO_2 concentration of about 4 % [317]. Despite low sensitivity to NH_3 for the application of breath gas analysis, the FOS offers the opportunity of exploring applications where both gases are required to be measured.

Chapter 9 introduces the work in developing a biosensor for measuring fentanyl which is an analgesic agent in the POC to maintain anaesthesia in critically ill patients. An FOS is developed by functionalizing an LPG with MIP nanoparticles which selectively bind to fentanyl molecules or its analogue for the detection of fentanyl from the liquid. A reference LPG was inscribed to the fibre for compensating the temperature effect to the measurement. The sensor was tested into the different concentration of carboxyl-fentanyl solution range from 25 ng/mL up to 1000 ng/mL. The wavelength of the LPG array sensor shows a gradual saturation as increasing the concentration of carboxyl-fentanyl in the solution with a minimum detectable concentration is 50 ng/mL. Due to the time limitation for my PhD, the cross-sensitivity of the sensor is not done. Despite of the high structural similarity between carboxyl-fentanyl and fentanyl (carboxyl-fentanyl is modified fentanyl with carboxyl group), the pharmaceutical role can be different (not clear about the pharmaceutical role of carboxyl-fentanyl). The binding behaviour of the two molecules should be the

same as they share the same binding sites with the nano MIPs. However, the sensor response is not guaranteed as they may create different refractive index change. Therefore, the sensor still needs to be validated to be able to demonstrate the sensitivity to fentanyl drug.

5.13 Future work

The currently proposed sensors described above are characterised in the laboratory to demonstrate proof of concept. To approve the reliability in clinical use, more tests are required to be done to validate the performance of such sensors in the complex clinical environment with massive clinical trials. The details of technical improvements for each specific sensor is described below.

The proposed LPG based IgM sensor is only with single LPG in which the temperature needs to be strictly controlled for the measurement. For the practical use, a reference LPG should be considered to be added into the detection system to compensate the temperature and bulk RI effect from the blood sample. As temperature could affect the equilibrium constant of antigen-antibody reaction [318], the sensor may have a different response at a different temperature. For the application in clinical POC, the effect of temperature to the sensor response to IgM should be investigated.

The proposed FPI CO_2 sensor has demonstrated the ability to measure CO_2 and RH from human breath. However, the breath gas measurement was carried out in a sampling bag under the help of an HME to avoid the condensation of water. The use of the HME makes the set-up relatively large. An optical fibre packaging technique [319] can be applied to accommodate the fibre tip into a tube perforated at the tip and covered with a gas permeable membrane, e.g. polytetrafluoroethylene (PTFE) membrane. Such a configuration would allow the gases permeate through the membrane and block out the condensed water. Thus the packaged sensor tip can be directly applied to a patient's mouth without considering the water condensation to the surface of sensor. Due to the limitation of response and recovery time, the proposed sensor cannot measure CO_2 from breath-to-breath, further work can be carried out by reducing the thickness of the film which may reduce the time of CO_2

diffusing into film, but a higher dye concentration is likely to be used for producing sufficient colour change for compensating the reduced film thickness. Drying the film at supercritical condition will leads to highly porous silica aerogel film which may also help to improve the sensor response time [320].

For the integrated NH_3 and CO_2 sensor in Chapter 8, the sensitivity to NH_3 can be optimised by adjusting the concentration of TSPP doped in the film before applying it for the breath gas analysis. And more of work should be done in investigating the interference of RH to the fibre sensors. The same fibre sensor package technique described above can be applied for this sensor to remove the water condensation for the breath gas measurement. The two films contain the two dyes for NH_3 and CO_2 may be integrated into a composite film by casting one film on the top of another on the tip of an optical fibre with a gas permeable membrane (e.g. PTFE) in between to stop the ion exchange and maintains two separate pH of the two films. In this case, the reported two-tip sensor may be converted into a one-tip sensor system which provides an even smaller size than the current two-tip sensor.

For the reported carboxyl-fentanyl sensor, the cross-sensitivity test needs to be done to evaluate the specificity of the developed sensor. Sensor measurement with fentanyl needs to be further investigated in order to claim the the sensor is able to detect fentanyl drug for the clinical application.

Bibliography

[1] MARKETSANDMARKETS. Biosensors Market by Application, Technology, Product, and Geography-Global Forecast to 2022 (2017).

[2] R.L. Riley, THe work of breathing and its relation to respiratory acidosis, Annals of Internal Medicine 41(1) (1954) 172-176.

[3] Ł. Dziuda, Fiber-optic sensors for monitoring patient physiological parameters: A review of applicable technologies and relevance to use during magnetic resonance imaging procedures, Journal of biomedical optics 20(1) (2015) 010901.

[4] V. Mishra, N. Singh, U. Tiwari, P. Kapur, Fiber grating sensors in medicine: Current and emerging applications, Sensors and Actuators A: Physical 167(2) (2011) 279-290.

[5] D. Tosi, S. Poeggel, I. Iordachita, et al., Fiber Optic Sensors for Biomedical Applications, Opto-Mechanical Fiber Optic Sensors (2018) 301-333.

[6] R. Correia, S. James, S.W. Lee, S.P. Morgan, S. Korposh, Biomedical application of optical fibre sensors, Journal of Optics 20(7) (2018) 073003.

[7] M. Ding, G. Brambilla, Optical fibres and sensors for biomedical applications, Biophotonics for Medical Applications, Woodhead Publishing (2015) 53-78.

[8] A.G. Mignani, F. Baldini, Fibre-optic sensors in health care, Physics in Medicine & Biology 42(5) (1997) 967.

[9] T. Togawa, T. tamura, P.A. Oberg, Biomedical Sensors and Instruments, 2nd ed., CRC Press: Boca Raton (2011).

[10] D. Tosi, E.G. Macchi, G. Braschi, et al., Fiber-optic combined FPI/FBG sensors for monitoring of radiofrequency thermal ablation of liver tumors: ex vivo experiments, Appl. Opt. 53(10) (2014) 2136-2144.

[11] J.W. Arkwright, I.D. Underhill, S.A. Maunder, et al., Design of a high-sensor count fibre optic manometry catheter for in-vivo colonic diagnostics, Opt. Express 17(25) (2009) 22423-22431.

[12] E.G. Macchi, D. Tosi, G. Braschi, et al., Optical fiber sensors-based temperature distribution measurement in ex vivo radiofrequency ablation with submillimeter resolution, J Biomed Opt 19(11) (2014) 117004.

[13] S.A. Grant, R.S. Glass, A sol–gel based fiber optic sensor for local blood pH measurements, Sensors and Actuators B: Chemical 45(1) (1997) 35-42.

[14] N. Nath, S.R. Jain, S. Anand, Evanescent wave fibre optic sensor for detection of L. donovani specific antibodies in sera of kala azar patients, Biosensors and Bioelectronics 12(6) (1997) 491-498.

[15] L.K. Cao, G.P. Anderson, F.S. Ligler, et al., Detection of Yersinia pestis fraction 1 antigen with a fiber optic biosensor, Journal of Clinical Microbiology 33(2) (1995) 336-341.

[16] L. Dziuda, F.W. Skibniewski, M. Krej, et al., Monitoring respiration and cardiac activity using fiber Bragg grating-based sensor, IEEE Transactions on Biomedical Engineering 59(7) (2012) 1934-1942.

[17] H. Jafarzadeh, Laser Doppler flowmetry in endodontics: a review, International Endodontic Journal 42(6) (2009) 476-490.

[18] G.A. Thibodeau, The lymphatic system and immunity, Structure and function of the body, Elsevier (2012) 309-315.

[19] Janeway CA Jr, Travers P, Walport M, e. al., The Humoral Immune Response.

, 5th ed., New York: Garland Science (2001).

[20] J.S. Fellah, M.V. Wiles, J. Charlemagne, et al., Evolution of vertebrate IgM: complete amino acid sequence of the constant region of Ambystoma mexicanum μ chain deduced from cDNA sequence, European Journal of Immunology 22(10) (1992) 2595-2601.

[21] D.J. Vick, W.A. Hogge, D.E. Normansell, e. al, Determination of Normal Human Fetal Immunoglobulin M Levels, Clinical And Diagnostic Laboratory Immunology 2(1) (1995) 115–117.

[22] S.A. Haider, Serum IgM in Diagnosis of Infection in the Newborn, Archives of Disease in Childhood 47(253) (1972) 382-393.

[23] J.R.C. Lima, M.Z. Rouquayrol, M.R.M. Callado, et al., Interpretation of the presence of IgM and IgG antibodies in a rapid test for dengue: analysis of dengue antibody prevalence in Fortaleza City in the 20th year of the epidemic, Revista da Sociedade Brasileira de Medicina Tropical 45 (2012) 163-167.

[24] M.R. Ehrenstein, C.A. Notley, The importance of natural IgM: scavenger, protector and regulator, Nat Rev Immunol 10(11) (2010) 778-786.

[25] J.T. Cassidy, G.L. Nordby, Human serum immunoglobulin concentrations: Prevalence of immunoglobulin deficiencies, Journal of Allergy and Clinical Immunology 55(1) (1975) 35-48.

[26] G.T. Hermanson, Introduction to Bioconjugation, Elservier (2013) 1-125.

[27] H.H. Nguyen, J. Park, S. Kang, et al., Surface plasmon resonance: a versatile technique for biosensor applications, Sensors 15(5) (2015) 10481-510.

[28] Y.S. Fung, Y.Y. Wong, Self-Assembled Monolayers as the Coating in a Quartz Piezoelectric Crystal Immunosensor To Detect Salmonella in Aqueous Solution, Analytical Chemistry 73(21) (2001) 5302-5309.

[29] C.H.M.J. Van Elssen, H. Clausen, et al., Flow cytometry-based assay to evaluate human serum MUC1-Tn antibodies, Journal of Immunological Methods 365(1) (2011) 87-94.

[30] I. Abdel-Hamid, P. Atanasov, A.L. Ghindilis, et al., Development of a flow-through immunoassay system, Sensors and Actuators B: Chemical 49(3) (1998) 202-210.

[31] H. Mukundan, A.S. Anderson, W.K. Grace, et al., Waveguide-based biosensors for pathogen detection, Sensors 9(7) (2009) 5783-809.

[32] G.L. Duveneck, A.P. Abel, M.A. Bopp, et al., Planar waveguides for ultra-high sensitivity of the analysis of nucleic acids, Analytica Chimica Acta 469(1) (2002) 49-61.

[33] Y.F.S. Seah, H. Hu, C.A. Merten, Microfluidic single-cell technology in immunology and antibody screening, Molecular Aspects of Medicine 59 (2018) 47-61.

[34] D. Eicher, C.A. Merten, Microfluidic devices for diagnostic applications, Expert Review of Molecular Diagnostics 11(5) (2011) 505-519.

[35] Y. Hsin Chang, T.C. Chang, E.-F. Kao, et al., Detection of protein A produced by Staphylococcus aureus with a fiber-optic-based biosensor, Bioscience, biotechnology, and biochemistry 60(10) (1996) 1571-1574.

[36] J.-F. Masson, L. Obando, S. Beaudoin, et al., Sensitive and real-time fiber-optic-based surface plasmon resonance sensors for myoglobin and cardiac troponin I, Talanta 62(5) (2004) 865-870.

[37] A. Leung, P. Shankar, R. Mutharasan, Real-time monitoring of bovine serum albumin at femtogram/mL levels on antibody-immobilized tapered fibers, Sensors and Actuators B: Chemical 123(2) (2007) 888-895.

[38] P.V. Preejith, C.S. Lim, A. Kishen, et al., Total protein measurement using a fiber-optic evanescent wave-based biosensor, Biotechnology Letters 25(2) (2003) 105-110.

[39] B.J. Tromberg, M.J. Sepaniak, T. Vo-Dinh, et al., Fiber-optic chemical sensors for competitive binding fluoroimmunoassay, Analytical chemistry 59(8) (1987) 1226-1230.

[40] S.M. Tripathi, W.J. Bock, P. Mikulic, et al., Long period grating based biosensor for the detection of Escherichia coli bacteria, Biosensors and Bioelectronics 35(1) (2012) 308-312.

[41] R.A. Darnall, The role of CO(2) and central chemoreception in the control of breathing in the fetus and the neonate, Respiratory physiology & neurobiology 173(3) (2010) 201-212.

[42] M.I. Canto, E.C. Gorospe, E.J. Shin, et al., Carbon Dioxide (CO2) Cryotherapy Is a Safe and Effective Treatment of Barrett's Esophagus (BE) with HGD/Intramucosal Carcinoma, Gastrointestinal Endoscopy 69(5) (2009) AB341.

[43] M. Perrin, A. Fletcher, Laparoscopic abdominal surgery, Continuing Education in Anaesthesia Critical Care & Pain 4(4) (2004) 107-110.

[44] R.K.L. Wong, Postoperative Pulmonary Atelectasis, CHEST 40(3) (1961) 302-307.

[45] P.R. Murray, H. Masur, Current Approaches to the Diagnosis of Bacterial and Fungal Bloodstream Infections for the ICU, Critical care medicine 40(12) (2012) 3277-3282.

[46] C.R. Mahon, G. Manuselis, Textbook of diagnostic microbiology, Elsevier (2011) 873-889.

[47] K. Dabrowski, J. Glogowski, Studies on the role of exogenous proteolytic enzymes in digestion processes in fish, Hydrobiologia 54(2) (1977) 129-134.

[48] I. Björck, Y. Granfeldt, H. Liljeberg, et al., Food properties affecting the digestion and absorption of carbohydrates, The American journal of clinical nutrition 59(3) (1994) 699S-705S.

[49] B. Alberts, A. Johnson, J. Lewis, et al., How cells obtain energy from food, (2002).

[50] G.A. Thibodeau, The respiratory system, Structure and function of the body Elsevier(2012) 338-341.

[51] J.B. West, Gas transport by the blood, Respiratory physiology: the essentials, Wolters Kluwer (2012) 93-103.

[52] H.S. Joanne, D.N. David, J.B. McManus, et al., Clinical study of multiple breath biomarkers of asthma and COPD (NO, CO_2 , CO and N_2O) by infrared laser spectroscopy, Journal of Breath Research 5(3) (2011) 037108.

[53] M.S. BHENDE, A.E. THOMPSON, D.F. HOWLAND, Validity of a disposable end-tidal carbon dioxide detector in verifying endotracheal tube position in piglets, Critical Care Medicine 19(4) (1991) 566-568.

[54] A.-M. Kelly, S. Klim, Agreement between arterial and transcutaneous PCO2 in patients undergoing non-invasive ventilation, Respiratory Medicine 105(2) (2011) 226-229.

[55] D. Gozal, Sleep-disordered breathing and school performance in children, Pediatrics 102(3) (1998) 616-620.

[56] J.H. Storre, F.S. Magnet, M. Dreher, et al., Transcutaneous monitoring as a replacement for arterial PCO2 monitoring during nocturnal non-invasive ventilation, Respiratory Medicine 105(1) (2011) 143-150.

[57] P. Mirtaheri, T. Gjovaag, P.R. Worsley, et al., A review of the role of the partial pressure of carbon dioxide in mechanically loaded tissues: the canary in the cage singing in tune with the pressure ulcer mantra, Ann Biomed Eng 43(2) (2015) 336-47.

[58] B. Stuart, Infrared Spectroscopy: Fundamentals and Applications, John Wiley and Sons (2004).

[59] S. Sivaramakrishnan, R. Rajamani, B.D. Johnson, Dynamic Model Inversion Techniques for Breath-by-Breath Measurement of Carbon Dioxide from Low Bandwidth Sensors, IEEE Sensors Journal 10(10) (2010) 1637-1646.

[60] B.R. Jones, M.J. Dorsey, Sensitivity of a disposable end-tidal carbon dioxide detector, Journal of Clinical Monitoring 7(3) (1991) 268-270.

[61] S.M. Kanan, O.M. El-Kadri, I.A. Abu-Yousef, et al., Semiconducting metal oxide based sensors for selective gas pollutant detection, Sensors 9(10) (2009) 8158-96.

[62] J.W. Severinghaus, A.F. Bradley, Electrodes for Blood PO_2 and PCO_2 Determination, Journal of Applied Physiology 13(3) (1958) 515-520.

[63] J.U. White, Very long optical paths in air, J. Opt. Soc. Am. 66(5) (1976) 411-416.

[64] G. Stewart, F.A. Muhammad, B. Culshaw, Sensitivity improvement for evanescent-wave gas sensors, Sensors and Actuators B: Chemical 11(1) (1993) 521-524.

[65] W. Jin, H.L. Ho, Y.C. Cao, et al., Gas detection with micro- and nano-engineered optical fibers, Optical Fiber Technology 19(6) (2013) 741-759.

[66] F. Yang, W. Jin, Y. Lin, et al., Hollow-Core Microstructured Optical Fiber Gas Sensors, Journal of Lightwave Technology 35(16) (2017) 3413-3424.

[67] J. Chen, A. Hangauer, R. Strzoda, et al., Sensitivity Limits for Near- Infrared Gas Sensing with Suspended-core PCFs directly coupled with VCSELs, OSA Publishing (2010) JThB7.

[68] H. Segawa, E. Ohnishi, Y. Arai, et al., Sensitivity of fiber-optic carbon dioxide sensors utilizing indicator dye, Sensors and Actuators B: Chemical 94(3) (2003) 276-281.

[69] K. Wysokinski, M. Napierala, T. Stanczyk, et al., Study on the Sensing Coating of the Optical Fibre CO_2 Sensor, Sensors 15(12) (2015) 31888-903.

[70] Royce N. Dansby-Sparks, Jun Jin, et al., Fluorescent-Dye-Doped Sol-Gel Sensor for Highly Sensitive Carbon Dioxide Gas Detection below Atmospheric Concentrations, Anal. Chem 82 (2010) 593–600.

[71] C.-W. Wu, C.-C. Chiang, Sandwiched Long-Period Fiber Grating Fabricated by MEMS Process for CO_2 Gas Detection, Micromachines 7(3) (2016) 35.

[72] A. Mills, Q. Chang, Colorimetric polymer film sensors for dissolved carbon dioxide, Sensors and Actuators B: Chemical 21(2) (1994) 83-89.

[73] P. Wolkoff, Indoor air humidity, air quality, and health – An overview, International Journal of Hygiene and Environmental Health 221(3) (2018) 376-390.

[74] A.V. Arundel, E.M. Sterling, J.H. Biggin, et al., Indirect health effects of relative humidity in indoor environments, Environmental Health Perspectives 65 (1986) 351-361.

[75] G.D. Winter, Formation of the Scab and the Rate of Epithelization of Superficial Wounds in the Skin of the Young Domestic Pig, Nature 193 (1962) 293.

[76] F.U. Hernandez, S.P. Morgan, B.R. Hayes-Gill, et al., Characterization and Use of a Fiber Optic Sensor Based on PAH/SiO_2 Film for Humidity Sensing in Ventilator Care Equipment, IEEE Transactions on Biomedical Engineering 63(9) (2016) 1985-1992.

[77] D. Gomez, S.P. Morgan, B.R. Hayes-Gill, et al., Polymeric optical fibre sensor coated by SiO2 nanoparticles for humidity sensing in the skin microenvironment, Sensors and Actuators B: Chemical 254 (2018) 887-895.

[78] A. Tetelin, V. Pouget, J.L. Lachaud, et al., Dynamic behavior of a chemical sensor for humidity level measurement in human breath, IEEE Transactions on Instrumentation and Measurement 53(4) (2004) 1262-1267.

[79] A.F.P.v. Putten, M.J.A.M.v. Putten, M.H.P.M.v. Putten, et al., Multisensor microsystem for pulmonary function diagnostics, IEEE Sensors Journal 2(6) (2002) 636-643.

[80] P.H. Breen, Importance of Temperature and Humidity in the Measurement of Pulmonary Oxygen Uptake per Breath During Anesthesia, Annals of Biomedical Engineering 28(9) (2000) 1159-1164.

[81] Shinzo Muto, Hiroshi Sato, Toshiki Hosaka, Optical Humidity Sensor Using Fluorescent Plastic Fiber and Its Application to Breathing-Condition Monitor, Japanese Journal of Applied Physics 33(10R) (1994) 6060.

[82] Y. Xiao, J. Zhang, X. Cai, et al., Reduced graphene oxide for fiber-optic humidity sensing, Opt. Express 22(25) (2014) 31555-31567.

[83] M. Konstantaki, S. Pissadakis, S. Pispas, et al., Optical fiber long-period grating humidity sensor with poly(ethylene oxide)/cobalt chloride coating, Appl. Opt. 45(19) (2006) 4567-4571.

[84] X.F. Huang, D.R. Sheng, K.F. Cen, et al., Low-cost relative humidity sensor based on thermoplastic polyimide-coated fiber Bragg grating, Sensors and Actuators B: Chemical 127(2) (2007) 518-524.

[85] S.F. Correia, P. Antunes, E. Pecoraro, et al., Optical fiber relative humidity sensor based on a FBG with a di-ureasil coating, Sensors 12(7) (2012) 8847-60.

[86] W. Xu, W.-B. Huang, X.-G. Huang, et al., A simple fiber-optic humidity sensor based on extrinsic Fabry–Perot cavity constructed by cellulose acetate butyrate film, Optical Fiber Technology 19(6, Part A) (2013) 583-586.

[87] J.E. Ryer-Powder, Health effects of ammonia, Plant/Operations Progress 10(4) (1991) 228-232.

[88] P.E. Heckelman, J.F. Kinneary, M.J. O'Neil, et al., The Merck index: an encyclopedia of chemicals, drugs, and biologicals (1996).

[89] W.J. Visek, Ammonia metabolism, urea cycle capacity and their biochemical assessment, Nutrition reviews 37(9) (1979) 273-282.

[90] A.J. Vince, S.M. Burridge, Ammonia production by intestinal bacteria: the effects of lactose, lactulose and glucose, Journal of medical microbiology 13(2) (1980) 177-91.

[91] W. Ament, J.R. Huizenga, E. Kort, et al., Respiratory ammonia output and blood ammonia concentration during incremental exercise, International journal of sports medicine 20(2) (1999) 71-77.

[92] L.R. Narasimhan, W. Goodman, C.K.N. Patel, Correlation of breath ammonia with blood urea nitrogen and creatinine during hemodialysis, Proceedings of the National Academy of Sciences 98(8) (2001) 4617-4621.

[93] D.J. Kearney, T. Hubbard, D. Putnam, Breath Ammonia Measurement in Helicobacter pylori Infection, Digestive Diseases and Sciences 47(11) (2002) 2523-2530.

[94] F. Winquist, A. Spetz, I. Lundström, B. Danielsson, Determination of ammonia in air and aqueous samples with a gas-sensitive semiconductor capacitor, Analytica Chimica Acta 164(C) (1984) 127-138.

[95] C.N. Xu, N. Miura, Y. Ishida, et al., Selective detection of NH_3 over NO in combustion exhausts by using Au and MoO3 doubly promoted WO3 element, Sensors and Actuators, B: Chemical 65(1) (2000) 163-165.

[96] A.L. Kukla, Y.M. Shirshov, S.A. Piletsky, Ammonia sensors based on sensitive polyaniline films, Sensors and Actuators, B: Chemical 37(3) (1996) 135-140.

[97] R.M. Tiggelaar, T.T. Veenstra, R.G.P. Sanders, et al., Analysis systems for the detection of ammonia based on micromachined components modular hybrid versus monolithic integrated approach, Sensors and Actuators, B: Chemical 92(1-2) (2003) 25-36.

[98] G.H. Mount, B. Rumburg, J. Havig, et al., Measurement of atmospheric ammonia at a dairy using differential optical absorption spectroscopy in the mid-ultraviolet, Atmospheric Environment 36(11) (2002) 1799-1810.

[99] B. Timmer, W. Olthuis, A.v.d. Berg, Ammonia sensors and their applications—a review, Sensors and Actuators B: Chemical 107(2) (2005) 666-677.

[100] A. Yimit, K. Itoh, M. Murabayashi, Detection of ammonia in the ppt range based on a composite optical waveguide pH sensor, Sensors and Actuators, B: Chemical 88(3) (2003) 239-245.

[101] J.W. Erisman, R. Otjes, A. Hensen, et al., Instrument development and application in studies and monitoring of ambient ammonia, Atmospheric Environment 35(11) (2001) 1913-1922.

[102] Q. Zhou, D. Kritz, L. Bonnell, et al., Porous plastic optical fiber sensor for ammonia measurement, Appl. Opt. 28(11) (1989) 2022-2025.

[103] W. Cao, Y. Duan, Optical fiber-based evanescent ammonia sensor, Sensors and Actuators B: Chemical 110(2) (2005) 252-259.

[104] S. Korposh, S. Kodaira, W. Batty, et al., Nanoassembled thin-film gas sensor II. An intrinsic highly sensitive fibre-optic sensor for ammonia detection, Sensor. Mater 21(4) (2009) 179-189.

[105] Z.L. Poole, P. Ohodnicki, R. Chen, et al., Engineering metal oxide nanostructures for the fiber optic sensor platform, Opt. Express 22(3) (2014) 2665-2674.

[106] G. Dooly, H. Manap, S. O'Keeffe, et al., Highly Selective Optical Fibre Ammonia Sensor for use in Agriculture, Procedia Engineering 25 (2011) 1113-1116.

[107] G. Kamarchuk, A. Pospelov, I. Kushch, Sensors for Exhaled Gas Analysis: An Analytical Review, Elsevier (2013) 264-300.

[108] M.F.Philip, W.H. Peng, M.M.F.Alan N. Sandler, A Review of the Use of Fentanyl Analgesia in the Management of Acute Pain in Adults Anesthesiology 90(2) (1999) 576-599.

[109] A.S. Black, G.N. Newcombe, J.L. Plummer, et al., Spinal anaesthesia for ambulatory arthroscopic surgery of the knee: a comparison of low-dose prilocaine

and fentanyl with bupivacaine and fentanyl, BJA: British Journal of Anaesthesia 106(2) (2011) 183-188.

[110] R. Rubin, Illicit fentanyl driving opioid overdose deaths, JAMA 318(22) (2017) 2174-2174.

[111] G.K. Gourlay, S.R. Kowalski, J.L. Plummer, et al., Fentanyl Blood Concentration-Analgesic Response Relationship in the Treatment of Postoperative Pain, Anesthesia & Analgesia 67(4) (1988) 329-337.

[112] J.R. Gill, P.T. Lin, L. Nelson, Reliability of postmortem fentanyl concentrations in determining the cause of death, Journal of medical toxicology : official journal of the American College of Medical Toxicology 9(1) (2013) 34-41.

[113] M. Michiels, R. Hendriks, J. Heykants, A sensitive radioimmunoassay for fentanyl. Plasma level in dogs and man, European journal of clinical pharmacology 12(2) (1977) 153-8.

[114] S.R. Kowalski, G.K. Gourlay, D.A. Cherry, et al., Sensitive gas liquid chromatography method for the determination of fentanyl concentrations in blood, Journal of pharmacological methods 18(4) (1987) 347-55.

[115] J. Schuttler, P.F. White, Optimization of the radioimmunoassays for measuring fentanyl and alfentanil in human serum, Anesthesiology 61(3) (1984) 315-20.

[116] R.J. Woestenborghs, D.R. Stanski, J.C. Scott, et al., Assay methods for fentanyl in serum: gas-liquid chromatography versus radioimmunoassay, Anesthesiology 67(1) (1987) 85-90.

[117] S. Korposh, I. Chianella, A. Guerreiro, et al., Selective vancomycin detection using optical fibre long period gratings functionalised with molecularly imprinted polymer nanoparticles, The Analyst 139(9) (2014) 2229-2236.

[118] T.H. Nguyen, S.A. Hardwick, T. Sun, et al., Intrinsic Fluorescence-Based Optical Fiber Sensor for Cocaine Using a Molecularly Imprinted Polymer as the Recognition Element, IEEE Sensors Journal 12(1) (2012) 255-260.

[119] L. Wen-xu, C. Jian, Continuous Monitoring of Adriamycin in Vivo Using Fiber Optic-Based Fluorescence Chemical Sensor, Analytical Chemistry 75(6) (2003) 1458-1462.

[120] L. Li, H. Ding, B. Di, et al., Rapid detection of propofol in whole blood using an automated on-line molecularly imprinted pretreatment coupled with optical fibre detection, Analyst 137(23) (2012) 5632-8.

[121] F. Xiao, G.S. Chen, J.L. Hulsey, Monitoring bridge dynamic responses using fiber Bragg grating tiltmeters, Sensors 17(10) (2017) 2390.

[122] D. Pugliese, M. Konstantaki, I. Konidakis, et al., Bioresorbable optical fiber Bragg gratings, Opt. Lett. 43(4) (2018) 671-674.

[123] S. Ghetia, R. Gajjar, P. Trivedi, Classification of fiber optical sensors, Int. J. Electron. Commun. Comput. Technol 3 (2013) 442-445.

[124] D. Gloge, Bending Loss in Multimode Fibers with Graded and Ungraded Core Index, Appl. Opt. 11(11) (1972) 2506-2513.

[125] M.J. Adams, An introduction to optical waveguides, Wiley New York (1981).

[126] G. Keiser, Optical Fiber Communications, McGraw-Hill (2000).

[127] J.A. Buck, Fundamentals of optical fibers, John Wiley & Sons (2004).

[128] A.F. Garito, J. Wang, R. Gao, Effects of Random Perturbations in Plastic Optical Fibers, Science 281(5379) (1998) 962-967.

[129] I. Tafur Monroy, H.P.A. vd Boom, A.M.J. Koonen, et al., Data transmission over polymer optical fibers, Optical Fiber Technology 9(3) (2003) 159-171.

[130] S. Wäldchen, J. Lehmann, T. Klein, et al., Light-induced cell damage in live-cell super-resolution microscopy, Scientific Reports 5 (2015) 15348.

[131] C. Eggeling, J. Widengren, R. Rigler, et al., Photobleaching of Fluorescent Dyes under Conditions Used for Single-Molecule Detection: Evidence of Two-Step Photolysis, Analytical Chemistry 70(13) (1998) 2651-2659.

[132] R. DAHL, Light-Emitting Diodes: A Primer. https://www.photonics.com/a36706/Light-Emitting_Diodes_A_Primer. (Accessed 21/May 2018).

[133] L.O. Inc., A primer on photodiodes: The Dominant technology for light detection applications. https://www.advancedphotonix.com/wp-content/uploads/2016/08/Primer-on-Photodiodes.pdf. (Accessed 22-03 2019).

[134] O. Optics, QE Optical Bench Options. http://www.oceanoptics.jp/products/benchoptions_qe.html. (Accessed 21/May 2018).

[135] S.J. Mihailov, Fiber Bragg Grating Sensors for Harsh Environments, Sensors 12(2) (2012) 1898.

[136] D. Wu, T. Zhu, G.-Y. Wang, J.-Y. Fu, X.-G. Lin, G.-L. Gou, Intrinsic fiber-optic Fabry-Perot interferometer based on arc discharge and single-mode fiber, Appl. Opt. 52(12) (2013) 2670-2675.

[137] I. Del Villar, A.B. Socorro, M. Hernaez, et al., Sensors Based on Thin-Film Coated Cladding Removed Multimode Optical Fiber and Single-Mode Multimode Single-Mode Fiber: A Comparative Study, Sensors (2015) 7.

[138] Y.L. Fang, C.T. Wang, C.C. Chiang, A Small U-Shaped Bending-Induced Interference Optical Fiber Sensor for the Measurement of Glucose Solutions, Sensors 16(9) (2016) 1460.

[139] I.S.L. Abdul Hamid, Y. Mustapha Kamil, A. Abd Manaf, et al., Fabrication and characterization of micro fluidic based fiber optic refractive index sensor, Sensing and Bio-Sensing Research 13 (2017) 70-74.

[140] L. M.Tion, Reaction of High Silica Optical Fibers with Hydrofluoric Acid, Journal of the American Ceramic Society 67(2) (1984) C21-C22.

[141] K. Sergiy, S. Kodaira, W. Batty, et al., An Intrinsic Highly Sensitive Fibre Optic Sensor for Ammonia Detection, Sensors and Materials 21(4) (2009) 10.

[142] T.R. Dargaville, B.L. Farrugia, J.A. Broadbent, et al., Sensors and imaging for wound healing: a review, Biosensors & bioelectronics 41 (2013) 30-42.

[143] A.K. Sharma, R. Jha, B.D. Gupta, Fiber-Optic Sensors Based on Surface Plasmon Resonance: A Comprehensive Review, IEEE Sensors Journal 7(8) (2007) 1118-1129.

[144] T.A. Birks, Y.W. Li, The shape of fiber tapers, Journal of Lightwave Technology 10(4) (1992) 432-438.

[145] R. Black, S. Lacroix, F. Gonthier, et al., Tapered single-mode fibres and devices. II. Experimental and theoretical quantification, IEE Proceedings J-Optoelectronics 138(5) (1991) 355-364.

[146] M.I. Zibaii, H. Latifi, M. Karami, et al., Non-adiabatic tapered optical fiber sensor for measuring the interaction between α-amino acids in aqueous carbohydrate solution, Measurement Science and Technology 21(10) (2010) 105801.

[147] C. Teng, N. Jing, F. Yu, et al., Refractive index sensor based on a multi-notched plastic optical fiber, Appl. Opt. 56(7) (2017) 1833-1838.

[148] I. Del Villar, P. Zubiate, C.R. Zamarreño, et al., Optimization in nanocoated D-shaped optical fiber sensors, Opt. Express 25(10) (2017) 10743-10756.

[149] F. De-Jun, Z. Mao-Sen, G. Liu, et al., D-Shaped Plastic Optical Fiber Sensor for Testing Refractive Index, IEEE Sensors Journal 14(5) (2014) 1673-1676.

[150] Y. Wang, M. Yang, G. Zhang, et al., Fiber Optic Hydrogen Sensor Based on Fabry–Perot Interferometer Coated With Sol-Gel Pt/WO3 Coating, Journal of Lightwave Technology 33(12) (2015) 2530-2534.

[151] J. Hromadka, R. Correia, S. Korposh, Fabrication of fiber optic long period gratings operating at the phase matching turning point using an amplitude mask, EWOFS'2016 SPIE (2016) 4.

[152] M.M. Broer, R.L. Cone, J.R. Simpson, Ultraviolet-induced distributed-feedback gratings in Ce(3+) -doped silica optical fibers, Opt Lett 16(18) (1991) 1391-3.

[153] K.O. Hill, B. Malo, F. Bilodeau, et al., Photosensitivity in Eu2+ :Al2O3-Doped-Core Fiber: Preliminary Results and Application to Mode Converters, Optical Fiber Communication, OSA Publisher (1991) PD3.

[154] G. Meltz, W.W. Morey, W.H. Glenn, Formation of Bragg gratings in optical fibers by a transverse holographic method, Opt. Lett. 14(15) (1989) 823-825.

[155] L. Dong, J.L. Cruz, L. Reekie, et al., Enhanced photosensitivity in tin-codoped germanosilicate optical fibers, IEEE Photonics Technology Letters 7(9) (1995) 1048-1050.

[156] P.J. Lemaire, Enhanced UV photosensitivity in fibers and waveguides by high-pressure hydrogen loading, Optical Fiber Communications Conference, OSA Publisher (1995) WN5.

[157] E. Ertorer, M. Haque, J. Li, P.R. Herman, Femtosecond laser filaments for rapid and flexible writing of fiber Bragg grating, Opt. Express 26(7) (2018) 9323-9331.

[158] H.l. Liu, Z.w. Zhu, Y. Zheng, et al., Experimental study on an FBG strain sensor, Optical Fiber Technology 40 (2018) 144-151.

[159] J. Jung, H. Nam, B. Lee, et al., Fiber Bragg grating temperature sensor with controllable sensitivity, Appl. Opt. 38(13) (1999) 2752-2754.

[160] A. Martinez, M. Dubov, I. Khrushchev, et al., Direct writing of fibre Bragg gratings by femtosecond laser, Electronics Letters 40(19) (2004) 1170-1172.

[161] S.J. Mihailov, C.W. Smelser, P. Lu, et al., Fiber Bragg gratings made with a phase mask and 800-nm femtosecond radiation, Opt. Lett. 28(12) (2003) 995-997.

[162] R. Yun-Jiang, In-fibre Bragg grating sensors, Measurement Science and Technology 8(4) (1997) 355.

[163] Y. Pan, T. Liu, J. Jiang, et al., Simultaneous Measurement of Temperature and Strain Using Spheroidal-Cavity-Overlapped FBG, IEEE Photonics Journal 7(6) (2015) 1-6.

[164] L.Y. Shao, Y. Shevchenko, J. Albert, Intrinsic temperature sensitivity of tilted fiber Bragg grating based surface plasmon resonance sensors, Opt. Express 18(11) (2010) 11464-11471.

[165] Q. Wang, C. Liao, L. Xu, et al., Refractive index sensor based on side-polished fiber Bragg grating, 2015 Optoelectronics Global Conference (OGC), 2015, pp. 1-4.

[166] V. Bhatia, Applications of long-period gratings to single and multi-parameter sensing, Opt. Express 4(11) (1999) 457-466.

[167] X. Chen, L. Zhang, K. Zhou, et al., Real-time detection of DNA interactions with long-period fiber-grating-based biosensor, Opt. Lett. 32(17) (2007) 2541-2543.

[168] M.P. DeLisa, Z. Zhang, M. Shiloach, et al., Evanescent Wave Long-Period Fiber Bragg Grating as an Immobilized Antibody Biosensor, Analytical Chemistry 72(13) (2000) 2895-2900.

[169] G. Rego, O. Okhotnikov, E. Dianov, et al., High-temperature stability of long-period fiber gratings produced using an electric arc, Journal of Lightwave Technology 19(10) (2001) 1574-1579.

[170] M. Smietana, W.J. Bock, P. Mikulic, et al., Increasing sensitivity of arc-induced long-period gratings—pushing the fabrication technique toward its limits, Measurement Science and Technology 22(1) (2011) 015201.

[171] M. Yokota, H. Oka, T. Yoshino, Mechanically induced long period fiber grating and its application for distributed sensing, OFS 2002 (2002) 135-138.

[172] T. Erdogan, Cladding-mode resonances in short- and long-period fiber grating filters, J. Opt. Soc. Am. A 14(8) (1997) 1760-1773.

[173] S. Xuewen, Z. Lin, I. Bennion, Sensitivity characteristics of long-period fiber gratings, Journal of Lightwave Technology 20(2) (2002) 255-266.

[174] G. Rego, A review of refractometric sensors based on long period fibre gratings, The Scientific World Journal 2013 (2013).

[175] K. Sarfraz, W.J. Stephen, P.T. Ralph, Enhanced sensitivity fibre optic long period grating temperature sensor, Measurement Science and Technology 13(5) (2002) 792.

[176] Y. Koyamada, Numerical analysis of core-mode to radiation-mode coupling in long-period fiber gratings, IEEE Photonics Technology Letters 13(4) (2001) 308-310.

[177] H. Dobb, K. Kalli, D.J. Webb, Temperature-insensitive long period grating sensors in photonic crystal fibre, Electronics Letters 40(11) (2004) 657-658.

[178] A. Ulman, An Introduction to Ultrathin Organic Films: From Langmuir--Blodgett to Self--Assembly, Academic press (2013).

[179] J.J. Richardson, M. Björnmalm, F. Caruso, Technology-driven layer-by-layer assembly of nanofilms, Science 348(6233) (2015).

[180] K. Katagiri, S.-i. Yamazaki, K. Inumaru, et al., Anti-reflective coatings prepared via layer-by-layer assembly of mesoporous silica nanoparticles and polyelectrolytes, Polymer Journal 47 (2014) 190.

[181] S. Park, U. Han, D. Choi, et al., Layer-by-layer assembled polymeric thin films as prospective drug delivery carriers: design and applications, Biomaterials research 22 (2018) 29-29.

[182] Y. Wang, P.P. Joshi, K.L. Hobbs, et al., Nanostructured Biosensors Built by Layer-by-Layer Electrostatic Assembly of Enzyme-Coated Single-Walled Carbon Nanotubes and Redox Polymers, Langmuir 22(23) (2006) 9776-9783.

[183] L. Liu, L. Marques, R. Correia, et al., S. Korposh, Highly sensitive label-free antibody detection using a long period fibre grating sensor, Sensors and Actuators B: Chemical 271 (2018) 24-32.

[184] B.N. Nunes, L.F. Paula, Í.A. Costa, et al., Layer-by-layer assembled photocatalysts for environmental remediation and solar energy conversion, Journal of Photochemistry and Photobiology C: Photochemistry Reviews 32 (2017) 1-20.

[185] N. Joseph, P. Ahmadiannamini, R. Hoogenboom, et al., Layer-by-layer preparation of polyelectrolyte multilayer membranes for separation, Polymer Chemistry 5(6) (2014) 1817-1831.

[186] J.A. Syed, S. Tang, H. Lu, et al., Smart PDDA/PAA multilayer coatings with enhanced stimuli responsive self-healing and anti-corrosion ability, Colloids and Surfaces A: Physicochemical and Engineering Aspects 476 (2015) 48-56.

[187] I.D. Villar, I.R. Matias, F.J. Arregui, Fiber-optic chemical nanosensors by electrostatic molecular self-assembly, Current Analytical Chemistry 4(4) (2008) 341-355.

[188] A.-M. Pappa, S. Inal, K. Roy, et al., Polyelectrolyte Layer-by-Layer Assembly on Organic Electrochemical Transistors, ACS Applied Materials & Interfaces 9(12) (2017) 10427-10434.

[189] L. Zheng, L. Xiong, Layer-by-layer assembly of PA-EDTA/PAH multilayer films and their potential-switchable electrochemistry, Colloids and Surfaces A: Physicochemical and Engineering Aspects 289(1) (2006) 179-184.

[190] J. Sun, M. Gao, J. Feldmann, Electric Field Directed Layer-by-Layer Assembly of Highly Fluorescent CdTe Nanoparticles, Journal of Nanoscience and Nanotechnology 1(2) (2001) 133-136.

[191] A.P. Ngankam, P.R. Van Tassel, In Situ Layer-by-Layer Film Formation Kinetics under an Applied Voltage Measured by Optical Waveguide Lightmode Spectroscopy, Langmuir 21(13) (2005) 5865-5871.

[192] L. Dieguez, N. Darwish, N. Graf, et al., Electrochemical tuning of the stability of PLL/DNA multilayers, Soft Matter 5(12) (2009) 2415-2421.

[193] F. Boulmedais, C.S.Tang, B.Keller, Controlled Electrodissolution of Polyelectrolyte Multilayers: A Platform Technology Towards the Surface - Initiated Delivery of Drugs, Advanced Functional Materials 16(1) (2006) 63-70.

[194] O. Guillaume-Gentil, N. Graf, F. Boulmedais, et al., Global and local view on the electrochemically induced degradation of polyelectrolyte multilayers: from dissolution to delamination, Soft Matter 6(17) (2010) 4246-4254.

[195] H. Inoue, K. Sato, J.i. Anzai, Disintegration of Layer-by-Layer Assemblies Composed of 2-Iminobiotin-Labeled Poly(ethyleneimine) and Avidin, Biomacromolecules 6(1) (2005) 27-29.

[196] O. Hirofumi, W. Tao, L.S.WOO, Selective Methanol Gas Detection Using a U - Bent Optical Fiber Modified with a Silica Nanoparticle Multilayer, Electronics and Communications in Japan 100(2) (2017) 43-49.

[197] S. Korposh, N. Takahara, J.J. Ramsden, et al., Nano-assembled thin film gas sensors. 1. Ammonia detection by a porphyrin-based multilayer film, Journal of Biological Physics and Chemistry 6(3) (2006) 125-132.

[198] C. Elosua, N. de Acha, D. Lopez-Torres, et al., Luminescent Optical Fiber Oxygen Sensor following Layer-by-layer Method, Procedia Engineering 87 (2014) 987-990.

[199] L.L. Hench, J.K. West, The sol-gel process, Chemical reviews 90(1) (1990) 33-72.

[200] A. Burneau, J. Lepage, G. Maurice, Porous silica-water interactions. I. Structural and dimensional changes induced by water adsorption, Journal of non-crystalline solids 217(1) (1997) 1-10.

[201] K. Teshima, H. Sugimura, Y. Inoue, et al., Gas barrier performance of surface-modified silica films with grafted organosilane molecules, Langmuir 19(20) (2003) 8331-8334.

[202] R. Barabash, V. Zaitsev, T.a.a. Kovalchuk, et al., Low-temperature fluorination of silica by a nonaqueous solution of NH4F, The Journal of Physical Chemistry A 107(22) (2003) 4497-4505.

[203] B.D. MacCraith, C.M. McDonagh, G. O'Keeffe, et al., Sol-gel coatings for optical chemical sensors and biosensors, Sensors and Actuators B: Chemical 29(1–3) (1995) 51-57.

[204] D. Jeon, W. Yoo, J. Seo, et al., Fiber-optic pH sensor based on sol-gel film immobilized with neutral red, OPT REV 20(2) (2013) 209-213.

[205] J. Estella, P. de Vicente, J.C. Echeverría, et al., A fibre-optic humidity sensor based on a porous silica xerogel film as the sensing element, Sensors and Actuators B: Chemical 149(1) (2010) 122-128.

[206] C.S. Chu, Y.L.LO, T.W.Sung, Review on Recent Developments of Fluorescent Oxygen and Carbon Dioxide Optical Fiber Sensors, Photonic Sensors 1(3) (2011) 234-250.

[207] S.S. Prakash, C.J. Brinker, A.J. Hurd, Silica aerogel films at ambient pressure, Journal of Non-Crystalline Solids 190(3) (1995) 264-275.

[208] L.P. Singh, S.K. Bhattacharyya, R. Kumar, et al., Sol-Gel processing of silica nanoparticles and their applications, Advances in Colloid and Interface Science 214 (2014) 17-37.

[209] W. Stöber, A. Fink, E. Bohn, Controlled growth of monodisperse silica spheres in the micron size range, Journal of colloid and interface science 26(1) (1968) 62-69.

[210] T. Yoshioka, E. Nakanishi, T. Tsuru, et al., Experimental studies of gas permeation through microporous silica membranes, AIChE journal 47(9) (2001) 2052-2063.

[211] R.E. Cunningham, R. Williams, Diffusion in gases and porous media, Springer (1980).

[212] C.S. Cheung, S.M. Topliss, S.W. James, et al., Response of fiber-optic long-period gratings operating near the phase-matching turning point to the deposition of nanostructured coatings, J. Opt. Soc. Am. B 25(6) (2008) 897-902.

[213] X. Sun, P. Huang, J. Zhao, et al., Characteristic control of long period fiber grating (LPFG) fabricated by infrared femtosecond laser, Frontiers of Optoelectronics 5(3) (2012) 334-340.

[214] R.Y.N. Wong, E. Chehura, S.E. Staines, et al., Fabrication of fiber optic long period gratings operating at the phase matching turning point using an ultraviolet laser, Appl. Opt. 53(21) (2014) 4669-4674.

[215] S.W. James, R. Tatam, Optical fibre long-period grating sensors: characteristics and application, MEASUREMENT SCIENCE AND TECHNOLOGY 14 (2003) R49–R61.

[216] A. Singh, Study of modeling aspects of long period fiber grating using three-layer fiber geometry, Photonic Sensors 5(1) (2015) 32-42.

[217] H. Haus, W. Huang, S. Kawakami, et al., Coupled-mode theory of optical waveguides, Journal of Lightwave Technology 5(1) (1987) 16-23.

[218] A.M. Vengsarkar, P.J. Lemaire, J.B. Judkins, et al., Long-period fiber gratings as band-rejection filters, Journal of lightwave technology 14(1) (1996) 58-65.

[219] K.O. Hill, Aperiodic Distributed-Parameter Waveguides for Integrated Optics, Appl. Opt. 13(8) (1974) 1853-1856.

[220] A. Yariv, Coupled-mode theory for guided-wave optics, IEEE Journal of Quantum Electronics 9(9) (1973) 919-933.

[221] G.P. Agrawal, A.H. Bobeck, Modeling of distributed feedback semiconductor lasers with axially-varying parameters, IEEE Journal of Quantum Electronics 24(12) (1988) 2407-2414.

[222] Y. Yang, Z. Gu, Comparing and analysis of calculation methods of long-period fiber gratings transmission spectra, Optik - International Journal for Light and Electron Optics 124(15) (2013) 2234-2240.

[223] J.H. Chong, P. Shum, H. Haryono, et al., Measurements of refractive index sensitivity using long-period grating refractometer, Optics Communications 229(1-6) (2004) 65-69.

[224] M. Jiang, A.P. Zhang, Y.-C. Wang, et al., Fabrication of a compact reflective long-period grating sensor with a cladding-mode-selective fiber end-face mirror, Opt. Express 17(20) (2009) 17976-17982.

[225] G. Quero, S. Zuppolini, M. Consales, et al., Long period fiber grating working in reflection mode as valuable biosensing platform for the detection of drug resistant bacteria, Sensors and Actuators B: Chemical 230 (2016) 510-520.

[226] Y. Yin, Z.Y. Li, Z. Zhong, et al., Synthesis and characterization of stable aqueous dispersions of silver nanoparticles through the Tollens process, Journal of Materials Chemistry 12(3) (2002) 522-527.

[227] S.G. Penn, L. He, M.J. Natan, Nanoparticles for bioanalysis, Current Opinion in Chemical Biology 7(5) (2003) 609-615.

[228] G. Doria, J. Conde, B. Veigas, et al., Noble metal nanoparticles for biosensing applications, Sensors 12(2) (2012) 1657-1687.

[229] B. Dubertret, P. Skourides, D.J. Norris, et al., In vivo imaging of quantum dots encapsulated in phospholipid micelles, Science 298(5599) (2002) 1759-1762.

[230] Y. He, H. Yu, Multifunctional gold nanoparticles as signal transducers for fabrication of 1:2 molecular demultiplexer, Analytical and bioanalytical chemistry 407(22) (2015) 6741-6.

[231] M. Han, X. Gao, J.Z. Su, et al., Quantum-dot-tagged microbeads for multiplexed optical coding of biomolecules, Nature Biotechnology 19 (2001) 631.

[232] L. Hirsch, J. Jackson, A. Lee, et al., A whole blood immunoassay using gold nanoshells, Analytical Chemistry 75(10) (2003) 2377-2381.

[233] R.D. Averitt, D. Sarkar, N.J. Halas, Plasmon Resonance Shifts of Au-Coated Au2S Nanoshells: Insight into Multicomponent Nanoparticle Growth, Physical Review Letters 78(22) (1997) 4217-4220.

[234] S. Oldenburg, R. Averitt, S. Westcott, et al., Nanoengineering of optical resonances, Chemical Physics Letters 288(2-4) (1998) 243-247.

[235] N.T.K. Thanh, Z. Rosenzweig, Development of an aggregation-based immunoassay for anti-protein A using gold nanoparticles, Analytical chemistry 74(7) (2002) 1624-1628.

[236] H. Otsuka, Y. Akiyama, Y. Nagasaki, et al., Quantitative and reversible lectin-induced association of gold nanoparticles modified with α-lactosyl-ω-mercapto-poly (ethylene glycol), Journal of the American Chemical Society 123(34) (2001) 8226-8230.

[237] J. Cao, T. Sun, K.T.V. Grattan, Gold nanorod-based localized surface plasmon resonance biosensors: A review, Sensors and Actuators B: Chemical 195 (2014) 332-351.

[238] H. Aldewachi, T. Chalati, M.N. Woodroofe, et al., Gold nanoparticle-based colorimetric biosensors, Nanoscale 10(1) (2018) 18-33.

[239] A. Vincenzo, P. Roberto, F. Marco, et al., Surface plasmon resonance in gold nanoparticles: a review, Journal of Physics: Condensed Matter 29(20) (2017) 203002.

[240] S. Günter, C. Benedetto, Nanoparticulated Gold: Syntheses, Structures, Electronics, and Reactivities, European Journal of Inorganic Chemistry 2003(17) (2003) 3081-3098.

[241] M.H. Jazayeri, H. Amani, A.A. Pourfatollah, et al., Various methods of gold nanoparticles (GNPs) conjugation to antibodies, Sensing and Bio-Sensing Research 9 (2016) 17-22.

[242] R. Shukla, V. Bansal, M. Chaudhary, et al., Biocompatibility of Gold Nanoparticles and Their Endocytotic Fate Inside the Cellular Compartment: A Microscopic Overview, Langmuir 21(23) (2005) 10644-10654.

[243] C.E. E., M. Judith, G. Anand, M.C. J., W.M. D., Gold Nanoparticles Are Taken Up by Human Cells but Do Not Cause Acute Cytotoxicity, Small 1(3) (2005) 325-327.

[244] Z. Li, J.C. Barnes, A. Bosoy, et al., Mesoporous silica nanoparticles in biomedical applications, Chemical Society Reviews 41(7) (2012) 2590-2605.

[245] C.S. Chu, Y.L.Lo, Highly sensitive and linear optical fiber carbon dioxide sensor based on sol–gel matrix doped with silica particles and HPTS, Sensors and Actuators B: Chemical 143(1) (2009) 205-210.

[246] C. Bharti, U. Nagaich, A.K. Pal, et al., Mesoporous silica nanoparticles in target drug delivery system: a review, International journal of pharmaceutical investigation 5(3) (2015) 124.

[247] C. Graf, Q. Gao, I. Schutz, et al., Surface functionalization of silica nanoparticles supports colloidal stability in physiological media and facilitates internalization in cells, Langmuir 28(20) (2012) 7598-613.

[248] L.F. de Oliveira, K. Bouchmella, K.d.A. Gonçalves, et al., Functionalized Silica Nanoparticles As an Alternative Platform for Targeted Drug-Delivery of Water Insoluble Drugs, Langmuir 32(13) (2016) 3217-3225.

[249] S. Korposh, S.W.Lee, S. W. James, et al., Refractive index sensitivity of fibre-optic long period gratings coated with SiO 2 nanoparticle mesoporous thin films, Measurement Science and Technology 22(7) (2011) 075208.

[250] T. Matsoukas, E. Gulari, Monomer-addition growth with a slow initiation step: a growth model for silica particles from alkoxides, Journal of Colloid and Interface Science 132(1) (1989) 13-21.

[251] G. Bogush, C. Zukoski Iv, Studies of the kinetics of the precipitation of uniform silica particles through the hydrolysis and condensation of silicon alkoxides, Journal of Colloid and Interface Science 142(1) (1991) 1-18.

[252] S.K. Park, K. Do Kim, H.T. Kim, Preparation of silica nanoparticles: determination of the optimal synthesis conditions for small and uniform particles,

Colloids and Surfaces A: Physicochemical and Engineering Aspects 197(1-3) (2002) 7-17.

[253] H.G. Barth, Modern methods of particle size analysis, John Wiley & Sons (1984).

[254] J.T. Edward, Molecular volumes and the Stokes-Einstein equation, Journal of Chemical Education 47(4) (1970) 261.

[255] D.K. Carpenter, Dynamic light scattering: with applications to chemistry, biology, and physics, J.Chem.Educ 54(10) (1977).

[256] I. ISO13321, Methods for determination of particle size distribution part 8: Photon correlation spectroscopy, International Organisation for Standardisation (ISO) (1996).

[257] M.I. Limited, Dynamic light scattering common terms defined, 2011. http://www.biophysics.bioc.cam.ac.uk/wp-content/uploads/2011/02/DLS_Terms_defined_Malvern.pdf. (Accessed 06/09 2018).

[258] F. Mafuné, J.y. Kohno, Y. Takeda, et al., Structure and Stability of Silver Nanoparticles in Aqueous Solution Produced by Laser Ablation, The Journal of Physical Chemistry B 104(35) (2000) 8333-8337.

[259] L. N. Ngoc, V. L. Van, K. C. Dinh, et al., Synthesis and optical properties of colloidal gold nanoparticles, Journal of Physics: Conference Series 187(1) (2009) 012026.

[260] G.T. Hermanson, Microparticles and Nanoparticles, Bioconjugate Techniques, Elservier (2013) 580-587.

[261] J. Kimling, M. Maier, B. Okenve, et al., Turkevich Method for Gold Nanoparticle Synthesis Revisited, The Journal of Physical Chemistry B 110 (32) (2006) 15700-15707.

[262] M. Iqbal, G. Usanase, K. Oulmi, et al., Preparation of gold nanoparticles and determination of their particles size via different methods, Materials Research Bulletin 79 (2016) 97-104.

[263] J. Turkevich, P.C. Stevenson, J. Hillier, A study of the nucleation and growth processes in the synthesis of colloidal gold, Discussions of the Faraday Society 11 (1951) 55-75.

[264] A. Kang, D.K. Park, S.H. Hyun, et al., pH-dependent size distribution of gold nanoparticles investigated by in situ pH-monitoring throughout the synthetic reaction, Chemical Physics Letters 639 (2015) 230-233.

[265] M. Horisberger, M.F. Clerc, Labelling of colloidal gold with protein A. A quantitative study, Histochemistry 82(3) (1985) 219-23.

[266] C. Bonnard, D. Papermaster, J. Kraehenbuhl, The streptavidin-biotin bridge technique: application in light and electron microscope immunocytochemistry, Immunolabelling for electron microscopy (1984) 95-111.

[267] J. Polte, T.T. Ahner, F. Delissen, et al., Mechanism of Gold Nanoparticle Formation in the Classical Citrate Synthesis Method Derived from Coupled In Situ XANES and SAXS Evaluation, Journal of the American Chemical Society 132(4) (2010) 1296-1301.

[268] W. Haiss, N.T.K. Thanh, J. Aveyard, et al., Determination of Size and Concentration of Gold Nanoparticles from UV−Vis Spectra, Analytical Chemistry 79(11) (2007) 4215-4221.

[269] L. Marques, F.U. Hernandez, S.W. James, et al., Highly sensitive optical fibre long period grating biosensor anchored with silica core gold shell nanoparticles, Biosensors & bioelectronics 75 (2016) 222-31.

[270] M. Gambhir, S. Gupta, Review of Turn around Point Long Period Fiber Gratings, Journal of Sensor Technology 05(04) (2015) 81-89.

[271] D.G. Kinniburgh, General purpose adsorption isotherms, Environmental Science & Technology 20(9) (1986) 895-904.

[272] C.A. Barrios, M.J. Bañuls, V. González-Pedro, et al., Label-free optical biosensing with slot-waveguides, Opt. Lett. 33(7) (2008) 708-710.

[273] M. Barisik, S. Atalay, A. Beskok, et al., Size dependent surface charge properties of silica nanoparticles, The Journal of Physical Chemistry C 118(4) (2014) 1836-1842.

[274] Z. Abbas, C. Labbez, S. Nordholm, et al., Size-dependent surface charging of nanoparticles, The Journal of Physical Chemistry C 112(15) (2008) 5715-5723.

[275] M. Kobayashi, F. Juillerat, P. Galletto, et al., Aggregation and charging of colloidal silica particles: effect of particle size, Langmuir 21(13) (2005) 5761-5769.

[276] M. Porus, P. Maroni, M. Borkovec, Structure of adsorbed polyelectrolyte monolayers investigated by combining optical reflectometry and piezoelectric techniques, Langmuir 28(13) (2012) 5642-5651.

[277] L. Viau, T. Vrlinic, F.E. Jurin, et al., Elaboration of thin colloidal silica films with controlled thickness and wettability, Comptes Rendus Chimie 19(5) (2016) 665-673.

[278] I.D. Villar, I.R. Matías, F.J. Arregui, et al., Optimization of sensitivity in Long Period Fiber Gratings with overlay deposition, Opt. Express 13(1) (2005) 56-69.

[279] P.C. Weber, D.H. Ohlendorf, J.J. Wendoloski, et al., Structural Origins of High-Affinity Biotin Binding to Streptavidin, Science 243(4887) (1989) 85-88.

[280] J. Wong, A. Chilkoti, V.T. Moy, Direct force measurements of the streptavidin–biotin interaction, Biomolecular Engineering 16(1–4) (1999) 45-55.

[281] M. S. Art, E.C. Dyson, A.J. deMello, et al., Monitoring of Real-Time Streptavidin−Biotin Binding Kinetics Using Droplet Microfluidics, Analytical Chemistry 80(18) (2008) 7063-7067.

[282] G. Kemmer, S. Keller, Nonlinear least-squares data fitting in Excel spreadsheets, Nat Protoc 5(2) (2010) 267-81.

[283] J. Hromadka, R. Correia, S. Korposh, Fabrication of fiber optic long period gratings operating at the phase matching turning point using an amplitude mask, SPIE (2016) 99160Y.

[284] F.J. Arregui, Sensors based on nanostructured materials, Springer (2011).

[285] R. Saber, S. Sarkar, P. Gill, et al., High resolution imaging of IgG and IgM molecules by scanning tunneling microscopy in air condition, Scientia Iranica 18(6) (2011) 1643-1646.

[286] D.M. Czajkowsky, Z. Shao, The human IgM pentamer is a mushroom-shaped molecule with a flexural bias, Proc Natl Acad Sci U S A 106(35) (2009) 14960-5.

[287] W.R. Wong, O. Krupin, S.D. Sekaran, et al., Serological Diagnosis of Dengue Infection in Blood Plasma Using Long-Range Surface Plasmon Waveguides, Analytical Chemistry 86(3) (2014) 1735-1743.

[288] M.F. Goldstein, A.L. Goldstein, E.H. Dunsky, et al., Selective IgM immunodeficiency: retrospective analysis of 36 adult patients with review of the literature, Annals of Allergy, Asthma & Immunology 97(6) (2006) 717-730.

[289] M.F. Goldstein, A.L. Goldstein, E.H. Dunsky, et al., Pediatric Selective IgM Immunodeficiency, Clinical and Developmental Immunology 2008 (2008) 624850.

[290] J. Hromadka, S. Korposh, M.C. Partridge, et al., Multi-parameter measurements using optical fibre long period gratings for indoor air quality monitoring, Sensors and Actuators B: Chemical 244 (2017) 217-225.

[291] D. Atias, Y. Liebes, V. Chalifa-Caspi, et al., Chemiluminescent optical fiber immunosensor for the detection of IgM antibody to dengue virus in humans, Sensors and Actuators B: Chemical 140(1) (2009) 206-215.

[292] J. Choi, A.W. Gani, D.J.B. Bechstein, et al., Portable, one-step, and rapid GMR biosensor platform with smartphone interface, Biosensors and Bioelectronics 85 (2016) 1-7.

[293] C.J. Brinker, Sol-gel Science, Academic Press (1990).

[294] L. Liu, F. Hao, S.P. Morgan, et al., A reflection-mode fibre-optic sensor for breath carbon dioxide measurement in healthcare, Sensing and Bio-Sensing Research 22 (2019) 100254.

[295] H. Zhang, R.H. Byrne, Spectrophotometric pH measurements of surface seawater at in-situ conditions: absorbance and protonation behavior of thymol blue, Marine Chemistry 52(1) (1996) 17-25.

[296] A. Mills, Q. Chang, N. McMurray, Equilibrium studies on colorimetric plastic film sensors for carbon dioxide, Analytical Chemistry 64(13) (1992) 1383-1389.

[297] W.A. R., Heat and moisture exchangers and breathing system filters: their use in anaesthesia and intensive care. Part 2 – practical use, including problems, and their use with paediatric patients, Anaesthesia 66(1) (2011) 40-51.

[298] R. Wiebe, V. Gaddy, The solubility of carbon dioxide in water at various temperatures from 12 to 40 and at pressures to 500 atmospheres. Critical phenomena, Journal of the American Chemical Society 62(4) (1940) 815-817.

[299] F.J. Millero, T.B. Graham, F. Huang, et al., Dissociation constants of carbonic acid in seawater as a function of salinity and temperature, Marine Chemistry 100(1) (2006) 80-94.

[300] A. Stefánsson, P. Bénézeth, J. Schott, Carbonic acid ionization and the stability of sodium bicarbonate and carbonate ion pairs to 200°C – A potentiometric and spectrophotometric study, Geochimica et Cosmochimica Acta 120 (2013) 600-611.

[301] K. Iwashita, K. Tadanaga, T. Minami, Water permeation properties of SiO2 - RSiO3/2 (R = methyl, vinyl, phenyl) thin films prepared by the sol - gel method on nylon - 6 substrate, Journal of Applied Polymer Science 61(12) (1996) 2173-2177.

[302] S.J. Abhijit, A.P. Aldo, N.G. Kyle, et al., Lattice Boltzmann method for multi-component, non-continuum mass diffusion, Journal of Physics D: Applied Physics 40(23) (2007) 7593.

[303] A. Mills, A. Lepre, L. Wild, Breath-by-breath measurement of carbon dioxide using a plastic film optical sensor, Sensors and Actuators B: Chemical 39(1-3) (1997) 419-425.

[304] C.J. Brinker, G.C. Frye, A.J. Hurd, et al., Fundamentals of sol-gel dip coating, Thin Solid Films 201(1) (1991) 97-108.

[305] R. Selyanchyn, S. Korposh, W. Yasukochi, et al., A Preliminary Test for Skin Gas Assessment Using a Porphyrin Based Evanescent Wave Optical Fiber Sensor1, Sensors & Transducers 125(2) (2011) 54.

[306] K. Ariga, Y. Lvov, T. Kunitake, Assembling Alternate Dye−Polyion Molecular Films by Electrostatic Layer-by-Layer Adsorption, Journal of the American Chemical Society 119(9) (1997) 2224-2231.

[307] S. Takagi, M. Eguchi, D.A. Tryk, et al., Porphyrin photochemistry in inorganic/organic hybrid materials: Clays, layered semiconductors, nanotubes, and mesoporous materials, Journal of Photochemistry and Photobiology C: Photochemistry Reviews 7(2) (2006) 104-126.

[308] M.A. Castriciano, A. Romeo, V. Villari, et al., Structural Rearrangements in 5,10,15,20-Tetrakis(4-sulfonatophenyl)porphyrin J-Aggregates under Strongly Acidic Conditions, The Journal of Physical Chemistry B 107(34) (2003) 8765-8771.

[309] P.K. Dasgupta, S. Dong, Solubility of ammonia in liquid water and generation of trace levels of standard gaseous ammonia, Atmospheric Environment (1967) 20(3) (1986) 565-570.

[310] W. Knoche, Chemical Reactions of CO2 in Water, Biophysics and Physiology of Carbon Dioxide, Springer (1980) 3-11.

[311] G. Vlatakis, L.I. Andersson, R. Müller, et al., Drug assay using antibody mimics made by molecular imprinting, Nature 361(6413) (1993) 645.

[312] K. Smolinska-Kempisty, A. Guerreiro, F. Canfarotta, et al., A comparison of the performance of molecularly imprinted polymer nanoparticles for small molecule targets and antibodies in the ELISA format, Scientific reports 6 (2016) 37638.

[313] C. Alexander, H.S. Andersson, L.I. Andersson, et al., Molecular imprinting science and technology: a survey of the literature for the years up to and including 2003, Journal of Molecular Recognition: An Interdisciplinary Journal 19(2) (2006) 106-180.

[314] F. Canfarotta, A. Poma, A. Guerreiro, et al., Solid-phase synthesis of molecularly imprinted nanoparticles, Nature protocols 11(3) (2016) 443.

[315] R.J. Umpleby II, M. Bode, K.D. Shimizu, Measurement of the continuous distribution of binding sites in molecularly imprinted polymersElectronic, Analyst 125(7) (2000) 1261-1265.

[316] R. Venn, R. Goody, Synthesis and properties of molecular imprints of darifenacin: the potential of molecular imprinting for bioanalysis, Chromatographia 50(7-8) (1999) 407-414.

[317] L. Narasimhan, W. Goodman, C.K.N. Patel, Correlation of breath ammonia with blood urea nitrogen and creatinine during hemodialysis, Proceedings of the National Academy of Sciences 98(8) (2001) 4617-4621.

[318] R. Reverberi, L. Reverberi, Factors affecting the antigen-antibody reaction, Blood transfusion 5(4) (2007) 227.

[319] K. Bremer, M. Meinhardt-Wollweber, T. Thiel, et al., Sewerage tunnel leakage detection using a fibre optic moisture-detecting sensor system, Sensors and Actuators A: Physical 220 (2014) 62-68.

[320] K. Nobuyuki, F. Yoshito, K. Takashi, et al., Preparation of Highly Porous Silica Aerogel Thin Film by Supercritical Drying, Japanese Journal of Applied Physics 39(3A) (2000) L182.